UNIVERSITÄT SIEGEN

Inka Mueller

Inspection of Piezoelectric Transducers used for Structural Health Monitoring Systems

Schriftenreihe der Arbeitsgruppe
für Technische Mechanik
im Institut für Mechanik und Regelungs-
technik - Mechatronik

Herausgeber: Claus-Peter Fritzen

Band 11

Impressum
Prof. Dr.-Ing. Claus-Peter Fritzen
Arbeitsgruppe für Technische Mechanik
Institut für Mechanik und Regelungstechnik – Mechatronik
Universität Siegen
57078 Siegen
ISSN 2191-5601
URN urn:nbn:de:hbz:467-10862
Zugl.: Siegen, Univ., Diss., 2017

Inspection of Piezoelectric Transducers used for Structural Health Monitoring Systems

genehmigte
DISSERTATION
zur Erlangung des Grades eines Doktors
der Ingenieurwissenschaften

vorgelegt von
Inka Mueller, geb. Buethe, M.Sc.
geb. in Hannover

eingereicht bei der Naturwissenschaftlich-Technischen Fakultät
der Universität Siegen
Siegen 2016

Referent: Prof. Dr.-Ing. C.-P. Fritzen
Korreferent: Prof. Dr.-Ing. D. Söffker

Tag der mündlichen Prüfung
22. Dezember 2016

Acknowledgements

The following work was carried out during my time as research assistant at the Institute of Mechanics and Control Engineering - Mechatronics of the University of Siegen in the working group of Prof. Dr.-Ing. C.-P. Fritzen. I would like to sincerely thank him as my supervisor, who put my interest on the research area of Structural Health Monitoring as well as on this specific topic, and as my mentor, supporting me and my work. I would also like to thank Prof. Dr.-Ing. D. Soeffker for reviewing the thesis and taking over the second examiner responsibility, as well as Prof. Dr.-Ing. O. Nelles and Prof. Dr.-Ing. Ch. Zhang for their contributions to the doctoral procedure.

The support of the Studienstiftung des deutschen Volkes (German Academic Scholarship Foundation) during my study and research time is thankfully acknowledged. Parts of this work have also been funded within the EU project Smart Intelligent Aircraft Structures (SARISTU). The motivated team of researchers from all over Europe and especially the work and fruitful discussions with Maria Moix-Bonet from DLR, Martin Bach and Benjamin Eckstein from Airbus Group have encouraged me during this time. Although he might not know, Prof. V. Giurgiutiu has been a great scientific help with his book "Structural Health Monitoring with Piezoelectric Wafer Active Sensors" and valuable discussions at various conferences. Continuing the successful work between the University of Krasnodar, working group Prof. Glushkov, and the University of Siegen, working group Prof. Fritzen, has been a rewarding experience. Especially the collaborative work with Dr. Mikhail Golub and Dr. Alisa Shpak has lead to fruitful discussions and great times in the lab.

Working in the technical committee "Structural Health Monitoring" of the German Association of Non-Destructive Testing (DGZfP), I am grateful to be part of a very supportive community envisioning the future of SHM.

Throughout this work, the team of the working group including current and former members has always been supportive and provided great social times throughout the years. Especially I want to thank Gerhard Dietrich, whose help has most likely saved

me hours in the lab, and Henning Jung, with whom I loved to work regardless the matter, research, teaching or organizational issues. Moreover, I want to thank my former colleague Dr.-Ing. Cheng Yang for the reviewing help and some of my students, Dennis Hüsch and Digvijay Pawar, who have supported my work with their theses.

Last but not least, I want to thank my parents, my sister and my husband for always being supportive and accepting me as I am.

Siegen, January 2017 Inka Mueller

Abstract

This contribution focuses on a detailed analysis of piezoelectric wafer active sensors, aiming to develop and evaluate inspection methodologies. Piezoelectric wafer active sensors are commonly used for active structural health monitoring systems. With the piezoelectric effect they can generate and sense waves, which can interact with the structure and with possible defects in the structure. The method of using these effects is known as acousto-ultrasonics. To enable a self-check of an active structural health monitoring system, an inspection of the piezoelectric wafer active sensors is necessary. Their different possible defects could cause a malfunction of a structural health monitoring system. Either damage of the structure is not detected or an undamaged structure is classified as damaged and false alarm is reported by the structural health monitoring system.

An analysis of the effects of defect piezoelectric wafer active sensors on the generated wave field is presented. It shows that the defects change the wave field in a non-negligible way. This change depends on defect type, defect severity and type of transducer. It has a significant influence on the results of the structural health monitoring system.

In this contribution the electro-mechanical impedance is carefully selected as a physical quantity, which enables to draw conclusions on possible sensor faults. A physical model is developed to show the impact of geometric and material parameters on the electro-mechanical impedance. A numerical model is constructed to calculate the electro-mechanical impedance and the generated wave field with the same model. Moreover, different types of defects are simulated. Experimental studies are set up to validate the models and quantify realistic parameter deviations for different application scenarios. Based on this knowledge, different new model-based and model-free methods for inspecting piezoelectric wafer active transducers are developed.

A novel approach to evaluate the merit of these methods is another focal point of this contribution. Based on statistical methods the performance is measured by combining

the output of an inspection method with the effect of a defect on the result of the structural health monitoring system. When the application of this approach is carried out with numerical methods, the concept of model-assisted probability of detection is used. With the numerical model the electro-mechanical impedance as well as the generated wave field are simulated. The approach allows an application-based statement about the inspection method, used for a self-check.

Keywords: piezoelectric wafer active sensors (PWAS), defects of PWAS, structural health monitoring (SHM), electro-mechanical impedance (EMI), acousto-ultrasonics (AU), guided waves, *Lamb* waves, model-assisted probability of detection (MAPOD)

Kurzfassung

Der Fokus dieser Arbeit liegt in der detaillierten Analyse piezoelektrischer Sensoren, die als dünne Scheibe ausgeführt sind und auch aktiv angeregt werden können. Diese Sensoren werden als PWAS (Piezoelectric Wafer Active Sensors) bezeichnet. Es werden im Rahmen dieser Arbeit Methoden zur Überprüfung von PWAS entwickelt und getestet.

PWAS werden häufig für aktive Structural Health Monitoring (SHM) Systeme eingesetzt. Mithilfe des piezoelektrischen Effekts können sie geführte Wellen anregen und empfangen. Diese geführten Wellen interagieren bei ihrer Ausbreitung mit der Struktur und möglichen Schäden der Struktur. Die Möglichkeit der Nutzung dieser Wellen und Sensoren, Schäden zu detektieren, wird als Acousto-Ultrasonics bezeichnet.

Um eine Systemüberprüfung eines aktiven SHM Systems zu ermöglichen, ist eine Überprüfung der PWAS unabdingbar. Schädigungen verschiedener Art führen zu einer Verschlechterung der Zustandsüberwachungsmöglichkeiten des SHM Systems. Ein geschädigter PWAS kann sowohl dazu führen, dass ein Strukturschaden unentdeckt bleibt, als auch einen falschen Alarm auslösen. Bei einem solchen falschen Alarm wird vom SHM System fälschlicher Weise ein Strukturschaden gemeldet, obwohl nicht die Struktur, sondern ein Teil des SHM Systems, hier ein PWAS, defekt ist.

Die Effekte, die verschiedenartig geschädigte PWAS auf das von ihnen in die Struktur eingebrachte Wellenfeld haben, werden in dieser Arbeit aufgezeigt und analysiert. Die Analyse zeigt, dass der Einfluss auf das Wellenfeld nicht vernachlässigbar ist. Die resultierenden Änderungen sind dabei von der Art und der Größe des Schadens sowie des PWAS Typs abhängig. Das Ergebnis, das von einem SHM System ausgegeben wird, kann durch das geänderte Wellenfeld signifikant beeinflusst werden.

Die elektromechanische Impedanz wird als mögliche physikalische Kenngröße, die zur Überprüfung von PWAS genutzt werden kann, ausgemacht. Im Rahmen der Arbeit erfolgt eine detaillierte Analyse und die Entwicklung von Methoden zur Überprüfung von

PWAS, basierend auf dieser Größe. Ein physikalisch basiertes Modell wird aufgestellt, um den Einfluss von Geometrie- und Materialparametern auf die elektromechanische Impedanz zu untersuchen. Die Verwendung numerischer Methoden zur Modellierung des applizierten PWAS ermöglicht die Analyse des Wellenfeldes und der elektromechanischen Impedanz in einem Modell. Des Weiteren kann eine Modellierung von Schadensfällen verwirklicht werden. Mithilfe experimenteller Daten werden die Modelle validiert und realistische Streubreiten für die analysierten Größen identifiziert. Basierend auf diesen Erkenntnissen erfolgt die Entwicklung neuer modellbasierter und datenbasierter Methoden zur Überprüfung von PWAS.

Die Entwicklung eines neuen innovativen Ansatzes zur Bewertung der Leistungsfähigkeit von PWAS-Überwachungsmethoden stellt einen weiteren Schwerpunkt dieser Arbeit da. Basierend auf statistischen Methoden wird die Güte einer Überwachungsmethode durch die Kombination der Ergebnisse der Methode und der Auswirkungen eines PWAS-Defekts auf das Wellenfeld ermittelt. Wird dieser Ansatz basierend auf numerisch erzeugten Ergebnissen für das Wellenfeld und die elektromechanische Impedanz genutzt, so handelt es sich hierbei um eine modellbasierte Bestimmung der Entdeckungswahrscheinlichkeit für einen PWAS-Fehler (MAPOD - model-assisted probability of detection). Der Ansatz zur Bewertung der Leistungsfähigkeit ermöglicht eine anwendungsbezogene Aussage über den Einsatz der Methode zur PWAS Selbstdiagnose in einem definierten SHM System.

Schlagwörter: piezoelectric wafer active sensors (PWAS), Schädigungen von PWAS, structural health monitoring (SHM), elektromechanische Impedanz (EMI), acousto-ultrasonics (AU), geführte Wellen, *Lamb*wellen, modelbasierte Erkennungswahrscheinlichkeit - model-assisted probability of detection (MAPOD)

Contents

Nomenclature

Abbreviations

AANN	auto-associative neural networks
ARX	auto-regressive with exogenous input
AU	acousto-ultrasonics
CDF	cumulative distribution function
CFRP	carbon fiber reinforced plastic
DFT	discrete *Fourier* transform
DSS	door surround structure
EMI	electro-mechanical impedance
EOC	environmental and operational conditions
EPDM	ethylene propylene diene monomer
EU	European union
FE	finite element
FEM	finite element method
LDV	laser *Doppler* vibrometer
LS	linear spectrum
MAPOD	model-assisted probability of detection
NDT	non-destructive testing
NDE	non-destructive evaluation
PCA	principal component analysis
PDF	probability density function
POD	probability of detection
PSD	power spectral density
PVDF	polyvinylidene flouride
PWAS	piezoelectric wafer active sensor
RMS	root-mean-square value

SARISTU	EU-project “smart intelligent aircraft structures”
SH	shear-horizontal
SHM	structural health monitoring
ToF	time of flight
mil	a thousandth of an inch

Greek parameters

Φ	cumulative distribution function	–
$\delta_e = \tan\delta$	dielectric loss factor	–
η	mechanical loss factor	–
λ	wave length	mm
μ	mean	–
ν	*Poisson*'s ratio	–
ω	angular frequency	–
ρ	density	$\frac{\mathrm{kg}}{\mathrm{m}^3}$
σ	standard deviation for POD	–
τ	standard deviation for regression	–
θ	angle in cylindrical coordinate system	rad
ε	dielectric constant	$\frac{\mathrm{F}}{\mathrm{m}}$
ε_0	dielectric constant in vacuum	$\frac{\mathrm{F}}{\mathrm{m}}$
ε_r	relative dielectric constant	–
ζ	factor for the structural impedance to calculate the admittance of a bonded PWAS	–

Latin parameters

A_n	n^{th} antisymmetric mode	–
A	area	mm^2
B	susceptance = imaginary part of admittance	$\mathrm{S} = \frac{1}{\Omega}$
C	capacitance	F
DI	damage index for PWAS defects	–
E	*Young*'s modulus	$\frac{\mathrm{N}}{\mathrm{m}^2}$

E_c	coercive field	$\frac{\mathrm{V}}{\mathrm{m}}$
G	conductance = real part of admittance	$\mathrm{S} = \frac{1}{\Omega}$
I	current	A
J_n	n^{th} *Bessel* function of the first kind	–
L	inductance	$\frac{\mathrm{s}^2}{\mathrm{F}}$
$Q_m = \frac{1}{\eta}$	mechanical quality factor	–
R	resistance = real part of impedance	Ω
SC	slope coefficient	$\frac{1}{\Omega\mathrm{kHz}}$
SDI	structural damage index	–
S_n	n^{th} symmetric mode	–
T_c	temperature at *Curie* point	°C
V	voltage	V
X	reactance = imaginary part of impedance	Ω
Y	admittance = reciprocal of impedance	$\mathrm{S} = \frac{1}{\Omega}$
Z	impedance (spectrum)	Ω
a	damage size	e.g. mm
$\hat{a}$	measured damage size	e.g. mm
b	regression coefficient, intercept	e.g. –
c_l	longitudinal (=axial=pressure) wave velocity of the unbounded system (3D)	$\frac{\mathrm{m}}{\mathrm{s}}$
c_{l1D}	longitudinal phase velocity in thin rods (1D)	$\frac{\mathrm{m}}{\mathrm{s}}$
c_{l2D}	longitudinal phase velocity in plates (2D)	$\frac{\mathrm{m}}{\mathrm{s}}$
c_{ph}	phase velocity	$\frac{\mathrm{m}}{\mathrm{s}}$
c_{gr}	group velocity	$\frac{\mathrm{m}}{\mathrm{s}}$
c_R	velocity of the *Rayleigh* wave	$\frac{\mathrm{m}}{\mathrm{s}}$
c_S	shear (=transversal) wave velocity of the unbounded system (3D)	$\frac{\mathrm{m}}{\mathrm{s}}$
d_{31}	piezoelectric (strain/charge) coefficient	$\frac{\mathrm{C}}{\mathrm{N}} = \frac{\mathrm{m}}{\mathrm{V}}$
erf	error function	–
f	frequency	Hz
f	maximum likelihood function	–
h	thickness	mm
k	wave number	$\frac{1}{\mathrm{m}}$
k	electro-mechanical coupling coefficient	–

k_{str}	stiffness of the structure	–
k_p	planar coupling coefficient	–
k_P	stiffness of the plate	–
l	length of PWAS	mm
m	regression coefficient, slope	e.g. –
r	radial coordinate	e.g. mm
r_{pwas}	radius of PWAS	mm
t	time	s
u	displacement in z-direction	mm
w	width of PWAS	mm
x	function of a	e.g. –
y	function of $\hat{a}$	e.g. –
z	standardized deviation of $\hat{a}$ from regression	–

Tensors

$\underline{D}$	electrical flux vector, dielectric	
	displacement, charge Q per unit area A	$\frac{\mathrm{C}}{\mathrm{m}^2}$
$\underline{E}$	electric field vector	$\frac{\mathrm{V}}{\mathrm{m}}$
$\mathbf{I}$	*Fisher* information matrix	e.g. –
$\underline{Q}$	charge vector	C
$\mathbf{S}$	strain tensor	$\frac{\mathrm{mm}}{\mathrm{mm}}$
$\mathbf{T}$	stress tensor	$\frac{\mathrm{N}}{\mathrm{m}^2}$
$\mathbf{V}$	covariance matrix	e.g. –
$\mathbf{d}$	piezoelectric (strain/charge) coefficients	$\frac{\mathrm{C}}{\mathrm{N}} = \frac{\mathrm{m}}{\mathrm{V}}$
$\mathbf{g}$	piezoelectric voltage coefficients	$\frac{\mathrm{m}^2}{\mathrm{C}} = \frac{\mathrm{Vm}}{\mathrm{N}}$
$\mathbf{s}$	compliance tensor	$\frac{\mathrm{m}^2}{\mathrm{N}}$
ϕ	matrix with partial derivatives,	
	used for *Wald* method	–
ε	tensor of dielectric constants	$\frac{\mathrm{F}}{\mathrm{m}}$
$\underline{\Theta}$	parameter vector	*var.*

Indices and Superscripts

$1, 2, 3$	*Cartesian* coordinate system with coordinates x, y, z resp. x_1, x_2, x_3
$char$	characteristic
i	counter
p	planar
$pwas$	PWAS
r, θ, z	cylindrical coordinate system
str	structure
thr	threshold
$train$	training
CC	based on the correlation coefficient
CCh	based on the correlation coefficient of the *Hilbert* transform
E	value at constant electric field
H	data of the baseline
D	data of the new state
POD	POD
RMS	based on root mean square
T	value at constant stress

1 Introduction

1.1 Motivation

Regular inspection of various structures is a requirement for their safe use. Monitoring of their conditions is necessary, e.g. for critical infrastructure like bridges as well as aircraft or vessels. Potential methods for an automated and reliable monitoring are of great interest for constructors and operators. Under these circumstances, structural health monitoring (SHM) has been an intriguing research topic in the last decades. Recently, methods based on SHM are at the cutting edge of industrial application.

SHM is known as the continuous or periodical and automated method for monitoring and evaluating the condition of a monitoring subject. It is part of condition monitoring according to DIN ISO 17359. Determination and monitoring is realized by measurements with permanently installed or integrated transducers and the analysis of the measured data. An SHM system consists of the monitoring subject itself with the transducers, the storage unit as well as the signal processing unit and the automated expert system for diagnosis; definition translated from (*FA SHM*, 2014a).

A trustworthy monitoring is possible only if all parts of an SHM system work reliably. This includes a self-check of the integrated transducers. Especially for industrial applications, where the system will maintain its duty over years, this is of great importance and an objective for future work in the field of SHM.

Up to now, monitoring of structures and determination of their state is mainly performed with manual non-destructive testing methods. SHM is an advanced continuation of non-destructive testing methodologies. Procedures of non-destructive testing and monitoring have a long tradition in the human history. Highly sophisticated techniques have been developed especially in the last century, to detect cracks, cavities, or other defects. While e.g. liquid penetration tests can only detect defects open to the surface, X-ray-based methods enable a view inside the material, revealing defects even

in the interior of solid bodies. Ultrasonic testing is state of the art for the detection of defects close to the surface. For ultrasonic testing, elastic waves are generated to interact with a structure, its boundaries, and possible defects. The use of special ultrasonic scanning heads makes it possible to test the material in a specific direction and therefore enables the localization of a structural damage. These methods allow the non-destructive testing over an area under consideration at a certain fixed time.

A common point for advanced testing methods is the use of measurement equipment. The equipment, which is composed of different sensors and actuators, generally includes a self-check, which is executed e.g. after its booting. According to *Kolerus*, traditional condition monitoring systems used for long term monitoring need to include some self-check to ensure the reliability of the system (*Kolerus*, 2008). For the same reason, a self-check is necessary for an integrated SHM system, too.

This work focuses on SHM systems that use piezoelectric transducers, also called piezoelectric wafer active sensor (PWAS). Up to now, these transducers are not checked frequently. In most applications a transducer with proper state is taken for granted, which is in fact not always the case. Therefore an inspection of these transducers is indispensable.

The necessity of this research on this topic was already stated in the late 90's when Friswell and Inman published first works on sensor validation, referring to several kinds of transducers and explicitly including piezoceramic patches (*Friswell* and *Inman*, 1999). It is mentioned in (*Giurgiutiu*, 2014, p. 394) that *"the integrity of the sensor and the consistency of the sensor/structure interface are essential elements that can make or break an experiment"*. *Giurgiutiu* called in-situ self-diagnostic methods of PWAS *"mandatory"* already in 2002, (*Giurgiutiu* and *Zagrai*, 2002). However, still in 2010 *Lee* et al. mention that *"there has been little work on the sensor diagnosis which is applicable to active sensing devices used in SHM applications"* (*Lee* et al., 2010, p. 76). Recently the issue of reliability gains increasing attention, but up to now researchers focus on the reliability of the methods (*Aldrin* et al., 2011; *Chang*, 2014). This point has already been made in (*Boller*, 2000). It leads to the importance of reliability of the equipment in use, including the transducers. This is still a *"challenge"*, e.g. in the aircraft industry (*Dobmann* et al., 2014).

A reliable SHM system is only possible with properly working PWAS. A faulty PWAS will change the signal used for structural damage detection during an actuation and a sensing process. This might lead to false alarms. Depending on the monitored

object, false alarms are not only cost-intensive, but also result in a loss of confidence of stakeholders, such as wind farm operators or aviation companies. Moreover, without a reliability concept the authority approval e.g. by aviation authorities and classification societies is not possible. It has to handle the reliability of the whole SHM system including all parts.

The inspection of piezoelectric transducers is therefore a key feature to bring SHM into industrial application. A detailed description of transducer defects, the development of inspection methodologies, and an approach to evaluate these methodologies are the main objectives of this work.

1.2 Concept of structural health monitoring

For an appropriate setting of this work a short introduction to SHM beyond its pure definition is presented. SHM aims to a continuous or periodical, and automated determination and monitoring of the condition of a structure. The overlying objectives are an improved safety, knowledge discovery to enable improved designs as well as economical aspects, (*Fritzen*, 2012; *Farrar* et al., 2010).

Many SHM systems are planned to assist and complement traditional non-destructive testing methods such as ultrasonic testing. Partially, SHM systems are based on the same physical phenomena. One main difference is explained in fig. 1.1.

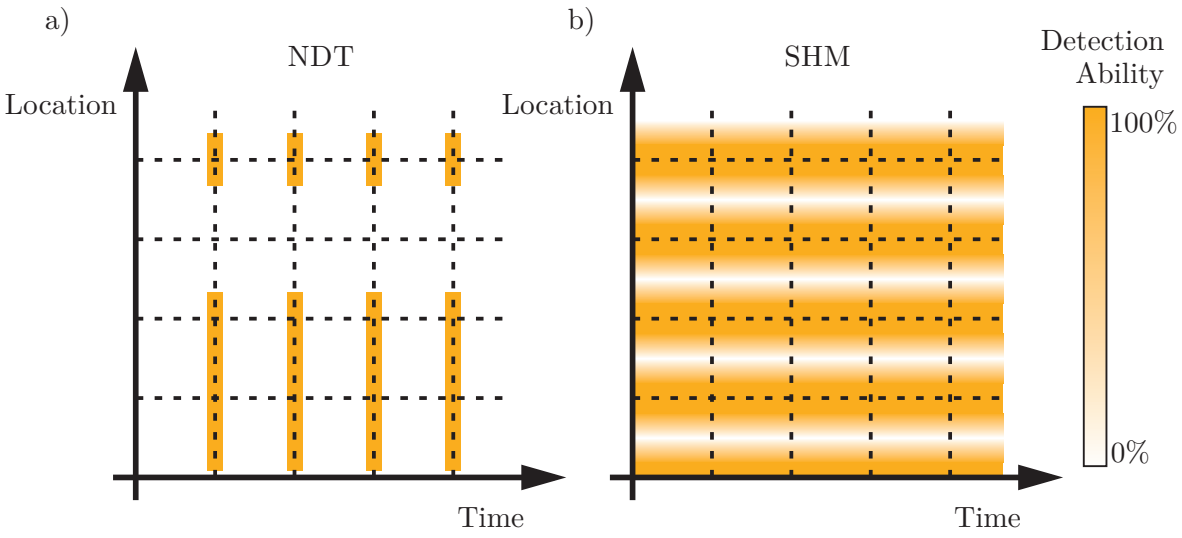

Figure 1.1: Comparison of the detection ability of NDT and SHM, depending on location and time.

For a plate-like structure, a specified area can be inspected at a given time with a fixed accuracy and reliability with ultrasonic testing. This is realized with a moving scanning head, which basically has the same distance to a possible damage location independent of the coordinates of the damage on the plate. For this testing method parts of the structure might be inaccessible, leading to either disassembly or non-inspected and therefore missed areas. By using an SHM system, the measurement equipment is positioned at fixed places. Independent of the used method or physical principle, not all areas of the structure can be monitored by the SHM system with the same accuracy. Nevertheless, an even distribution in those areas, which are of interest for monitoring, is favorable. The big advantage of an SHM system due to the automated measurement and evaluation as well as due to the fixed equipment is the possibility to monitor a structure on demand or continuously, even in those parts, which are not accessible at this time. No preceding disassembly or special measurement equipment is necessary. As NDT and SHM have their specific advantages and disadvantages, they can perfectly assist and complement each other. A possible combination is to use an SHM system for a damage detection and rough localization. Based on an alarm of the SHM system a detailed NDT inspection follows at the alarmed location, resulting in a damage assessment. This enables the initiation of further steps to reduce the effect of possible consequences.

According to *Farrar* and *Worden* the SHM process includes four steps, (*Farrar* and *Worden*, 2012):

1. *Operational evaluation*: to define the damage that is to be detected,
2. *Data acquisition*: to define the measurement system and measured data,
3. *Feature selection*: to extract the damage relevant information from the measured data via data analysis,
4. *Statistical modeling for feature discrimination*: to allow performance level decision, based on statistical models and comparisons.

Several physical principles can be used for the data acquisition and subsequent feature selection. Using mechanical measurements, vibration-based quantities such as eigenfrequencies or modal data are calculated, building one type of data. Another group of data can be built by measuring the propagation of the strain wave, used for acoustic emission and active inspection with guided waves. Other physical principles like electro-mechanical, electro-magnetic, or pure electric measurements are also possible. A commonly used example is the electro-mechanical impedance (EMI) spectrum.

According to the size of their inspection area, SHM methods are categorized into global and local methods, (*Fritzen*, 2012). Vibration-based quantities are global parameters that are located in a low frequency range. They are often used to monitor a whole structure. Guided waves have a much higher frequency content, which is more sensitive to small damages. They are known as a local method. Nevertheless, there is a transition zone between these two categories, as e.g. guided waves can travel long distances, especially in rod-like structures, which do not face a decrease of energy of the waves per area due to the increase of area.

The output of an SHM system gives information about the structure. This information can have different extent. *Rytter* defines four levels, which an SHM system can achieve, (*Rytter*, 1993):

1. Damage detection,
2. Damage localization,
3. Damage assessment, and
4. Damage consequence.

These levels have been used by various researchers. In addition another level can be added, either by splitting *damage assessment* into *damage size* and *damage type*, or by adding *damage healing* on top of these levels, (*Worden* and *Dulieu-Barton*, 2004; *Farrar* and *Worden*, 2012; *Fritzen*, 2012). According to these levels SHM methods can also be classified.

Another common classification is the distinction into active and passive methods, (*Fritzen*, 2012; *Giurgiutiu*, 2007). Passive methods use an external source of energy e.g. a bridge is excited by cars, driving across. Active methods introduce energy into the structure in a predefined manner. Therefore they have a higher energy consumption, compared to the passive methods. For methods using guided waves, acoustic emission is an example for a passive method, while the use of guided waves in acousto-ultrasonics represents an active method.

Finally, the data analysis after the measurements gives an output of the SHM system. There is a huge variety of analyzing methods. A possible classification divides these methods into model-based and model-free analyzing techniques. The reader is referred to wide discussions of this topic in (*Sohn* et al., 2004; *Figueiredo* et al., 2009; *Worden* et al., 2011; *Giurgiutiu*, 2007).

This work refers to acousto-ultrasonics as an active method based on guided waves. Piezoelectric transducers are used for actuating and sensing purposes.

1.3 Outline of the present work

The incentive and purpose of the present work is to contribute to the transfer of SHM into industrial applications. To fulfill this objective, the inspection of PWAS is a key component and the aim of this work.

Chapter 2 gives a short introduction into existing methods of acousto-ultrasonics and a detailed presentation of the basics of probability of detection (POD), which is to be used in the subsequent parts of the work. After a description of the physics of PWAS, possible transducer faults are listed. The chapter ends with a detailed discussion of the state of the art regarding inspection of sensors in general and inspection of PWAS for acousto-ultrasonics in particular. In chapter 3 the consequences are analyzed, defect PWAS have on the wave propagation and on the results of AU-based SHM. This is realized by showing experimental and numerical results. Chapter 4 deals with EMI-based methods for the inspection of PWAS. Experimental data show the sensibility of the EMI spectrum on PWAS faults. The chapter includes the development of an analytical model, which allows building a general understanding of the EMI. Numerical simulations are used to access the examination of the effects of PWAS faults in detail by modeling of well defined damage cases. Based on this knowledge model-based and model-free methods for the inspection of PWAS are developed. A novel performance assessment tool for specific SHM applications is developed in chapter 5. For the first time, the effects of defect PWAS on the SHM system and the results of a PWAS inspection method are combined to evaluate inspection methods for a specific application. After giving a description of the general approach it is applied to numerical results. In chapter 6 the above described knowledge and methods are tested using experiments. The developed methods for PWAS inspection are tested with experimental data from different experimental setups and compared to existing methods. Moreover, the quality assessment tool is tested with experimental data. The chapter concludes with the description and analysis of an application scenario of a door surround structure of an aircraft. The last chapter summarizes the most important results of this work and gives recommendations for possible future work.

2 Basics

2.1 Acousto-ultrasonics-based SHM

Ultrasonic guided waves can travel through structures and interact with discontinuities in these structures. A defined excitation, traveling, and sensing of these waves can give information about possible defects within the structure. Their use for SHM is called acousto-ultrasonics in this work, which coincides with e.g. (*Schubert*, 2012; *Bach*, 2012; *Torres-Arredondo*, 2013). *Giurgiutiu* calls it *"embedded ultrasonic NDE"* as this technique is based on the use of ultrasonic waves, uses embedded transducers for actuation and sensing and performs a non-destructive inspection (*Giurgiutiu*, 2007). First publications use acousto-ultrasonic methods to find changes in the material properties especially for anisotropic carbon fiber reinforced plastics (CFRP) (*Vary*, 1988). In the last years, the number of publications of acousto-ultrasonics (AU)-based SHM using guided waves has increased significantly. While in 2002 only one publication using *guided waves* in its heading can be found in the international journal *Structural Health Monitoring* from *Sage*, this number increased to nine in 2010 and even further to 21 in 2014.

2.1.1 Physics of guided waves

AU-based SHM uses mechanical elastic waves for the monitoring of structures. Depending on the kind of structure, different types of waves are used. In plate-like structures, *Lamb* waves are excited and can be used for SHM. In the following, a short overview on different waves will be given. It deliberately abstains from giving detailed derivations, as these can be found in the literature. A comprehensive analysis is given in (*Graff*, 1975), (*Rose*, 2004), and (*Möser* and *Kropp*, 2010). In (*Giurgiutiu*, 2007) the relationships between different types of waves are emphasized, leading to a detailed explanation of guided waves. Also (*Mengelkamp*, 2006; *Schulte*, 2010; *Moll*,

2011) and (*Torres-Arredondo*, 2013) give an overview including detailed equation-based derivations. The following description is based on these publications.

In a simple one-dimensional model of a beam, axial waves and flexural waves can be considered. The axial wave has a particle motion parallel to the direction of the propagating wave, fig. 2.1 a). Its wave speed does not depend on the frequency of the wave. For all waves described, the wave velocity depends on the material properties. Flexural waves result in a particle motion, which has both components, parallel and vertical to the direction of wave propagation, fig. 2.1 b). Their wave velocity depends on the frequency of the wave. It is therefore called *dispersive*. The phenomenon of dispersion is visible, when a wave package, including waves with different frequency content, is traveling along the waveguide. As the wave travels, the appearance of the wave package changes, because every frequency component travels at its own speed. This might e.g. cause a nonlinear stretching of the signal.

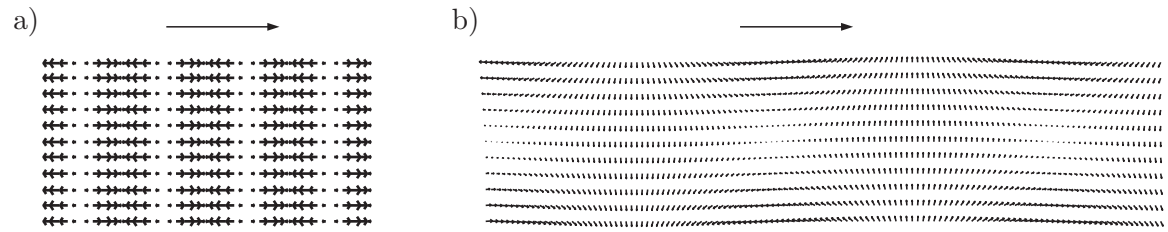

Figure 2.1: Particle displacement of axial and flexural waves in beams. The arrow placed above the sketches marks the direction of wave propagation a) Axial waves exhibit a particle motion parallel to the propagating wave. b) Flexural waves exhibit a particle motion parallel and vertical to the direction of wave propagation. Modeled in accordance with (*Giurgiutiu*, 2007).

Caused by the dispersion, flexural waves in beams also show another phenomenon, which is important for the AU-based SHM: The difference between phase velocity c_{ph} and group velocity c_{gr}. If the wave speed depends on the frequency, the group velocity of a wave package does not coincide with the phase velocity of the waves within the wave package. A common explanation could be made by using a modulated signal, based on two very close frequencies. Fig. 2.2 shows the effect of this phenomenon. The wave package travels a distance of $c_{gr}\,(t_2 - t_1)$ in the time interval between time t_1 and time t_2, visible as the maximum of the envelope function. The phase velocity c_{ph} is slower in the depicted case. Axial and flexural waves also exist for plates as plate waves in 2D with velocities c_{l2D} and c_{f2D}.

In an unbounded elastic body, three different types of waves can be found, showing two different velocities. The longitudinal pressure wave, velocity c_l, is faster than the two

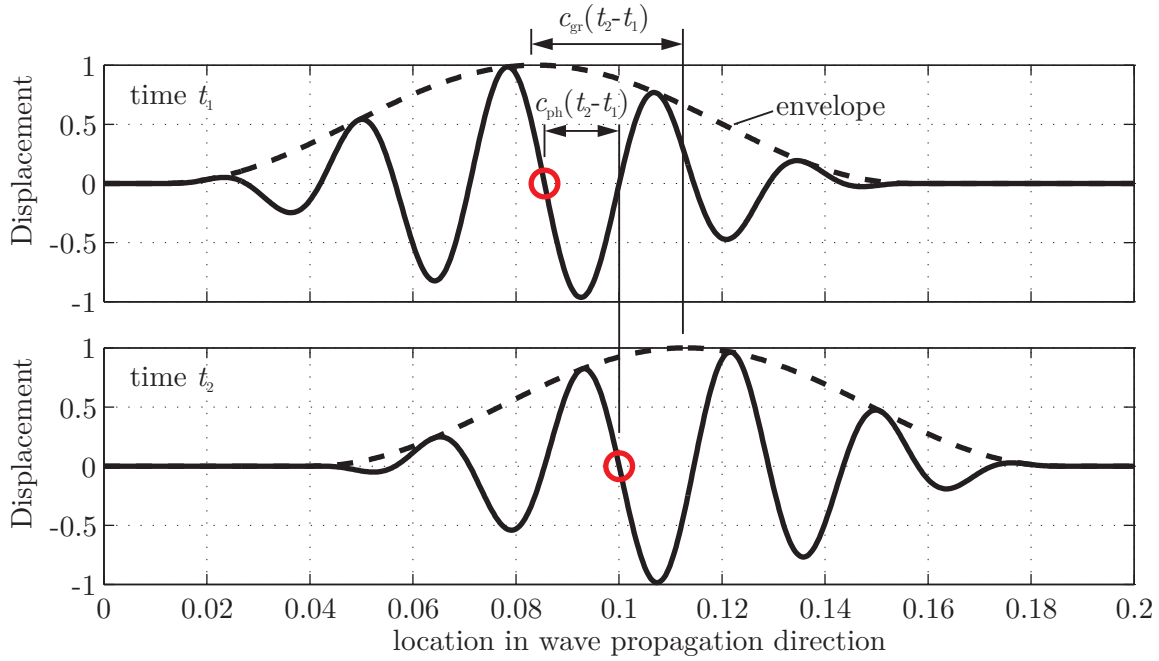

Figure 2.2: Visualization of phase velocity c_{ph} and group velocity c_{gr}.

transverse shear waves with the velocity c_S. Assuming wave propagation in x-direction, fig. 2.3 shows the particle motion of the longitudinal wave, the shear horizontal wave and the shear vertical wave. Assuming a straight crested wave propagating in x-direction, the shear horizontal wave has particle motion in the x-z-plane, while the shear vertical and the longitudinal pressure wave show particle motion in the x-y-plane.

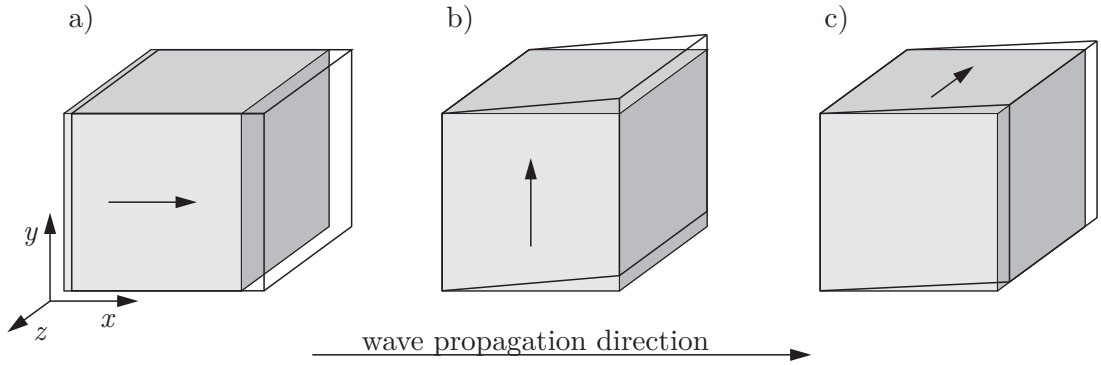

Figure 2.3: Visualization of the particle motion for a) longitudinal pressure wave, b) shear vertical wave and c) shear horizontal wave.

In semi-infinite media, *Rayleigh* waves can be found. These waves are also called surface acoustic waves. Based on the reflection at the boundary they travel along the surface, showing only a very little effective depth in the material. The wave speed is independent of the frequency. Its first historic description can be found in (*Rayleigh*, 1885).

In plate-like structures, the wave field is changed by the upper and lower boundaries. The different types of waves are reflected at the plate surfaces resulting in another group of waves, called guided waves. Guided waves split into shear horizontal waves and *Lamb* waves. Its first historic description can be found in (*Lamb*, 1917).

Similar to the shear horizontal wave in an unbounded elastic body, the particle motion of shear horizontal waves is perpendicular to the wave direction. Moreover, it is parallel to the surface of the plate. The shear horizontal wave exists in two different kinds, called *modes*. Depending on the symmetry of the particle motion to the mid-plane of the plate, they are called symmetric (S) or antisymmetric (A) modes. Higher orders of these modes also exist. Assuming wave propagation in x-direction, fig. 2.4 shows the particle motion for the first two symmetric and antisymmetric modes.

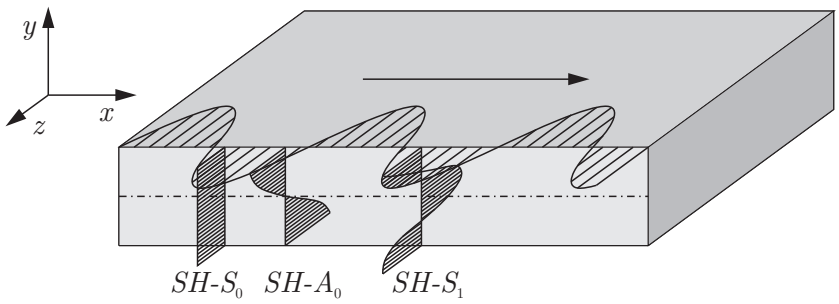

Figure 2.4: Visualization of the particle motion for the SH wave, showing $SH-S_0$, $SH-A_0$ and $SH-S_1$ mode. The arrow placed in x-direction marks the direction of wave propagation.

Except the first symmetric mode, called $SH-S_0$, all modes are dispersive. Therefore, the phase and group velocity depend on the frequency. All velocities show asymptotic behavior towards the velocity of the $SH-S_0$ mode for large frequencies. Moreover all modes apart from $SH-S_0$ only travel beyond certain cut-off frequencies.

Lamb waves also show symmetric and antisymmetric modes with different velocities. The particles move within the x-y-plane, assuming wave propagation in x-direction. The general symmetries for A and S modes are equivalent with the mode shapes, displayed in fig. 2.4. The higher the exciting frequency, the greater the change of the shape of the modes. This is shown in fig. 2.5. The *Lamb* wave dispersion data for figs. 2.5 to 2.7 has been calculated with the *Dispware Toolbox*, developed by (*Torres-Arredondo*, 2013). An aluminum plate ($E = 70$ GPa, $\rho = 2700$ kg/m^3, $\nu = 0.33$) with a thickness of 1.5 mm has been used as a basis.

Taken from (*Giurgiutiu*, 2007), fig. 2.6 shows the relationship of several types of waves. For low frequencies the phase velocity of the S_0 mode asymptotically approaches the

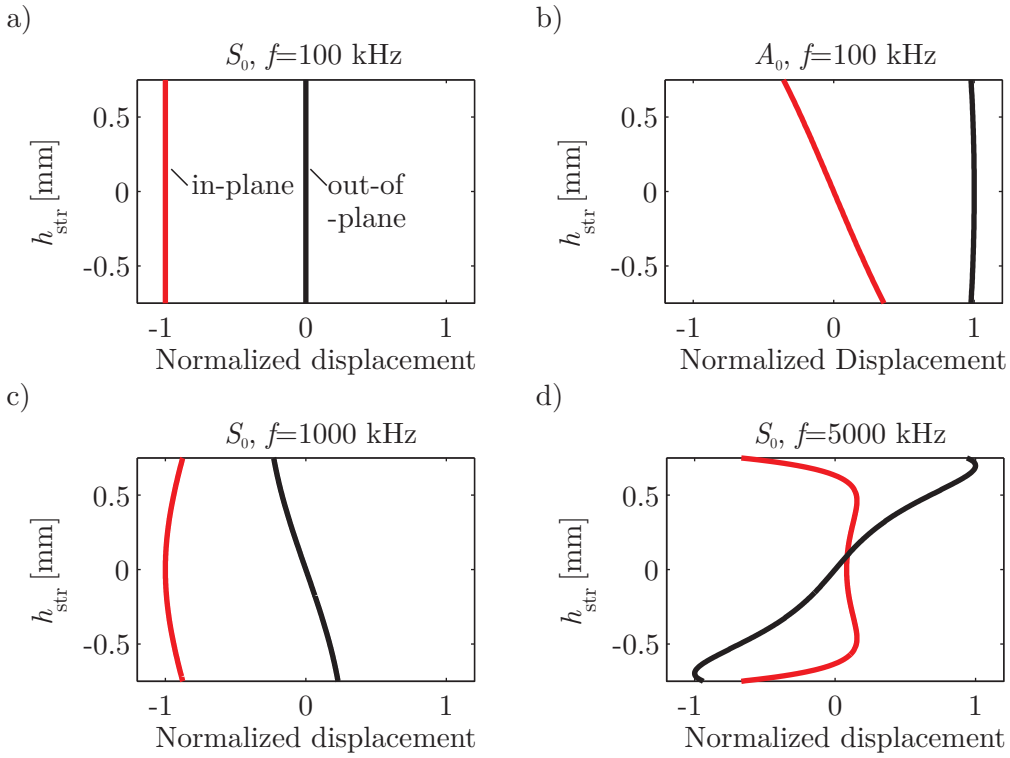

Figure 2.5: Particle motion for a) S_0 and b) A_0 mode at 100 kHz, particle motion for S_0 mode for c) 1000 kHz and d) 5000 kHz. The red curve shows the normalized in-plane displacement, the black curve shows the normalized out-of-plane displacement.

wave speed of an axial plate wave, the A_0 mode approaches the wave speed of a flexural wave. For high velocities both modes asymptotically approach the velocity of the *Rayleigh* wave. An explanation of this behavior can be found in the particle motion. For lower frequencies the main modes exhibit large particle motion over the whole plate cross section. The particle motion for higher frequencies is concentrated at the upper and lower surface of the plate. This behavior is very similar to the behavior of the *Rayleigh* waves, which show very little penetration in depth.

For guided waves the phase and group velocity do not only depend on the frequencies and the material properties, but also on the thickness of the plate. By multiplying frequency and thickness and using it as abscissa in velocity diagrams, these diagrams can be used for plates with different thicknesses, but made from the same material. Fig. 2.7 shows typical phase and group velocity diagrams for the symmetric and anti-symmetric modes. The number of propagating modes is increasing with the increase of frequency. For lower frequencies, only the A_0 and S_0 modes are excited.

An excited wave is composed of at least two-parts: A_0 and S_0 mode. Both modes are not necessarily excited equally strong. The process of transferring the electrical input, given to the PWAS, into a mechanical wave in the structure, is described in detail by

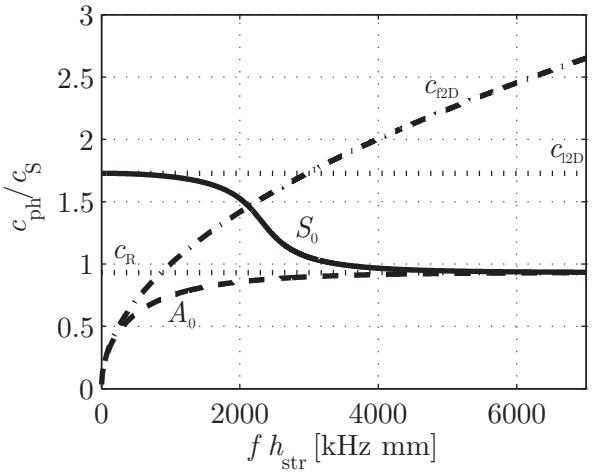

Figure 2.6: Relationship of the velocities of S_0 and A_0 modes to the velocity c_{l2D} of the axial plate wave, of the flexural wave c_{f2D} and the Rayleigh wave c_R for high and low frequencies, following (*Giurgiutiu*, 2007).

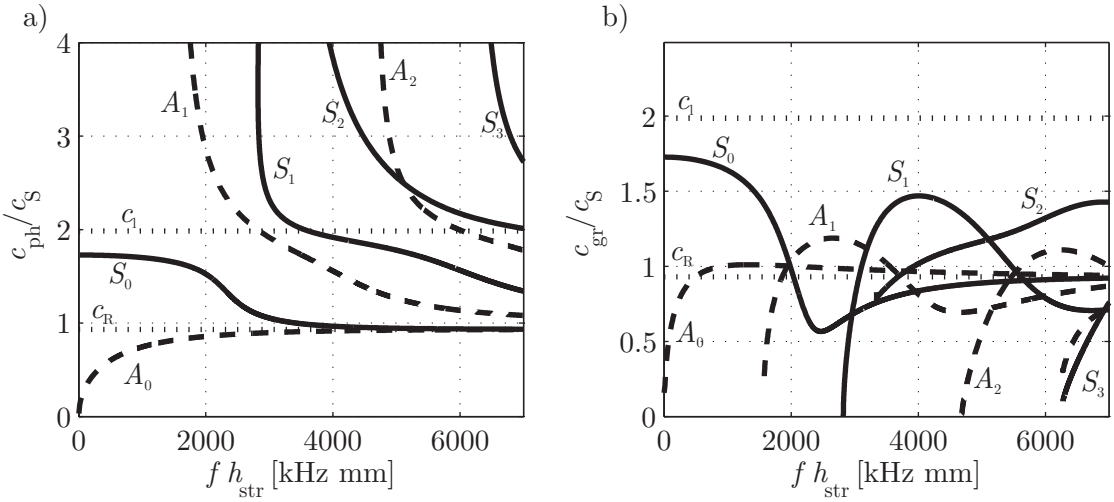

Figure 2.7: a) Phase and b) group velocity of several A_0 and S_0 modes over the frequency-thickness product.

Giurgiutiu in chapter 8 of (*Giurgiutiu*, 2007). It results in different excitation ratios of different modes. Especially if only one mode needs to be excited, this is an advantage.

Most literature discusses the derivation of the different types of waves for straight crested waves, e.g. (*Möser*, 2012; *Graff*, 1975). This coincides with the application for NDT with ultrasound, using arrays of piezoelectric transducers for a linear crested wave front. But a disc-shaped PWAS, as it is used in many SHM applications, does not exhibit a linear but a circular crested wave front. These wave fronts can be superimposed in an array to create a linear crested wave. Nevertheless, many applications use the single transducers. In (*Giurgiutiu*, 2007) a derivation of *Lamb* waves for the circular crested case is given, showing only negligible differences in the wave properties after a distance of only a few wavelength from the center of the PWAS.

For anisotropic layered materials the basics of guided waves are the same. Due to the angular dependency of the material properties and reflections of the waves at each interface between the layers, the mathematical description becomes much more complicated. Its analysis results in velocity curves with angular dependency at a given frequency for a specific material and lay-up, (*Schubert*, 2012; *Torres-Arredondo*, 2013).

2.1.2 Physics of AU-based damage detection

The generated waves can interact with discontinuities within a structure. These discontinuities could be geometrical features of the structure, such as thickness changes, stringers, or cut-outs. They could also be damages in the structure such as cracks or delaminations. To be able to distinguish between geometrical features and damages, most AU-based SHM methods are based on a comparison, therefore, information about the undamaged state is needed. The wave can interact with the discontinuity in different ways:

- The incoming wave is reflected at the discontinuity.
- The incoming wave changes its mode at the discontinuity.
- The transmitted part of the wave is changed by the discontinuity.

Depending on the excited mode, the excitation frequency and the type of damage, these interactions may vary. For higher modes the depth of the damage within the plate is also important. Especially damages in the mid-plane of the plate are hardly detectable by the A_0 mode. Depending on the kind of damage, different modes show a higher sensitivity. A short overview on investigations about this sensitivity is given in (*Ostachowicz* et al., 2012, p. 240).

For the monitoring of structures with acousto-ultrasonics, a careful selection of the excitation mode and the frequency is necessary. This selection is also depending on the data analysis method, to be used. A classification of possible methods is described in the next subsection.

2.1.3 Classification of AU-based methods

When using acousto-ultrasonics, it is possible to use the transducers in two different ways. Either one PWAS is used both for actuation and sensing of the wave at the same place, or one PWAS is used as an actuator, while another is used as a sensor.

The former is called *pulse-echo* and the latter is called *pitch-catch* in this work. This definition is in accordance with (*Giurgiutiu*, 2007) and divides the methods according to the use of PWAS. *Su* and *Ye* define the same terms in a different, phenomenon-based manner, (*Su* and *Ye*, 2009). All actuator-damage-sensor-paths, which include the physical phenomenon *reflection* at the damage are called pulse echo, even if actuator and sensor are not located in the same place. The difference of the definitions is visualized in fig. 2.8. For a 1D example, the definitions result in the same setups.

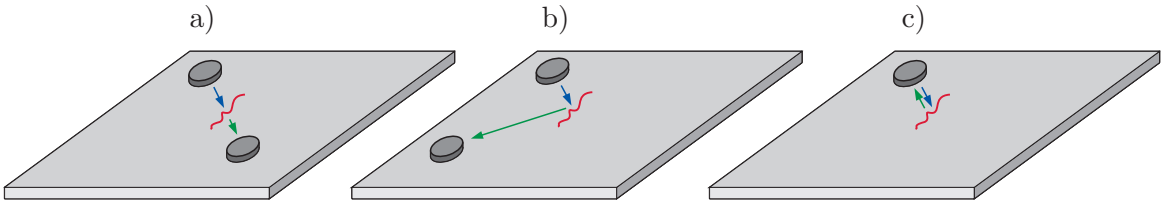

Figure 2.8: Visualization of the pitch-catch and pulse-echo method. The blue arrows mark the incoming wave, the green arrows show the part of the incoming wave, which is changed and recorded by another PWAS. Within this work only c) is called pulse-echo, while a) and b) are called pitch-catch.

As this work is focusing on piezoelectric transducers, only those experimental setups, which use a single transducer as both, actuator and sensor, are called pulse-echo, while setups, using actuator and sensor at different locations, are called pitch-catch. The selection of one of these terms defines the data, which can be used for data evaluation in the SHM system.

There is a huge variety of methods for data evaluation based on feature selection. The result of the data evaluation process is a damage index. It will be compared with a threshold, which is set using statistical modeling. Some possible damage indices are given in (*Farrar* and *Worden*, 2012). A huge variety can be found in (*Su* and *Ye*, 2009).

The standard (*FA SHM*, 2014b) gives an overview of possible methods in acousto-ultrasonics. The subsequent assorting has been developed by the author to provide a classification of the methods within the standard. The following groups can be established:

- *Methods based on statistical data processing.* An example for this method is the use of the principal component analysis and distance parameters.

- *Methods based on physical parameters.* Changes in amplitude, time of flight or other physical parameters are used to build a damage index.

- *Time-frequency-analysis.* Possible differences in the frequency content over time are evaluated to build a damage index, using e.g. the short time *Fourier* transform.
- *Time reversal methods.* Based on the assumption that damage will introduce non-linearity to the structure, while the undamaged structure behaves linearly, changes in the transfer function are used to build a damage index.
- *Model-based methods.* By using e.g., finite element method (FEM) or analytical methods, it is possible to compare gathered data with model data to gain information about the structural health. Depending on the model type, additional information as damage location or severity level can be obtained.
- *Methods using artificial intelligence.* The use of neural networks is a typical example. With pattern recognition different kind of damages can be grouped, making it possible to achieve higher levels in the scheme of *Rytter*.

This work focuses on a few simple algorithms for the data evaluation to show the general effects on the data and its evaluation, defect PWAS have.

Based on damage indices or data analysis, different methods of visualization exist, showing possible locations of a damage. More information can be referred in (*FA SHM*, 2014b).

2.1.4 Use case for SHM application

A simple example with a damage, simulated by an added mass of 23 g, will show how the signals look like and how the changes in the signals are related to increased damage indices.

In fig. 2.9a) the experimental setup is shown. The damage is located between PWAS 1 and PWAS 2. Three different paths have been analyzed, the damage is crossed by the path from PWAS 2 to PWAS 1, the path from PWAS 6 to PWAS 2 does not cross the damage, but it is in the vicinity of the path and reflected waves might come across the damage location and be sensed by the sensor. The path from PWAS 4 to PWAS 8 is located far from the structural damage. Therefore, no major change of the signal is expected. Fig. 2.9b), c), and d) show the measured signals of the undamaged and damaged state. While d) does not show any change of the signals, the signals in b) and c) are influenced by the damage. The first wave package changed for the path from

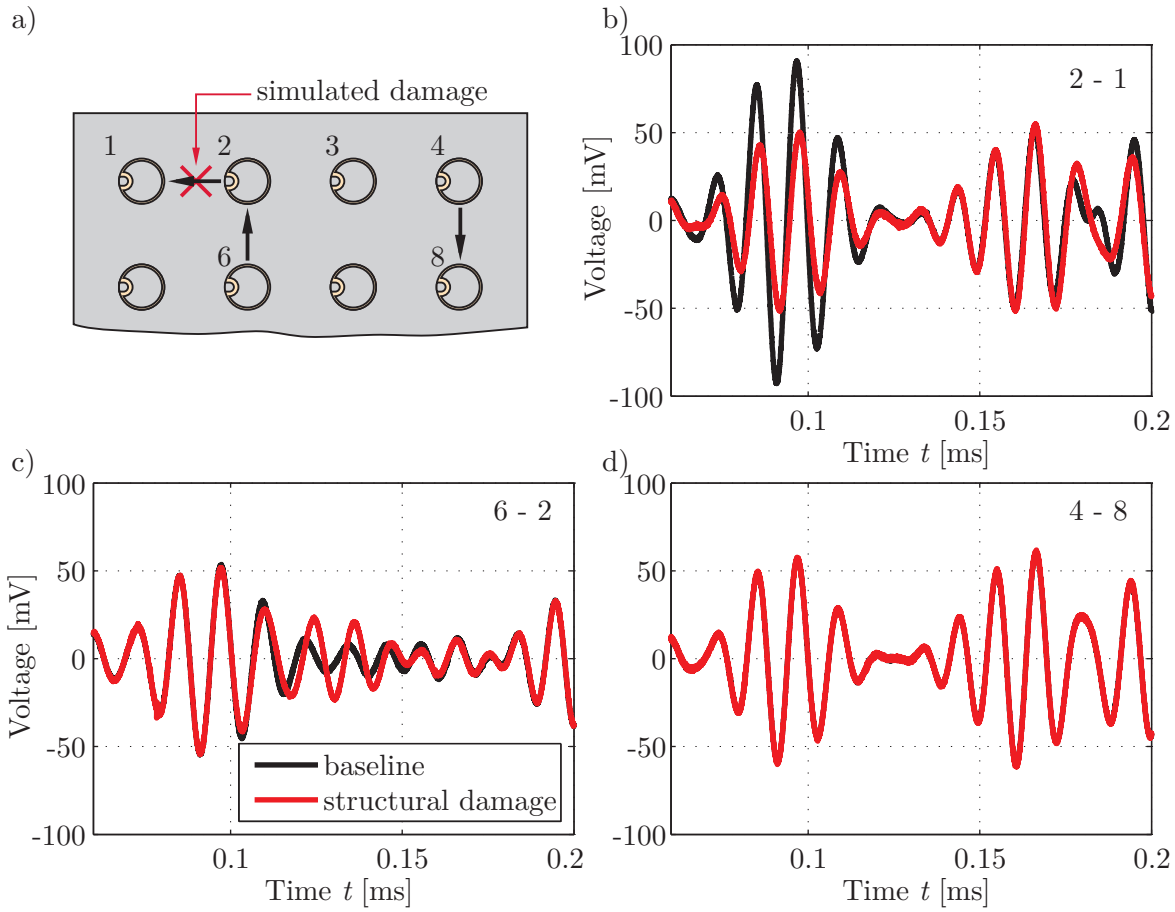

Figure 2.9: a) Experimental setup for a simulated structural damage, Measurements of the undamaged and damaged state, b) measured voltage at PWAS 1, PWAS 2 was used as actuator, c) measured voltage at PWAS 2, PWAS 6 was used as actuator, d) measured voltage at PWAS 8, PWAS 4 was used as actuator.

PWAS 2 to PWAS 1. However, it remains the same for the path between PWAS 6 and PWAS 2, but for this path reflections are changed, see c) .

This work does not focus on the methods for structural damage detection and does not include the development of new or further improvement of existing methods for structural damage detection, but the influence of defect transducers on the wave propagation is quantified by structural damage indices. The following three structural damage indices are used: SDI_{CC}, SDI_{CCh}, and SDI_{RMS}.

The structural damage indicator SDI_{CC} is based on the calculation of the correlation coefficient CC of the two time signals - the baseline and the new signal. This is the same for the structural damage indicator SDI_{CCh}, which does not use the raw time signal, but the absolute value of the *Hilbert* transform to decrease the effect of phase shifts within a wave package. For both the covariance matrix $\mathbf{V}$ has to be calculated first. For SDI_{RMS} the root-mean-square value (RMS) is calculated for the difference

signal of baseline y^H and new data y^D, which should be compared to the baseline. It is weighted with the RMS value of the baseline. The SDI can be calculated with:

$$CC(i) = \frac{V_{12}}{\sqrt{V_{11}V_{22}}}, \tag{2.1}$$

$$SDI_{CC}(i) = 1 - CC(i), \tag{2.2}$$

$$SDI_{RMS} = \sqrt{\frac{\sum (y_i^D - y_i^H)^2}{\sum (y_i^H)^2}}, \tag{2.3}$$

with y_i^H as the measured signal at the i-th time step of the baseline. The equivalent is true for the superscript D for the measurements at unknown, possibly damaged state.

The structural damage indices have been evaluated for the three signal paths, shown in fig. 2.9. The value is largest for the direct crossing path from PWAS 2 to PWAS 1, for all of the structural damage indices. The value from PWAS 6 to PWAS 2 is approximately half of it and close to zero for the path from PWAS 4 to PWAS 8.

2.2 Classical approach for probability of detection

This chapter gives an overview about the classical approach of probability of detection (POD), which was initially developed in the early 80s for NDT methods, as described in (*Berens*, 1988; *Department of Defense*, 2009; *Gandossi* and *Annis*, 2010). This approach is based on a cumulative distribution and replaced binomial statistics-based reliability evaluation (*Yee* et al., 1976). For the evaluation of inspection methods for piezoelectric transducers, the concept of POD will be addressed and adapted later in this work.

The main idea of POD is to specify a damage size, which can be detected with a specific NDT method, taking into account statistic variability. Special focus is set on the largest damage, that can be missed, as it cannot be guaranteed that two damages of the same size are detected both, when using the same NDT method. Several steps are necessary to calculate the POD as a function of damage size. To visualize the necessary steps, exemplary data is taken from the *Military Handbook* 1823 (*Department of Defense*, 2009).

In the following elaboration $\hat{a}$ describes a measurement quantity, related to the damage size a. The first step is to find a linear relationship between some monotonous increasing function of $\hat{a}$ and some monotonous increasing function of a. Historically the logarithm

has proven to be suitable in many cases. Nevertheless, direct proportionality as well as other functions can also be used to find this linear relationship. For the exemplary data, only a has to be scaled with logarithmic scale to achieve a linear correlation, as it is shown in fig. 2.10.

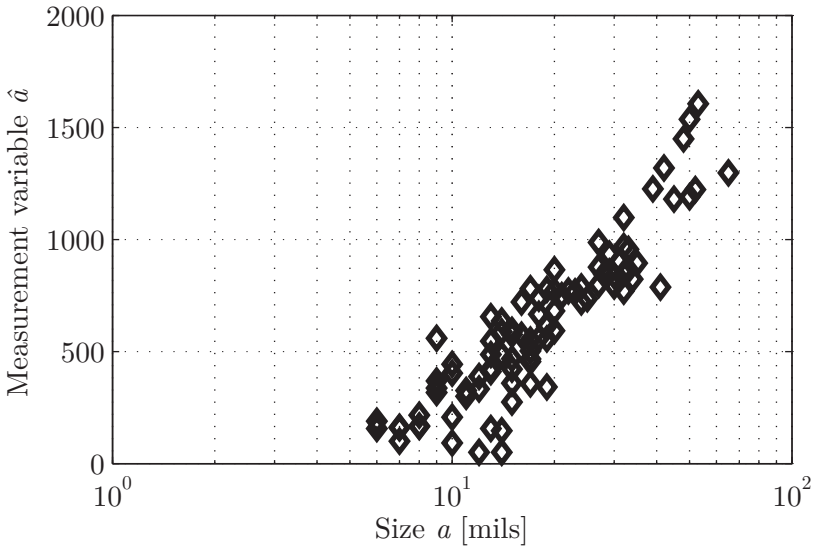

Figure 2.10: Exemplary data from (*Department of Defense*, 2009) shows a linear relationship between the measurement variable $\hat{a}$ and the damage size a on a logarithmic scale.

Defining the following

$$x = f(a) \tag{2.4}$$

$$y = f(\hat{a}), \tag{2.5}$$

the linear relationship can be calculated as best fit of existing measurement points, with the slope m and the intercept b

$$y = mx + b. \tag{2.6}$$

Fig. 2.10 shows that the data scatters around the regression line. Reasons for this scattering are other parameters than a, having an influence on $\hat{a}$, like damage location, temperature, parallax errors when reading the measured quantity etc. If these factors cannot be controlled and if their influence is more significant than the regression under observation, no linear regression is statistically significant. Therefore the influence of other factors should be as small as possible. This scattering can be described by a

standard deviation τ. The use of the Greek letter τ prevents multiple use of σ for different standard deviations.

To calculate the POD, a threshold $\hat{a}_{thr}$ is needed. y_{thr} can be calculated by a given $\hat{a}_{thr}$. Measured data of $\hat{a}$ lower than $\hat{a}_{thr}$ are considered as undamaged. This threshold is necessary, because even if x equals 0, y might be larger than b due to external influences. Therefore $\hat{a}_{thr}$ is often defined by measurement noise. The higher $\hat{a}_{thr}$, the bigger the smallest damage, which can be detected certainly. The smaller $\hat{a}_{thr}$ the higher is the risk of a "false alarm".

Fig. 2.11 shows the data points, the regression line and the distribution for exemplary values of a and $\hat{a}$. Moreover the threshold $\hat{a}_{thr}$ and some exemplary measurements of noise are given.

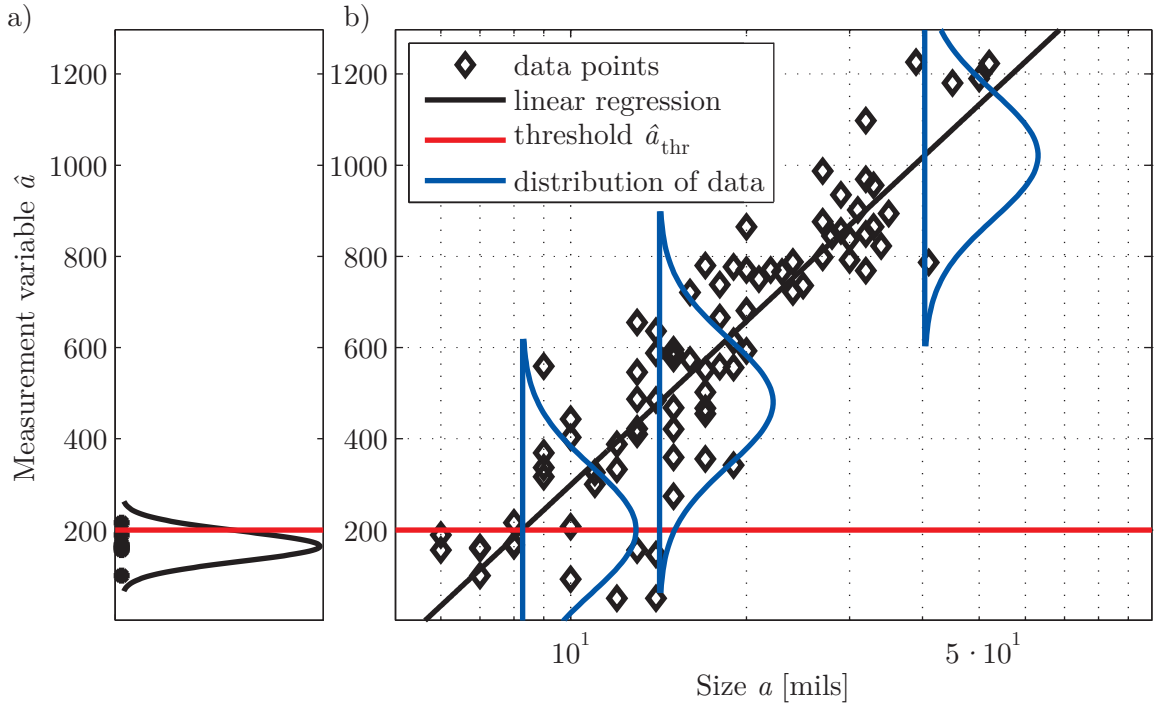

Figure 2.11: a) Distribution of measurement noise in absence of a damage and $\hat{a}_{thr}$, b) linear regression of $\hat{a}$ vs a, distributions and $\hat{a}_{thr}$.

Using the distribution of the data, which is centered at the regression line, only those damages are detected, whose $\hat{a}$ values are above $\hat{a}_{thr}$. The area under the distribution curve, located above the threshold, is increasing with increasing a, resp. x. 50% is located above the threshold for the specific case where the regression line crosses the horizontal threshold line. The relative area above the threshold $\hat{a}_{thr}$ plotted against the parameter a is given in the POD curve, as the area above the threshold gives the POD at a certain parameter value of a, see fig. 2.12.

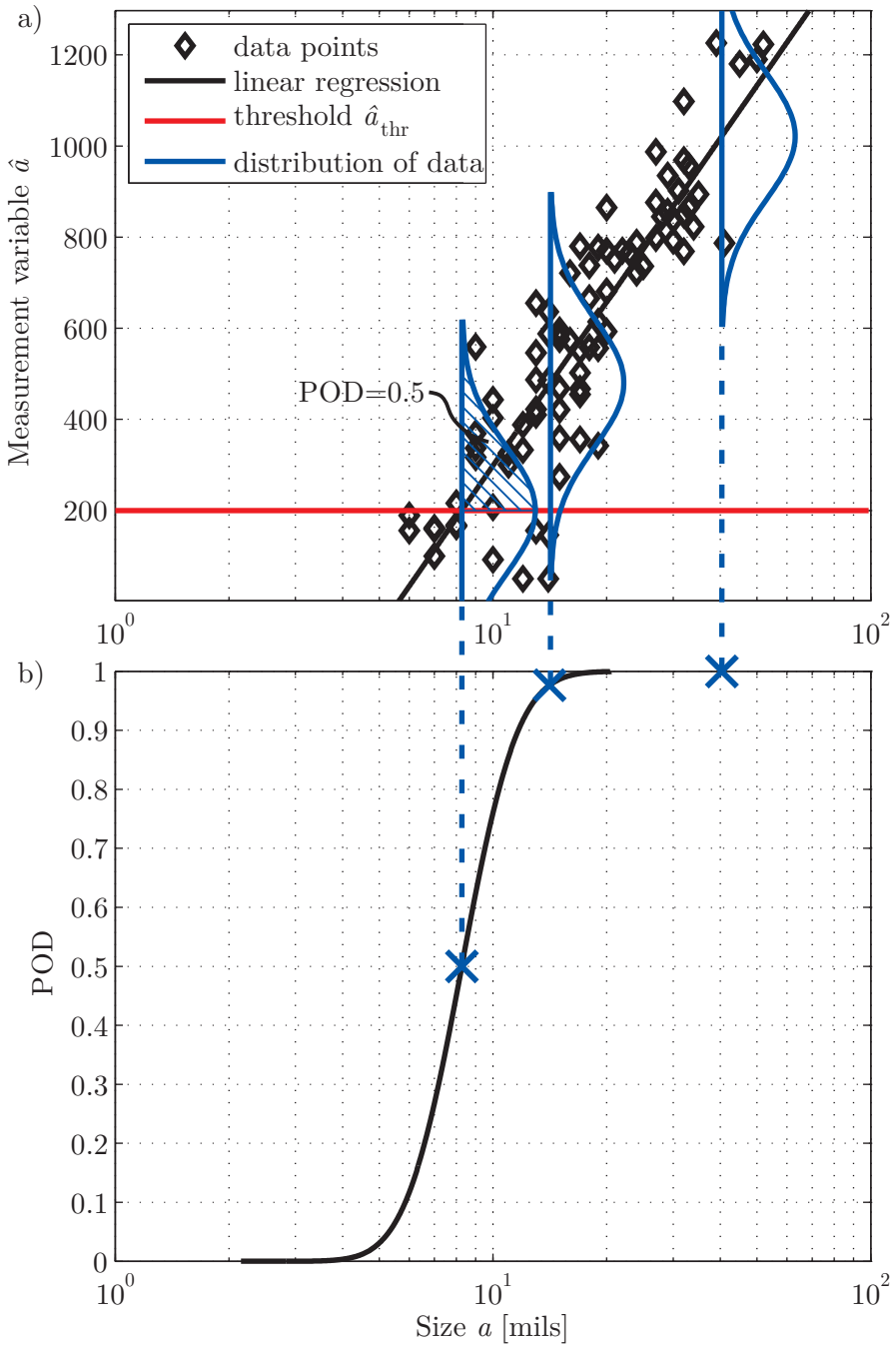

Figure 2.12: Graphical derivation of POD curve without confidence bounds. In b) the values of the area under the distribution curve, located above the threshold, are shown for different a. The distribution curves and their relation to the threshold $\hat{a}_{thr}$ are shown in a).

It can be calculated by subtracting the cumulative distribution Φ from $-\infty$ to y_{thr} of a probability density function (PDF) with mean $b + mx$ and standard deviation τ from 1 (fig. 2.13). This distribution follows a cumulative distribution function (CDF) with mean μ_{POD}, where the regression line equals $\hat{a}_{thr}$, and a standard deviation σ_{POD}, according to the following equations:

$$POD(a) \rightarrow \text{Probability } (\hat{a}(a) > \hat{a}_{thr}) \tag{2.7}$$

$$\rightarrow \text{Probability } (y(x) > y_{thr}), \tag{2.8}$$

$$POD(a) = 1 - \Phi\left[\frac{y_{thr} - (b + mx)}{\tau}\right] \tag{2.9}$$

$$= 1 - \Phi\left[\frac{\frac{y_{thr}}{m} - \frac{b}{m} - x}{\frac{\tau}{m}}\right] \tag{2.10}$$

$$= \Phi\left[\frac{x - \frac{y_{thr} - b}{m}}{\frac{\tau}{m}}\right]. \tag{2.11}$$

Within these formulas, Φ is a cumulative distribution function with

$$\Phi\left(\mu_{POD}, \sigma_{POD}\right) = \frac{1}{2}\left[1 + \text{erf}\left(\frac{x - \mu_{POD}}{\sigma_{POD}\sqrt{2}}\right)\right], \tag{2.12}$$

$$\mu_{POD} = \frac{y_{thr} - b}{m}, \tag{2.13}$$

$$\sigma_{POD} = \frac{\tau}{m}. \tag{2.14}$$

Here erf is the error function. From the calculated POD curve the probability of detection of a damage with a given size a can be obtained, fig. 2.12.

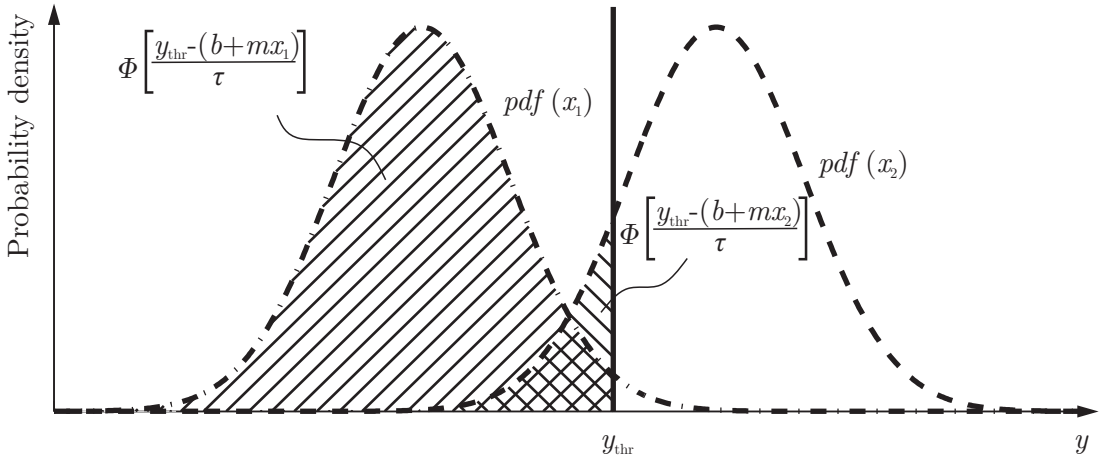

Figure 2.13: Visualization of $\Phi\left[\frac{y_{thr}-(b+mx)}{\tau}\right]$ to calculate the POD

This probability of detection has only 50% confidence level. A standard confidence level in NDT is 95%. To calculate this, different methods exist. One of the first approaches is described in (*Berens*, 1988) and is based on statistics, shown in (*Cheng*

and *Iles*, 1988). The following description is based on (*Department of Defense*, 2009; *Gandossi* and *Annis*, 2010). To calculate the confidence bounds of the POD, the covariance matrix for the parameters μ_{POD} and σ_{POD} has to be known. To estimate their entries, the covariance matrix for the parameters of the regression line and the distribution around this regression line have to be determined. This is possible by using the *Fisher* information matrix $\mathbf{I}$. To obtain the *Fisher* information matrix $\mathbf{I}$ it is necessary to calculate the maximum likelihood function f of the standardized deviation, called z, of the measured values to the regression line. The different entries within the information matrix are calculated by partially differentiating the logarithm of the function f according to the parameters Θ_i, which are in this case m, b and τ. In this way a 3×3 matrix $\mathbf{I}$ is calculated. The inverse of this matrix gives the covariance matrix $\mathbf{V}$ regarding the three parameters.

$$z = \frac{(y - (b + mx))}{\tau}, \tag{2.15}$$

$$f = \Pi_{i=1}^{n} \frac{1}{\sqrt{2\pi}} e^{-\frac{1}{2}\left(\frac{(y-(b+mx))}{\tau}\right)^2} = \Pi_{i=1}^{n} \frac{1}{\sqrt{2\pi}} e^{-\frac{1}{2}z^2}, \tag{2.16}$$

$$I_{ij} = -E\left(\frac{\partial}{\partial\Theta_i \partial\Theta_j} \log(f)\right), \tag{2.17}$$

$$\mathbf{V} = \mathbf{I}^{-1} = \begin{bmatrix} \sigma_b^2 & \sigma_{bm}^2 & \sigma_{b\tau}^2 \\ \sigma_{bm}^2 & \sigma_{mm}^2 & \sigma_{m\tau}^2 \\ \sigma_{b\tau}^2 & \sigma_{m\tau}^2 & \sigma_\tau^2 \end{bmatrix}. \tag{2.18}$$

The covariance matrix of the two parameters μ_{POD} and σ_{POD} from the POD function can be calculated under the assumption of linearity of the relation between μ_{POD}, resp. σ_{POD} and the parameters b, m, and τ. This method is also called "*Wald* method" and its application for POD is described in (*Department of Defense*, 2009, p. 90).

$$Var\left(f\left(\Theta\right)\right) = \phi^{'} Var\left(\Theta\right) \phi \tag{2.19}$$

ϕ is a matrix which contains all first partial derivatives of the new parameters as functions of the first parameters. The derivatives are evaluated at the specific interesting locations of the first set of parameters Θ.

Here m, b, and τ represent the first set of parameters and μ_{POD} with σ_{POD} are the new parameters. This results in

$$\Theta = \begin{bmatrix} b & m & \tau \end{bmatrix} \tag{2.20}$$

$$Var\left(\Theta\right) = \begin{bmatrix} \sigma_b^2 & \sigma_{bm}^2 & \sigma_{b\tau}^2 \\ \sigma_{bm}^2 & \sigma_{mm}^2 & \sigma_{m\tau}^2 \\ \sigma_{b\tau}^2 & \sigma_{m\tau}^2 & \sigma_\tau^2 \end{bmatrix}, \tag{2.21}$$

$$\phi = \begin{bmatrix} \frac{\partial \mu_{POD}}{\partial b} & \frac{\partial \sigma_{POD}}{\partial b} \\ \frac{\partial \mu_{POD}}{\partial m} & \frac{\partial \sigma_{POD}}{\partial m} \\ \frac{\partial \mu_{POD}}{\partial \tau} & \frac{\partial \sigma_{POD}}{\partial \tau} \end{bmatrix} \tag{2.22}$$

$$= \frac{-1}{m} \begin{bmatrix} 1 & 0 \\ \mu_{POD} & \sigma_{POD} \\ 0 & -1 \end{bmatrix}, \tag{2.23}$$

$$\mathbf{V}\left(\mu_{POD}, \sigma_{POD}\right) = \phi^{'} Var\left(\Theta\right) \phi \tag{2.24}$$

$$= \begin{bmatrix} \sigma_{\mu_{POD}}^2 & \sigma_{\mu_{POD}\sigma_{POD}}^2 \\ \sigma_{\mu_{POD}\sigma_{POD}}^2 & \sigma_{\sigma_{POD}}^2 \end{bmatrix}. \tag{2.25}$$

To calculate the 95% confidence interval, the variance of the POD curve has to be calculated. For this the distribution of a resp. x values for a specific POD level needs to be studied. The z-score for $\alpha = 95\%$ is used for the standard normal distribution. The value of a for a given POD level follows a normal distribution with mean at the POD curve and a standard deviation $\sigma_{a|POD}$. The index $a|POD$ refers to a specified value, describing the variation of a for a specified value of the POD. $\sigma_{a|POD}$ has to be a function of the entries of the covariance matrix of μ_{POD} and σ_{POD}. To calculate the variance $\sigma_{a|POD(\mu_{POD},\sigma_{POD})}$, a function $a = f\left(POD|\mu_{POD}, \sigma_{POD}\right)$ is defined with the help of the underlying PDF of the POD curve. Each a can be calculated with μ_{POD} and σ_{POD} with a specific $z(a)$. From this $\sigma_{a|POD(\mu_{POD},\sigma_{POD})}$ can be derived. The following equations are visualized in fig. 2.14:

$$a_\alpha\left(POD|\mu_{POD}, \sigma_{POD}\right) = \mu_a\left(POD|\mu_{POD}, \sigma_{POD}\right) + z\left(\alpha\right)\sigma_{a|POD(\mu_{POD},\sigma_{POD})}, \tag{2.26}$$

$$z\left(\alpha = 95\%\right) \approx 1.645, \tag{2.27}$$

$$a|_{POD} = \mu_{POD} + z\left(a\right)\sigma_{POD}, \tag{2.28}$$

$$\sigma_{a|POD(\mu_{POD},\sigma_{POD})}^2 = \sigma_{\mu_{POD}}^2 + 2z\left(a\right)\sigma_{\mu_{POD}\sigma_{POD}}^2 + z\left(a\right)^2\sigma_{\sigma_{POD}}^2. \tag{2.29}$$

From the 95% confidence interval of the POD curve, the $a_{90|95}$ value can be obtained, which is defined as the corresponding a value at the intersection of the 95% confidence interval of the POD curve and an ordinate value of 0.9. The $a_{90|95}$ value is commonly

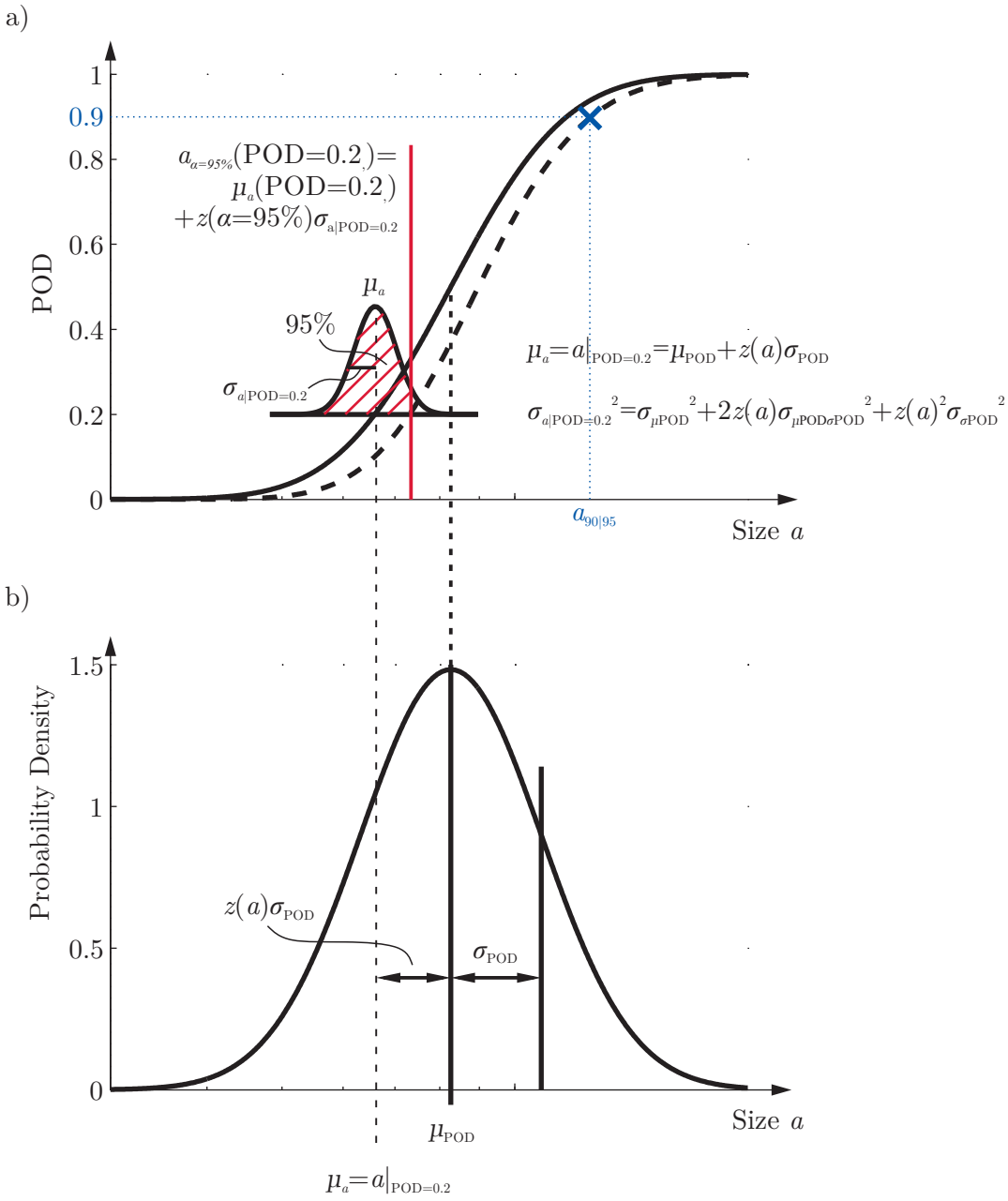

Figure 2.14: POD curve with 95% confidence interval and visualization of calculation of confidence bound

used in NDT. The meaning of this value is to specify, which value of a can be detected by measuring of $\hat{a}$ with a probability of 90% at a confidence level of 95%.

This procedure of calculating the POD curve from a linear regression line is only possible if the following prerequisites, listed in detail in (*Department of Defense*, 2009), are valid:

- linearity of the parameters, m and b should be constants,
- uniform variance, $\mathbf{V}(y_i, y_i) = \sigma^2$,
- uncorrelated observations, $\mathbf{V}(y_i, y_j) = 0, i \neq j$, and

- normal errors have a multivariate normal distribution.

If $\hat{a}$ is only available as binary data, the so called "hit/miss" approach can be taken. Data of $\hat{a}$ vs. a can be easily transferred to hit/miss data by using the threshold limit between the binary states 0 and 1. Details on this can also be found in (*Department of Defense*, 2009).

Moreover it is possible that the given data is left and/or right censored, i.e. below or above the measurement range of $\hat{a}$. This case complicates especially the calculation of the confidence bounds and is described in detail in (*Berens*, 1988; *Department of Defense*, 2009). It is out of scope for the application within this work and therefore not discussed here.

2.3 Physics of piezoelectric wafer active sensors

PWAS are one type of piezoelectric transducers. Three different designs of PWAS are shown in fig. 2.15. The most simple type is a piezoceramic disc with a wrap-around electrode, which enables the soldering of both contacts on top of the transducer. It can be adhered e.g. with *Z*70 glue, which is also used for strain gauges (*HBM*, 2016). The other two types of PWAS are already capsulated in wrapping material. The PWAS produced by *Acellent* contains a piezoceramic disc with wrap-around electrode, contacted with small wires, which are embedded in a polyimide layer. The cabling is eased by connectors, already connected to the so called *SMART Layer*. From the surface, which is adhered to the structure, the ceramic disc is easily visible (*Acellent technologies, Inc.*, 2005), see fig. 2.15c). The PWAS produced by *Invent* and sold by *PI Ceramic* also uses a piezoceramic embedded into layers, made from polyimide (often called Kapton) or epoxy resin matrix. The piezoceramic is sputtered with surface electrodes and contacted with a copper mesh. The embedding is realized from both sides. It enables a mechanical stabilization with prepressure of approximately 20 MPa at ambient temperature (*Gall* et al., 2009; *PICeramic*, 2007). Both embedded transducers can either be bonded on the surface - called secondary bonding, e.g. with the two component epoxy adhesive *Hysol EA9394* or *Delo Duopox1895*, or be integrated directly in a newly fabricated structure, this is also called co-bonding.

PWAS use the direct and converse piezoelectric effect to sense and excite guided waves. The physics and mathematical formulations of the piezoelectric effect, are described in a variety of literature. The following summary is based on (*Giurgiutiu*, 2007; *Ikeda*,

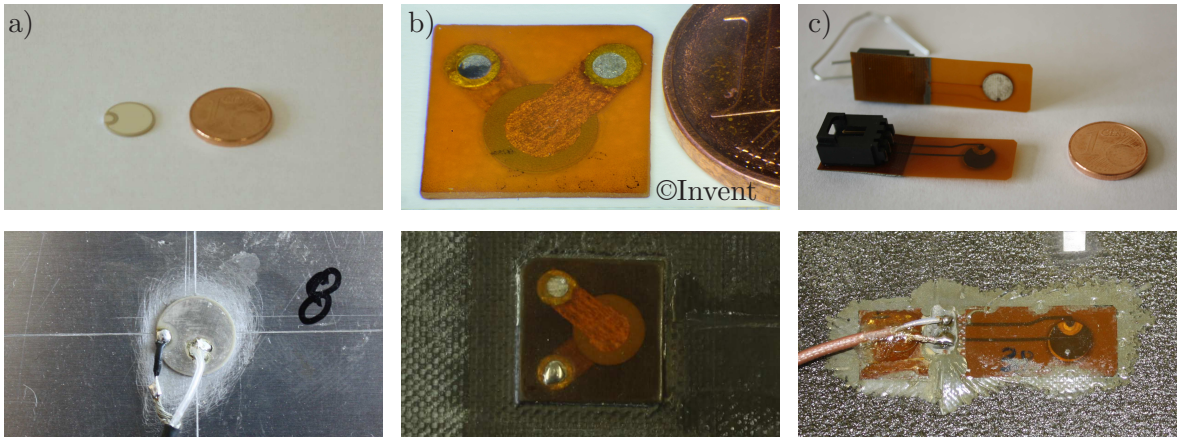

Figure 2.15: Types of PWAS: a) simple piezoceramic disc with wrap-around electrode pattern, produced by *PI Ceramic*, b) *DuraAct*: Embedded disc with electrodes on top and below the disc, produced by *Invent*, sold by *PI Ceramic*, c) *SMART Layer*: Embedded disc with wrap-around electrode pattern, produced by *Acellent*. The first row shows the single transducers, in the second row the bonded transducers are depicted.

1996; *Jaffe* et al., 1971). The direct piezoelectric effect describes the phenomenon of the creation of electric charge, when mechanical load is applied. For PWAS this effect is used for the sensing of waves. The converse piezoelectric effect describes the phenomenon of deformation, when voltage is applied. This is used for the excitation of waves with PWAS.

Several materials exist which possess the piezoelectric property. Most materials need to be produced from a raw material, which is isotropic in this process stage. Due to poling, which is the exposure of the material to a very high electric field, the coercive field E_c, the elements in the material are aligned. This increases the dielectric constant significantly and creates an orthotropic material, revealing isotropy in the plane, which is perpendicular to the poling direction.

In general the piezoelectric effect is not linear and moreover other effects like the electrostriction superpose it, leading to a nonlinear behavior between the electric and mechanical quantities. Nevertheless, the effect can be modeled linearly in a certain strain range for most piezoelectric materials. It is only valid for temperatures clearly below the *Curie* point. Above this point the lattice of the atoms in the piezoelectric material changes. The so called paraelectric phase is entered and the material does not show piezoelectric behavior any more.

The mathematical formulation describes the conjunction between the mechanical and electrical quantities and is given in index notation:

$$D_i = d_{ikl} T_{kl} + \varepsilon_{ik}^T E_k, \tag{2.30}$$

$$S_{ij} = s_{ijkl}^E T_{kl} + d_{kij} E_k. \tag{2.31}$$

Within this equation the following parameters are used:

- Stress **T**, given in $\frac{\mathrm{N}}{\mathrm{m}^2}$,
- Strain **S**, given in $\frac{\mathrm{mm}}{\mathrm{mm}}$,
- Elastic compliance **s** given in $\frac{\mathrm{m}^2}{\mathrm{N}}$,
- Dielectric constant ε, which equals the relative dielectric constant multiplied by the dielectric constant in vacuum ε_0 ($\varepsilon_0 = 8.85 \cdot 10^{-12}\ \frac{\mathrm{F}}{\mathrm{m}}$),
- Electric field $\underline{E}$, given in $\frac{\mathrm{V}}{\mathrm{m}}$,
- Dielectric displacement $\underline{D}$, defined by charge Q per unit area A at stress **T**, given in $\frac{\mathrm{C}}{\mathrm{m}^2}$, and
- Piezoelectric constant **d**, it links the dielectric displacement $\underline{D}$ with stress **T**, as well as strain **S** with electric field $\underline{E}$, given in $\frac{\mathrm{C}}{\mathrm{N}} = \frac{\mathrm{m}}{\mathrm{V}}$, also called piezoelectric charge constant.

The superscripts T and E represent a special state for the specific parameter, T represents zero stress, while E represents zero voltage e.i. no electric field, short circuit.

Although eqs. (2.30) and (2.31) completely describe the piezoelectric effect, these equations are mainly used for describing the actuation. The sensing behavior can be described by the following equations, having **S** and $\underline{E}$ isolated on the left side:

$$E_i = -g_{ikl} T_{kl} + \beta_{ik}^T D_k, \tag{2.32}$$

$$S_{ij} = s_{ijkl}^D T_{kl} + g_{kij} D_k, \tag{2.33}$$

with **g** being the piezoelectric voltage coefficient, see (*Giurgiutiu*, 2007), as it connects the stress with the electric field in eq. (2.32). Thereafter **d** can be also called piezoelectric strain coefficient or piezoelectric charge coefficient. The equations can be rewritten in several forms, making it easier to be used for the evaluation of stresses, polarization etc. The index notation shows that the mechanical quantities stress **T** and strain **S** are tensors of second order, while the electrical quantities $\underline{D}$ and $\underline{E}$ have vector character.

The piezoelectric constant **d**, respectively piezoelectric voltage coefficient **g** needs to link this. Assuming multiple symmetry in the piezoelectric material, the *Voigt* notation can be used, simplifying eqs. (2.30) and (2.31):

$$\underline{D} = \mathbf{d}\,\underline{T} + \varepsilon^T \underline{E}, \tag{2.34}$$

$$\underline{S} = \mathbf{s}^E \underline{T} + \mathbf{d}^{tr} \underline{E} \tag{2.35}$$

While $\underline{T}$ and $\underline{S}$ are $[6 \times 1]$ vectors and $\underline{D}$ and $\underline{E}$ are $[3 \times 1]$ vectors, $\mathbf{s}$ is a $[3 \times 6]$ matrix. $\mathbf{d}$ is a $[3 \times 6]$ matrix, which has to be transposed for the second equation to calculate $\underline{S}$, and ε is a $[3 \times 3]$ matrix, with only diagonal elements. In the *Voigt* notation the following order is used within $\underline{T}$ to include the elements of the matrix $\mathbf{T}$:

$$\begin{bmatrix} T_1 \\ T_2 \\ T_3 \\ T_4 \\ T_5 \\ T_6 \end{bmatrix} = \begin{bmatrix} T_{11} \\ T_{22} \\ T_{33} \\ T_{23} \\ T_{13} \\ T_{12} \end{bmatrix}. \tag{2.36}$$

Similar relations are used for the strain, including a factor 2 for S_{ij} if $i \neq j$. All necessary transformations are given e.g. in (*Ikeda*, 1996).

$$\begin{bmatrix} S_1 \\ S_2 \\ S_3 \\ S_4 \\ S_5 \\ S_6 \end{bmatrix} = \begin{bmatrix} S_{11} \\ S_{22} \\ S_{33} \\ 2S_{23} \\ 2S_{13} \\ 2S_{12} \end{bmatrix} \tag{2.37}$$

There is a huge variety of piezoelectric materials. Well known are ceramics as barium titanate $BaTiO_3$ and lead zirconate titanate $Pb(Zr,Ti)O_3$, known as PZT. But also more flexible materials like polyvinylidene flouride, PVDF, have piezoelectric properties. PVDF is known as a good sensor, which is sensitive to heat. Nevertheless, the relatively small stiffness, compared to piezoelectric ceramic, prohibits its use as actuator for structures. Within this work PWAS of type $Pb(Zr,Ti)O_3$ are used for the AU-based inspection. Two main categories of this type exist. They are distinguished

by their coercive field E_c into *hard* and *soft* PZTs. Hard PZTs exhibit a large linear drive region, showing small strain magnitudes. Their temperature at *Curie* point is relatively large ($T_C \approx 250°C$). Soft PZTs exhibit a large induced strain, showing a smaller linear region, which is equal to a relatively large hysteresis. Their temperature at *Curie* point is above $150°C$, but below those of hard PZTs. (*Giurgiutiu*, 2007) gives a threshold of $E_C = 1\frac{kV}{mm}$ to divide those two categories.

For these piezoelectric materials many components of these vectors and tensors are equal to zero. This is mainly due to the isotropy in the x-y-plane, assuming a poling in z-direction. In the matrices $\mathbf{d}$ has three, $\mathbf{s}$ has five and ε has two independent entries. These values are complex due to losses in electric, mechanical and electromechanical part. Values for representative piezoelectric materials are given in (*Gautschi*, 2002; *Giurgiutiu*, 2007) as well as in appendix A.3. Their experimental evaluation is described e.g. in (*Jaffe* et al., 1971) and (*IRE*, 1961).

$$\begin{bmatrix} D_1 \\ D_2 \\ D_3 \end{bmatrix} = \begin{bmatrix} 0 & 0 & 0 & 0 & d_{15} & 0 \\ 0 & 0 & 0 & d_{15} & 0 & 0 \\ d_{31} & d_{31} & d_{33} & 0 & 0 & 0 \end{bmatrix} \begin{bmatrix} T_1 \\ T_2 \\ T_3 \\ T_4 \\ T_5 \\ T_6 \end{bmatrix} + \begin{bmatrix} \varepsilon_{11}^T & 0 & 0 \\ 0 & \varepsilon_{11}^T & 0 \\ 0 & 0 & \varepsilon_{33}^T \end{bmatrix} \begin{bmatrix} E_1 \\ E_2 \\ E_3 \end{bmatrix} \tag{2.38}$$

$$\begin{bmatrix} S_1 \\ S_2 \\ S_3 \\ S_4 \\ S_5 \\ S_6 \end{bmatrix} = \begin{bmatrix} s_{11}^E & s_{12}^E & s_{13}^E & 0 & 0 & 0 \\ s_{12}^E & s_{11}^E & s_{13}^E & 0 & 0 & 0 \\ s_{13}^E & s_{13}^E & s_{33}^E & 0 & 0 & 0 \\ 0 & 0 & 0 & s_{55}^E & 0 & 0 \\ 0 & 0 & 0 & 0 & s_{55}^E & 0 \\ 0 & 0 & 0 & 0 & 0 & 2(s_{11}^E - s_{12}^E) \end{bmatrix} \begin{bmatrix} T_1 \\ T_2 \\ T_3 \\ T_4 \\ T_5 \\ T_6 \end{bmatrix} + \begin{bmatrix} 0 & 0 & d_{31} \\ 0 & 0 & d_{31} \\ 0 & 0 & d_{33} \\ 0 & d_{15} & 0 \\ d_{15} & 0 & 0 \\ 0 & 0 & 0 \end{bmatrix} \begin{bmatrix} E_1 \\ E_2 \\ E_3 \end{bmatrix} \tag{2.39}$$

To describe the piezoelectric effect the electro-mechanical coupling coefficient k is defined as the relation of converted energy to the whole energy input. The converted energy is the amount of energy, converted from electrical to mechanical energy or vice versa. This factor is direction dependent. For the applications within this work the pla-

nar coupling coefficient k_p is of relevance. It describes the electromechanical coupling under uniform radial tension or compression:

$$k_p = \frac{d_{31}}{\sqrt{\frac{1}{2}(s_{11} + s_{12})\varepsilon_{33}}}. \tag{2.40}$$

For other calculations k_{31} is needed.

$$k_{31} = \frac{d_{31}}{\sqrt{s_{11}^E \varepsilon_{33}}} \tag{2.41}$$

Piezoelectric materials are used in multiple types of sensors, like force sensors, acceleration sensors etc. A detailed description can be found in (*Gautschi*, 2002). Moreover they can be used as actuators e.g. as a stack for a linear motor, see e.g. (*Jaffe* et al., 1971). To send and receive ultrasonic waves, they are implemented in ultrasonic heads for NDT applications. For AU-based SHM the transducers are permanently attached to the structure. For this application the heads used in NDT are too bulky and heavy. PWAS are good transducers, as their bonding is relatively simple, they are lightweight and comparably cheap (< 10€). They exist in different geometries. Almost all transducers, used in this work, are circular PWAS.

2.4 Electro-mechanical impedance (EMI) of PWAS

Within this work the electro-mechanical impedance (EMI) and especially the admittance will be used frequently. The impedance is the frequency dependent complex ratio of voltage and current. The admittance is defined as the reciprocal of the impedance. Its general behavior for a free PWAS is therefore discussed shortly. By neglecting any deformations caused by mechanical loading, a PWAS can be modeled as a simple capacitor with capacitance C:

$$C = \varepsilon_{33} \frac{A}{h}, \tag{2.42}$$

with A being the area of the PWAS, perpendicular to the poling direction and h being the thickness in poling direction, taken as 3. The admittance Y as reciprocal of the impedance is

$$Y(\omega) = i\omega C. \tag{2.43}$$

Taking into account the mechanical deformations additional parts have to be added. For a strip-like PWAS with thickness h, width w and length l, which is vibrating in its longitudinal direction along l, this leads to the admittance Y_p, see e.g. (*Ikeda*, 1996).

$$Y_p(\omega) = i\omega C \left(1 - k_{31}^2 \left(1 - \frac{\tan(k\frac{l}{2})}{k\frac{l}{2}}\right)\right) \tag{2.44}$$

with the coupling coefficient k_{31} and the wave number $k = \frac{\omega}{c}$, c is the wave speed of the 1D axial wave in a bar, (*Ikeda*, 1996; *Giurgiutiu*, 2014). The derivation is given in the appendix appendix A.2. To get this result the equation of motion for longitudinal vibration has to be solved for the strip-like PWAS in l direction, taking into account eq. 2.30 and 2.31, as well as stress free ends. The electro-mechanical impedance is calculated from this by evaluating the inverse of the admittance.

For an exemplary PWAS with $l = 70$ mm, $w = 10$ mm, $h = 0.2$ mm, and material *PIC255*, the susceptance as the imaginary part of the admittance has a linear progression, interrupted by the electromechanical resonances, fig. 2.16.

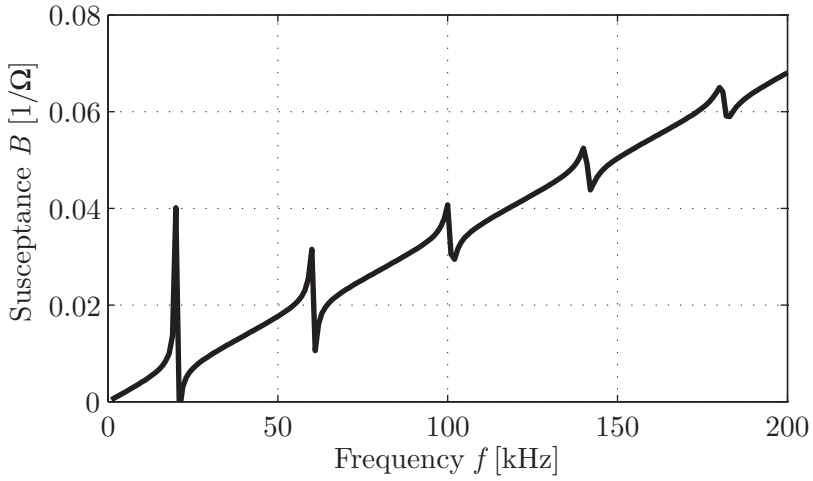

Figure 2.16: Susceptance as imaginary part of the admittance for a rectangular PWAS ($l = 70$ mm, $w = 10$ mm, $h = 0.2$ mm, *PIC255*). The electro-mechanical resonances disrupt the constant slope, caused by the capacitance.

For this strip-like PWAS it is possible to build a simplified electrical circuit as a simplified model of the PWAS itself near the fundamental resonance frequency, fig. 2.17. It consists of a main capacitance C_0 in one branch and a series connection of a capacitance C_1, an inductor with inductance L_1 and an *Ohm*ic resistance R in the second branch. C_0 is the capacitance in absence of mechanical deformations, the other quantities depend on electrical and mechanical quantities of the strip, including the first

longitudinal eigenfrequency. A detailed explanation neglecting the *Ohm*ic resistance including higher resonance frequencies can be found in (*Ikeda*, 1996).

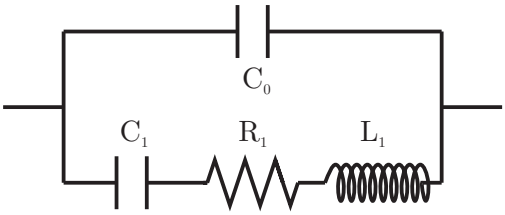

Figure 2.17: Model of electric circuit including the fundamental resonance frequency of the PWAS.

Using this model helps to understand that with the admittance spectrum, the electromechanical resonance and antiresonance can be found. In the resonance frequencies the admittance tends to infinity, while at antiresonances it tends to 0. As the admittance is the reciprocal of the impedance, the relation is opposite for the impedance. At the resonance the current is highest, capacitance C_1 and inductance L_1 cancel each other leaving the *Ohm*ic resistance. At the antiresonance the current oscillates within the circuit, as the impedances of the two branches are equal with opposite sign.

The admittance of a circular unbounded PWAS can be calculated in a similar, but more complex way, as now two coordinates have to be taken into account, a cylinder coordinate system has to be used. It is given in eq. (2.45). *Bessel* functions of the first kind J_n are necessary to calculate the admittance. A detailed description of the necessary steps for a similar problem is discussed in detail in section 4.2. Therefore, only the result is given here. A detailed derivation can be found in (*Giurgiutiu*, 2007). The resonances are discussed also in (*Ikeda*, 1996).

$$Y(\omega) = i\omega C_0 \left(1 - k_p^2 \left(1 - \frac{(1+\nu)J_1(k\ r_{pwas})}{k\ r_{pwas} J_0(k\ r_{pwas}) - (1-\nu)J_1(k\ r_{pwas})}\right)\right) \tag{2.45}$$

Here k is the wave number, r_{pwas} is the radius of the PWAS disc and ν is the *Poisson*'s ratio. For an exemplary PWAS with $r_{pwas} = 5$ mm, $h = 0.5$ mm, and material *PIC255* with increased mechanical loss factor $\eta = 1/Q_m$ by factor 4 the susceptance spectrum is given in fig. 2.18. η has been increased to improve the visibility of the slope as otherwise the changes at the resonances dominate the trend.

It has to be kept in mind that this model is a model of the free PWAS, which is not attached to the structure. The connection with the structure is discussed in section 4.2.

The PWAS is attached to the structure via a bonding layer. For many applications an adhesive layer is used to connect the structure and the PWAS. When an electric

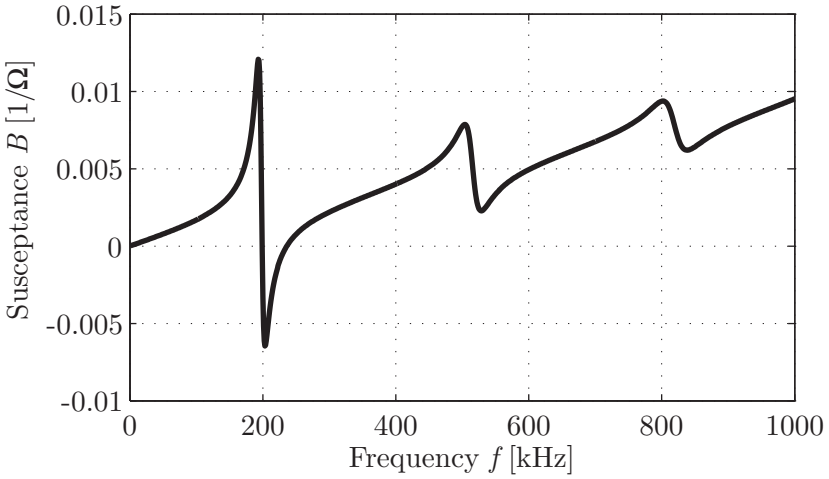

Figure 2.18: Susceptance as imaginary part of the admittance for a circular PWAS ($r_{pwas} = 5\,\text{mm}$, $h = 0.5\,\text{mm}$, *PIC255* with $Q_m = 20$) with $f = \frac{1}{2\pi}\omega$. The electromechanical resonances disrupt the constant slope, caused by the capacitance.

voltage is applied at the PWAS and it reacts with deformation, the bonding layer will weaken the absolute value of deformation transferred to the structure. The effect is the same for the sensing of deformations within the structure. This effect has been neglected in many models of attached PWAS. A possibility to model the shear-lag effect is described in detail e.g. in (*Giurgiutiu*, 2007).

2.5 Types of PWAS faults

For simple PWAS, bonded to the structure, the system unit "PWAS" consists of the bonding layer, the soldered connections and the PWAS itself, either embedded or not. Consistently the following defects are possible:

- Defect of the soldering connection,
- Degradation of the adhesive layer,
- Degradation of the piezoelectric material, also called aging,
- Debonding of the PWAS from the structure, and
- Cracks and breakage.

Tests to characterize the sensor performance and its durability have shown degradation effects for PWAS under temperature cycling loads, debonding, and cracks as well as fracture under cyclic mechanical loading (*Blackshire* et al., 2005). *Mulligan* et al. describe cracks in the PWAS when the structure experiences impacts in the near vicinity of the transducer, (*Mulligan* et al., 2011). This can be the case for tool drops during

manufacturing of smart structures or due to impacts when the structure is in use. *Gall* et al. describe cracks in embedded transducers as consequence of mechanical loading, (*Gall* et al., 2009). The degradation of piezoceramics is described in (*Jaffe* et al., 1971). Other researchers describe the effect of debonding in the context of investigations about the bonding layer in general, (*Yelve* et al., 2014; *Sun* and *Atluri*, 2001). *Eckstein* lists breakage, degradation of PWAS, degradation of adhesive and debonding as possible damage types, (*Eckstein*, 2007). The effect of debonding is treated frequently in the literature. Mostly the aim is not the identification of debonded transducers, but the investigation of the effect of debonded transducers on the SHM algorithms. In the context of identification of defect PWAS, most literature deals with cracked or broken transducers. Fig. 2.19 shows examples for documented PWAS faults from the literature, (*Taylor* et al., 2013; *Gall* et al., 2009; *Blackshire* et al., 2005).

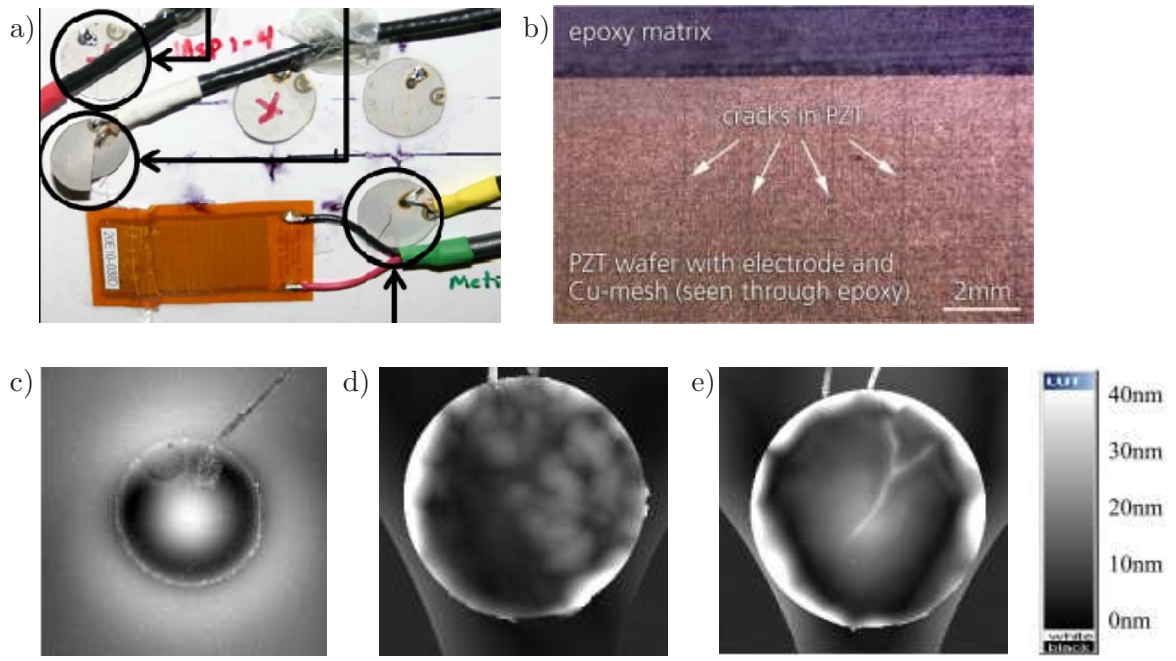

Figure 2.19: a) Realistic sensor breakage during long term testing, taken from (*Taylor* et al., 2013); b) cracks in embedded transducer during tension tests, taken from (*Gall* et al., 2009); maximum displacement depicted for c) healthy PWAS, d) debonded PWAS and e) cracked PWAS after mechanical treatment, taken from (*Blackshire* et al., 2005)

If the soldering point is defect, no electric signal will reach the PWAS. Also if the breakage leads to a clear separation of the two soldering points, the electric signal will break down. These cases are easy to detect, as no excitation or sensing is possible at all. All the other defects mentioned, including other cases of breakage, have an effect on the excited wave, when used as actuator, and the received signal, when used as sensor. The

changes might be misinterpreted by the SHM system as structural damages. Therefore, a possibility to check the transducers is absolutely necessary. The kind of application, e.g. co-bonded or secondary bonded, as well as the type of transducer, influence, which type of damage is possible and likely to occur.

This work focuses on defects of the PWAS in the form of cracks as well as breakage and reduced serviceability of the adhesive layer in form of debonding and degradation, which do not lead to a complete breakdown of the PWAS function, but can be misinterpreted by the SHM system.

2.6 State of the art for PWAS inspection

Transducer inspection requires the detection of sensor faults. Independent of the types of sensors and their application area, a variety of methods exist, which use the redundancy of sensor data. Based on the sensor data the sensor system and its relations including redundant information is modeled. The difference between the model and new measurements is used to achieve information about the sensors state. *Kullaa* calls this *hardware redundancy*, (*Kullaa*, 2010). An overview of a method for sensor signal validation, based on null-space and a posteriori probabilities is given by (*Ray* and *Luck*, 1991). *Dunia* et al. describe the use of principal component analysis (PCA) to identify faulty sensors from their data, (*Dunia* et al., 1996). The squared prediction error is used as decision parameter. As sensor faults, bias, complete failure, drifting, and precision degradation are mentioned. *Kullaa* additionally mentions gain, noise and constant with noise, (*Kullaa*, 2010). In the context of model predictive control *Pranatyasto* and *Qin* also use a PCA-based method for the failure modes gross error as well as spikes, sensor failure and random noise for a fluid catalytic cracker system of an oil refinery, (*Pranatyasto* and *Qin*, 2001) . *Benaicha* et al. use PCA but add hierarchical contribution plots and test multiple fault cases with a mathematical model, (*Benaicha* et al., 2010). Also using redundancy, in (*Baljak* et al., 2012) spatial and temporal correlation is assumed and a decision tree is used to achieve a classification of sensor faults of wireless sensor systems.

The aforementioned literature is not focusing the application for structural dynamics or SHM. Putting the topic of sensor fault detection into the context of smart structures, *Friswell* and *Inman* use the redundancy of sensor data and mention accelerometers, strain gauges, PVDF film sensors, optical fiber sensors and also piezoceramic

patches, (*Friswell* and *Inman*, 1999). Here the modal filtering approach uses the redundancy within the sensor signals to find faulty sensors. White noise was added or multiplied with their original signal. Using PCA as an alternative to more complex auto-associative neural networks (AANN), *Worden* checks sensors for measurements of structural dynamics, (*Worden*, 2003). If flawed sensors are identified due to redundancy inherent in the measurements, the modeled sensor signal of the PCA model differs from the measured sensor signal. A correction of the faulty sensor signal can be achieved with ARX-models (auto-regressive with exogenous input). For the application within an SHM system the difference between measured and modeled sensor signal can also be caused by a structural damage or a change of environmental and operational conditions (EOC). If sensor fault and structural damage cannot be separated, the advantage of transducer inspection vanishes. This fact is mentioned in (*Kullaa*, 2010) and taken into consideration in (*Kullaa*, 2011). A multiple hypothesis test is used to identify faulty sensors. Accelerometers or strain gauges are mentioned as possible sensors as the method is used in the context of SHM. The effect of EOC and structural damage is considered in (*Kraemer* and *Fritzen*, 2007) with an additional parameter. The mutual information concept uses the level of redundancy of two signals. Additionally, the use of auto-regressive models is presented as a complementary method. The differentiation between sensor fault and structural damage is based on the assumption that structural damage is recognized by several sensors, while a sensor fault only has an effect on a single sensor. This assumption cannot be made for some applications, see e.g. (*Xing* and *Fritzen*, 2007), and it depends on the chosen parameters for damage detection, sensor network, and size of the damage. *Jones* and *Parker* show a method to detect debonded accelerometers from the output power covariance at the reference and current states, suggesting three bonding metrics (*Jones* and *Parker*, 2011). Common to all listed approaches is a purely mathematical approach without relations to physical quantities.

Another type of redundancy, mentioned in (*Kullaa*, 2010), is *analytical redundancy*, which is created e.g. via the use of analytical models or finite element models. While the use of physical relations of this kind of models is increased compared to PCA, another factor needs to be considered. The model has to be very precise to achieve a good agreement for each single measurement. The numerical costs are therefore comparably high and it is difficult to detect small sensor faults.

Above mentioned approaches all use the normal measurement data of the sensors to identify if a sensor is faulty. The advantage of this is, that no additional measurements are necessary. This also leads to a disadvantage as this makes the distinction between structural damage and sensor fault very difficult, especially for the case of small defects and wide spread sensor network. Moreover sensor faults of piezoelectric transducers have different, partially frequency dependent effects on the measured quantity for structural damage detection. The classification into gain, drifting etc. does not satisfy the effects of faulty PWAS.

Several works specifically focus on PWAS. (*Blackshire* et al., 2005; *Blackshire* et al., 2006; *Gall* et al., 2009; *Gall*, 2012; *Bach* et al., 2013) are not focused on the detection of PWAS faults during usage, but deal with the durability, long term integrity and investigations of the typical damage patterns. For these investigations, methods for detecting faulty PWAS are necessary and have been applied. However, the methods, used for testing the durability, are not necessarily applicable for a bonded PWAS during employment and operation. *Gall* et al. use stereo microscopy to evaluate the PWAS state, (*Gall* et al., 2009). For the investigated capsulated PWAS under pretension, cracks can be seen with microscopy. These cracks are also audible and visible in curves depicting electric charge over strain during one load cycle in a four-point bending test. The slope of electric charge over strain is introduced as an indicator for the sensor function. A decrease in slope indicates degraded sensor functionality. This procedure is also used in (*Bach* et al., 2013). *Blackshire* et al. describe the use of displacement field imaging, using a near field scanning interferometry system, (*Blackshire* et al., 2005). Via a scanning of the applied PWAS under operation the maximum displacement field is evaluated. Areas close to cracks and debonded areas show higher maximum displacement, other treatments revealed a decreasing maximum displacement, which is interpreted as degradation of sensor performance. Researchers from *Sherebrocke University* (*Mulligan* et al., 2011; *Masson* et al., 2013; *Mulligan* et al., 2014) mainly focus on finding signal correction factors, which enable a reliable structural damage detection although the transducer is damaged. In (*Mulligan* et al., 2011) the capacitance is chosen as PWAS damage sensitive feature. Other investigations have shown, that the capacitance describes the PWAS faults insufficiently (*Buethe* et al., 2014a). Consistently in (*Masson* et al., 2013; *Mulligan* et al., 2014) a much more elevated method of finding signal correction factors, using finite element simulations, calculated with *COMSOL*, and using the susceptance as PWAS damage sensitive feature, is described.

A method of fault detection for PWAS is discussed in (*Sohn*, 2009). Suggesting to use a time reversal index, a symmetry index and a *Lamb* wave energy ratio index, the capacitance is used as first indicator. All other indices are used to separate structural damage and changes of EOC from PWAS faults. The two damage cases of debonding and sensor cracking are discussed. For cracking of PWAS it is shown in (*Buethe* et al., 2014a) that the capacitance describes the PWAS faults insufficiently.

Various publications deal with the effect of parameters within the bonding layer like effects of the adhesive layer thickness. Partly they also deal with the effect of debonding, (*Faria*, 2003; *Ha* and *Chang*, 2010; *Sun* and *Atluri*, 2001; *Lanzara* et al., 2009; *Tinoco* et al., 2010; *Boehme* et al., 2010; *Moharana* and *Bhalla*, 2014). Mostly a description of the effects on the suggested structural damage detection method is described. PWAS fault detection is not focused.

While some of the aforementioned PWAS inspection possibilities are not feasible for the implementation in an SHM system, the measurement of the EMI is possible, especially when using a simplified measurement circuit, as described in (*Overly*, 2007). It can be easily implemented in the acousto-ultrasonic measurement device. This is done by the *PZT Inspector*, a device developed at the University of Siegen, (*Fritzen* et al., 2014).

The use of the EMI to detect faulty PWAS in the context of SHM is discussed as a side issue in (*Giurgiutiu* and *Zagrai*, 2002; *Pacou* et al., 2002). It is the main topic in (*Park* et al., 2006a; *Park* et al., 2006b; *Park* et al., 2007). Also *Lee* and *Sohn*; *Eckstein*; *Bach* et al. discuss the use of the EMI, (*Lee* and *Sohn*, 2006; *Eckstein*, 2007; *Bach* et al., 2007). Further work is published in (*Park* et al., 2008; *Overly* et al., 2009; *Lee*, 2009; *Lee* and *Sohn*, 2010; *Taylor* et al., 2013). Different ideas to use the EMI have been developed. *Park* et al. describes the use of the susceptance spectrum in a low frequency range, (*Park* et al., 2006a). Thereafter a debonding of the PWAS results in an increased susceptance slope while a PWAS breakage leads to a decreased slope. As described before the susceptance slope is closely related to the capacitance. The capacitance and its standard deviation over a batch of transducers is also used in (*Overly* et al., 2009). For severe damages these methods have proven to be valuable. Nevertheless, small cracks without spalling are not detected with this method (*Buethe* et al., 2014b). Recently *Rugina* et al. published a numerical and experimental study on the use of the EMI for structural damage detection. The paper focuses on the comparison of analytical, numerical, and experimental results for the detection of cracks in circular aluminum plates. It also includes the analysis of the

influence of confounding factors like the PWAS bonding condition on the structural damage detection with EMI, (*Rugina* et al., 2015). They explicitly give the example of central debonding of the PWAS which does not affect the slope of the susceptance. In (*Kamas* et al., 2015) an analytical model of the EMI for a free PWAS including in-plane and out-of-plane modes is shown. The authors state that "modeling of a free PWAS is useful for ... sensor screening and quality control prior to installation on the monitored structure".

In the second edition *Giurgiutiu* claims: "For PWAS, a sensor self-diagnostic method is readily available through the E/M impedance" (EMI) "technique...", (*Giurgiutiu*, 2014, p. 384). The described technique, which uses the imaginary part of the impedance (reactance X) is based on the free-vibration resonances, which are suppressed when the PWAS is bonded properly. A debonding of the PWAS will be recognized with this quantity. The usage of resonances is a necessary and a major point for transducer inspection. Nevertheless, other PWAS faults like the degradation of the piezoelectric material will effect the electro-mechanical impedance differently. Moreover only the measurement curves are given, which need to be interpreted automatically.

To the author's knowledge the effects of PWAS faults on AU-based methods are not brought into relation with methods for transducers inspection. The EMI is a very promising quantity to be used for transducer inspection, as it combines electrical and mechanical quantities.

Chapter 2 has given an overview on the basics of AU-based SHM, necessary background information about the PWAS used for AU-based SHM and the EMI spectrum, which will be a key parameter in this work. Different PWAS faults, which need to be detected by a PWAS inspection method, have been introduced. Based on this basic information, the state of the art for transducer inspection is given. Moreover the basics of POD are explained for further use in this work.

3 Effects of defect PWAS on acousto-ultrasonics - experiments & simulations

There is a variety of influences on the results of methods, based on acousto-ultrasonics, such as changing temperature, changing prestress, damages within the structure or changes of the transducers and its bonding layer. In this chapter the effects of transducer breakage, transducer debonding, degradation of the adhesive, and insufficient bonding are considered. These defect types are shown in fig. 3.1.

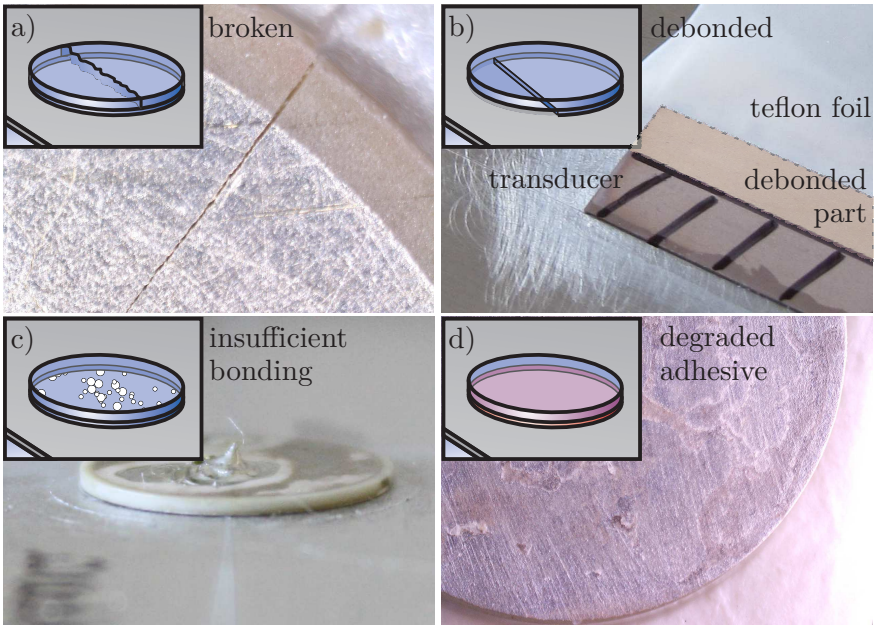

Figure 3.1: Typical PWAS defects, analyzed in chapters 3 and 4, a) broken/cracked PWAS, b) partially debonded PWAS, c) insufficient bonding caused by partial contamination of the bonding surface, d) PWAS with degraded adhesive layer, close-up shows the adhesive layer after chemical treatment and subsequent detachment from the structure.

For all defects, the changes of the generated wave field are discussed. Experimental data is given to show the phenomena, finite element-based calculations are used to

analyze the influence of different parameters and enable additional studies with reduced experimental effort.

Many of the experimental results for simple piezoelectric discs with wrap-around electrode have been conducted in a comparative study. The setup including the defect types is depicted in fig. 3.2. The structure is an aluminum plate with a thickness of 1 mm and dimensions of 500 mm x 500 mm. It is equipped with 16 simple disc-shaped PWAS with wrap-around electrode, *PIC255*, $d = 10$ mm, $h = 0.5$ mm.

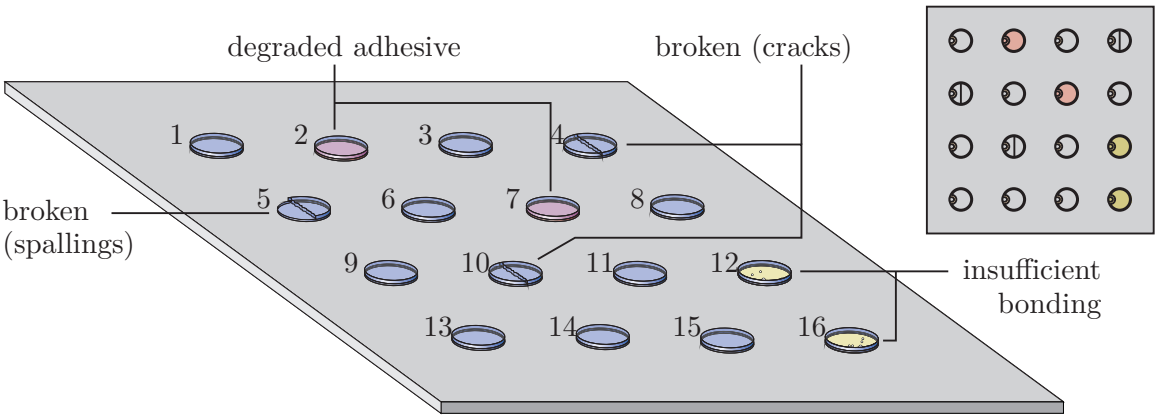

Figure 3.2: Experimental setup for a comparative study of PWAS defects on an aluminum plate. Defect cases, including broken PWAS with cracks and spalling, PWAS with a degraded adhesive layer as well as insufficient bonding caused by partial contamination of the bonding surface, are tested.

The effect on the wave field can be visualized very well, if the displacement or velocity for a grid of points is known. Therefore the use of a laser scanning vibrometer is beneficial. In this work, two different experimental setups for the visualization of the wave field are used: a 3D scanning laser vibrometer and a 1D laser vibrometer mounted on an x-y-table. The description of both setups can be found in appendix A.1.

3.1 Effects of breakage

Cracks and spalling are examples of transducer breakage with different extent. Various types of PWAS show different characteristics for this kind of defects. This section describes two exemplary cases and the effects on the wave propagation.

3.1.1 Breakage caused by tool drop

Transducer breakage can be caused by falling objects, like manufacturing equipment, dropped during assembly. The failure mode, which can be caused by this so-called *tool*

drop, is simulated in an experimental setup with falling masses, see appendix A.1, for simple piezoelectric discs with wrap-around electrode. The impact causes dents and cracks as well as spalling, depending on the transducer geometry, impact location, and the impact energy.

Data of two simple discs with wrap-around electrode (*PIC255*, $d = 10\,\text{mm}$, $h = 0.5\,\text{mm}$) is evaluated. The two transducers have been impacted twice, each, with a mass of 53.5 g from a 350 mm height for the first impact and a 450 mm height for the second impact. Two different damage levels have been introduced. The defects are shown in fig. 3.3. One PWAS is affected with a dent and cracks originating at the dent, the other PWAS is broken resulting in spalling.

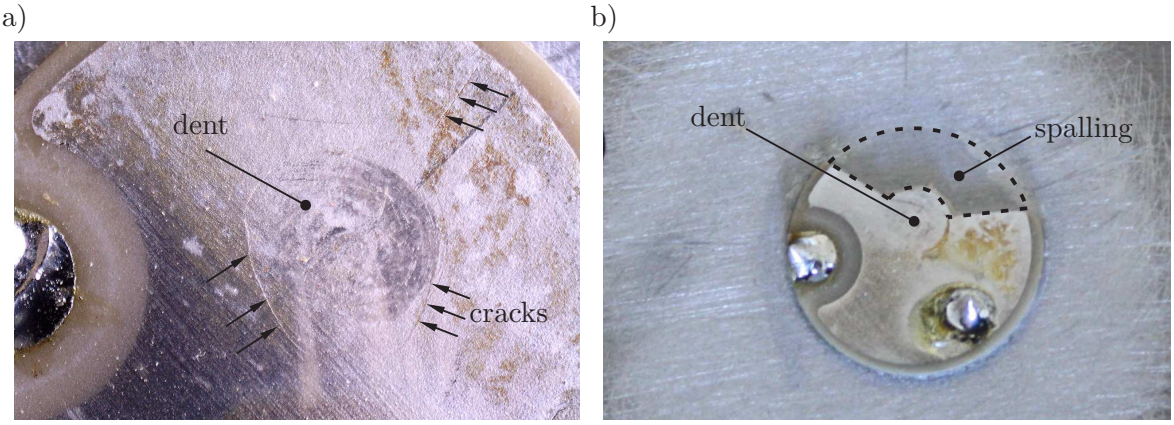

Figure 3.3: Micrographs of the defects, caused by tool drop. a) dent and cracks, but no spalling, b) dent and spalling

The generated wave field, which is transferred into the structure, is visualized by mapping the vibration velocity at the reverse side of the plate, opposite to the PWAS attachment. The maxima of the velocity signals in the out-of-plane direction gives an impression in one shot. the out-of-plane direction is defined as z-direction in this work. Figs. 3.4 and 3.5 both a) show that the generated wave field is not fully symmetric for the undamaged case, which has already been described in (*Moll* et al., 2012). Moreover the maximum is not exactly in the middle, which is partly due to orientation misalignment. This is hardly preventable as the positioning of the PWAS and the plate is done manually. One additional major factor for this is the wrap-around electrode. Nevertheless, the maximum amplitudes show a good agreement between both transducers. The defect cases show a very irregular pattern for the cracked PWAS, with their maxima below the maximum amplitude of the undamaged case. The grooves with lower velocity amplitude visualize the tracks of the cracks. Presumably the impact resulted

in a dent and spalling but also in a decreased energy transmission performance between PWAS and structure.

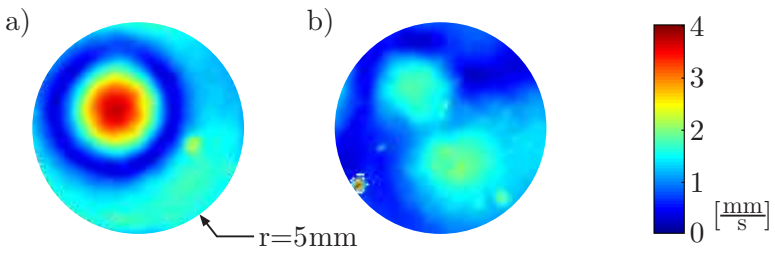

Figure 3.4: Maxima of the velocity field in z-direction, generated by the PWAS and transferred to the structure a) before and b) after impacting the PWAS for the defect cracks without spalling

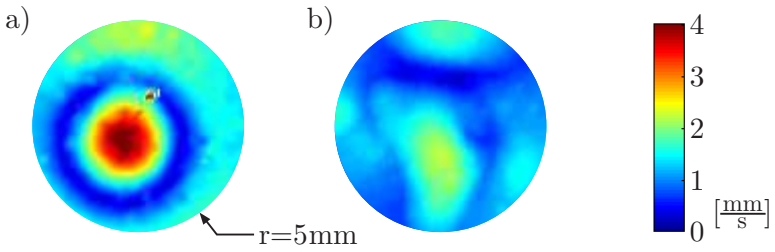

Figure 3.5: Maxima of the velocity field in z-direction, generated by the PWAS and transferred to the structure a) before and b) after impacting the PWAS for the defect cracks with spalling

For the SHM system, the signal received by the other transducers and its change due to defect PWAS is of great importance. Pitch-catch experiments have been conducted with the *PZT Inspector* (appendix A.1) in wave propagation mode. As input signal a five cycle *Hanning* windowed cosine with a central frequency of 85 kHz has been used. Fig. 3.6 depicts the signal with the first wave package for similar paths, which are shortest in the network of the experimental setup (for the numbering and locations refer to fig. 3.2). The cross-talk at the beginning of the signal has been omitted. While for the PWAS with spalling almost no useful signal is left, the useful signal for the cracked PWAS is comparably larger. The effect of the defect is highly direction dependent, as the decrease of the amplitudes differs between the two directions, which are perpendicular to each other. Additionally the direction dependency of the undamaged signal is visible.

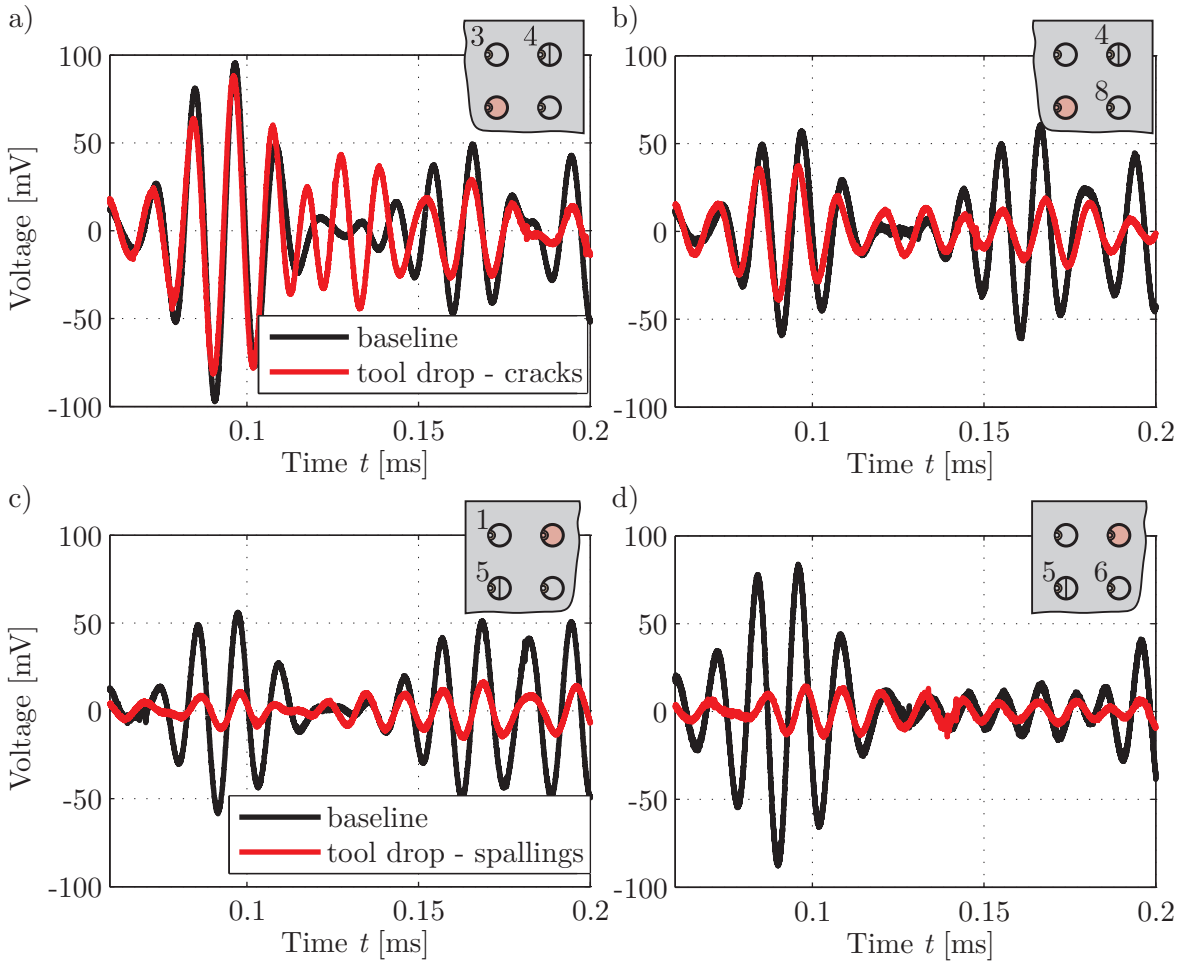

Figure 3.6: Recorded signal before and after impacting the PWASs for both defects of PWAS, neighboring the defect ones. The signal is generated by the inspected and impacted PWAS. a) Path PWAS 4 - PWAS 3, b) Path PWAS 4 - PWAS 8, c) Path PWAS 5 - PWAS 1, d) Path PWAS 5 - PWAS 6

3.1.2 Breakage caused by distributed forces

The effect of a breakage caused by distributed forces over a line for the case of embedded transducers is examined in another experiment. A specified area of the transducer has been partitioned with a chisel. The embedded transducer of type *SMART Layer* (*Acellent technologies, Inc.*, 2005) with a diameter 0.25″ and a thickness 10 mil is secondary bonded with *Hysol EA 9394* (*Corporation*, 2002) on a coated aluminum sample. The PWAS material is similar to *PIC255*. It is excited with a windowed cosine train of five cycles with a frequency of 130 kHz and a maximum amplitude of 100 V. Two different defect stages have been introduced, which are shown in fig. 3.7. In the first stage, 5% of the PWAS area have been partitioned, in the second stage 40% of the PWAS is detached. The wave field, generated by the transducer, is captured with a 3D scanning laser vibrometer, the experimental setup is explained in appendix A.1.

It measures the vibration velocity at the back of the plate, opposite to the PWAS attachment.

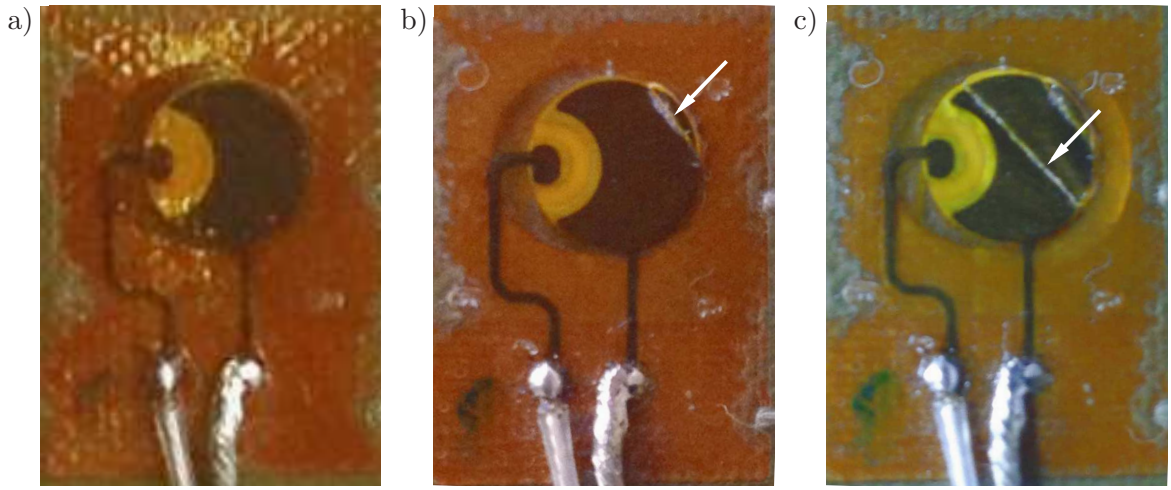

Figure 3.7: a) Undamaged embedded PWAS, used to examine breakage caused by line forces, b) first defect stage, 5% of the PWAS is detached, c) second defect stage, 40% of the PWAS is detached.

Fig. 3.8 shows snapshots of the wave propagation. An area bigger than the transducer itself is investigated. The dashed circle marks the approximate position of the PWAS at the back of the aluminum sample. In fig. 3.8b) the decrease of the amplitude for the small defect can be seen. In fig. 3.9 the second defect stage with two different scales is shown, exhibiting the decrease in amplitude and the change of the generated wave field.

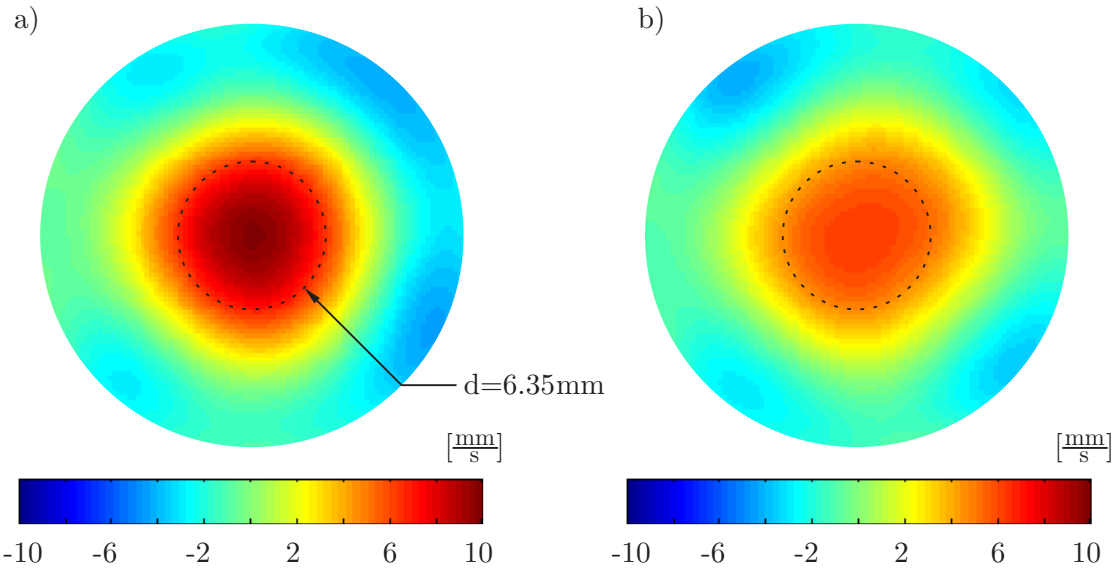

Figure 3.8: Snapshot of the velocity field in z-direction, generated by the PWAS and transferred to the structure a) before and b) after the first defect stage, the dotted circle gives the approximate location of the PWAS.

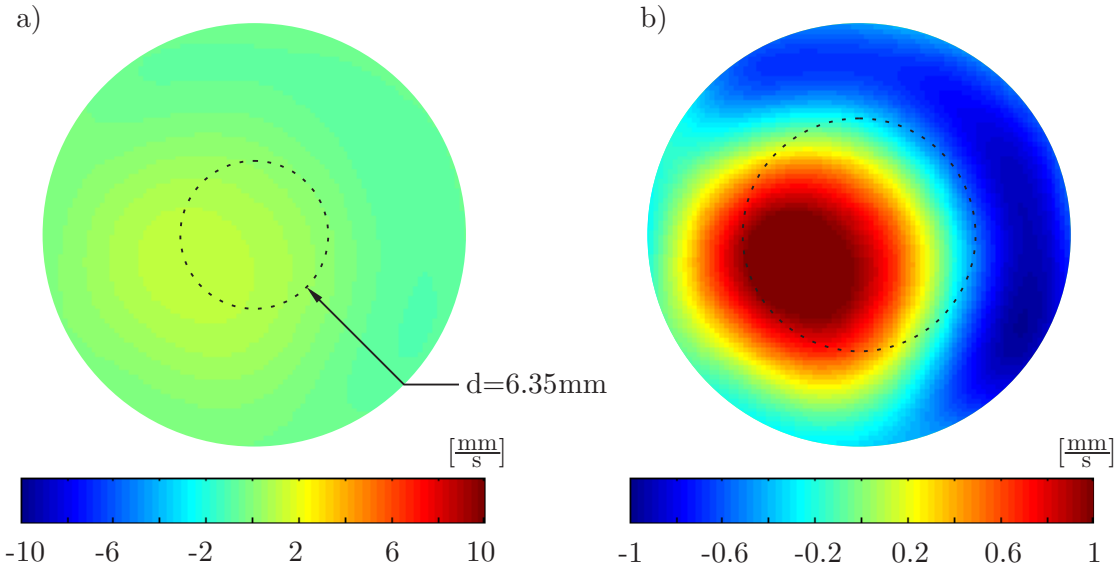

Figure 3.9: Snapshot of the velocity field in z-direction, generated by the PWAS and transferred to the structure after the second defect stage with same scaling as in fig. 3.8 in a) and with different scaling in b). The dotted circle gives the approximate location of the PWAS.

Moreover the maxima of the velocity amplitudes are evaluated. Already for the undamaged case fig. 3.10 shows a non-symmetric behavior, which is most likely caused by the wrap-around electrode. The first defect state leads to a decrease of the wave field. The same is the case for the second defect state, which is much more severe, fig. 3.11.

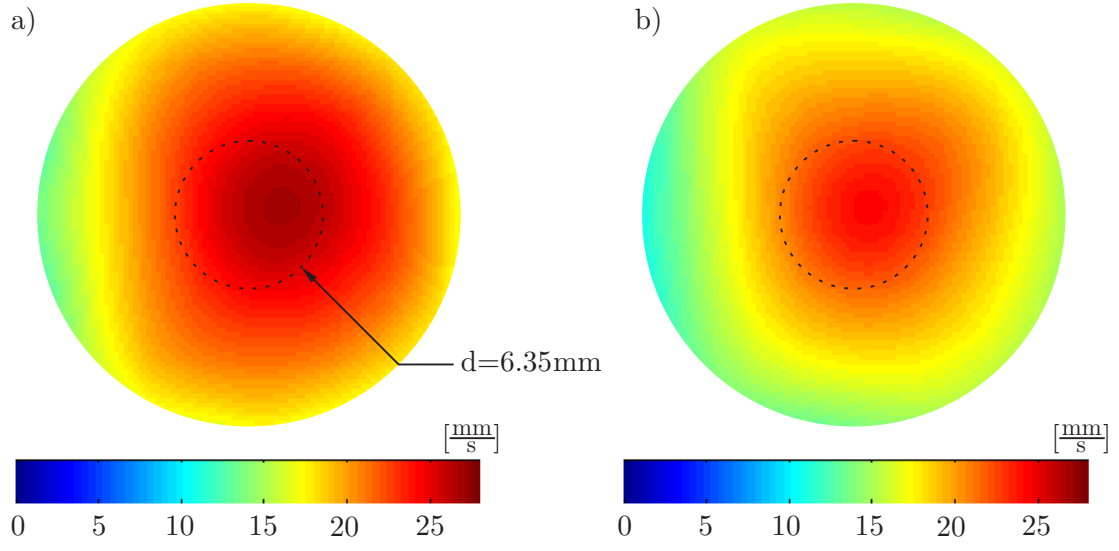

Figure 3.10: Maxima of the velocity field in z-direction, generated by the PWAS and transferred to the structure a) before and b) after the first defect stage, the dotted circle gives the approximate location of the PWAS.

The change of the velocity time series at specific points gives a good indication on the change, which is sensed by other PWAS. Four specific points equally distributed

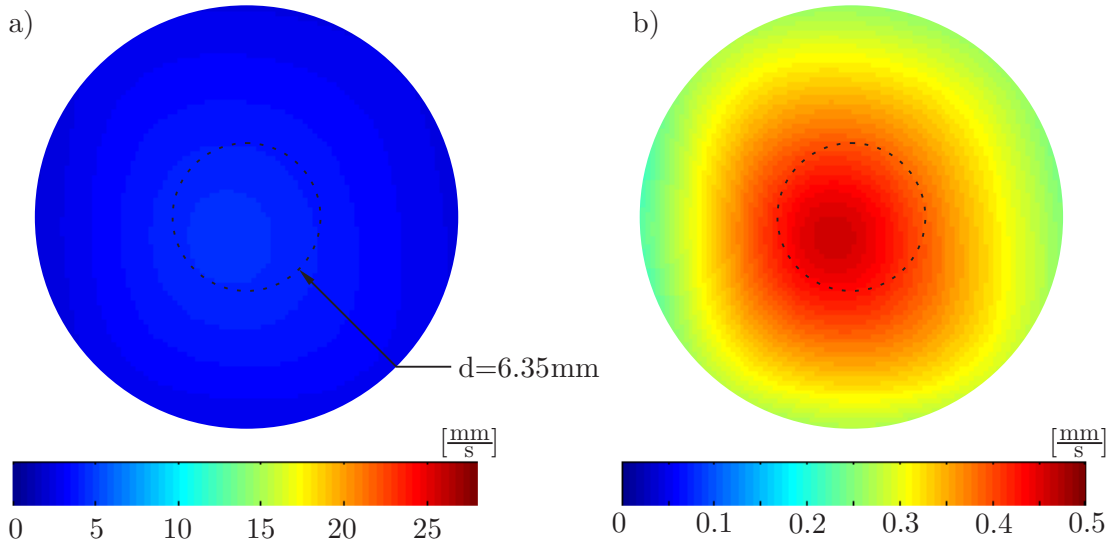

Figure 3.11: Maxima of the velocity field in z-direction, generated by the PWAS and transferred to the structure for the second defect stage with same scaling as in fig. 3.10 in a) and with different scaling b), the dotted circle gives the approximate location of the PWAS.

around the PWAS circumference are evaluated. They have a distance of 30 mm to the location of the PWAS center, the color coding is show in fig. 3.12.

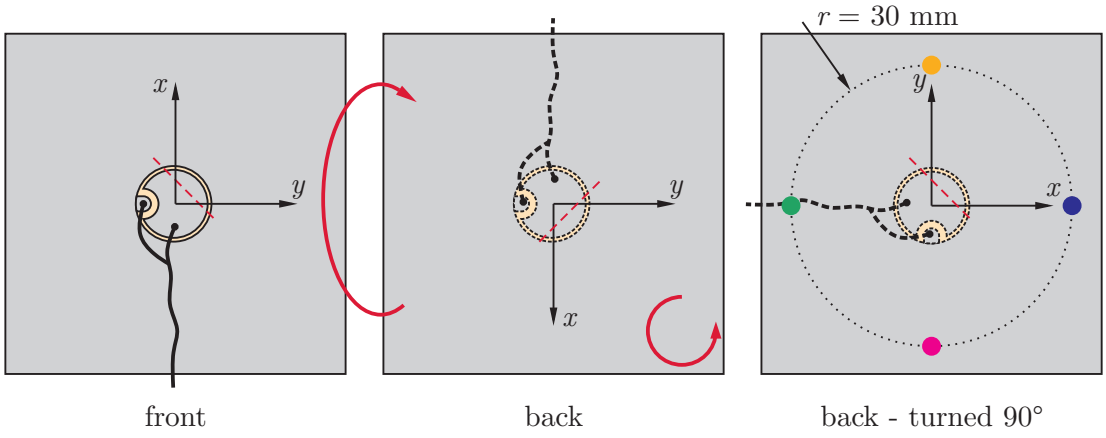

Figure 3.12: Visualization of the experimental setup and the location of evaluation points for the time series analysis of the velocity field for the defect of breakage caused by line force.

The time series are shown in fig. 3.13. The undamaged state shows that the velocity amplitude is uneven for the ideal case mainly due to the wrap-around electrode. The first defect stage leads to more similar time lines. The higher similarity of the four time lines is caused by the fact that the defect is placed opposite to the location of the electrode. The reduction of active PWAS area leads to a slightly decreased amplitude. The second defect stage leads to a major decrease in amplitude.

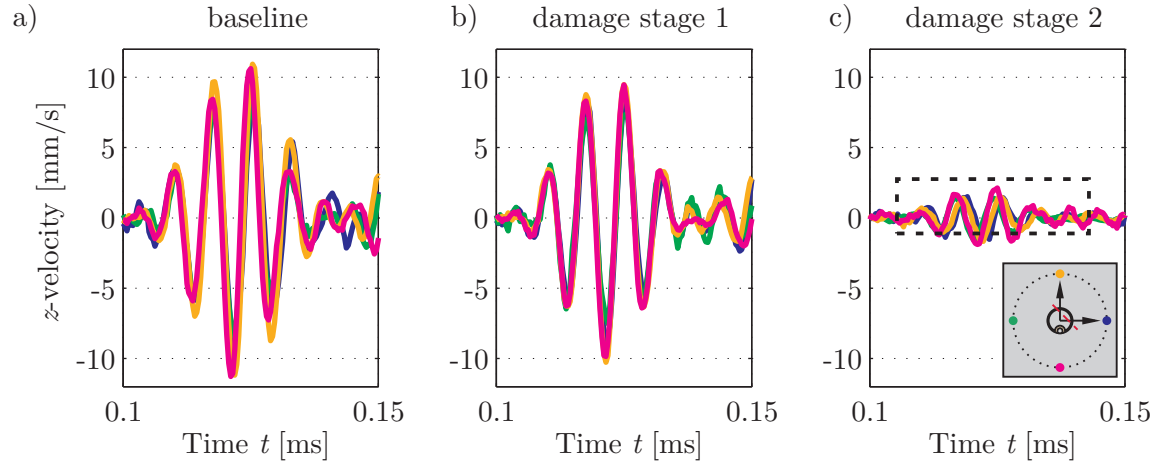

Figure 3.13: Time series of the velocity in z-direction, generated by the PWAS and transferred to the structure for four specific points on the sample, displayed for a) the undamaged case and b), c) both defect stages.

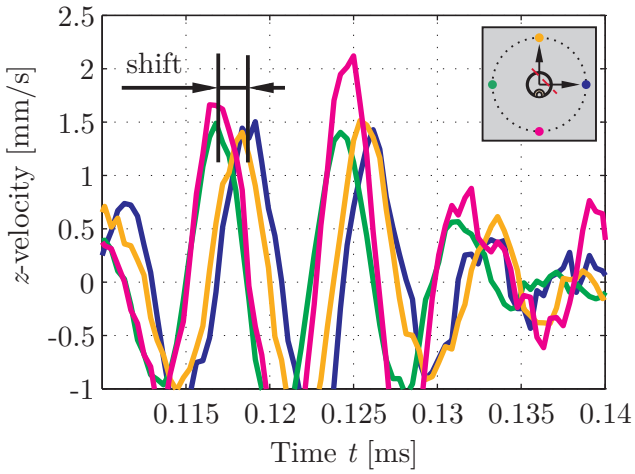

Figure 3.14: Time series of the velocity in z-direction, generated by the PWAS and transferred to the structure for four specific points on the sample, zoom according to marked area in fig. 3.13 c) for the second defect stage

A zoom on the time series of the second defect stage (fig. 3.14) shows a shift in time. The signals of the two evaluation points which are close to the undamaged part of the PWAS arrive earlier than the two other signals. The defects have a significant effect on the generated wave field.

Using the laser *Doppler* vibrometer (LDV) it is possible to analyze the generated wave field of defect transducers in detail. The use of numerical models enables the thorough observation for these cases, excluding additional influences like EOC or the effect of the wrap-around electrode. The numerical model in the time domain is introduced in the following section.

3.2 Numerical model in time domain

For this defined defect of breakage caused by line forces the use of a numerical model with the FEM is introduced. This work does not focus on finite element calculations, but the FEM is used as a tool for the description of phenomena caused by undamaged and defect PWAS. It therefore does not include a detailed description of the numerical methods. The use of commercial FEM software is convenient as the software is well documented, (*COMSOL*, 2013). A short description of the used numerical models is given in the context of the analysis of the results, obtained from these models. The numerical models, based on FEM, simplify the analysis of a series of defects with slightly varied defect parameters. In experiments the introduction of a defect with slightly varied defect parameters, which have been predefined is almost impossible and linked to enormous efforts. This is simplified by using numerical methods. Nevertheless, the numerical model also includes some simplifications, compared to the experimental setup. In this work the wrap-around electrode is not replicated. Instead a disc shaped transducer without any irregularities is assumed. Underneath the piezoelectric element an adhesive layer is modeled, which connects the piezoelectric material with the structural component, fig. 3.15. The structure is simulated as a simple plate.

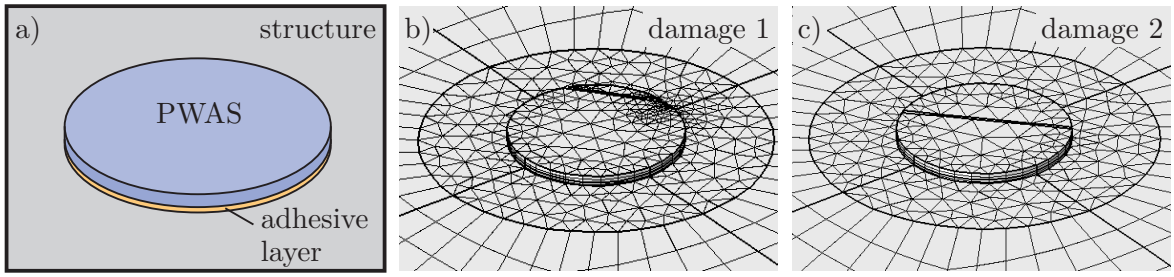

Figure 3.15: Geometrical Setup in *COMSOL* with PWAS, adhesive layer and structure a) undamaged PWAS, b) mesh for first defect stage, 5% of the PWAS is detached, c) mesh for second defect stage, 40% of the PWAS is detached.

The undamaged state is modeled with a stack of PWAS, adhesive and structure. The effect of the wrap-around electrode is neglected. The piezoelectric material is defined with the linear piezoelectric equations in the stress charge form and all piezoelectric constants as solid elements. The structure as well as the adhesive are modeled as solids, likewise, but without the piezoelectricity as linear elastic materials. For all three materials damping is considered. The use of damping is highly important for the adequate modeling of the energy transfer from the PWAS to the structure and the other way around. For the piezoelectric material not only mechanical losses, but also electric

losses and dielectric losses are represented in the model. As input signal a *Hanning* windowed five cycle cosine train with a frequency of 130 kHz already introduced for the experiment has been used. It is sampled with 10^7 samples per second. The excitation signal is given as voltage to the lower surface of the PWAS, while no voltage was applied at the upper surface of the PWAS. This leads to a difference, defined by the excitation signal and the actuation of the PWAS due to the piezoelectric effect. Three materials are defined, the piezoelectric material similar to *PIC255*, the adhesive layer in accordance to *Hysol EA 9394* and the material of the aluminum structure. The geometric properties are chosen according to the nominal values of the experimental validation. To have a consistent meshing type, the PWAS itself, the adhesive layer and a defined area around the PWAS are modeled with free triangular mesh, which is swept through all the materials. The rest of the structure is modeled with a mapped quad geometry, also swept over the thickness of the structure. The structure therefore consists of hexahedral and prism elements. As solving algorithms the generalized alpha method, described in (*COMSOL*, 2013), has been used with fixed time stepping. The details are given in appendix A.1.

Both defect stages have been modeled with a cut in the PWAS according to the pictures of the defect in fig. 3.7. The width of the cut has been modeled with $\frac{1}{20}$ of the PWAS radius. Two ways of modeling for the excitation are possible: Either both parts or only one part of the PWAS are still excited. The excitation of both parts is only possible, if a small connection of the two parts is still intact. If only the part, connected to the soldering points, which is the bigger part for this case, is excited, no electrical connection of the defect parts electrode to the electrode is available. Both ways of modeling the excitation have been tested, as the micrograph (fig. 3.16) of the defect PWAS with removed conduction layer gives hints for both ways. Especially the upper conduction layer is very likely put into two parts. For comparison the data of the numerical model has been shifted in time. This shift is necessary as the data of the 3D-LDV was taken with a pretrigger and the laser data evaluation results in a time shift due to data transfer and decoding. The shift is constant for all defect stages and the undamaged state as the experimental setup has not been changed.

The comparison of the time data of the undamaged state from the numerical model and the experimental results shows good correlation (fig. 3.17 a)). While the experimental data is somewhat spread, the numerical data is the same for all four evaluation points. The wrap-around electrode causes the differences in the experiment. The amplitude is

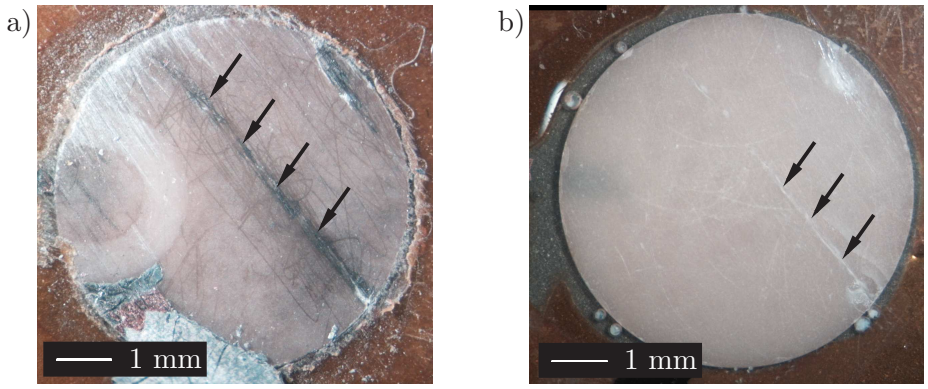

Figure 3.16: Micrographs of the defect PWAS: a) With removed conduction layer, it seems like both parts are not connected any more. The two defects exhibit a greyish color. The larger defect is marked with arrows. b) With removed conduction layer and slightly polished surface, it seems like both parts are still in contact. The white colored crack is not visible throughout the whole PWAS and is marked with arrows.

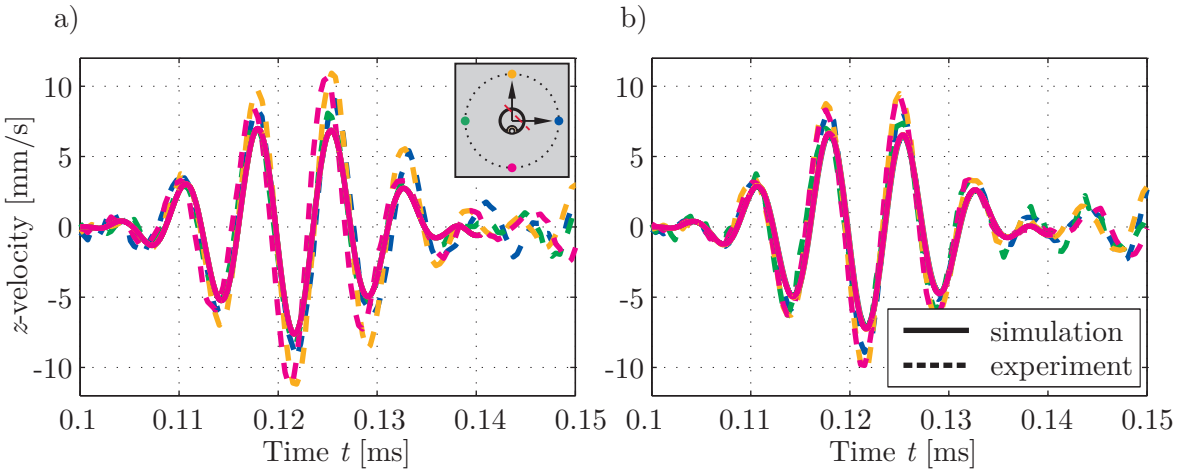

Figure 3.17: Velocity in z-direction at the points, defined in fig. 3.12 taken from the experiment (dash-dotted) and the numerical model (continuous line) a) undamaged state, b) defect stage 1.

slightly to small in the numerical results. No correction factor for the amplitude was used. The differences are probably caused by estimated parameters like the damping of the adhesive layer etc. Especially for parameter studies the numerical model of the undamaged state can be used very well, as it models the physical phenomena from the experiment. The first defect stage is modeled with separate parts. It leads to a reduction of the amplitude for the out-of-plane velocity in z-direction in the FE-model and in the experiment. The effect is larger for the experiment than in the results of the numerical model, which might be caused by an underestimation of the defect. No change of phase between the four points is detectable. Also for the second defect stage a reduction of the amplitude is visible in the experiment and in the model, see fig. 3.18.

Again, the effect is smaller for the numerical model, possibly due to additional defects like debonding of the PWAS or partial debonding of the conduction layer at the top surface. The easy removable connection layer in the visual and destructive inspection of the PWAS after the experiment is a hint for this reason. The results of the two ways of modeling the defect are shown as a) and b) in fig. 3.18. While the modeling with connection between the broken parts does not show any change of phase, this effect is visible for the experiment and the numerical model without any connection of the broken parts. The modeling shows that the second way with clearly separated parts leads to more realistic results and should therefore be used for the numerical modeling of sensor breakage caused by line forces.

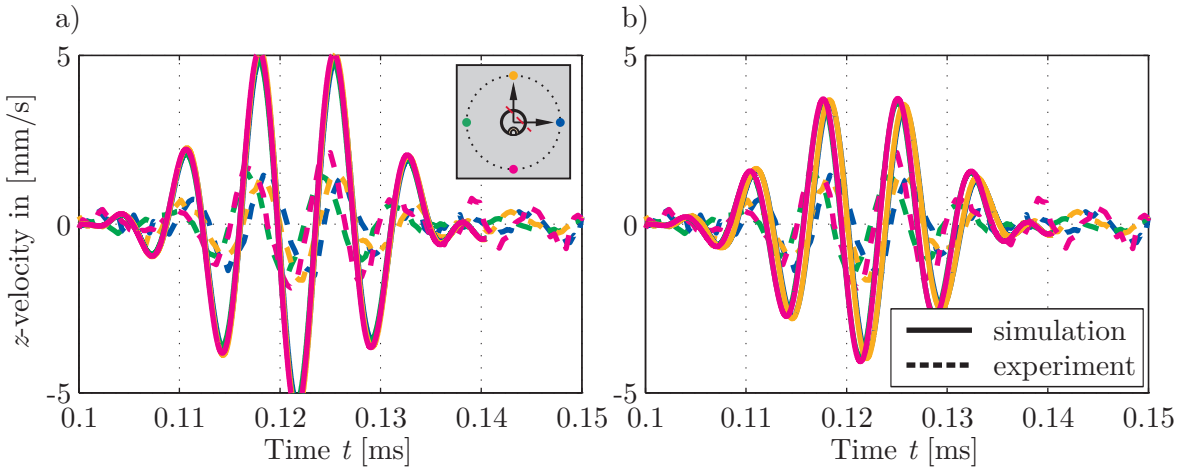

Figure 3.18: Velocity in z-direction at the points, defined in fig. 3.12 taken from the experiment (dash-dotted) and the numerical model (continuous line) for defect stage 2 a) modeled with connection between the two broken parts, b) modeled without connection of the two parts.

3.3 Effects of debonding

The effects of debonding on the wave propagation are shown with the help of the results from two experiments, one using a rectangular and one using a circular transducer. The first experimental setup is depicted in fig. 3.19. A rectangular PWAS type *PIC255* (70 mm x 10 mm x 0.2 mm) has been partially bonded to an aluminum plate of thickness 1 mm and other dimensions 500 mm x 500 mm. The debonded area is half of the PWAS size. The debonding is realized via partial bonding with superglue while a part of the bonding area is covered with a teflon foil preventing this area to be glued. After the investigation on this experimental setup, the PWAS is fully glued

on the plate and the wave propagation is analyzed again. This allows the comparison with the undamaged state, using the same transducer. This type of transducer defect is also investigated using numerical methods. The use of a long PWAS with a small width makes it possible to analyze this problem as a 2D-problem, which simplified the modeling. This PWAS has no wrap-around electrode, which alters the wave propagation. Therefore, an isolated analysis of debonding phenomena is possible. No contact forces are included in the model.

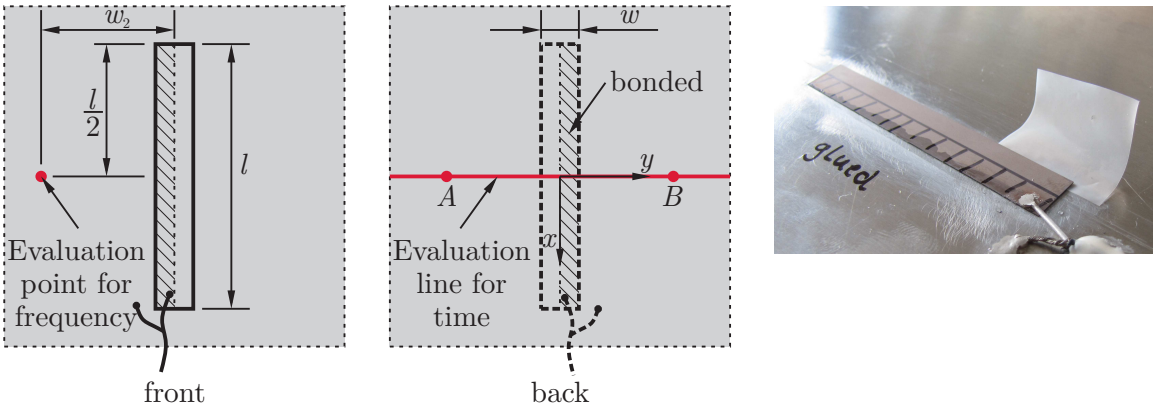

Figure 3.19: First experimental setup for the analysis of debonding of piezoelectric transducers, $w = 10$ mm, $l = 7$ mm, $w_2 = 50$ mm. The bonded area is cross-hatched.

The evaluation line is placed in the symmetry axis of the PWAS. At the back of the plate the velocity in z-direction is measured at multiple points with a distance of 1 mm along the evaluation line with the 1D laser vibrometer (appendix A.1). This measurement is completed for 80, 100 and 180 kHz. At the front of the plate the velocity in z-direction is measured at a single point with a distance of 50 mm to the middle of the PWAS. This measurement is completed for frequencies from 20 to 200 kHz with an increment of 5 kHz. As input signal a *Hanning* windowed cosine train with 5 cycles and specified central frequency is used.

For the line measurements the evaluation at a central frequency of 80 kHz shows that the measured velocity is symmetric for the fully bonded PWAS (fig. 3.20, evaluated at time $t = 0.1$ ms). For the debonded case the measured velocity at both sides of the PWAS is not the same. Three main effects superimpose. The whole pattern exhibits a slight shift to the right, which is caused by a shift of the center of the bonded part to the right. Moreover the highest velocity values are higher on the bonded and lower on the debonded part compared to the measurements of the fully bonded PWAS. At the location of the PWAS, after the windowed input signal has passed, for the case of the debonded PWAS additional vibrations are visible. This is possibly caused by

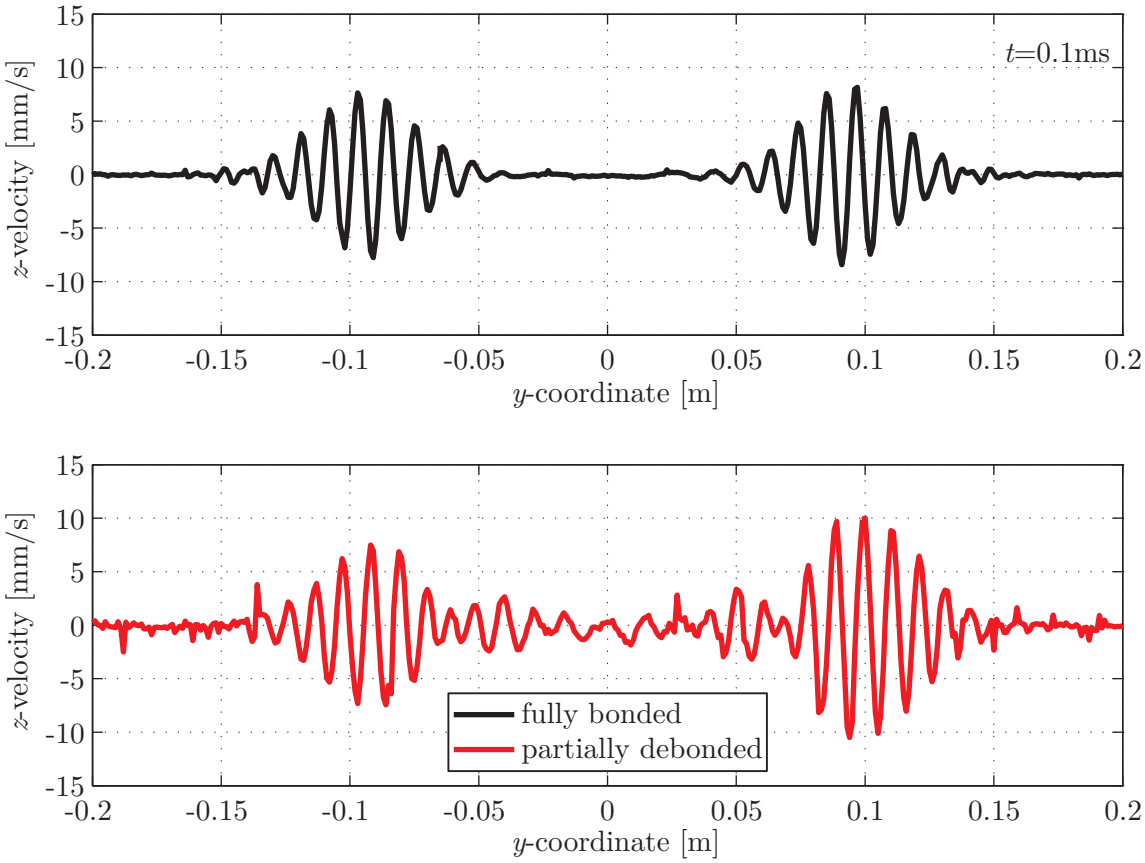

Figure 3.20: Comparison of velocity snapshots at the evaluation line for the debonded and fully bonded case at a time t=0.1ms for a central frequency of 80 kHz.

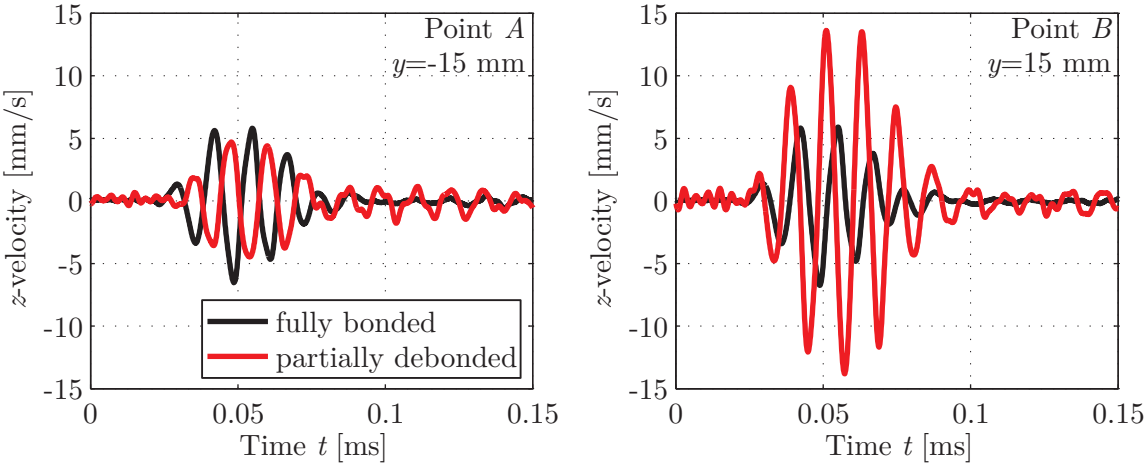

Figure 3.21: Comparison of the velocity over time for two points with equal distance (15 mm) to the PWAS center for the debonded and fully bonded case at a central frequency of 80 kHz.

energy, trapped in the debonded part of the PWAS, which is slowly transferred to the plate. Fig. 3.21 shows the comparison of the velocity over time for two specific points A and B, both having a distance of 15 mm to the PWAS center. The signals confirm the findings obtained from the snapshots in fig. 3.20.

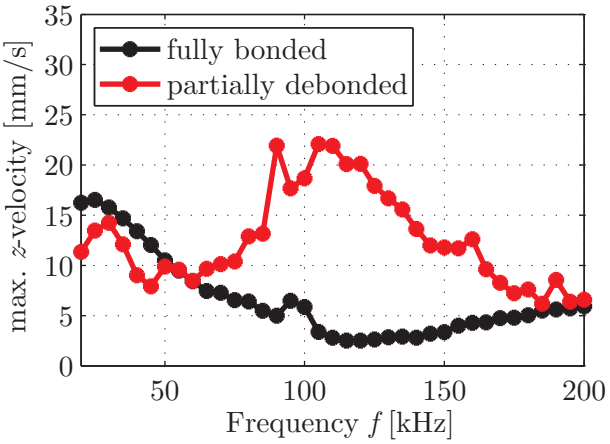

Figure 3.22: Frequency response for the fully bonded and partially debonded case.

From the measurements at a single point for several frequencies a frequency response can be calculated by evaluating the maximum of the *Hilbert* transform for each frequency. Fig. 3.22 shows that the debonding leads to a change in the frequency response. The smaller attachment area does not lead to a decrease of the amplitude in the structure for all frequencies. For most frequencies the maximum velocity in z-direction is even higher for the detached state than for the fully bonded case. Only for low frequencies from 20 to 50 kHz, the amplitudes are larger for the fully bonded case. This is caused by the change of bonded dimensions, which have to fit to the exciting frequency. The frequency response is smooth for the undamaged case, while for the debonded case some fluctuations are detectable.

A detailed insight into the motion for the debonded transducer is possible with the help of a numerical model, set up and calculated with *COMSOL*. The example can be modeled as a two-dimensional problem, which saves a lot of computing time due to the reduction of degrees of freedom. A very thin bonding layer is modeled with one element over the thickness, the PWAS as well as the structure are modeled with 3 elements over the thickness. To solve the problem in time domain the methods described in appendix A.1 are used.

Fig. 3.23 shows the velocity perpendicular to the surface of the plate, evaluated at the back side of the plate, opposite to the PWAS location. The effects, shown in this figure, are similar to the experiment. Fig. 3.23 and fig. 3.20 show the snapshot for the same time, the differences of nominal values results from a pretrigger in the experiment. For the undamaged, fully bonded case the velocity is symmetric to the PWAS. For the debonded case the velocity at the debonded side is smaller than for the fully bonded side. At a central frequency of 80 kHz, the amplitude for the debonded case is not

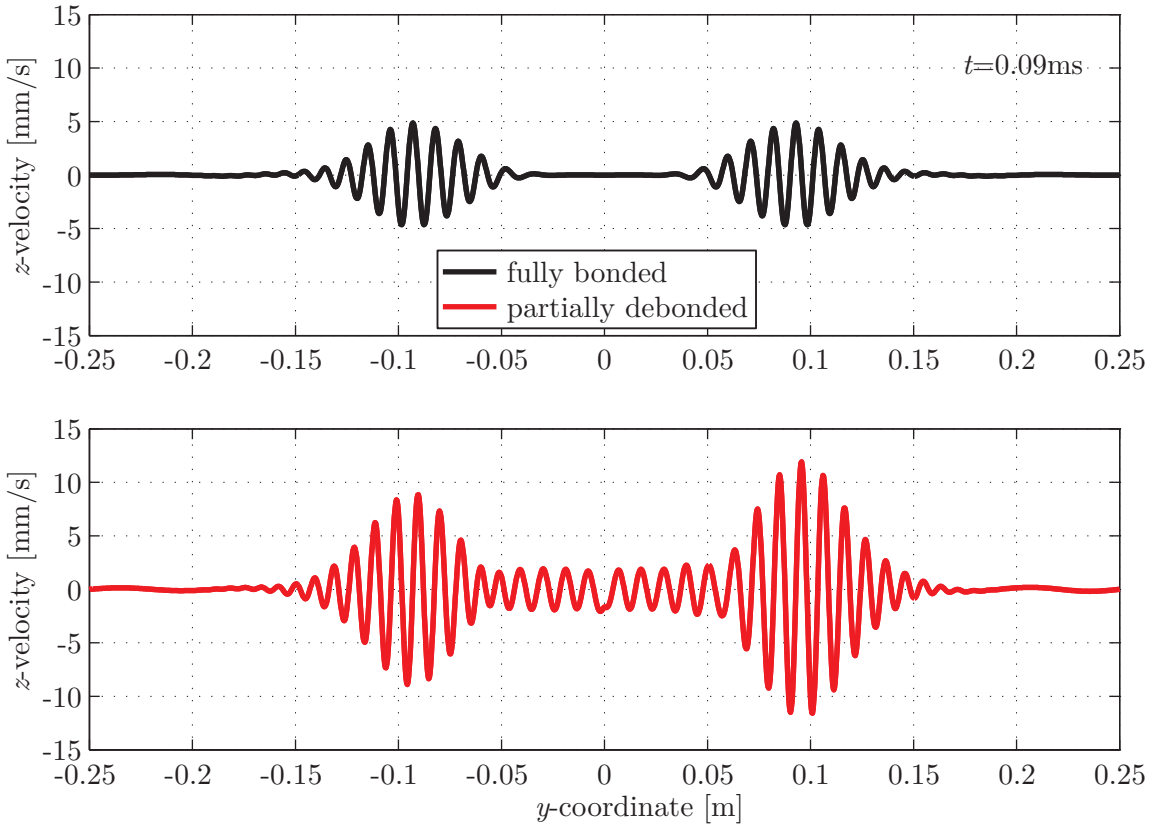

Figure 3.23: Velocity snapshot at the evaluation line for the debonded and fully bonded case at a time t=0.09ms for a central frequency of 80 kHz calculated with *COMSOL*.

smaller, but bigger than for the fully bonded case. Additionally it can be seen that for the debonded case the plate does not stop to vibrate after the input signal decays, but continues ringing, which is not the case for the fully attached PWAS.

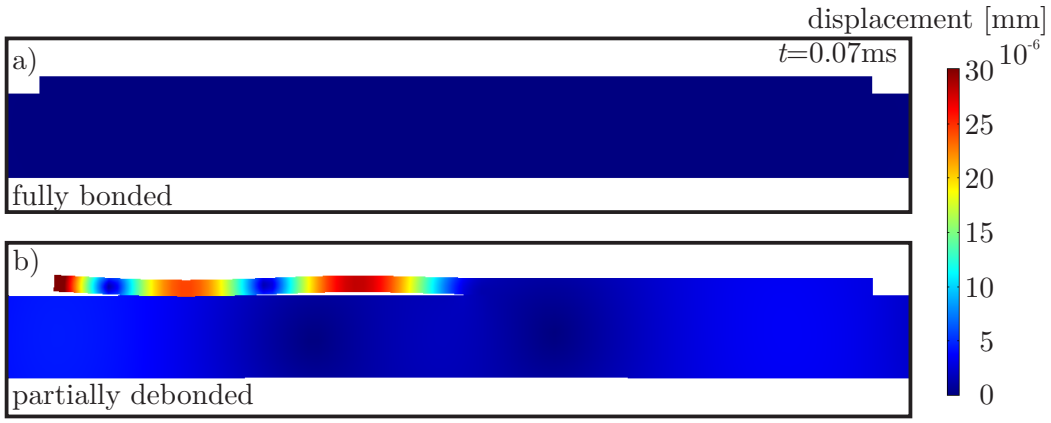

Figure 3.24: Comparison of the total displacement from the a) fully bonded and b) debonded case for t=0.07 ms, which is slightly after the decay of the windowed input signal, calculated with *COMSOL*. The deformation is shown with an amplification factor of 2000.

The debonded part moves after the input signal is decayed, which is visible in fig. 3.24. While for the fully bonded case no total displacement is visible, the debonded part of

the PWAS is still vibrating. This phenomenon can be explained by some energy saved in the debonded part of the PWAS, which is continuously transferred to the structure after the decay of the input signal.

After this detailed analysis of the phenomena for the case of debonding, a more realistic case of debonding shall be analyzed. It is realized with a circular PWAS. The debonding is again implemented via partial bonding with superglue while a part of the bonding area has been covered with teflon foil preventing this area to be glued. Several measurements have been performed, combining different orientations of the soldering point and the debonded area as well a different sizes of the debonded area. More information about the complete data set can be found in (*Golub* et al., 2014). The results will be used in section 6.5. The main aspects of debonding effects for a circular PWAS shall be shown for the smallest debonding case, analyzed and compared to the undamaged state. For this case $\frac{1}{4}$ of the PWAS diameter is covered with a teflon foil, leading to a debonded area of approx. 20%. The PWAS soldering point and the orientation of the debonded area exhibit a 135° turn. The experimental setup is shown in fig. 3.25.

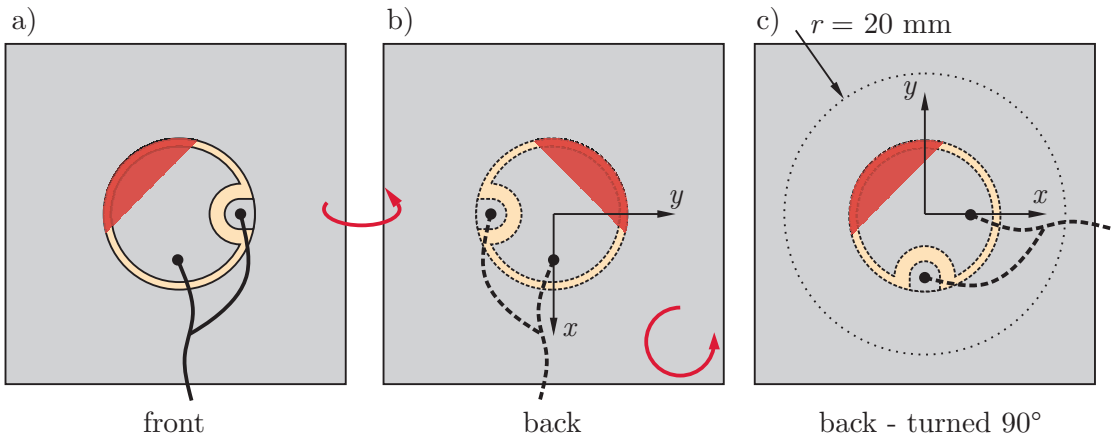

Figure 3.25: Experimental setup to analyze debonding of circular PWAS, a) shows the front, b) shows the back and the orientation, which is realized in the x-y-table for the 1D LDV, c) shows the orientation which is used in the following analysis.

Two different PWAS are examined, one for the debonded case, one for the undamaged resp. baseline case. The two PWAS are of same type, a simple disc shaped *PIC151* PWAS with wrap-around electrode from *PI Ceramic* is used. Both PWAS have different distances to the edges of the supporting aluminum flat plate with a thickness of 2 mm. Therefore only the first part of the signal without reflections is evaluated. A five cycle cosine train is applied to the PWAS at different frequencies between 30 kHz and 180 kHz. For this analysis the selected frequencies of 30, 100 and 170 kHz are shown.

The velocity perpendicular to the plate surface is measured at a distance of 20 mm on a circle around the PWAS center. The measurements points are located on the dotted circle, shown in fig. 3.25 c).

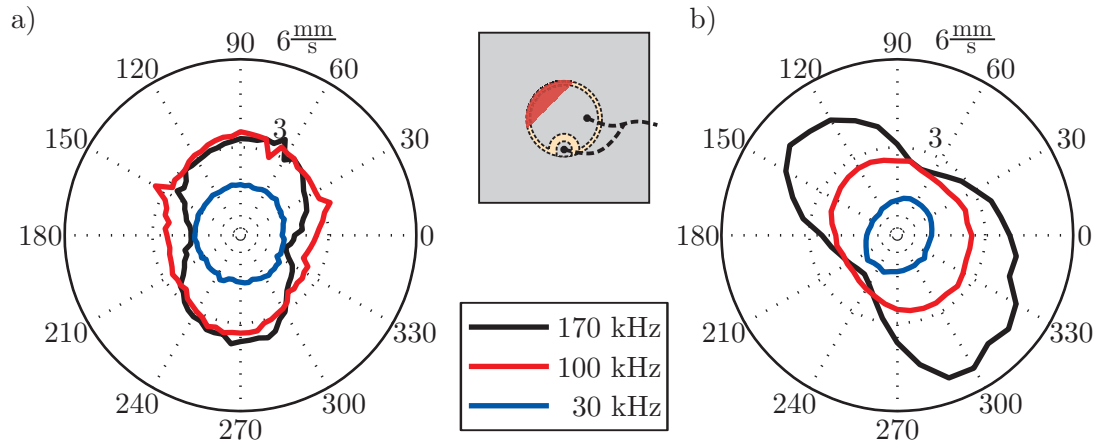

Figure 3.26: Maximum velocity in z-direction amplitude at different angles for different frequencies for a) fully bonded PWAS, b) partially debonded PWAS

In a first step, the maximum amplitude of the recorded velocity signals for the three different frequencies is evaluated for the fully bonded and partially debonded case. Therefore the absolute value of the *Hilbert* transform taken from the filtered signal is used. As described in (*Moll* et al., 2012) already for the fully bonded PWAS the wrap-around electrode leads to a non-axisymmetric wave field. The degree of this deviation from the axisymmetric wave field highly depends on the actuation frequency. As shown in fig. 3.26 for 30 kHz the maximum amplitudes are almost the same for all directions, with a difference of only 20% between the lowest and the peak value. The differences for different angles are clearly visible for a central frequency of 170 kHz. The maximum value is more than double of the smallest value. Highest values are achieved in the axis of the wrap-around electrode elongated through the center of the PWAS, while the smallest velocity is located on the axis perpendicular to the axis described. These findings are consistent with (*Moll* et al., 2012). The debonding leads to a turning of this angular dependency. The largest values can be found on the axis cutting the debonded area in two halves and crossing the PWAS center. The smallest values are shifted 90° to this axis. The debonding therefore leads to effects, similar to the wrap-around electrode. The effect of the debonding can be seen at different frequencies and its extent depends on the frequency. At a frequency of 30 kHz the largest value is approx. 1.5 of the smallest value, while for 170 kHz a factor 3 is present. The effects of a debonding are therefore highly angular and frequency dependent. This is

additionally shown with the help of time series, taken at two different points at the circle, chosen around the PWAS, for different frequencies. The first point is opposite to the wrap-around electrode and 45° to the symmetry line of the defect. The second point is located 90° shifted to the first one as well as to the wrap-around electrode and 135° to the symmetry line of the defect. They are marked in figs. 3.27 and 3.28.

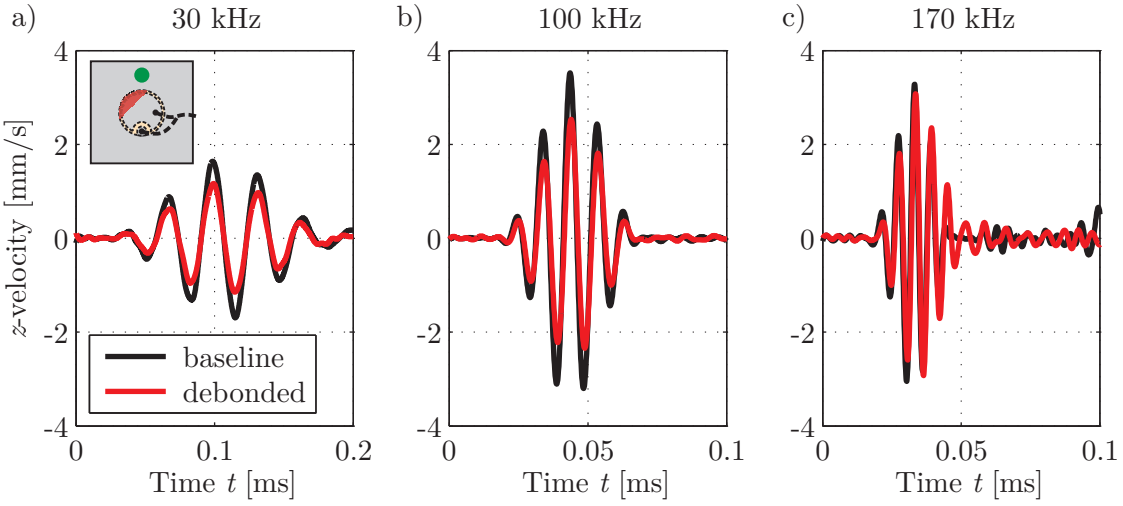

Figure 3.27: Time series for different frequencies, a) 30 kHz, b) 100 kHz, and c) 170 kHz, for the fully bonded and debonded PWAS at a distance of 20 mm on the y-axis.

For the first point the time series for 30 kHz, 100 kHz, and 170 kHz are shown in fig. 3.27 for the fully bonded and defect case. For all frequencies a reduction of the maximum velocity amplitude is visible. Especially for 170 kHz, additional vibration after the decay of the input signal is visible for the debonded case. Due to the location of the PWAS on the structure it can be assured that these vibrations are caused by the debonded PWAS and are not caused by additional reflections from edges of the structure. This additional vibration is in accordance with the findings for the simplified 2D case.

For the second point the time series for equivalent frequencies are shown in fig. 3.28 for the fully bonded and defect case. For this point the debonding does not lead to a decrease of velocity amplitude for all frequencies. For 170 kHz an increase of amplitude is visible, caused by the debonding defect. The shift and turn of the characteristic velocity field leads to these results. Summarizing, for different frequencies, debonding locations, PWAS orientations and sensing PWAS locations the effect of PWAS debonding on AU-based SHM is highly different.

Moreover fig. 3.28 c) shows that the phase difference between the debonded and the fully bonded case exhibits a change from the beginning till the decay of the input

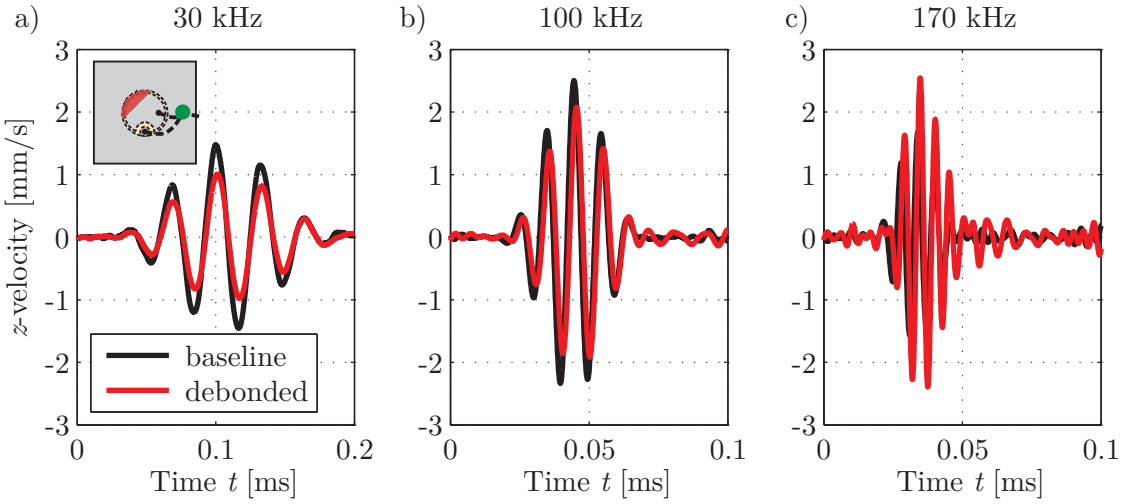

Figure 3.28: Time series for different frequencies, a) 30 kHz, b) 100 kHz, and c) 170 kHz, for the fully bonded and debonded PWAS at a distance of 20 mm on the x-axis.

signal. This might not be caused by a phase difference but by a change of the carrier frequency. In (*Golub* et al., 2014) a detailed analysis based on *Garbor* wavelets is given. In this work the analysis is performed with the use of the short-time *Fourier* transform, which can be used to calculate the power spectral density (PSD) and the linear spectrum (LS).

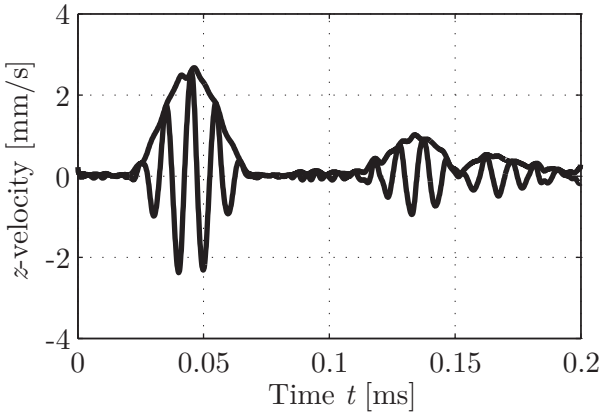

Figure 3.29: Exemplary signal in time domain and its *Hilbert* transform, the measurement was taken at 0° with a central frequency of 100 kHz.

The PSD for the measured signals is time and frequency dependent. As exemplary data, the signal measured at 0° with a central frequency of 100 kHz is used, fig. 3.29. Using the discrete *Fourier* transform (DFT) algorithms the PSD is calculated with a spectrogram. It shows the power of the signal for specified time intervals at different frequencies. The maximum of these frequencies is called carrier frequency to distinguish between the central frequency of the input signal and the carrier frequency of the analyzed measurement, which are not necessarily identical, but should be at least

similar. For the calculation of the PSD a *Hanning* window of a length of 128 data points is used to achieve a smooth PSD curve.

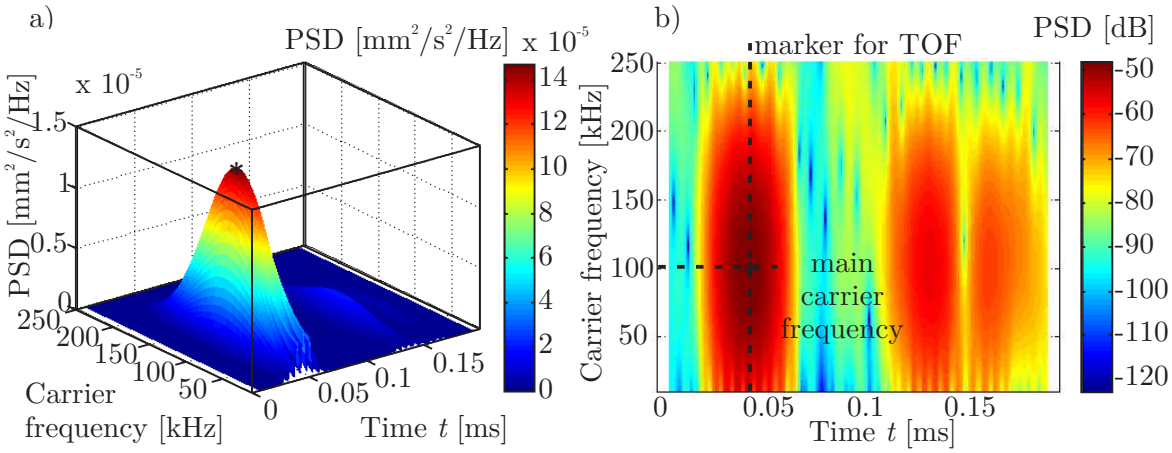

Figure 3.30: PSD of the sample signal, shown in fig. 3.29 with different power at different times and frequencies. a) Linear display of PSD, 3D view, b) the PSD is displayed in decibel, the maximum is marked to determine the carrier frequency.

Fig. 3.30 shows the same PSD in two different forms. Fig. 3.30 a) has a great similarity to the time signal, shown in fig. 3.29, especially when omitting the carrier frequency axis. Here the PSD is displayed linearly. In fig. 3.30 b) the PSD is displayed in decibel, which enables a detailed look at the frequency content of the different wave packages from fig. 3.29. The maximum of the PSD can be used to determine the carrier frequency and the time, at which the maximum power is present at the measurement location. This can help to evaluate the time of flight (ToF), which is usually defined using the start of a wave package.

For further analysis the PSD for all frequencies at the highest power are evaluated from the measurements taken at different angles. The resulting diagrams for the two different frequencies 100 kHz and 170 kHz for the fully bonded and partially debonded PWAS are shown in fig. 3.31. This is used to investigate the relationship of the angle of wave propagation and carrier frequency or other parameters, which can be evaluated with the help of the DFT. The linear spectrum (LS), which in general yields an amplitude of the input signal, can be calculated from the power spectrum. The power spectrum is derived from the PSD via normalization with a constant factor, called equivalent noise bandwidth, see e.g. (*Heinzel* et al., 2002). Due to the use of the *Hanning* window for the DFT, differences between the amplitudes, evaluated from the time signals, as shown in fig. 3.26 are caused. Nevertheless, the dependency of PSD and angle show the same trends as the maximum amplitude at different angles, shown in fig. 3.26.

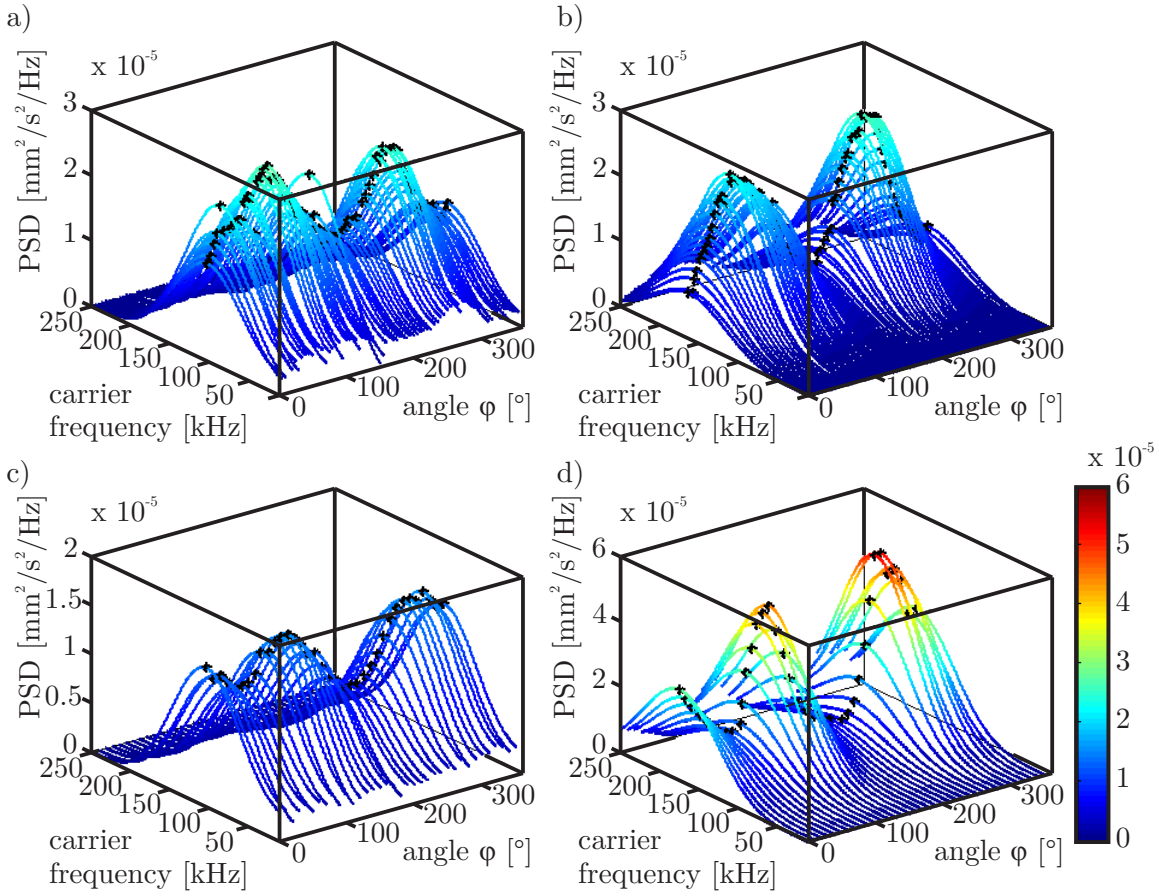

Figure 3.31: Maximum PSD for different angles for a) undamaged PWAS, central frequency 100 kHz, b) undamaged PWAS, central frequency 170 kHz, a) debonded PWAS, central frequency 100 kHz, a) debonded PWAS, central frequency 170 kHz.

The power is angular and frequency dependent. The induced debonding increases this effect especially for 170 kHz.

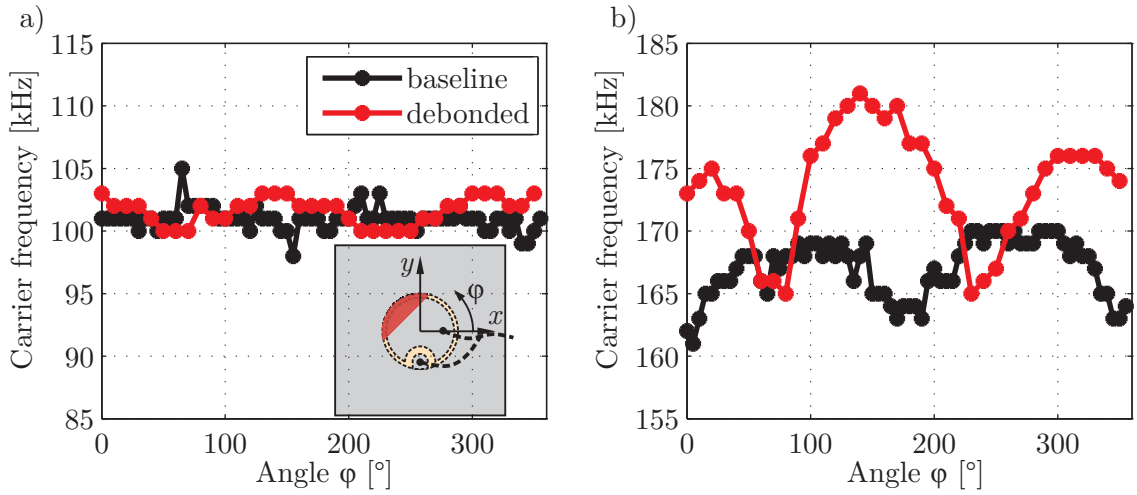

Figure 3.32: Angular dependency of the carrier frequency for a fully bonded and a partially debonded PWAS at a) 100 kHz and b) 170 kHz.

Fig. 3.31 also shows the angular dependency of the carrier frequency. This is depicted in detail in fig. 3.32. While for 100 kHz the central frequency mainly coincides with the carrier frequency, for 170 kHz differences can be seen. For the undamaged case the carrier frequency shows angular dependencies with a maximum carrier frequency at 90° and 270°, which is the direction of the wrap-around electrode. Minima are at 180° and around 0°. All evaluated carrier frequencies are slightly below the central frequency of 170 kHz. The generated pattern shifts approximately 45° and the carrier frequency increases about 5 kHz to 10 kHz for the debonded case. The debonding leads to a similar behavior in its main direction, cutting the debonding in two halves and crossing the PWAS center. This effect superimposes with the effect of the wrap-around electrode, which can be seen at 0°.

This effect is possibly caused by trapped energy and is especially visible for frequencies next to resonance frequencies. Therefore maps of the velocity in z-direction have been made from the back of the plate and from the front of the plate, taking measurements at the PWAS surface. Soldering points, cabling, and the edge of the PWAS limit the measured area. Therefore a circular area with a radius of 4 mm is analyzed on a PWAS with a radius of 5 mm. For the visualization a PWAS with a debonded area of 50% was used, where effects are more obvious. For the measurements from the back of the plate a larger area is analyzed, as the center of the PWAS cannot be located as accurately as from the front. The coordinate system is dependent on the measurement equipment, therefore small sketches placed next to the resulting maps show the location and orientation of the debonded area. As input signal a windowed cosine train with a central frequency of 170 kHz has been chosen.

Fig. 3.33 shows maps of the out-of-plane velocity, measured at the surface of the PWAS. In a) the velocity distribution at a single time step is displayed. The selected time is more than 2.5 times as large as the length of the input signal. For this experimental setup this is a time after the input signal has decayed and before reflections will reach the PWAS. Large vibrations can be seen in the debonded part of the PWAS, exhibiting trapped energy. The maxima of the velocity are shown in fig. 3.33 b). As there is no adhesive layer and structure, which prevent free vibrations of the PWAS, the amplitude is much larger for this part of the PWAS. The debonded area matches the area with larger amplitudes. Compared to the debonded case, the velocity map for the undamaged PWAS, which is depicted in fig. 3.33 c) is quite symmetric, exhibiting

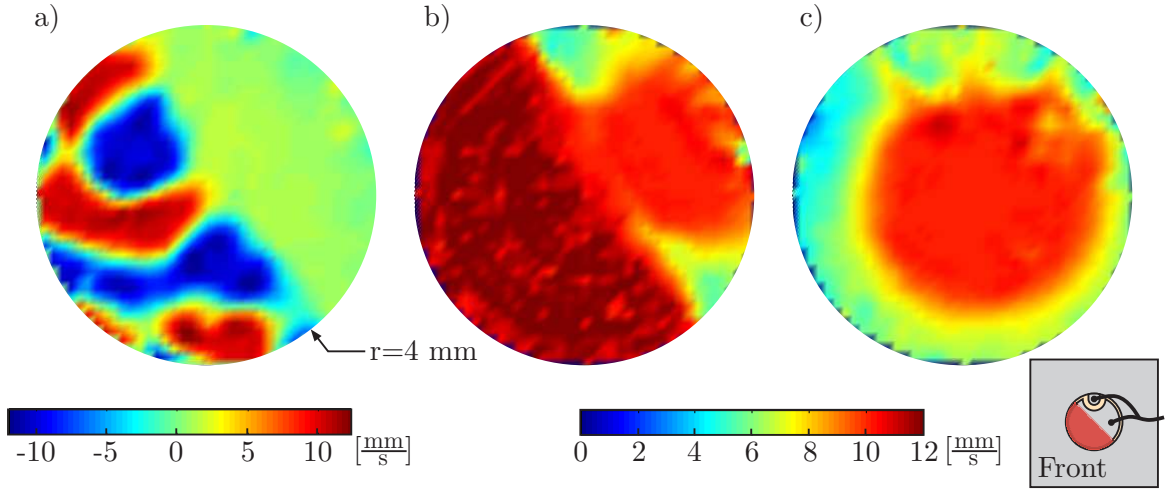

Figure 3.33: Out-of-plane velocity, measured from the front of the PWAS in a circular area with a radius of 4 mm. The small sketch shows the orientation of the PWAS and the debonded area. The input signal has a central frequency of 170 kHz. a) debonded PWAS: velocity in z-direction at time step 800, after the input signal is decayed, b) debonded PWAS: maxima of velocity in z-direction, c) perfectly bonded PWAS: maxima of velocity in z-direction.

minor deviations at the locations of the wrap-around electrode and the soldering points.

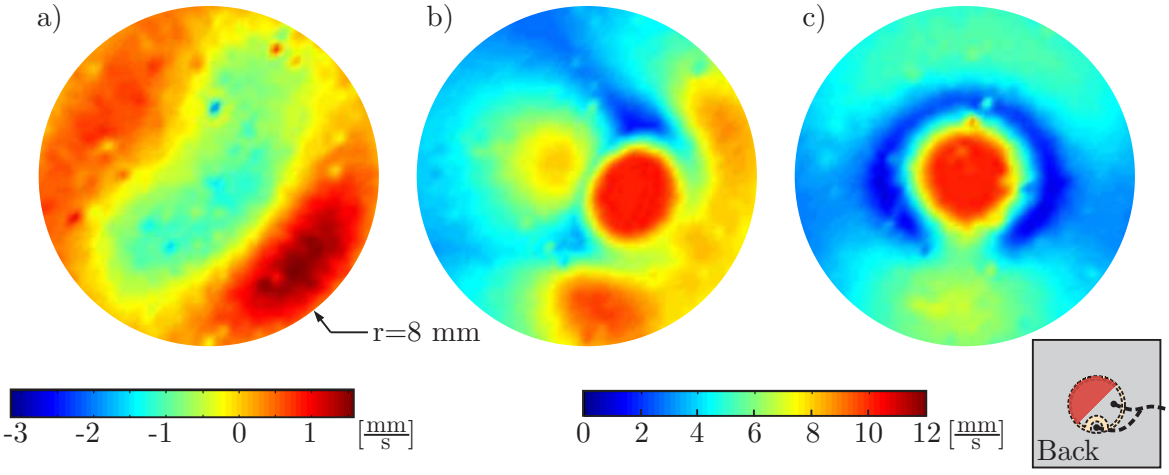

Figure 3.34: Out-of-plane velocity, measured from the back of the plate opposite to PWAS position in a circular area with a radius of 8 mm. The small sketch shows the orientation of the PWAS and the debonded area. a) debonded PWAS: velocity in z-direction at time step 800, after the input signal is decayed, b) debonded PWAS: maxima of velocity in z-direction, c) perfectly bonded PWAS: maxima of velocity in z-direction.

Fig. 3.34 shows maps of the out-of-plane velocity, measured at the back of the structure, opposite to the PWAS. A larger area with diameter 8 mm is shown. The undamaged PWAS in fig. 3.34 c) displays an almost symmetric distribution of the maxima from the measured wave field, compared to the debonded PWAS from fig. 3.34 b). Contrary

to the measurements at the top, from the back the bonded part has larger velocity amplitudes for the maxima and also for the single time step, shown in a). This is due to the fact that only the bonded part delivers energy to the structure. This confirms the findings of the 2D experiments and simulations.

Although the debonding of a PWAS does not necessarily lead to smaller amplitudes, the defect type debonding has major effects on the generated wave field, which lead to difficulties for SHM methods. The effect is highly angular and frequency dependent.

3.4 Effects of degradation of the adhesive layer

Degradation of the adhesive layer can be caused by environmental and operational conditions. To show the influence on the generated wave field, data of a simple disc with a wrap-around electrode (*PIC255*, $d = 10$ mm, $h = 0.5$ mm) are evaluated. The degradation of the bonding layer can be caused e.g. by chemicals dissolving the adhesive material. For this type of transducer, attached to the structure with *Z70* adhesive from *HBM*, the use of the solvent dimethylformamide can cause degradation, if it is applied locally on the attached PWAS for a distinct time of several hours or days. The experimental study described in fig. 3.2 includes the analysis of the effects, degradation of the adhesive layer has.

The defect extent cannot be seen with micrographs, but when removing the PWAS after finishing the experiments, the adhesive layer can be examined. An exemplary picture is shown in fig. 3.1 d). Effects on the generated wave field are visualized with the help of the velocity field generated by the PWAS, depicted in fig. 3.35.

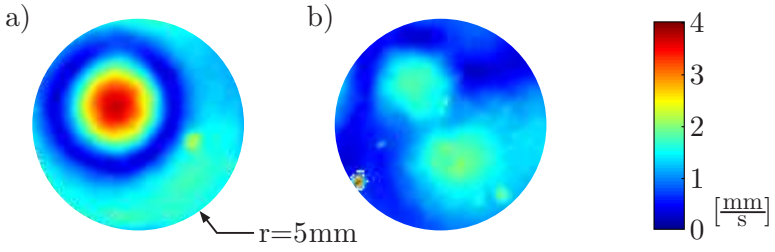

Figure 3.35: Maxima of the velocity field in z-direction, generated by the PWAS and transferred to the structure a) before and b) after treatment of the PWAS with dimethylformamide

The recorded signal of neighboring PWAS gives an idea on how an SHM system is affected by a degraded adhesive layer. Fig. 3.36 shows that the amplitude is decreasing

in all directions. Moreover fig. 3.36c) and d) show, that for the defect PWAS a difference of the signals, depending on the direction of the traveling signal can be seen. If the defect PWAS is used as sensor, the signal is smaller then, if it is used as actuator. Again, the dependence of the signal on the direction of the PWAS is visible in the data of the undamaged and defect case.

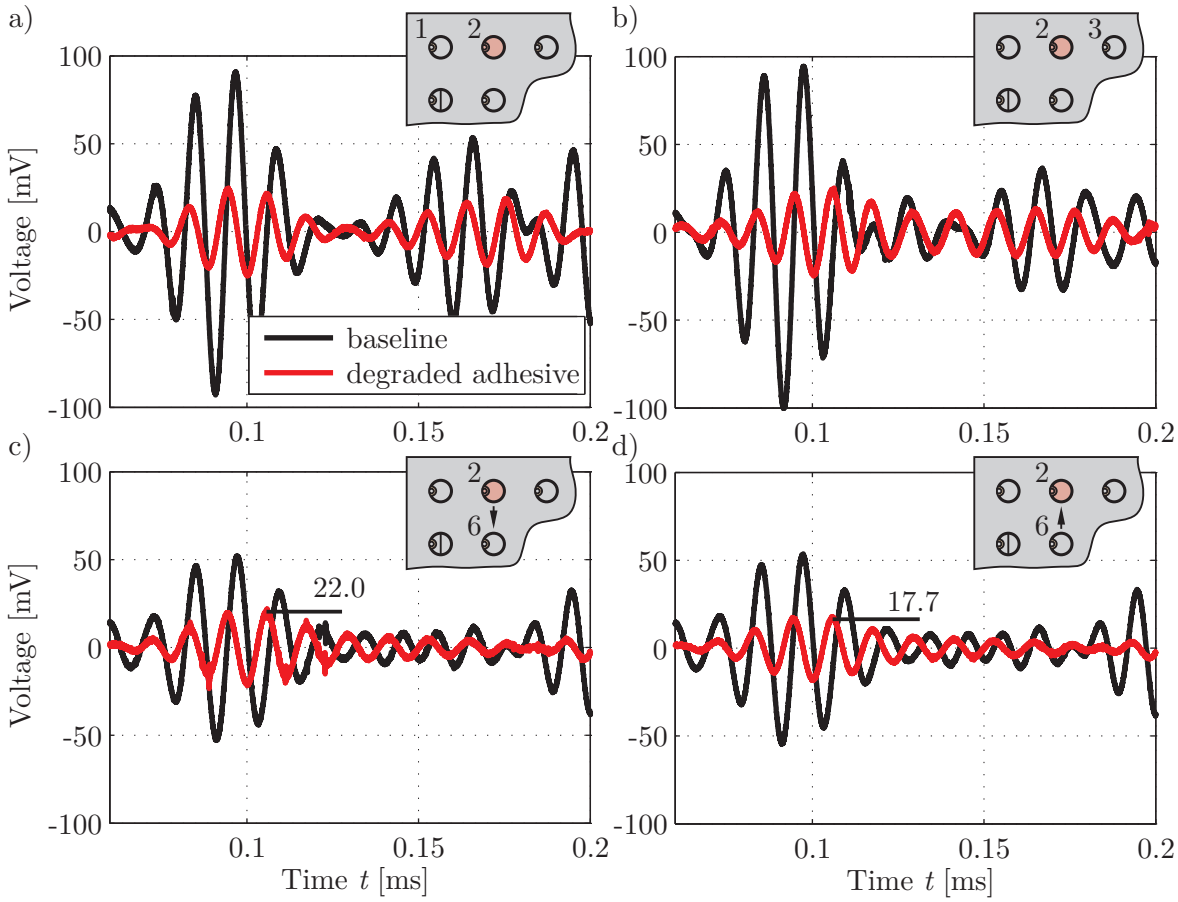

Figure 3.36: Recorded signal before and after treatment of the PWAS with dimethyformamide. a) Path PWAS 2 - PWAS 1, b) Path PWAS 2 - PWAS 3, c) Path PWAS 2 - PWAS 6, d) Path PWAS 6 - PWAS 2

Further investigations on the effect of other chemicals on the bonding layer can be found in the Studentwork of *D. Pawar* (*Pawar*, 2014).

3.5 Effects of insufficient bonding conditions

Contaminated bonding surfaces can lead to insufficient bonding. This defect type has its origin in the assembly of the SHM system, therefore no comparison with the same transducer is possible. The visualization of the generated wave field with the maxima of the velocities of the structure below the PWAS shows that the generated wave field

is not symmetric and irregular, fig. 3.37. Compared to other similar transducers, the highest amplitudes are approximately the same. It is therefore interesting to analyze the generated wave field using the sensed signal of other transducers. The setup of fig. 3.2 opens the possibility to compare similar paths, which have the same distance also to reflecting edges. While the two paths from PWAS 1 to 2 and from PWAS 4 to 3 yield similar recorded signals, this is not the case for the comparison of path PWAS 13 to 14 with path PWAS 16 to 15. As shown in fig. 3.38 the generated wave field of the PWAS attached to a contaminated surface has a much lower amplitude.

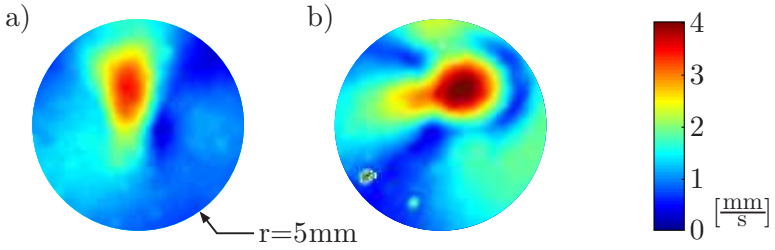

Figure 3.37: Maxima of the velocity field, generated by the PWAS and transferred to the structure for two PWAS attached on a plate with wax-contaminated surface

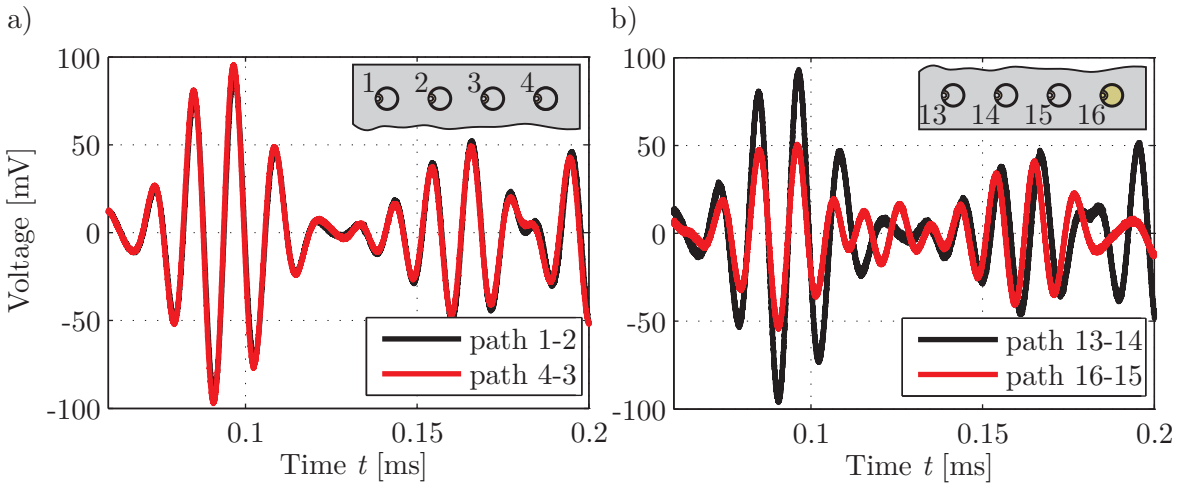

Figure 3.38: Recorded signal of similar paths a) Path PWAS 1 - PWAS 2, Path PWAS 4 - PWAS 3, b) Path PWAS 13 - PWAS 14, Path PWAS 16 - PWAS 15

Summarized, the different PWAS faults lead to a changed wave propagation. This change can affect the amplitude as well as the phase. The effect often depends on the central frequency of the input signal as well as on the angle of emission.

4 Inspection of PWAS using the EMI spectrum

As shown in chapter 3, the influences of defect piezoelectric wafer active sensor (PWAS) on the generated wave field are significant and non-negligible for SHM systems, as they can lead to false alarm. The present chapter deals with the electro-mechanical impedance (EMI) spectrum. This physical quantity, on which the inspection of PWAS can be based, is presented and discussed in detail. Special focus is put on the susceptance as imaginary part of the admittance which is the reciprocal of the impedance spectrum, as detailed in section 2.4.

4.1 Effects of defect PWAS on the EMI

Susceptance curves for different types of PWAS defects are shown, similar to the description of effects on the wave propagation of defect PWAS in chapter 3. They depict exemplary changes of the susceptance spectrum caused by PWAS defects. For many additional examples of susceptance spectra from applications the reader is referred to chapter 6.

Breakage

Breakage of simple disc-shaped transducers with wrap-around electrode, as described in section 3.1.1, leads to a change of the susceptance spectrum. The changes of the susceptance spectrum differ for PWAS with cracks including spalling compared to cracks without spalling. If spalling is present, the capacitance of the transducer is changed due to a change of the area A. This causes a decrease in the susceptance spectrum's slope, see fig. 4.1. Moreover the resonance is shifted. No change of the slope is present for the case of PWAS with cracks without spalling. Nevertheless, the resonance range is shifted by this defect, see fig. 4.2.

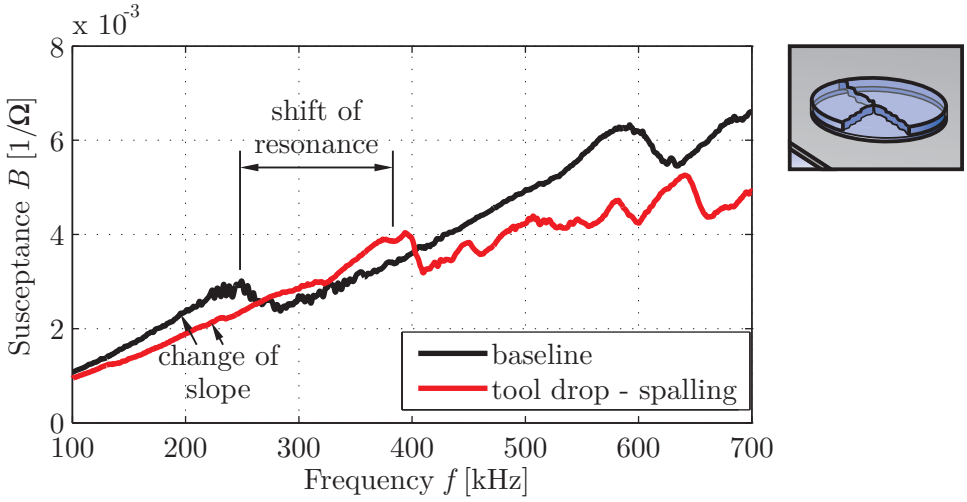

Figure 4.1: Susceptance spectra of a simple undamaged PWAS and a broken simple PWAS with spalling.

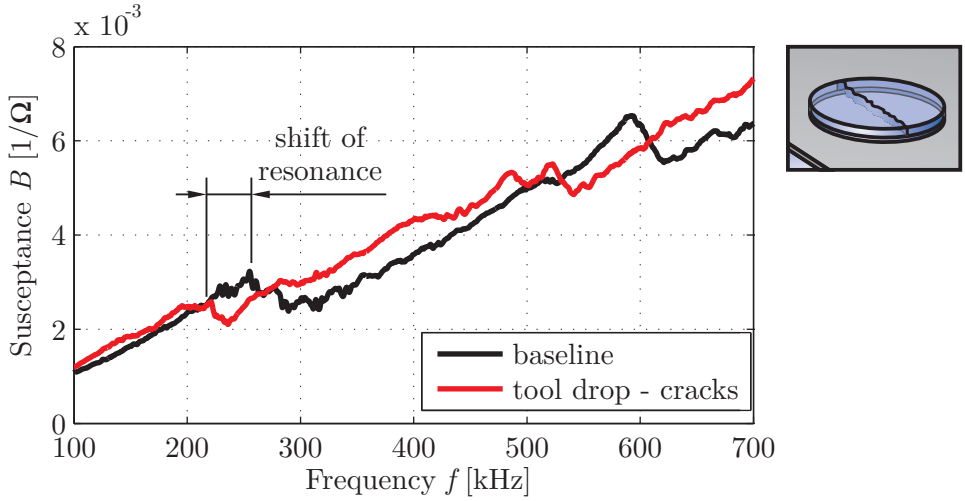

Figure 4.2: Susceptance spectra of a simple undamaged PWAS and a broken simple PWAS with cracks - no spalling.

Even though embedded transducers of type *DuraAct* are effected with prepressure, see section 2.3, bending forces with strain levels of approx. 0.5 % positive strain lead to breakage. The cracks can be seen through the embedding *Kapton* layer, as shown in fig. 4.3. These cracks result in a changed susceptance spectrum, depicted in fig. 4.4. Additional measurements have shown that samples, which faced higher levels of strain, exhibit higher distortions of the spectrum. Although the general effects of these cracks are similar to those, described for simple piezoelectric disc-shaped transducers (fig. 4.2), the characteristic change of the resonance range is less dominant. This is most likely caused by the prepressure inside the embedding.

Additional tests have shown, that the changes inside the susceptance spectrum are even more dominant when prestrain is present during the measurement of the EMI

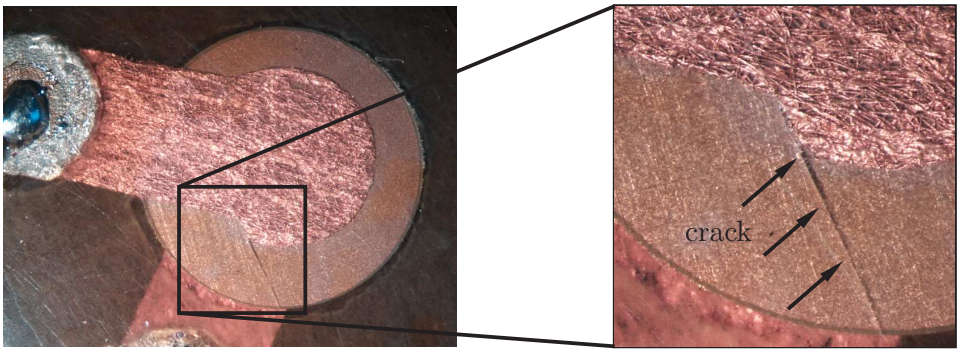

Figure 4.3: Cracks in the *DuraAct* embedded transducer after bending in a four point bending test with strains of up to 1%, measured at the surface of the bending probe. The cracks can be seen though the embedding *Kapton* layer.

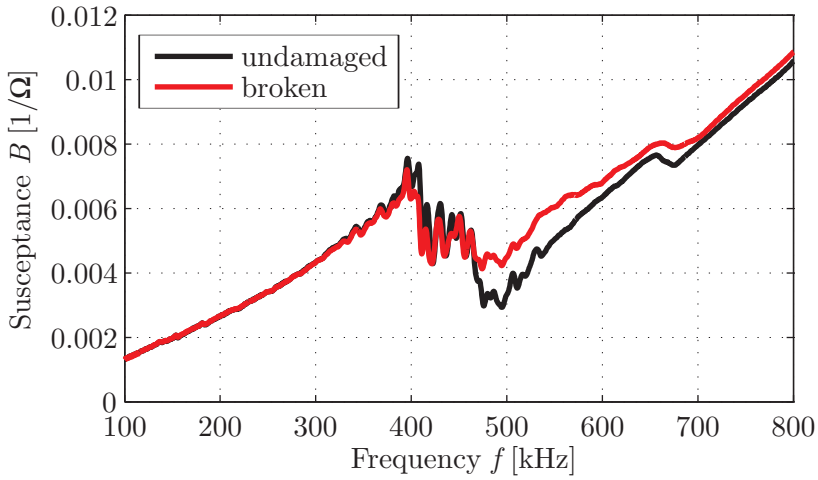

Figure 4.4: Susceptance curves for embedded PWAS, which show cracks after bending in a four point bending test. At 0.45% no cracks are visible. First cracks can be seen at 0.5% strain, the loading to higher strain levels leads to more cracks. All samples have been tested at zero strain level.

spectrum. This seems to be caused by a partial detachment of the two flanks of the fracture.

Debonding

Debonding can be caused by bending, if the structure is much more flexible than the PWAS itself. This is the case for many PWAS based on piezoceramic discs. The effect of debonding on the wave propagation has been shown in section 3.3. For this test four PWAS are fully bonded, while four PWAS show partial debonding. The debonding is simulated by the use of teflon foil, which prevents the adhesive layer to fully cover the interface between PWAS and structure. The foil is removed after the bonding process is finished. For the four partially debonded PWAS an area of approximately 20% has been debonded. The orientation of the debonded area in relation to the location of the wrap-around electrode has been changed.

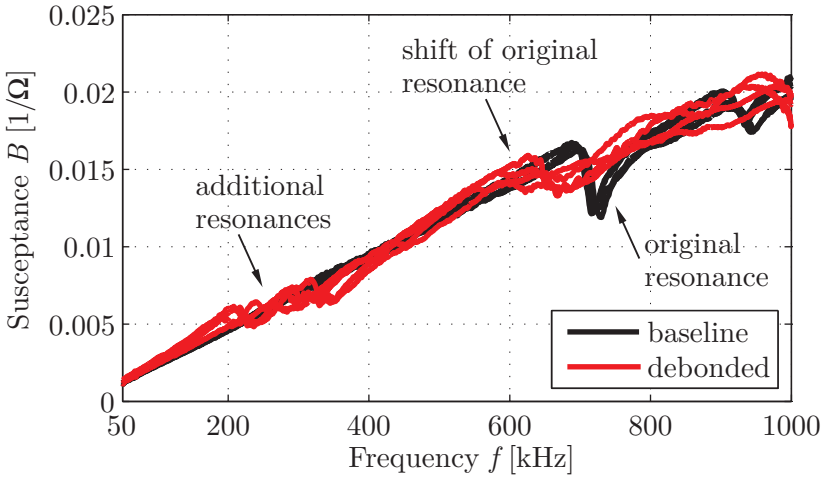

Figure 4.5: Effects of 20% debonded area on the susceptance spectrum. Four completely bonded PWAS are compared with four partially debonded PWAS. The orientation of the debonding relative to the wrap-around electrode has been changed.

Fig. 4.5 shows that for all four debonded PWAS, changes in the susceptance spectrum are present. Three of the four PWAS exhibit a slightly higher slope in the frequency intervals between the resonances, although a regression line over the whole frequency range from 50 kHz to 1000 kHz will lead to similar results for the defect and undamaged case. For the debonded PWAS an additional eigenfrequency can be found between 200 kHz and 350 kHz. Its characteristics are less pronounced for the single PWAS, whose slope is most similar to the four undamaged transducers. A shift of the original resonance towards lower frequencies is visible and its features are less pronounced.

Degradation of the bonding layer

The degradation of the bonding layer can be caused by chemicals, dissolving the adhesive layer or doing harm on this bond between structure and transducer. The treatment and the effects on the wave propagation are described in section 3.4. The effects on the susceptance spectrum for a simple disc-shaped transducer with wrap-around electrode can be seen in fig. 4.6. The degradation of the bonding layer leads to a detachment which results in a susceptance spectrum similar to the one of the free-standing PWAS.

A treatment with dimethylformamid also has an effect on embedded transducers, even if they are co-bonded to the structure. The case of *DuraAct* transducer is shown in fig. 4.7. As it can be seen, the effect varies a lot from the effect for the simple transducers. The resonance range is less pronounced with increasing treatment duration. The susceptance spectrum of the damaged embedded PWAS is similar to the spectrum of the undamaged simple transducer. From this it can be assumed that the treatment

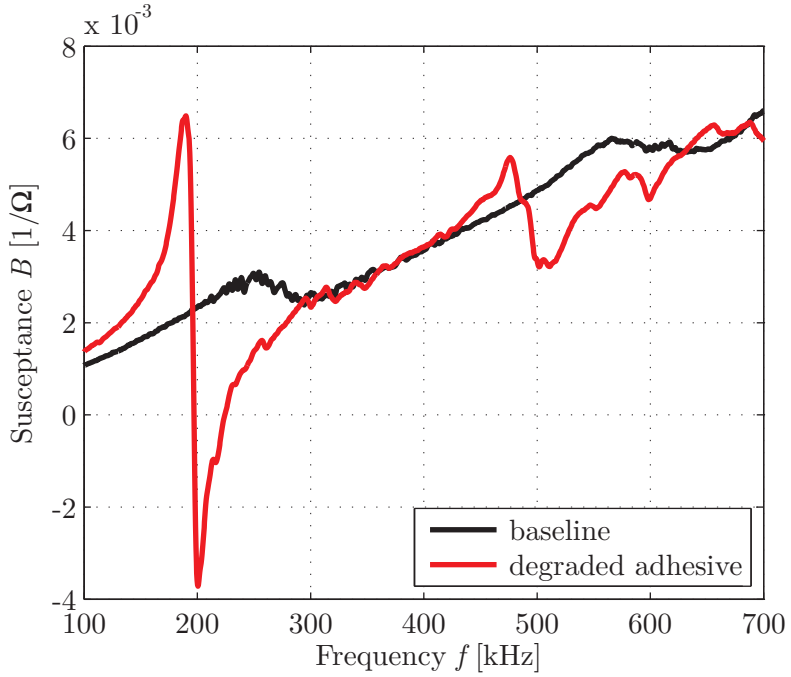

Figure 4.6: Susceptance spectrum of a simple PWAS with degraded adhesive layer compared to a perfectly bonded PWAS.

with the chemical substance mainly attacks the embedding, while the bond between PWAS and structure is still in a good condition.

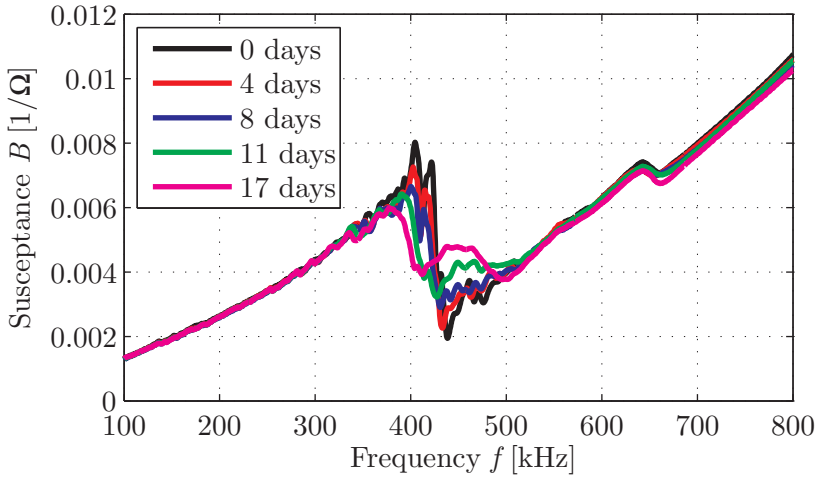

Figure 4.7: Susceptance spectra for an embedded *DuraAct* PWAS at different stages of degraded adhesive layer caused by treatment with dimethylformamid.

Insufficient Bonding

The influence of partial contamination of the bonding surface, leading to insufficient bonding, on the susceptance spectrum is tested with the setup described in section 3.5. The aluminum structure has been contaminated with wax before the bonding of two simple disc-shaped transducers with wrap-around electrode. The susceptance spectra

of these two PWAS are compared with those of a perfectly bonded transducer in fig. 4.8. The effect on the susceptance spectrum is very similar to those, caused by degradation of the bonding layer, which results from a chemical treatment. The spectrum converges to the spectrum of a free-standing PWAS with increasing defect size.

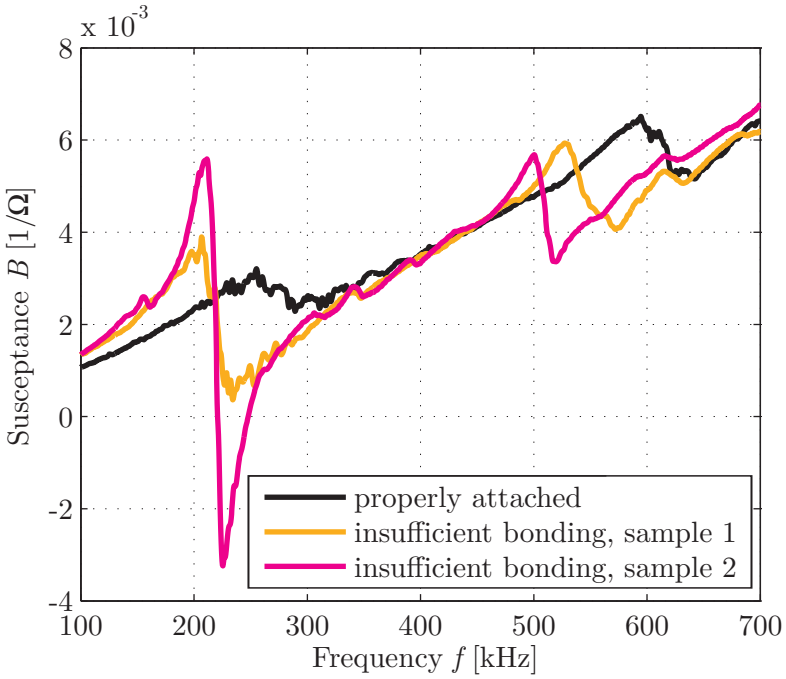

Figure 4.8: Susceptance spectrum of a simple PWAS bonded on a contaminated bonding area compared to a perfectly bonded PWAS.

All described defects of PWAS lead to significant changes in the susceptance spectrum. Different defects have different effects on the susceptance slope, shift the resonances and change its characteristic shape.

4.2 Development of a physics-based analytical model of the susceptance

To be able to use the susceptance spectrum for the inspection of PWAS, it is important to understand the relationships between different physical quantities and the interdependencies with the susceptance spectrum. This is possible by using analytical models. This section therefore focuses on physics-based analytical models of the undamaged PWAS, which are attached to a structure.

In section 2.4 simple models of the electro-mechanical impedance have already been given. These models describe the EMI for the case of a free-standing PWAS, not

connected to a structure. The connection with the structure has a large effect on this quantity and therefore needs to be taken into account. For structural damage detection with the EMI method, the effect of the stiffness of the structure on the impedance of the attached PWAS is the basis of the methods. For a strip-like PWAS, as described in the first part of section 2.4, with thickness h, width w and length l, *Liang* et al. developed a model for the EMI of a bonded PWAS. It is based on the impedance spectra of the free PWAS Z_p and the structure Z_s, (*Liang* et al., 1994). This model relies on the simplification that the PWAS can be modeled as a passive material, which has no coupling from mechanical to electrical energy:

$$Y(\omega) = i\omega \frac{wl}{h} \left(\frac{d_{31}^2 c_{22}^E Z_p}{Z_s + Z_p} \frac{\tan kl}{kl} + \varepsilon_{33}^T - d_{31}^2 c_{22}^E \right). \tag{4.1}$$

In this equation c_{22} is the *Young*'s modulus component of the matrix in 2-direction and k is the wave number, calculated with the related wave velocity for the strip-like PWAS. Equation (4.1) simplifies, if kl is small:

$$Y(\omega) = i\omega \frac{wl}{h} \left(\varepsilon_{33}^T - \frac{Z_s}{Z_s + Z_p} d_{31}^2 c_{22}^E \right). \tag{4.2}$$

This model is suitable, if the focus is put on the influence of structural changes on the impedance in the frequency range lower than the first PWAS eigenfrequency. The general influence of geometric parameters as l, w, and h and material parameters as c_{22} can be seen. Nevertheless, if the PWAS itself and its bonding condition are focused, this model is not suitable, as the bonding layer and the dynamic behavior are missing. *Xu* and *Liu* have introduced the effect on the bonding layer adapting the impedance of the structure with a factor ζ, defined through the stiffness of the structure k_s and the adhesive layer k_B, (*Xu* and *Liu*, 2002):

$$Y(\omega) = i\omega \frac{wl}{h} \left(\frac{d_{31}^2 c_{22}^E Z_p}{\zeta Z_s + Z_p} \frac{\tan kl}{kl} + \varepsilon_{33}^T - d_{31}^2 c_{22}^E \right), \tag{4.3}$$

$$\zeta = \frac{1}{1 + \frac{k_s}{k_B}}. \tag{4.4}$$

Their numerical 2D study on the effect of ζ was used to describe the effects of debonding. k_B is a function of the bonding process and the adhesive layer thickness. Nevertheless, k_B has not been defined analytically. This has been done in (*Bhalla* and *Soh*, 2004), providing an analytical solution for ζ and further explanations on the effect for quadratic PWAS. *Sirohi* and *Chopra* also define a correction factor for the shear lag

effect, using the results of strain gauges and piezoelectric strain sensors, (*Sirohi* and *Chopra*, 2000).

The bonding layer itself has no influence if it is as stiff as the PWAS and very thin. For this case the pin force model is valid. It states that all shear stress is transferred between PWAS and structure at the end of the PWAS. This is not the case for most applications. Nevertheless, the assumption of pin forces is a good approximation for many modeling approaches in SHM and comparably simple. Within this work, it is necessary to look at the details of the transition of forces from PWAS to the structure. The effect of the bonding layer can be described by the shear lag effect. A comprehensive overview on the shear lag parameter and its effects are given in (*Giurgiutiu*, 2014). The smaller the shear stresses, the adhesive can bear, the larger is the shear lag effect. It leads to a loss of energy transfer from the actuating PWAS to the structure and vice versa. The shear lag effect is also important, if the PWAS geometry should be optimal for the actuation of a specific mode at a certain frequency, $\frac{\lambda}{2} = l_{PWAS,\text{eff}}$, as the effective PWAS length is decreasing with increasing shear lag.

For circular PWAS *Giurgiutiu* gives a detailed derivation of the susceptance for a PWAS attached to a structure. He is, in the first place, neglecting the bonding layer but including the dynamics and a detailed derivation of the stiffness of the structure, (*Giurgiutiu*, 2007, chap. 3). It has been used partly for the following model. As described above, the adhesive layer is of great importance for the objectives of this work and therefore has to be implemented in the model. Moreover the modeling of the structure has to be less detailed, as the focus is on the PWAS and its adhesive layer.

In the following, an analytical axisymmetric model of the electro-mechanical impedance is described, which focuses on the description of the circular PWAS and its bonding to the structure. The detailed derivation of the necessary steps provides a profound understanding of the model. The model of the attached PWAS is taken from (*Giurgiutiu*, 2007). The derivation of the description of the bonding stiffness of the adhesive layer is based on a concept, described in (*Dugnani*, 2009).

For a circular PWAS the equations of electro-mechanical coupling of piezoelectricity are needed in cylindrical coordinates:

$$S_{rr} = s_{11}^E T_{rr} + s_{12}^E T_{\theta\theta} + d_{31} E_z, \tag{4.5}$$

$$S_{\theta\theta} = s_{12}^E T_{rr} + s_{11}^E T_{\theta\theta} + d_{31} E_z, \text{ and} \tag{4.6}$$

$$D_z = d_{31}^E \left(T_{rr} + T_{\theta\theta}\right) + \varepsilon_{33}^T E_z. \tag{4.7}$$

Equations (4.5) to (4.7) include the following variables:

- **S** strain tensor with components S_{rr} and $S_{\theta\theta}$,
- **T** stress tensor with normal stresses T_{rr} and $T_{\theta\theta}$,
- $\underline{E}$ electrical field with E_z component in z-direction,
- $\underline{D}$ electrical flux with D_z electrical flux in z-direction, and
- **s** compliance tensor for piezoelectric material. Here there is no difference between cylindrical coordinates and *Cartesian* coordinates, as z-direction is the same and the piezoelectric material is orthotropic with in-plane isotropy in x-y-plane. Therefore $1, 2, 3$ instead of r, θ, z can be used.
- **d** piezoelectric (strain/charge) coefficient, for the same reason as for **s**, $1, 2, 3$ instead of r, θ, z can be used, and
- ε dielectric constant with component ε_{33}.

The calculation of strain components in cylindrical coordinates simplifies, if axial symmetry is assumed:

$$S_{rr} = \frac{\partial u_r}{\partial r}, \tag{4.8}$$

$$S_{\theta\theta} = \frac{1}{r}\frac{\partial u_\theta}{\partial \theta} + \frac{u_r}{r} = \frac{u_r}{r}, \tag{4.9}$$

$$S_{r\theta} = \frac{1}{r}\frac{\partial u_r}{\partial \theta} + \frac{u_\theta}{r} + \frac{\partial u_\theta}{\partial r} = 0. \tag{4.10}$$

To calculate the impedance spectrum as the complex ratio of voltage and current in the frequency domain, in the first place the current has to be calculated. The current I is the time derivative of the total charge Q. The total charge can be derived by integrating the electric displacement D_z over the area of the PWAS. Equations (4.5), (4.6), (4.8) and (4.9) are therefore rearranged to yield T_{rr} and $T_{\theta\theta}$ for the insertion to calculate D_z in eq. (4.7), as soon as u_r is known:

$$T_{rr} = \frac{1}{s_{11}^E\left(1-\nu_a^2\right)}\left[\frac{\partial u_r}{\partial r} + \nu_a\frac{u_r}{r} - d_{31}E_z\left(\nu_a+1\right)\right], \tag{4.11}$$

$$T_{\theta\theta} = \frac{1}{s_{11}^E\left(1-\nu_a^2\right)}\left[\nu_a\frac{\partial u_r}{\partial r} + \frac{u_r}{r} - d_{31}E_z\left(\nu_a+1\right)\right], \tag{4.12}$$

with ν_a being the *Poisson*'s ratio ν_{12} of the piezoelectric material.

As the problem is axisymmetric, u_r has the following form eq. (4.13), assuming harmonic displacement:

$$u_r\,(r,t) = \hat{u}_r(r)e^{-i\omega t}. \tag{4.13}$$

To determine u_r, the stresses at an infinitesimal element are analyzed to derive the equation of motion in polar coordinates. It is shown in fig. 4.9.

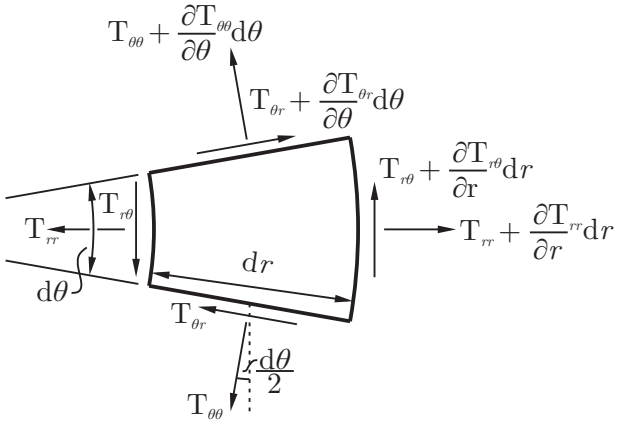

Figure 4.9: Infinitesimal element of PWAS for the derivation of equation of motion.

The axial symmetry leads to no changes with θ. As small angels can be assumed for the infinitesimal element the sinusoidal terms can be simplified with $\sin\frac{\theta}{2} = \frac{\theta}{2}$. This leads to the equation of motion in cylindrical coordinates for axisymmetric problems eq. (4.14). The full derivation is given in the appendix.

$$\frac{\partial^2 u_r}{\partial r^2} + \frac{1}{r}\frac{\partial u_r}{\partial r} - \frac{u_r}{r^2} = \frac{1}{c^2}\frac{\partial^2 u_r}{\partial t^2} = -\frac{\omega^2}{c^2}u_r \tag{4.14}$$

with u_r being the displacement in r-direction and c the wave speed of axial waves:

$$c = \sqrt{\frac{1}{\rho s_{11}^E\,(1-\nu_a^2)}}. \tag{4.15}$$

Here ρ is the material density. Equation (4.14) can be solved with a change of variables, using the wave number k and a new variable φ, eq. (4.17). This new variable is the constant φ_a, eq. (4.18), when the outer radius of the PWAS r_{pwas} is put as r into φ:

$$k = \frac{\omega}{c}, \tag{4.16}$$

$$\varphi = k\,r, \tag{4.17}$$

$$\varphi_a = k\,r_{pwas}. \tag{4.18}$$

Equation (4.14) can be transferred into a *Bessel*'s differential equation, eq. (4.19):

$$\varphi^2 \frac{\mathrm{d}^2 u_r}{\mathrm{d}\varphi^2} + \varphi \frac{\mathrm{d}u_r}{\mathrm{d}\varphi} + u_r \left(\varphi^2 - 1\right) = 0. \tag{4.19}$$

This leads to eq. (4.20):

$$\hat{u}_r(\varphi) = A J_1(\varphi). \tag{4.20}$$

The general solution for the equation of motion eq. (4.14) for a harmonic excitation with frequency ω is given in eq. (4.21):

$$u_r(r,t) = A J_1\left(\frac{\omega r}{c}\right) e^{i\omega t}, \tag{4.21}$$

with J_1 being the first *Bessel* function of the first kind. For later use the following derivative, eq. (4.22), is important:

$$\frac{\mathrm{d}J_1(x)}{\mathrm{d}x} = J_0(x) - \frac{1}{x} J_1(x). \tag{4.22}$$

The factor A needs to be found from the boundary conditions. Assuming a deformation in r independent of z for the PWAS disc of thickness h_{pwas}, *Giurgiutiu* uses the idea of equalizing two forces at the edge of the PWAS ($r = r_{pwas}$). It has to be valid at all points at the circumference.

$$-T_{rr} h_{pwas} = k_{str\&adh} u_r(r_{pwas}). \tag{4.23}$$

Using eq. (4.11), the boundary condition eq. (4.23) can be used for the evaluation of A. For this calculation E_0 is the amplitude in $E_z = E_0 e^{i\omega t}$. Moreover the abbreviation χ is used, which is defined by eqs. (4.24) and (4.25):

$$\chi(\omega) = \frac{k_{str\&adh}}{k_{pwas}}, \tag{4.24}$$

$$k_{pwas} = \frac{h_{pwas}}{r_{pwas} s_{11}^E (1 - \nu_a)}. \tag{4.25}$$

A detailed derivation of χ, resp. $k_{str\&adh}$ for this new model is given later. This leads to A, eq. (4.26):

$$A = \frac{(1 + \nu_a)\, d_{31} E_0 r_{pwas}}{\frac{\omega}{c} r_{pwas} J_0 \frac{\omega}{c} r_{pwas} - (1 - \nu_a - \chi(1 + \nu_a)) J_1\left(\frac{\omega}{c} r_{pwas}\right)}. \tag{4.26}$$

Using this solution, u_r can be calculated, eq. (4.27):

$$u_r(r,t) = \frac{(1+\nu_a)\, d_{31} E_0 r_{pwas}}{\frac{\omega}{c} r_{pwas} J_0 \frac{\omega}{c} r_{pwas} - (1-\nu_a-\chi\,(1+\nu_a))\, J_1\left(\frac{\omega}{c} r_{pwas}\right)} J_1(\frac{\omega}{c} r) e^{-i\omega t}. \tag{4.27}$$

With this T_{rr}, $T_{\theta\theta}$ and D_z can be calculated, eq. (4.28):

$$D_z = \frac{d_{31}}{s_{11}^E\,(1-\nu_a)} \left(\frac{1}{r}\frac{\partial\,(r u_r)}{\partial r}\right) + E_z \left(\varepsilon_{33} - \frac{2 d_{31}^2}{s_{11}^E\,(1-\nu_a)}\right). \tag{4.28}$$

Integration of D_z over A leads to Q, eqs. (4.29) and (4.30):

$$Q = 2\pi \int_0^{r_{pwas}} r D_z \mathrm{d}r, \tag{4.29}$$

$$Q = CV \left(1 - k_p^2 \left(1 - \frac{u_r\,(r_{pwas})}{d_{31} E_z r_{pwas}}\right)\right). \tag{4.30}$$

Inside this equation, C and V are capacitance and voltage and k_p is the planar coupling coefficient, eqs. (4.31) to (4.33):

$$C = \varepsilon_{33} \frac{\pi r_{pwas}^2}{h_a}, \tag{4.31}$$

$$V = E_z h_a, \tag{4.32}$$

$$k_p^2 = \frac{2 d_{31}^2}{\varepsilon_{33} s_{11}^E\,(1-\nu_a)}. \tag{4.33}$$

The current I is the time derivative of the electrical charge Q. In Q only V depends on the time, as the time dependency of $u_r\,(r_{pwas})$ and E_z cancels for harmonic time dependency. This leads to $I = i\omega Q$. The admittance Y is the quotient of I and V:

$$Y = \frac{I}{V} = i\omega C \left(1 - k_p^2 \left(1 - \frac{u_r\,(r_{pwas})}{d_{31} E_z r_{pwas}}\right)\right). \tag{4.34}$$

Taking $\hat{u}_r\,(r_{pwas})$ from eq. (4.27) resp. eq. (4.13) and using $\varphi_a = \frac{\omega}{c} r_{pwas}$ leads to:

$$Y = i\omega C \left(1 - k_p^2 \left(1 - \frac{(1+\nu_a)\, J_1\,(\varphi_a)}{\varphi_a J_0\,(\varphi_a) - (1-\nu_a)\, J_1\,(\varphi_a) + \chi\,(\omega)\,(1+\nu_a)\, J_1\,(\varphi_a)}\right)\right). \tag{4.35}$$

The susceptance B is the imaginary part of Y. It has to be ensured that many of the parameters used, have complex values as damping has to be taken into account with

$$s_{11}^E = \hat{s}_{11}^E (1 - i\eta), \tag{4.36}$$

$$\varepsilon_{33}^{T} = \hat{\varepsilon}_{33}^{T}(1 - i\delta). \tag{4.37}$$

This leads to complex values in C, c and k_p and also in $\chi(\omega)$ and Y in eqs. (4.34) and (4.35). Otherwise Y is purely imaginary.

Giurgiutiu presents a detailed definition of $\chi(\omega)$, which includes a frequency dependency of k_{str}. If the electro-mechanical impedance is to be used for the detection of structural damages, it is necessary to include this information in the model. Especially if only a low voltage and a short frequency sweep are used, as the analysis should be focused on the PWAS and its bonding layer, this is not necessary. If structural changes should be detected, single resonance peaks in the resonance spectrum within a small frequency range are compared. If this is the case, the calculation of k_{str} as a frequency dependent quantity is mandatory. As this is not the aim within this work, the analytical model can include a much more simple model of the structural stiffness, which is the model of two parallel stiffnesses: one of an endless plate with a hole in form of the disc-shaped transducer, one of a disc-shaped plate, both modeled with the material of the structure:

$$k_{str} = \frac{2h_{str}E_{str}}{r_{pwas}(1 - \nu_{str}^2)}. \tag{4.38}$$

The stiffness of the PWAS is the stiffness of a disc-shaped material with the properties of the PWAS material and has been defined in eq. (4.25).

For the description of χ, the stiffness of the adhesive layer is still missing. This is of great importance, as the adhesive layer includes the shear lag effect, as described in e.g. (*Giurgiutiu*, 2007; *Bhalla* and *Soh*, 2004). Its stiffness has to be included, to be able to account for this effect and possible defects of the bonding layer. Therefore the stiffness of the structure and the adhesive layer is modeled as a serial connection of springs, with k_{str} being frequency independent and k_{adh} being a function of the frequency. The stiffness of the adhesive layer reduces $k_{str\&adh}$:

$$k_{str\&adh} = \frac{1}{\frac{1}{k_{str}} + \frac{1}{k_{adh}}}. \tag{4.39}$$

For $k_{adh} \to \infty$ the combined stiffness $k_{str\&adh}$, eq. (4.39), equals k_{str}.

The following derivation assumes that the maximum difference of the displacements of the piezoelectric element at its surface towards the structure and of the adhesive layer at its surface towards the structure can be described with $\Delta u_{r,shear}$ and is given

at r_{pwas}, see fig. 4.10. The function of displacement in the adhesive layer, caused by shear, is described by $u_{rs}(r, z)$. This derivation of u_{rs} is based on an idea of (*Dugnani*, 2009) and especially uses the same boundary conditions.

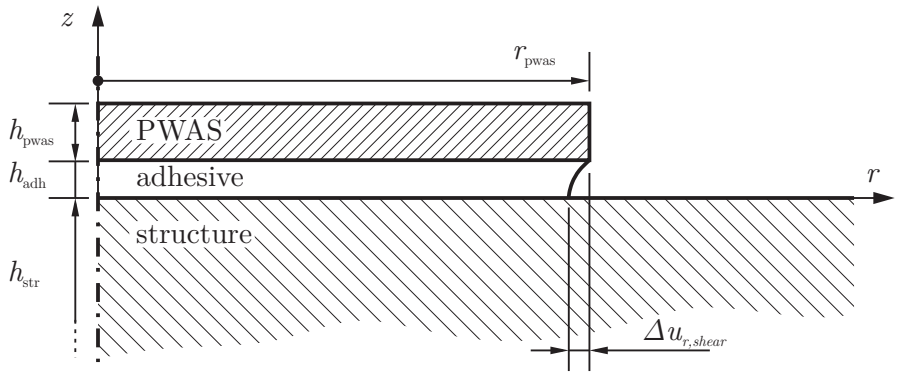

Figure 4.10: Definition of $\Delta u_{r,shear}$ in the axisymmetric system of the PWAS attached to the structure with an adhesive layer.

Taking an infinitesimal element of the bonding layer, for the adhesive the shear stresses T_{rz} play a major role. In contrast to the derivation of eq. (4.14), here the stresses are dependent on z. Due to the axial symmetry, $T_{\theta r} = 0$ and all partial derivatives of θ vanish. For ease of visualization, these parts are not shown in fig. 4.11.

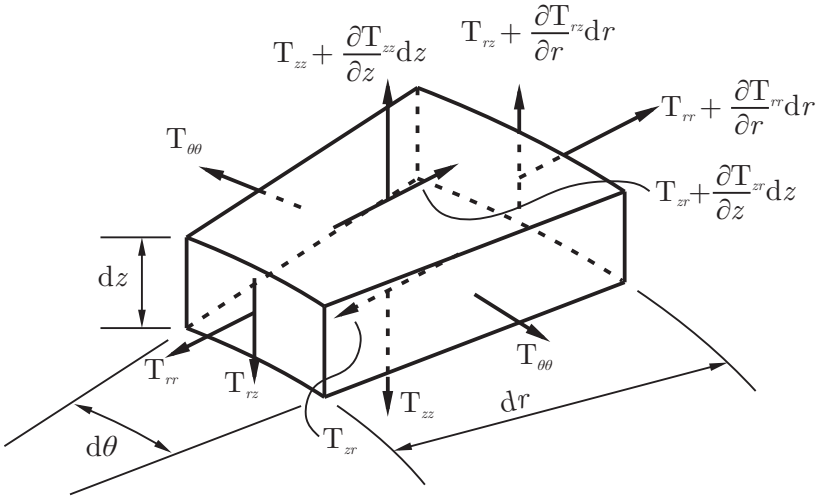

Figure 4.11: Stresses at an infinitesimal element of the adhesive layer.

The sum of all forces in r-direction, neglecting all entries which are small of second order (e.g. dr^2) leads to eq. (4.40):

$$\frac{\partial T_{rr}}{\partial r} + \frac{T_{rr} - T_{\theta\theta}}{r} + \frac{\partial T_{rz}}{\partial z} = 0. \tag{4.40}$$

For the bonding layer the effect of shear is more important than transverse contraction. The shear stresses T_{rz} are calculated neglecting the change of the thickness of the

adhesive layer. T_{rr} and $T_{\theta\theta}$ are calculated according to eqs. (4.11) and (4.12) with u_{rs} instead of u_r:

$$T_{rz} = G_{adh}\left(\frac{\partial u_{rs}}{\partial z} + \frac{\partial u_z}{\partial r}\right) = G_{adh}\left(\frac{\partial u_{rs}}{\partial z}\right), \tag{4.41}$$

$$\frac{\partial^2 u_{rs}}{\partial r^2} + \frac{1}{r}\frac{\partial u_{rs}}{\partial r} - \frac{u_{rs}}{r^2} + \underbrace{\left(\frac{1-\nu_{adh}}{2}\right)}_{\alpha}\frac{\partial^2 u_{rs}}{\partial z^2} = 0. \tag{4.42}$$

Using the following for u_{rs}

$$u_{rs} = R(r)Z(z), \tag{4.43}$$

this differential equation can be solved with separation of variables:

$$\frac{\mathrm{d}^2 R}{\mathrm{d}r^2}Z + \frac{1}{r}\frac{\mathrm{d}R}{\mathrm{d}r}Z - \frac{RZ}{r^2} + \alpha\frac{\mathrm{d}^2 Z}{\mathrm{d}z^2}R = 0 \tag{4.44}$$

$$Z\left(\frac{\mathrm{d}^2 R}{\mathrm{d}r^2} + \frac{1}{r}\frac{\mathrm{d}R}{\mathrm{d}r} - \frac{R}{r^2}\right) = -\alpha\frac{\mathrm{d}^2 Z}{\mathrm{d}z^2}R \tag{4.45}$$

$$\frac{1}{R}\left(\frac{\mathrm{d}^2 R}{\mathrm{d}r^2} + \frac{1}{r}\frac{\mathrm{d}R}{\mathrm{d}r} - \frac{R}{r^2}\right) = -\alpha\frac{1}{Z}\frac{\mathrm{d}^2 Z}{\mathrm{d}z^2} = \text{const.} = -\gamma^2. \tag{4.46}$$

Now the left part is depending on r and the right part is only dependent on z. Both parts can be solved independently:

$$r^2\frac{\mathrm{d}^2 R}{\mathrm{d}r^2} + r\frac{\mathrm{d}R}{\mathrm{d}r} - R\left(\gamma^2 r^2 - 1\right) = 0. \tag{4.47}$$

Equation (4.47) is a *Bessel*-type differential equation and can be solved with change of variables using $\kappa = \gamma r$ in the same way as it was done for eq. (4.14). Also in this case the function needs to be zero in the middle of the PWAS for the axisymmetry. This results in:

$$R(r) = C_1 J_1(\gamma r). \tag{4.48}$$

The right part of eq. (4.46) can be solved with *sinh*, *cosh* or exponential functions, respectively,

$$\frac{1}{Z(z)}\frac{\mathrm{d}^2 Z}{\mathrm{d}z^2} = \frac{\gamma^2}{\alpha} \tag{4.49}$$

$$Z(z) = C_3 e^{\frac{\gamma z}{\sqrt{\alpha}}} + C_4 e^{-\frac{\gamma z}{\sqrt{\alpha}}}. \tag{4.50}$$

This leads to an equation for the component of the displacement in radial direction caused by shear inside the adhesive layer u_{rs}.

$$u_{rs}(r,z) = C_1 J_1(\gamma r)\left(C_3 e^{\frac{\gamma z}{\sqrt{\alpha}}} + C_4 e^{-\frac{\gamma z}{\sqrt{\alpha}}}\right) \tag{4.51}$$

The constants C_n in eq. (4.51) are defined by the boundary conditions:

- $u_{rs} = 0$ for $z = 0$, at the structure the relative displacement in radial direction caused by shear is zero,
- $u_{rs}(r, z = h_{adh}) = \Delta u_{r,shear} \frac{J_1\left(\frac{\omega r}{c}\right)}{J_1\left(\frac{\omega r_{pwas}}{c}\right)}$, the same modes as in the piezoelectric transducer are formed in the adhesive layer, the shear component only adds resp. subtracts from u_r, and
- $u_{rs}(r = 0, z) = 0$, needed for axisymmetry.

The third boundary condition has already been used for $R(r)$. The first boundary condition leads to $C_3 = -C_4$. This way $Z(z)$ simplifies to

$$Z(z) = 2C_3 \sinh\left(\frac{\gamma z}{\sqrt{\alpha}}\right) \tag{4.52}$$

and C_3 and C_1 can be combined to one constant, which can be determined by using the second boundary condition. Moreover from this boundary condition the constant $\gamma = \frac{\omega}{c} = k$ can be estimated as wave number:

$$C_{13} J_1\left(\frac{\omega}{c} r\right) \sinh\left(\frac{\frac{\omega}{c} h_{adh}}{\sqrt{\alpha}}\right) = \Delta u_{r,shear} \frac{J_1\left(\frac{\omega r}{c}\right)}{J_1\left(\frac{\omega r_{pwas}}{c}\right)}, \tag{4.53}$$

$$C_{13} = \Delta u_{r,shear} \frac{\left(\sinh\left(\frac{\frac{\omega}{c} h_{adh}}{\sqrt{\alpha}}\right)\right)^{-1}}{J_1\left(\frac{\omega r_{pwas}}{c}\right)}. \tag{4.54}$$

This leads to u_{rs}

$$u_{rs}(r,z) = \Delta u_{r,shear} \frac{J_1\left(\frac{\omega r}{c}\right)}{J_1\left(\frac{\omega r_{pwas}}{c}\right)} \frac{\sinh\left(\frac{\frac{\omega}{c} z}{\sqrt{\alpha}}\right)}{\sinh\left(\frac{\frac{\omega}{c} h_{adh}}{\sqrt{\alpha}}\right)}. \tag{4.55}$$

Knowing the shear component of the displacement in radial direction inside the adhesive layer, makes it possible to calculate k_{adh} with the help of an energy conservation equation. The total strain energy U, stored in the adhesive layer, has to be equal to half of the work W of the external load F with F assumed as dead line load, accord-

ing to *Clapeyron*'s theorem, which is valid for linear elastic systems. This F can be expressed by k_{adh} and $\Delta u_{r,shear}$:

$$F = k_{adh} \Delta u_{r,shear}. \tag{4.56}$$

The strain energy U derives from an integral:

$$U = \iiint_V \frac{T_{rz}^2}{2G_{adh}} r \mathrm{d}\theta \mathrm{d}r \mathrm{d}z = \frac{1}{2} \left(2\pi r_{pwas}\right) F \Delta u_{r,shear} = \frac{W}{2} \tag{4.57}$$

$$T_{rz} = G_{adh} \frac{\partial u_{rs}}{\partial z} = G_{adh} \Delta u_{r,shear} \frac{J_1\left(\frac{\omega r}{c}\right)}{J_1\left(\frac{\omega r_{pwas}}{c}\right)} \frac{\cosh\left(\frac{\frac{\omega}{c} z}{\sqrt{\alpha}}\right)}{\sinh\left(\frac{\frac{\omega}{c} h_{adh}}{\sqrt{\alpha}}\right)} \frac{\omega}{c\sqrt{\alpha}} \tag{4.58}$$

$$U = \iiint_V \underbrace{\frac{1}{2G_{adh}} \left(\frac{G_{adh} \Delta u_{r,shear}}{J_1\left(\frac{\omega r_{pwas}}{c}\right) \sinh\left(\frac{\frac{\omega}{c} h_{adh}}{\sqrt{\alpha}}\right)} \frac{\omega}{c\sqrt{\alpha}} \right)^2}_{P}$$

$$\left(J_1\left(\frac{\omega r}{c}\right)\right)^2 \cosh\left(\frac{\frac{\omega}{c} z}{\sqrt{\alpha}}\right)^2 r \mathrm{d}\theta \mathrm{d}r \mathrm{d}z \tag{4.59}$$

$$= 2\pi P \int \left(J_1\left(\frac{\omega r}{c}\right)\right)^2 r \mathrm{d}r \int \left(\cosh\left(\frac{\frac{\omega}{c} z}{\sqrt{\alpha}}\right)\right)^2 \mathrm{d}z. \tag{4.60}$$

The two integrals can be solved e.g. with the help of symbolic programming, e.g. *Maple* (*Maplesoft TM*, 2016).

$$\int_{r=0}^{r_{pwas}} \left(J_1\left(\frac{\omega r}{c}\right)\right)^2 r \mathrm{d}r = \frac{r_{pwas}}{2\frac{\omega}{c}}$$
$$\left[\frac{\omega}{c} r_{pwas} J_0^2\left(\frac{\omega}{c} r_{pwas}\right) - 2 J_0\left(\frac{\omega}{c} r_{pwas}\right) J_1\left(\frac{\omega}{c} r_{pwas}\right) + \frac{\omega}{c} r_{pwas} J_1^2\left(\frac{\omega}{c} r_{pwas}\right)\right] \tag{4.61}$$

$$\int_{z=0}^{h_{adh}} \left(\cosh\left(\frac{\frac{\omega}{c} z}{\sqrt{\alpha}}\right)\right)^2 \mathrm{d}z = \frac{c\sqrt{\alpha}}{4\omega} \left[\sinh\frac{\omega}{c}\frac{h_{adh}}{\sqrt{\alpha}} + 2\frac{\omega}{c}\frac{h_{adh}}{\sqrt{\alpha}}\right]. \tag{4.62}$$

This leads to k_{adh}. For small ratios of $\frac{\omega}{c}\frac{h_{adh}}{\sqrt{\alpha}}$, as h_{adh} is the largest possible z, it is possible to simplify the equation, with $\sinh x \approx x$, resulting in the same result, as it is given in (*Dugnani*, 2009):

$$k_{adh} = \frac{G_{adh}}{2} \frac{\left(\frac{\omega}{c\sqrt{\alpha}}\right)^2}{\sinh^2\left(\frac{\frac{\omega}{c} h_{adh}}{\sqrt{\alpha}}\right)} \left(\frac{\sinh\left(\frac{\frac{\omega}{c} h_{adh}}{\sqrt{\alpha}}\right)}{2\frac{\omega}{c\sqrt{\alpha}}} + h_{adh} \right)$$
$$\cdot \frac{1}{2} \frac{\frac{\omega}{c} r_{pwas} J_0^2\left(\frac{\omega}{c} r_{pwas}\right)^2 - 2 J_0\left(\frac{\omega}{c} r_{pwas}\right) J_1\left(\frac{\omega}{c} r_{pwas}\right) + \frac{\omega}{c} r_{pwas} J_1^2\left(\frac{\omega}{c} r_{pwas}\right)}{\frac{\omega}{c} J_1^2\left(\frac{\omega}{c} r_{pwas}\right)}, \tag{4.63}$$

$$k_{adh} \approx \frac{G_{adh}}{2h_{adh}} \frac{\frac{\omega}{c} r_{pwas} J_0^2\left(\frac{\omega}{c} r_{pwas}\right)^2 - 2J_0\left(\frac{\omega}{c} r_{pwas}\right) J_1\left(\frac{\omega}{c} r_{pwas}\right) + \frac{\omega}{c} r_{pwas} J_1^2\left(\frac{\omega}{c} r_{pwas}\right)}{\frac{\omega}{c} J_1^2\left(\frac{\omega}{c} r_{pwas}\right)}. \tag{4.64}$$

With this result, the influence of the bonding line can be included in eq. (4.39) and this is inserted in eq. (4.24) to find χ for the modeling of the susceptance B as imaginary part of the admittance Y in eq. (4.35). An analytical model for the use of the electro-mechanical impedance to inspect attached PWAS and their bonding layer has been presented.

In (*Berlincourt* and *Krueger*, 2000) a frequency dependency of the dielectric constant ε_{33} is given with -2.4% per frequency decade. This is consistent with the results given in (*Hooker*, 1998). *Hooker* also shows additional frequency dependencies for other constants, which have not been implemented in the model, (*Hooker*, 1998).

Additionally, temperature dependency of the used parameters is given in (*Hooker*, 1998; *PICeramic*, 2004). This can be included in the model. Instead of modeling the temperature dependency for all parameters of the model, only the four major parameters of the PWAS r_{pwas}, h_{pwas}, d_{31} and ε_{33} as well as the shear modulus of the adhesive G_{adh} are taken into consideration. The temperature effect is artificially increased, compared to the data, given in (*Hooker*, 1998; *PICeramic*, 2004). This is distinctive especially for the thermal expansion perpendicular to the polarization direction. The thermal sensitivity factors for r_{pwas}, h_{pwas}, d_{31}, ε_{33} and G_{adh} are $0.08\%/K$, $-0.003‰/$ K, $0.1\%/$ K, $0.25\%/$ K and $0.8\%/$ K for *PIC255* and similar piezoelectric materials, like they are used in the embedded transducers from *Acellent*. More information about the temperature dependency of different materials can be found in (*Berlincourt* and *Krueger*, 2000; *Li* et al., 2009; *PiezoSystems*, 2011; *Wolf* and *Trolier-McKinstry*, 2004).

The model enables the detailed discussion of the influence of parameters without the necessity of various experiments. Examples of geometry variations are the change of PWAS radius or thickness and changes of the adhesive layer thickness. Also the influence of the piezoelectric material with d_{31} and ε_{33} can be examined without additional experimental effort. Fig. 4.12 shows the effects for selected parameters. The case of a simple PWAS on aluminum is used as a baseline.

The changes of r_{pwas} and h_{pwas} lead to the same new value for the capacitance C, which is reduced by a factor 2. This leads to a decrease of the susceptance slope.

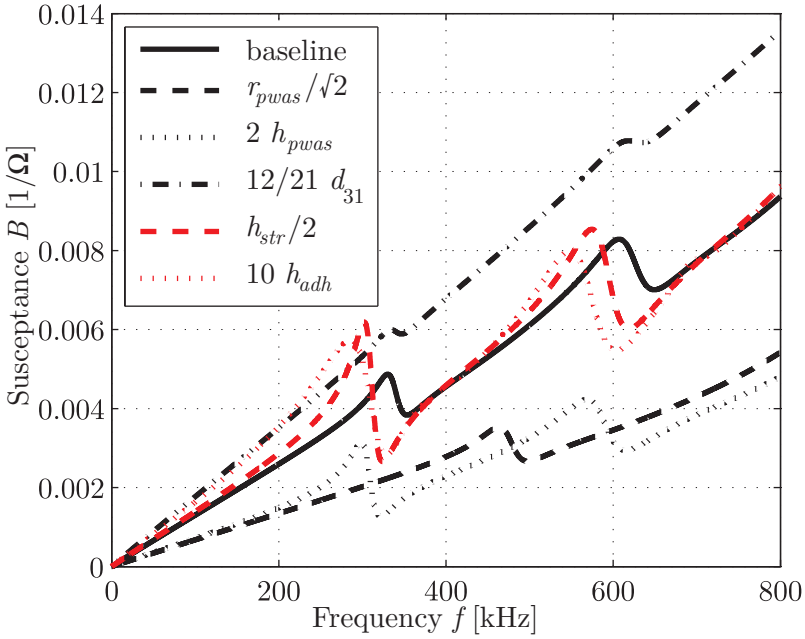

Figure 4.12: Effect analysis for five specific model parameters, r_{pwas}, h_a, d_{31}, h_s and h_{adh}.

First the geometrical parameters of the PWAS are focused. While with a change of h_{pwas} the eigenfrequency stays in approximately the same frequency range, this is not the case for r_{pwas}, which also influences the dominant factor $\varphi_a = \frac{\omega}{c} r_{pwas}$. This leads to a shift of eigenfrequencies to a higher frequency range. A single reduction of the capacitance C would differ from an increase of h_{pwas}, as h_{pwas} is also a factor in k_{pwas} (see eqs. (2.42) and (4.25)). The material constant d_{31} is not part of the capacitance C. In the coupling factor k_p^2, it can be found as d_{31}^2. From the baseline value of $-210 \cdot 10^{-12} \frac{C}{N}$, which is the specific value of *PIC151*, it was reduced to the specific value of *PIC181* with $-120 \cdot 10^{-12} \frac{C}{N}$. This relative reduction by less than half leads to an increase of the susceptance slope and a less pronounced eigenfrequency behavior, as the difference of the susceptance spectrum from the linear relationship of $i\omega C$ is decreased with a decreased factor k_p^2. These parameters are key factors in eq. (4.35). The other two parameters, of which the influence is depicted in fig. 4.12 are part of $\chi(\omega)$ and therefore part of the structural and adhesive layer stiffness k_{str} and k_{adh}. The reduction of h_{str} from 2 mm to 1 mm leads to a more pronounced resonance behavior, as the stiffness of the structure is reduced. Consequently the PWAS can move more easily. The same explanation yields an increased bonding layer. With increased thickness of the adhesive layer, leaving G_{adh} the same, the difference of movement from the PWAS and the structure is increased and the PWAS can move more freely. While for a decreased thickness of the structure the energy transfer to the plate is higher, the

opposite is true for an increased thickness of the adhesive layer, leading to an increased shear lag effect, although the effects on the susceptance spectrum are similar.

For the comparison with experimental results it is necessary to model the cabling, too. Especially for larger structures, the influence of the cables is significant and cannot be neglected. The cabling is therefore added to model the measured susceptance Y_{meas}, instead of the susceptance Y of the bonded transducer. The cabling can be modeled via a serial connection of a resistance R_c, an inductor with L_c and the parallel connection of a conduction of the isolation G_c and a capacitance C_c. The measured admittance is parallel to the parallel connection (*Boege* and *Plaßmann*, 2007). The model is visualized in fig. 4.13 with L_C, R_C, C_C, G_C and the length of the cable l_{cable} leading to Y_{meas}. Typical values for the used cables are given in the appendix A.3. The characteristic inductance L_c of the cable can be calculated with the characteristic impedance Z_{char} of the cable and its capacitance C_c, assuming good shielding:

$$L_c = Z_{char}^2 C_c, \tag{4.65}$$

$$Y_{meas} = \frac{1}{(i\omega L_c + R_c)\, l_{cable} \frac{1}{G_c l_{cable} + i\omega C_c l_{cable} + Y}}. \tag{4.66}$$

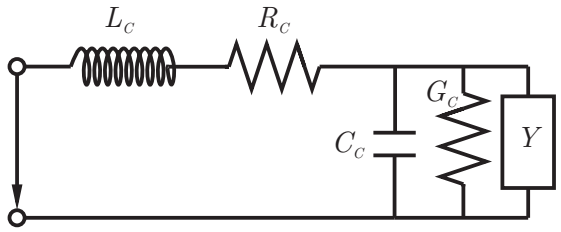

Figure 4.13: Model of circuit correction for a connecting cable.

4.3 Validation of a physics-based analytical model of the susceptance

The applicability of this model is shown via comparisons with experimental data. Three different cases are investigated: a simple piezoceramic disc with wrap-around electrode attached to an aluminum plate, an embedded piezoceramic disc with wrap-around electrode attached to an aluminum plate, and an embedded disc co-bonded to a CFRP

sample. For all cases several samples are measured and the associated model is compared in a frequency range, which includes the first eigenfrequency of the attached PWAS. If not mentioned explicitly, all experiments were conducted at ambient temperature to decrease the influence of temperature.

For the simple transducer, nine PWAS made from *PIC151* material, with a diameter of 10 mm and a thickness of 0.5 mm from *PI Ceramic* have been used. They are attached to an aluminum plate ($AlMg_3$) with a thickness of 2 mm. As adhesive, *Z*70 superglue from *HBM* was used (*HBM*, 2016). As for the adhesive no material data is available, the material data of a two component adhesive was used, which is employed for the other two cases. Its thickness is estimated. The detailed parameters are listed in table 4.1. The susceptance spectra of the model and the experiments fit very well, as depicted in fig. 4.14. While the eigenfrequency as well as the slope is represented nicely, the values of the section below the eigenfrequency with constant slope are slightly lower than the mean susceptance spectrum of the measurements.

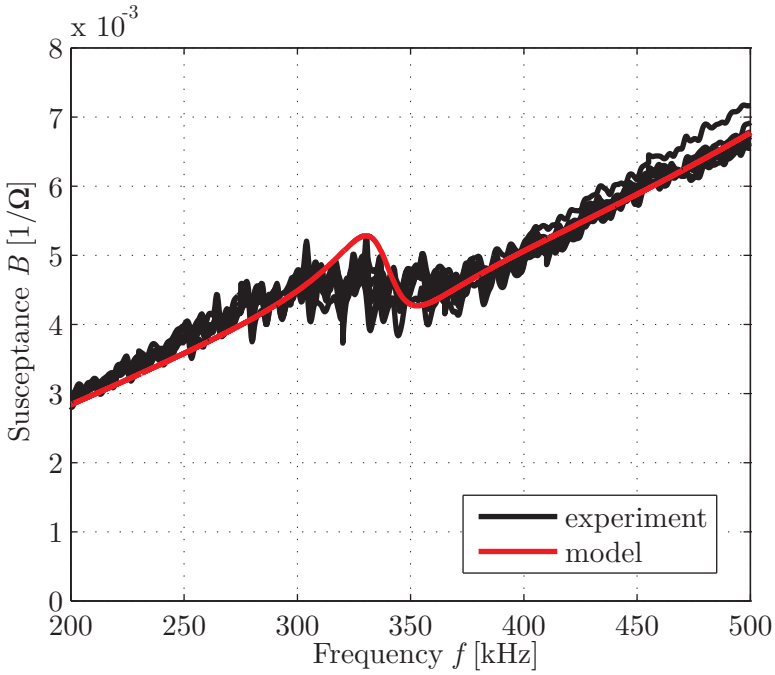

Figure 4.14: Comparison of analytical model and experimental susceptance spectra for the case of a simple *PIC151* transducer, attached to an aluminum plate.

For the embedded transducer on an coated aluminum plate, six *Acellent SMART Layer* PWAS have been applied on aluminum samples with *Hysol EA 9394*, a two component structural paste adhesive from *Henkel* (*Corporation*, 2002). Compared to *Z70* from *HBM*, the adhesive layer is much thicker as the paste is not as inviscid as the superglue. The thickness has been measured in an embedded micro-section for another

sample, which was produced in a similar procedure (fig. 4.15). Tests have shown that the thickness varies due to manufacturing variations. This is also visible in the high scattering of the experimental data. The susceptance spectra of the model and the experiments fit very well, see fig. 4.16. The resonance phenomenon as well as the slope is represented nicely. The position of both sections with constant slope is slightly lower than the mean spectrum of the measurements.

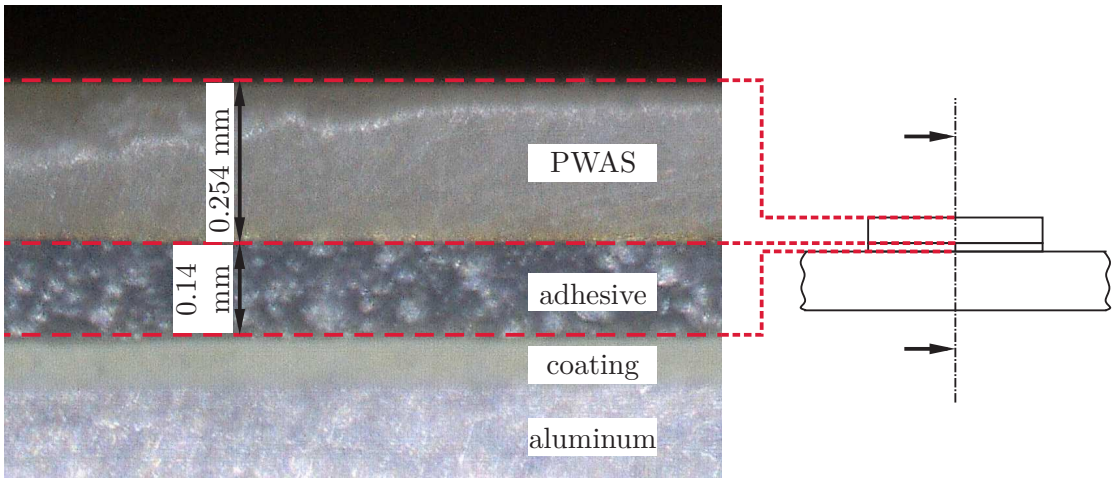

Figure 4.15: Micro-section of an embedded PWAS from *Acellent*, attached to a coated aluminum plate with adhesive *Hysol EA 9394*.

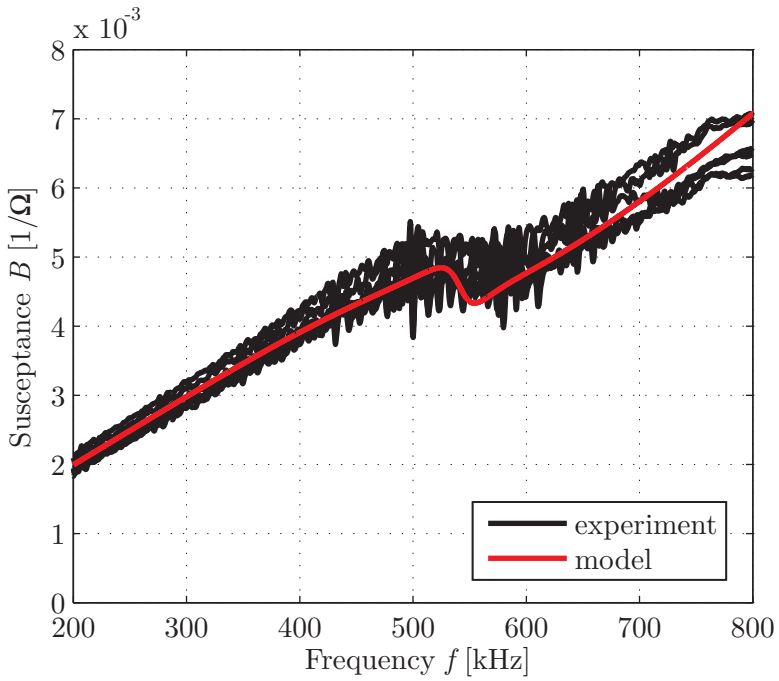

Figure 4.16: Comparison of analytical model and experimental susceptance spectra for the case of an embedded transducer, attached to an aluminum plate.

In a similar experiment also the temperature dependency of the model has been tested. One of the samples from fig. 4.16 was measured at a temperature of 20 °C, 40 °C, 60 °C,

and 80 °C. Fig. 4.17 shows the resulting susceptance spectra for the model in a) and for the measurement in b). Both graphs match very well. Changes of the temperature lead to a significant change of the slope of the susceptance. An increased temperature leads to an increased slope. Moreover the eigenfrequency shifts towards lower frequencies and the characteristic is more pronounced. All these features are visible in the model, too.

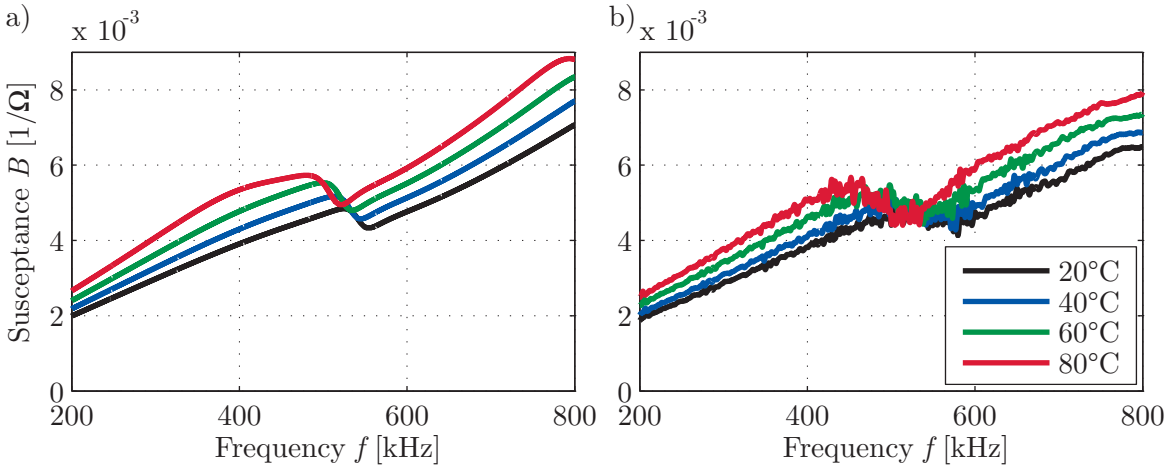

Figure 4.17: Comparison of a) analytical model including modeling of temperature dependency and b) measured data for 20 to 80 °C.

For the embedded transducer on a CFRP plate, 17 *Acellent SMART Layer* PWAS have been co-bonded on CFRP samples. The samples are quasi-isotropic with an equivalent elastic modulus estimated at 70 GPa. The co-bonding process leads to a much better connection between the PWAS and the structure, as no adhesive is used, but the matrix of the fiber-matrix-combination of the CFRP is used as bonding layer. It is very thin and quite stiff. Studies of the co-bonding process, published in (*Bach* et al., 2013; *Moix-Bonet* et al., 2014), have shown, that the co-bonding process, which takes place in the autoclave at high temperatures (180 °C) leads to an increased capacitance and that the embedding of the transducer can change the placement of the fibers in the area of the co-bonded transducer. Therefore the increase of capacitance value is included in the model via artificial increase of the relative dielectric constant ε_{33}. The matching of the susceptance spectra of the model and the experiments is less good than for the other cases under consideration, fig. 4.18. The effect of the eigenfrequency on the susceptance spectrum is not represented very well. Moreover the resonance frequency itself is less exact. This might be caused by the change of the fiber placement in the area of the co-bonded transducer or the change of other material parameters in the co-bonding process. Moreover the lay-up of the CFRP locally leads to a different stiffness in x-

and y-direction. This effect is not considered by the axisymmetric model. The slope is represented quite well by the model. The experimental data exhibit very similar resonance behavior but comparably large deviations regarding the slope.

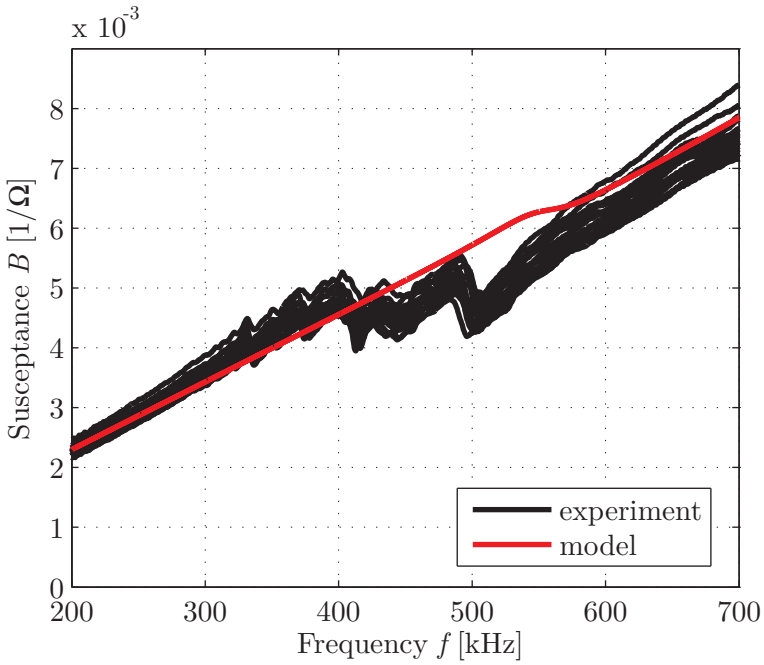

Figure 4.18: Comparison of analytical model and experimental susceptance spectra for the case of an embedded transducer, co-bonded to a CFRP plate.

The cases show that the model is able to predict the susceptance spectrum of piezoelectric transducers attached to structures. Only the mechanical quality factor, which determines the damping, had to be reduced artificially for all cases to achieve satisfying agreement between experimental results and analytical model. The accuracy of the model works especially well for applications with secondary bonded transducers, which exhibit an adhesive layer.

Table 4.1 summarizes the geometrical and material constants which were used to model the three cases. It also shows that many parameters are necessary to be able to analytically describe the susceptance spectrum. For many applications, this detailed definition of the parameters is hardly accessible. The knowledge of all parameters and possibly also their temperature dependency promotes opportunities to find faulty transducers as they do not match with the model.

The deviations in the experimental data show that attached PWAS with the same nominal set of parameters also exhibit differences in their susceptance spectra. These differences are most likely caused by deviations of the parameters around their nominal values, e.g. slightly different radius, differences in the thickness of the adhesive layer,

Case		simple PWAS secondary bonded *PIC151* on $AlMg_3$	embedded PWAS secondary bonded *PIC255* on $AlMg_3$	embedded PWAS co-bonded *PIC255* on CFRP
d_{pwas}	$10^{-3}m$	10	6.35	6.35
h_{pwas}	$10^{-3}m$	0.5	0.254	0.254
ρ	$\frac{kg}{m^3}$	7800	7800	7800
Q_m		10	16	8
s_{11}^E	$10^{-12}\frac{m^2}{N}$	15.0	15.9	15.9
ν		0.34	0.34	0.2
d_{31}	$10^{-12}\frac{C}{N}$	-210	-175	-175
$\tan\delta$	10^{-3}	20	20	20
$\varepsilon_{33}^T/\varepsilon_0$		2400	1750	2200
G_{adh}	$10^9 Pa$	1.46	1.46	2.89
η_{adh}		0.4	0.4	0.04
E_{str}	$10^9 Pa$	70	70	70
h_{str}	$10^{-3}m$	2	2	2
ν_{str}		0.33	0.33	0.33
h_{adh}	$10^{-3}m$	0.02	0.10	0.02
δ_{freq}	$\frac{1}{100dec.}$	-2.4	-2.4	-2.4
l_{cable}	m	2	2	2

Table 4.1: Geometrical and material parameters for the three cases used to show the applicability of the analytical model

etc. *Bochuang Ceramic, Inc.* (2008) provide a tolerance of ±20% for their material constants. The experimental data also exhibit variations around the general trend of the spectrum. These fluctuations are caused by the eigenfrequencies of the structure and its condition. As the model only includes a very simple, frequency independent representation of the structural stiffness, these effects are not represented by the analytical model.

With this model, it is possible to gain an insight into the dependencies of the parameters and the susceptance spectrum. Also its use for comparisons with experimental data is conceivable. The possibility to model PWAS defects is limited. As the model is based on axial symmetry, non-symmetric defect cases can be modeled only in a simplified form. Moreover for the usage on CFRP the calculation of an equivalent elastic modulus

is necessary. Although CFRP does not fulfill the prerequisite of axial symmetry, a modeling approximation is possible.

A possibility of modeling PWAS defects is the use of a numerical model. This is developed in the following section 4.4.

4.4 Design of a numerical model to calculate the EMI of PWAS

The modeling of the EMI spectrum of a bonded transducer is modeled again with *COMSOL*. The advantage of this commercial software is its simple use for multiphysics-based problems like the piezoelectric effect. The numerical modeling of the wave propagation in time domain with *COMSOL* has been shown in section 3.2. Additional information about the settings used is given in appendix A.1. For details about the numerical background of *COMSOL* the reader is referred to (*COMSOL*, 2013). This work does not focus on the development of numerical models but uses existing software for the analysis of the influence of PWAS defects on the EMI spectrum for bonded PWAS on structures with the help of numerical models.

The numerical model for the EMI spectrum can be calculated in the frequency domain, unlike the procedure in the experimental setup, which is based on a frequency sweep and later conversion of time data into the frequency domain. The modeling in the frequency domain shortens the duration of a calculation to a great extent, which is of interest for parameter analysis, for which several calculations have to be realized. Especially, if a very dense frequency sampling is not necessary, the advantages of the calculations in the frequency domain are invincible. The model consists of the structure, the adhesive layer, and the PWAS itself without including the wrap-around electrode. As for the modeling of wave propagation in the time domain, the upper surface of the PWAS is attached with no voltage while the voltage is applied to the lower surface. The frequency at which this voltage is altered is changed for the evaluation in the frequency domain. To calculate the susceptance spectrum, it is necessary to evaluate the current and divide it by the voltage, similar to the procedure explained in section 4.2. For this an integration over the PWAS' lower surface is necessary, realized directly in *COMSOL*. The integration is frequency dependent and its division by the input voltage leads to the susceptance spectrum.

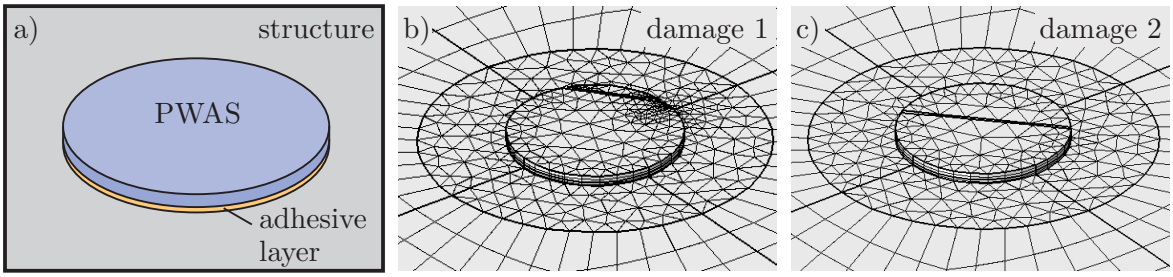

Figure 4.19: Geometrical setup in *COMSOL* with PWAS, adhesive layer and structure a) undamaged PWAS, b) mesh for defect 1, area separation 5%, c) mesh for defect 2, area separation 40%.

For the first validation of the numerical model, the material constants are chosen in accordance to section 3.2, which is the experimental setup, used for validation of the numerical model in the time domain. The experimental setup is described in detail in section 3.1.2 and shortly reviewed here for the ease of reading. An embedded transducer of type *Acellent* was broken due to a line force, applied with a chisel. The defect has been introduced in two stages, the first stage is a separation of 5% of the PWAS area, the second stage is a detachment of 40% of the PWAS surface area, the setup and the mesh is depicted in fig. 4.19.

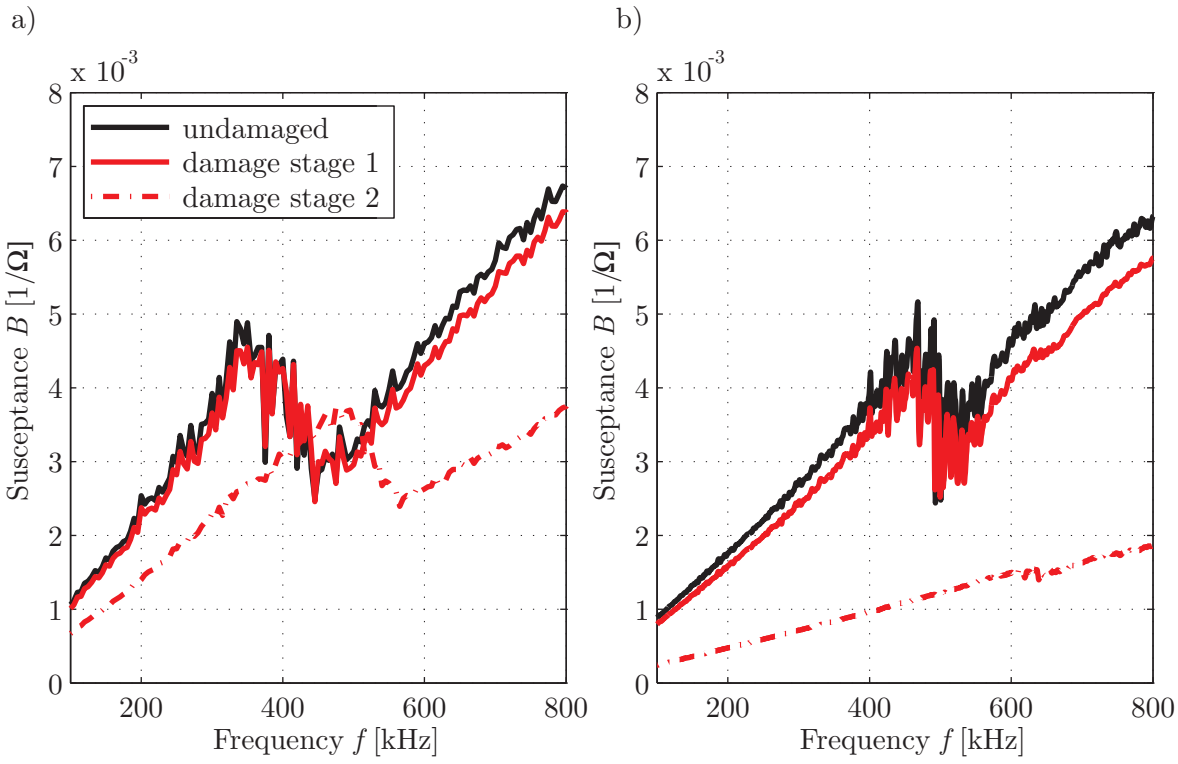

Figure 4.20: Susceptance spectra for the undamaged state and two defect stages, a) spectra calculated using a numerical model, b) spectra resulting from an experiment.

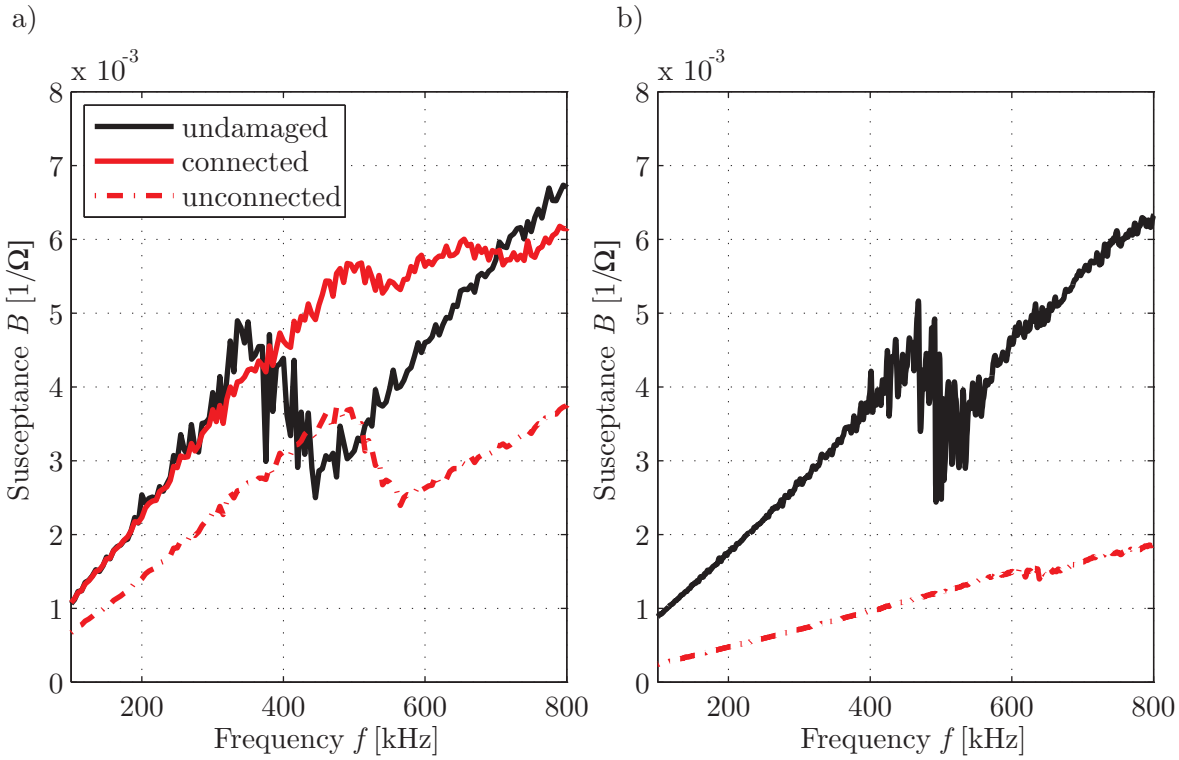

Figure 4.21: Susceptance spectra for the undamaged state and the second defect stage, a) spectra calculated using a numerical model, two different ways of modeling are compared. Connected: both parts of the broken PWAS are still electrically connected, unconnected: only the main part is electrically connected, b) measured susceptance spectra.

As it can be seen in fig. 4.20, the susceptance spectra of the undamaged state as well as of the two defect stages can be modeled very well with the help of the numerical model. For the first defect stage, a reduction of the susceptance slope is visible. The reduction of the piezoelectric active area leads to a decreased slope. The eigenfrequency is approximately the same. For the second defect stage, both, eigenfrequency and susceptance slope, are changed considerably. The susceptance slope is decreased, while the eigenfrequency is shifted to higher frequencies. The active area of the PWAS decreased considerably due to the impact of the chisel. It is a linear factor in the capacitance, being a linear factor in the susceptance spectrum itself. The change of the PWAS geometry due to the detached 40% part leads to a shift of the eigenfrequency to higher frequencies. The differences of the exact susceptance spectra of numerical model and experimental results are possibly caused by the inaccurate estimated parameters like the damping of the adhesive, as well as they result from the fact that the experiment includes the cabling and therefore the susceptance spectrum is slightly changed by the cabling. An underestimation of the introduced defect has been noticed already in section 3.2. As this is also the case for the frequency domain the results again show

high consistency. This consistency is also stressed when comparing the results for two different ways of modeling the defect, also discussed in section 3.2. For one way of modeling both broken parts are still connected to the electrical circuit, for the second way only the main part with the soldering points is still connected to the electric circuit. In fig. 4.20, only the results for the second way, when the main part is electrically active, are shown, as this has been evaluated as best modeling practice in the time domain. Fig. 4.21 depicts the susceptance spectra for both ways of modeling. Again it can be clearly seen that separated parts without any electrical connection reflect the results from the experiment much better. If both parts are still connected, only the eigenfrequency is shifted to higher frequencies, while the slope of the susceptance spectrum stays almost constant. This behavior is not present for the case of defect due to breakage introduced by a chisel, nevertheless, these defect cases exist, like it is shown in section 4.1 for the cases of tool drop without spalling and cracks in an embedded transducer caused by bending load.

For the second validation example, the material constants and setup of the experiment described in section 4.1 for the case of cracks due to bending load are used. In this example, a CFRP strip builds the structure. On top of the structure an embedded PWAS of type *DuraAct* is co-bonded to the surface. Similar to the procedure of model-validation for co-bonded PWAS an increased value of ε_{33} has been introduced. In a four-point bending test the transducer is placed on the tension side. Cracks are audible and visible from 0.5% strain. For this bending experiment with embedded transducers co-bonded on CFRP-strips, the numerical model leads to the resulting susceptance spectra depicted in fig. 4.22a). The phenomenon caused by the cracking does not result in a decrease of the susceptance slope in the experiment, fig. 4.22b). This is confirmed by the numerical model, too. The frequency range, for which the susceptance is effected by the eigenfrequency is decreased in its range, which leads to a larger offset for the second linear section of the susceptance spectrum.

The numerical model is able to predict the susceptance spectrum for bonded piezoelectric transducers. Especially the effects caused by the PWAS defect are represented by the numerical model very well. This has been shown by validation with two experimental setups including two different damages. Although the numerical modeling is associated with more computational costs than the analytical model, it is valuable for the analysis of transducer defects and its effects on the wave propagation and the susceptance spectrum. With the help of numerical models it is possible to model series

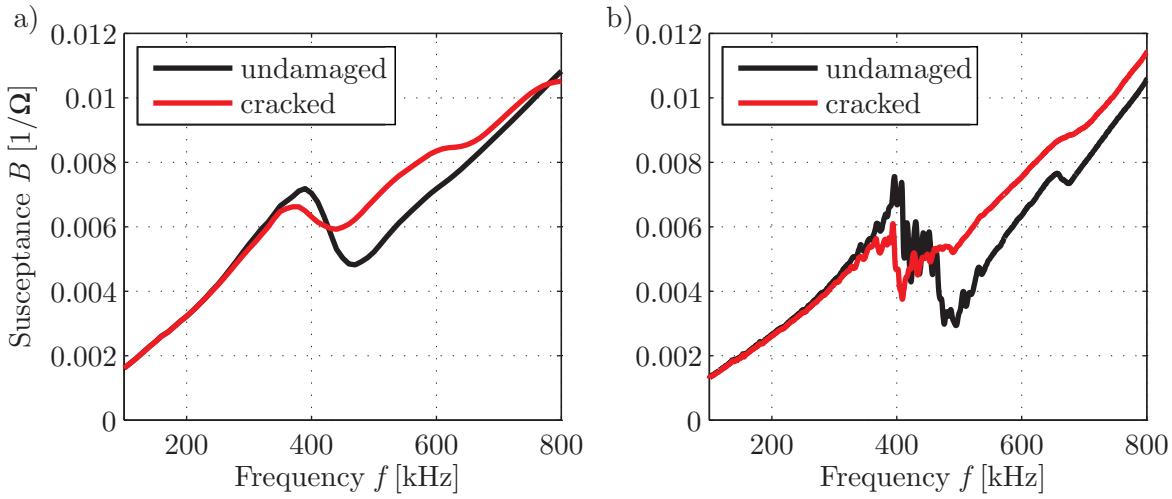

Figure 4.22: Susceptance spectra for undamaged and broken PWAS, a) modeled with *COMSOL*, b) experimental data.

of undamaged and defect PWAS and calculate the wave propagation as well as the susceptance spectra for these cases. The data can be used for further analysis e.g. for performance assessment of methods to detect faulty PWAS.

4.5 New methods for PWAS inspection

Based on the susceptance spectrum, different methods for model-free PWAS inspection exist (*Park* et al., 2006a; *Overly* et al., 2009; *Taylor* et al., 2013). However, these methods show poor performance especially for those types of transducer defects, which do not include spalling or separation of flanks of a breakage (*Buethe* et al., 2014a). As described in section 4.2, also models of the susceptance spectrum exist. Within this work model-based methods as well as model-free methods are developed and applied. The general explanation and procedure is given in the following sections, while their application is shown in chapter 6. All methods are based on a comparison of new data with other measurements, either preliminary measurements from the undamaged state or of other transducers and necessary assumptions. The model-based methods use the adapted model, presented and validated in sections 4.2 and 4.3, the model-free methods make use of existing procedures for the comparison of data, which are applied in the context of PWAS inspection.

4.5.1 Model-based methods

The use of analytical or numerical models as baseline or part of the baseline is a common procedure for many SHM applications. For the PWAS inspection it is possible to use the analytical model, described in section 4.2. The main idea of these model-based methods is to estimate the input parameters of the model by adapting the model to experimental data. Based on these estimated parameters a statement about the current health status of the PWAS shall be possible. The necessary steps for this procedure are visualized in fig. 4.23. Two different approaches, based on this idea are explained in the following. Both include temperature compensation and assume to have baseline measurements in a specified temperature range.

For the first approach the temperature is taken as a known parameter. This is possible if temperature is measured close to the PWAS or no large temperature gradient between temperature measurement location and PWAS location is present. For the second approach only the temperature of one measurement has to be known. In most cases this is easily achievable during the setup of the SHM system. The general procedure is very similar for both approaches. They are, therefore, explained alongside.

In a first step the model is adapted to the real PWAS. Starting with a parameter set p_{init} taken from data sheets, the parameters are adapted to achieve a better fit of model and a baseline measurement. This baseline measurement is taken at a defined temperature to shift the model parameters towards their possible realistic quantity. According to (*Rugina* et al., 2015) and various data sheets, e.g. (*PICeramic*, 2004; *Bochuang Ceramic, Inc.*, 2008) the piezoelectric constant and the relative dielectric constant may vary about 10% to 20% from their nominal value. Geometric parameters are ought to vary about 1%, while other parameters like stiffness, mechanical loss factor etc. may vary about 5% from their nominal value. Experiments have shown that the adhesive layer shows the biggest variation. The parameter can be adapted in this first step between -30% and 50%. These values define an approximate corridor for the first step *adaptation* and might be changed according to the experimental setup, used. The result of this step is an adapted model with a parameter set p_{adapt}.

In the second step *training* this adapted model is compared to training data, consisting of susceptance spectra. These spectra are measured at the baseline state of the PWAS within the whole temperature range under consideration. For the first approach the temperature should be known, for the second approach this temperature does not

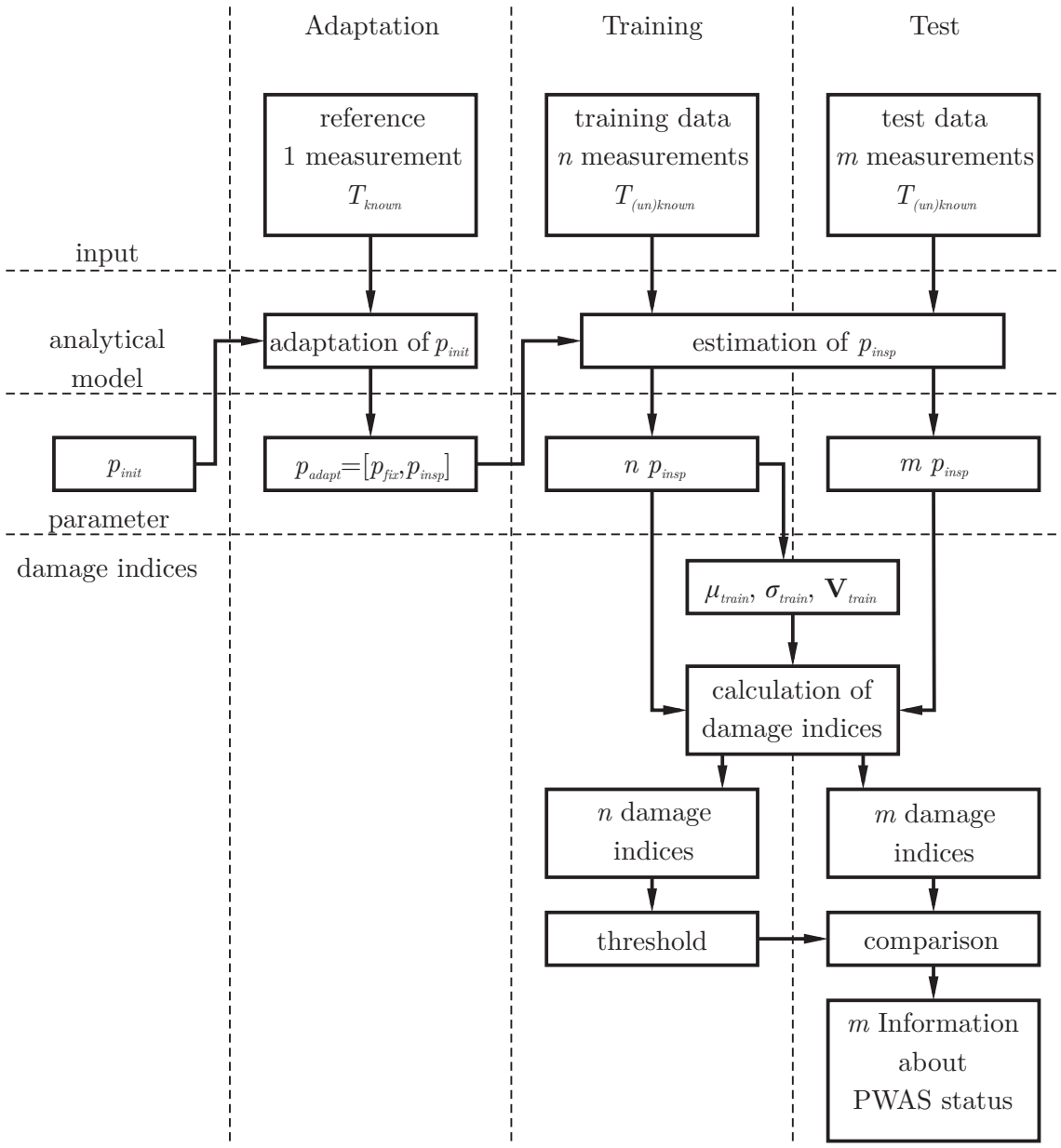

Figure 4.23: Flow chart for model-based methods, including the three phases *adaptation*, *training* and *test*

have to be known. In the training step a reduced parameter set for each susceptance spectrum is estimated individually. While geometrical parameters like the thickness of the adhesive layer and PWAS radius and material parameters like stiffness and *Poisson*'s ratio are constant for the PWAS under consideration, other parameters might change due to defects of the PWAS. These parameters build the reduced parameter set p_{insp}. The set p_{insp} is estimated based on the optimal adjustment of the analytical model to the measured susceptance spectrum. For the first approach, the temperature is known and therefore not included in the reduced parameter set p_{insp}. For the second approach, the temperature is unknown and therefore included in p_{insp}. The resulting

n parameter sets p_{insp}, adjusting the model best to n baseline susceptance spectra, are used for further steps to build damage indices and a threshold.

From the parameter sets p_{insp} of the training data mean and standard deviation for each parameter are calculated. For the approach with known temperature, p_{insp} is extended by the measured temperature T. The parameter sets are normalized via subtraction of mean μ_{train} and division by standard deviation σ_{train}. The result are n normalized parameter sets $p_{insp,n}$. The damage index is built by using the *Mahalanobis* squared distance. As the data is already normalized with its mean, this is not necessary anymore. Each parameter set $\underline{p}_{i,insp,n}$ is divided by the covariance matrix $\mathbf{V}_{train}$ of the training data $\underline{p}_{insp,n}$ and multiplied with itself to calculate the damage index $DI(i)$ for this ith parameter set:

$$DI(i) = \underline{p}_{i,insp,n}^{T} \mathbf{V}_{train} \left(\mathbf{p}_{insp,n}\right)^{-1} \underline{p}_{i,insp,n}. \tag{4.67}$$

Taking these n damage indices, a threshold DI_{thr} is built based on statistical methods. Assuming a false call rate of 1%, the test of single multivariate normal outlier is used, which is described in (*Rencher*, 2002). It is based on *Hotelling*'s T^2-statistics and its combination with the F-distribution of *Fischer*.

An alternative procedure, leading to the same results is to calculate a PCA model. PCA is not explained in this work, the interested reader is referred to (*Mujica* et al., 2011; *Torres-Arredondo*, 2013). The advantage of the use of PCA is that the data can be reduced to significant features, if some parameters of p_{insp} are highly correlated. Then only the important principal components should be used for the calculation of the damage index with the *Mahalanobis* squared distance. For this case this leads to different, better results. Another alternative procedure to evaluate DI, using the *Mahalanobis* squared distance, is the use of a self organizing map (*Kohonen*, 2001). This approach is in favor for applications which can be described only with nonlinear dependency of the parameters. It is described in detail in (*Buethe* et al., 2014b).

The last step *test* is very similar to the training step, as also at first the set p_{insp} is estimated based on the optimal adjustment of the analytical model to the measured susceptance spectrum. As measured susceptance spectra, m test measurements are available. For these test measurements the state of the PWAS is unknown. The transducer might be defect or not. The estimation leads to m sets of p_{insp}. They are normalized with mean and standard deviation of the *training* data, μ_{train} and σ_{train}.

This is of great importance, as the training data build the baseline data model. With the covariance matrix V_{train} of the training data, the m normalized sets $p_{insp,n}$ are used to calculate m damage indices DI with the *Mahalanobis* squared distance. By comparing them to the threshold DI_{thr} information about the state of the transducer for the m test measurements is achieved.

The estimation of parameters for an optimal adjustment of the analytical model to the measured susceptance is based on an optimization procedure. The *MATLAB* function *lsqnonlin* is used. As optimization function, the normalized squared difference between model and measured susceptance spectrum is used adding a penalty term for large changes of a defect relevant parameter. As different parameters have a similar effect on the susceptance spectrum, the estimated parameters might differ from the real parameters. The effect increases with the number of parameters, estimated. Nevertheless, the pattern built by parameter sets of the undamaged PWAS is different from the parameter sets estimated by comparison of susceptance curves of a defect PWAS.

For these model-based PWAS inspection methods, the initial parameter set needs to have a high accuracy. A large number of parameters need to be known for this procedure. Otherwise the differences of the analytical model and the measured susceptance spectrum, even for the undamaged case, is large. This leads to a reduced sensitivity and only large PWAS defects can be detected.

4.5.2 Model-free methods

If the parameters of a bonded PWAS are not known beforehand, e.g. if the bonding material is not characterized to find the material parameters, or if the adhesive layer thickness is unknown, model-based methods cannot be applied successfully. An alternative to model-based methods is the use of baseline measurements in model-free methods.

The main idea is to compare the susceptance spectra of baseline measurements with those of new measurements. If the PWAS is defect, the changes of the susceptance spectrum can be recognized in this comparison. Different methods for this comparison exist, which will be presented shortly. Additional methods have been developed and are explained in detail in this section.

Several publications lead by *Park* exist, which use the change of the susceptance slope as indicator for the state of a PWAS, see (*Park* et al., 2006a; *Park* et al., 2006b; *Park*

et al., 2007; *Overly* et al., 2009; *Taylor* et al., 2013). This method is therefore used as reference in the applications. Taking a frequency interval with constant susceptance slope in a lower frequency range, the slope coefficient SC can be calculated, based on the building of a regression line, see fig. 4.24 a).

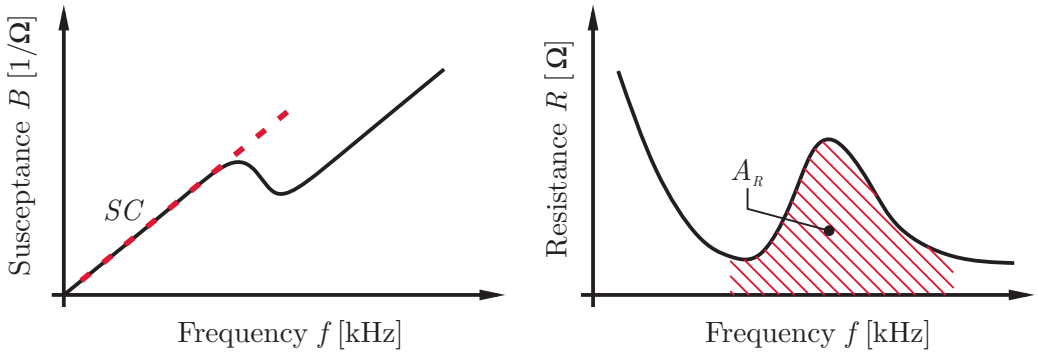

Figure 4.24: Exemplary spectrum for a) Susceptance B and b) Resistance R to visualize the defect sensitive features slope coefficient SC and area under resistance spectrum A_R.

The use of specific features from the susceptance spectrum is also possible, using the susceptance slope as one of the features. Other features can be the resonance frequency, the difference of minimum and maximum susceptance in the frequency range around the eigenfrequency and others. The changes of these features can be combined to a damage parameter with the help of a PCA and calculation of a distance, e.g. T^2 or *Mahalanobis* squared distance. This method is presented in (*Buethe*, 2011; *Xing*, 2016) and is not detailed in this work.

Another possibility of comparing two susceptance spectra is the calculation of the correlation coefficient CC. The correlation coefficient can be calculated using the covariance matrix $\mathbf{V}$, including the covariance and variances of the two spectra, to be compared, the baseline and the tested one. $\mathbf{V}$ therefore is a 2×2 matrix. Before calculating the covariance matrix, the susceptance spectrum is smoothed. This helps to minimize the effect of structural changes. For this application, the correlation coefficient CC varies between 0 and 1 with 1 showing best matching. From this parameter a damage index DI_{CC} can be calculated easily by its subtraction from 1:

$$CC(i) = \frac{V_{12}}{\sqrt{V_{11} V_{22}}}, \tag{4.68}$$

$$DI_{CC}(i) = 1 - |CC(i)| \,. \tag{4.69}$$

In general the correlation coefficient might vary between -1 and 1. As the general slope is always positive, the range between -1 and 0 can be neglected. The damage index DI_{CC} will therefore vary between 0 and 1 even without taking the absolute value. The correlation coefficient is 1 for two susceptance curves, which only differ by a proportional change of the spectrum. Therefore, the phenomenon, which is used when analyzing the susceptance slope SC is neglected when using the correlation coefficient. With DI_{CC} the focus is on those parts of the spectrum, which do not exhibit a constant slope. The resonance and its effects on the susceptance spectrum vary differently for different types of PWAS defects. These changes are used and recognized, when using DI_{CC}. For temperature compensation it is favorable that the change of the slope is not detected by DI_{CC}, as the main effect of a temperature change is a change of the slope. Nevertheless, a temperature change also leads to a shift of the resonance frequencies. This shift causes an increase of DI_{CC}. It is therefore necessary to have a baseline for several temperatures in the temperature range under consideration. Depending on the smallest PWAS defect, which should be detected by the model-free method, the set of baselines should include temperatures in medium to fine intervals. For many cases an interval of 5 °C has proven to give good results, in (*Zhou* et al., 2009) 10 to 20 °C are used.

The correlation coefficient has been used for structural damage detection with guided waves in many applications but also has shown some disadvantages. Therefore a small note on this regard is stated here. For wave propagation data, alternating signals with varying amplitude exist. While a change of amplitude, even if it is big, does not change the correlation coefficient, a small phase shift leads to big changes of the correlation coefficient. With increasing phase shift the absolute value of the correlation coefficient-based damage index can even decrease back to 0 again for a phase shift of 180°. These phenomena result in reduced capabilities for structural damage detection. In contrast to wave propagation data, susceptance spectra follow a clear trend with a positive slope, interrupted by the resonance phenomenon. Therefore, the disadvantages of the correlation coefficient for wave propagation data, just described, do not have a major effect for susceptance spectra, as no phase shift effect is possible.

Using the resistance R as an impedance-based quantity is an alternative approach, based on the EMI spectrum. The capability is indicated by *Park* et al., see (*Park* et al., 2006a, fig.16). A defect sensitive parameter, based on R, is evaluated in (*Moix-Bonet* et al., 2014) and called resistance peak area. In (*Buethe* et al., 2014a) it is

defined as area A_R under the resistance in a specified frequency range around the PWAS resonance frequency, see fig. 4.24b):

$$A_R = \int_{f_{start}}^{f_{end}} R(f)df. \tag{4.70}$$

Different defects have different effects on A_R. Spalling might cause a shift and decrease of the resistance spectrum, different type of cracks might either cause a shift or a decrease of the spectrum.

None of the model-free methods includes temperature compensation. It is therefore necessary to have baselines at different temperature levels and measure the temperature. For each measurement the baseline has to be selected according to its environmental temperature. The alternative of using the best-fit as baseline and not measuring the temperature is not tested in this work.

4.5.3 Baseline-free method

The section heading is highly deceptive, as in general no baseline-free methods exist. Nevertheless, the baseline might also be an assumption of similarity in a batch. This is the case for this method. It will be beneficial for checking piezo-based SHM systems after system installation. For these cases often no baseline is available, especially a baseline measurement of exactly the same PWAS is never available. In addition, if the inspection of the transducers has never been done and shall be retrofitted, this method might be useful.

The method is based on the assumption that a batch of equal transducers, which is bonded in the same way on the same structure at comparable places and is experiencing the same EOC will show similar susceptance spectra, if all transducers are undamaged and perfectly glued. Based on this assumption, e.g. batches, where all transducers are insufficiently bonded, are a challenge for this baseline-free method. Far more than half of the transducers should be intact, to be able to use this method.

The main idea is to compare many transducers of the same type, which are part of a sensor network on a structure. If the spectrum of one transducer significantly differs from the others, it is assumed that this transducer exhibits some defect.

The method is also based on the correlation coefficient, defined in eq. (4.69). Instead of comparing two susceptance spectra, the spectra of a batch of m transducers are

compared pairwise. A similar method, using the comparison within a batch has been described in (*Park* et al., 2007; *Overly* et al., 2009). As defect sensitive feature the susceptance slope was used. In this work the damage index is not calculated by using the standard deviation of the susceptance slope but the differences of the mean correlation coefficient for single transducers compared to other similar transducers is used:

$$CC_{ij} = \frac{V_{ij}}{\sqrt{V_{ii}V_{jj}}}, \tag{4.71}$$

$$CC_{\in n} = \frac{1}{m-1}\sum CC_{ni} \qquad i \in 1,...,m/n, \tag{4.72}$$

$$CC_{\notin n} = \frac{1}{(m-1)^2 - m + 1}\sum CC_{ij} \qquad i,j \in 1,...,m/n, i \neq j, \tag{4.73}$$

$$DI_{CC,b}(n) = \left|CC_{\notin n} - CC_{\in n}\right|. \tag{4.74}$$

The mean of all correlation coefficients from all transducer pairs of the batch, except of PWAS n is calculated, $CC_{\notin n}$ eq. (4.73). From this value the mean of all correlation coefficients from pairs of PWAS n and any other transducer of the batch, $CC_{\in n}$ eq. (4.72), is subtracted. For mathematical reasons the absolute value is built. If PWAS n is defect, $CC_{\notin n}$ is larger than $CC_{\in n}$. If PWAS n is not defect, they have the same order of magnitude and might get negative. For these cases evaluation of the absolute value is necessary. In any case like this $DI_{CC,b}$ is close to zero.

For many applications a difficulty of this baseline free procedure is the fact, that all transducers have to be of the same type, bonded in the same way and located at a similar structure with equal thickness and stiffness. Moreover the cable length should be similar. These points often prevent the use of all PWAS in one batch. Instead subgroups of transducers can be built, which can be treated as a batch as they fulfill the requirements. An overview and introduction of model- and baseline-free methods is also given in (*Buethe* et al., 2014a).

The EMI is the focus of this chapter. A physical model is developed, enabling a profound understanding of the impacts, geometric and material parameters have. A numerical model is set up to simulate different type of defects. Experimental studies are used to validate the models. New model-based and model-free methods for the inspection of PWAS are introduced. Their evaluation is shown in the next chapter, their application is described in chapter 6.

5 Evaluation of the performance for methods to inspect PWAS

To assess the quality or performance of a PWAS inspection method, several procedures are possible. If the operator of the SHM system is able to define specific types of PWAS defects and their sizes, that have to be detected by the PWAS inspection method, tests can be conducted to evaluate, whether the method is able to detect these defects. For this procedure it is necessary to be able to introduce this specific defect type repetitively. A possible statistical method for this performance evaluation is the "29 of 29" procedure, based on a binomial distribution. The value of 29 is based on the fact, that with this number a probability p of 0.9 with a confidence of 95% can be achieved, see (*Gandossi* and *Annis*, 2010) for the details of this procedure.

However, many operators of SHM systems are not able to define specific PWAS defects and sizes that have to be detected by the PWAS inspection method. For these cases it is necessary to find another way to evaluate its performance.

In this chapter a new procedure for the assessment of the performance of a PWAS inspection method is developed. It takes the algorithm for the detection of structural damages of the SHM system under consideration into account and combines it with the PWAS inspection method using statistical methods. The main idea of this approach is the prevention of the following instance: The PWAS inspection is able to find a debonding of 20% with a high confidence level. Unfortunately this extent of debonding already leads to large changes in the generated wave field and these changes already lead to an increased false call rate of the SHM system. In this case, even if the PWAS inspection method has been tested and may even be certified for a specific defect type and size, it is not suitable to be used with the specified SHM system. It is therefore necessary to consider the algorithm of the SHM system as well as the PWAS inspection method.

Also another aspect needs to be considered. In section 6.4 it will be shown that there is a transition for PWAS between healthy state and failure. PWAS with minor defects still might be used for SHM. But it has to be ensured, that their defects will be detected before structural damage detection is influenced by a faulty transducer.

It is necessary to take into account both, the effects of a PWAS defect on the output of an SHM system and the effects of a PWAS defect on the results of the PWAS inspection method. They have to be linked to be able to evaluate the performance of a PWAS inspection method.

5.1 Description of the general approach based on POD

The general idea of any performance assessment is to describe, how good a measured quantity describes a physical factor. In the NDT sector the measured quantity often is given as some measured damage size $\hat{a}$ and the factor, which needs to be described, is given as a real damage size a. The real damage size a might be a length, an area, a depth or other geometrical parameters, with which a damage can be described. The measured damage size $\hat{a}$ is specific for the used method. For ultrasonic testing it is the equivalent geometric parameter, which can be extracted from the ultrasonic scan, e.g. the area of delamination or the crack length. For performance assessment of PWAS inspection methods in many cases it is not favorable to describe the effect with a real defect size. The real defect size, e.g. the size of a crack in a transducer is irrelevant for the SHM system operator. Much more interesting is the effect, the defect transducer has on the potential outcome of the SHM system algorithm.

If the defect of the PWAS is detected, before the wave field, generated by the PWAS, is disturbed, so that an algorithm for structural damage detection would lead to false alarms, the performance is defined as good. The factor, which is equivalent to the real damage size for NDT, is therefore a quantity, which describes, how much the defect PWAS changes the result of the SHM system algorithm. This is the case, if the structural damage indicator SDI itself is used. The measured quantity is the result of the PWAS inspection method DI as it describes the output of the system as a damage indicator for the transducer.

Summarizing, the used quantity a in NDT is replaced by the structural damage index SDI for the performance assessment of PWAS inspection methods. The measured quantity, which is described by $\hat{a}$ in NDT is replaced by the damage indicator of the PWAS inspection method. With these quantities and assumptions it is possible to analyze and determine, if a defect of the PWAS is detected, before the changes in the wave field lead to a related false alarm in the SHM system.

The general procedure follows the steps described in section 2.2. In the first place a linear dependency between functions of SDI and DI has to be found. Common mathematical functions are logarithms, but also square root or other transformations are possible. If a linear dependency is found, regression analysis is performed. It results in a regression line with two parameters, slope m and intercept b. Moreover the distribution of the data around the regression line is analyzed, leading to the standard deviation τ. Slope m, intercept b, and standard deviation τ as well as their covariance matrix build the basis for calculating the POD curve. Moreover a threshold for DI has to be defined. For the inspection of PWAS this threshold DI_{thr} is defined by the measurement noise for DI. This can be evaluated by multiple measurements of the undamaged state and calculation of the damage indicator for PWAS faults. For the ideal case, the damage indicator indicates no damage, e.g. 0 for DI_{CC}. Nevertheless, changes of EOC and imprecision in the measurement procedure lead to small changes of the damage indicator from its ideal level. Depending on the distribution of this data, a threshold is calculated. Common definitions define the threshold at 95% or 99% of all data points of the undamaged state. The latter leads to a false call rate of 1% for the PWAS inspection procedure. The POD curve is calculated using m, b, τ, and DI_{thr}. Therefore σ_{POD} and μ_{POD} are evaluated and used to build the cumulative distribution function, which is the POD curve. It is the 50% confidence interval. To calculate other confidence intervals, like the 95% confidence bound, the covariance matrix is used. With the *Wald* method a linear transfer of the scattering of the data is done. Similar to the procedure, used in NDT, for the performance analysis the $SDI_{90|95}$ value is evaluated from the POD curve.

Several information can be extracted from the POD curve. The $SDI_{90|95}$ is the value, the structural damage detection indicator reaches, before a defect PWAS can be detected with 90% probability of detection at a confidence level of 95%. From the SHM system also a threshold for the structural damage indicator is available. If values of SDI are above this level SDI_{thr}, the SHM system alarms, as structural damage is

expected by the SHM system. If $SDI_{90|95}$ is below SDI_{thr}, the defect of the PWAS is detected before the changes of the wave field, caused by the faulty PWAS, lead to false alarm of the SHM system for structural damage detection. Its performance can be evaluated as good. If $SDI_{90|95}$ is larger than SDI_{thr} this leads to a higher false call rate, as some defect PWAS can cause changes of the generated wave field and lead to structural damage indicators above SDI_{thr}, before they have been detected by the PWAS inspection system. The occurrence of missed structural damages due to a faulty PWAS is highly improbable, as the effects of faulty PWAS and structural damage had to cancel each other.

The larger the relation between $SDI_{90|95}$ and SDI_{thr} the higher the false call rate, if SDI_{thr} is kept constant. An alternative to a high false call rate is the increase of SDI_{thr}. Especially, if small damages are of minor importance for the structure and therefore for the SHM system, it is possible to increase the threshold for the structural damage detection to prevent false positives. This leads to a decreased sensitivity of the SHM system for structural damage detection. Nevertheless, the probability of false calls due to defect transducers is reduced and in many cases it also reduces the probability of false calls due to changes in the structure, caused by changing EOC, purely influenced by the algorithms for structural damage detection.

Finally, it should be ensured that a structural damage has negligible influence on the damage indicator from PWAS inspection.

5.2 Performance assessment based on numerical results

To show the applicability of the method, described in section 5.1, a set of numerical simulations, realized with *COMSOL* is performed and analyzed with the use of POD. The numerical realization of a POD curve is called model-assisted probability of detection (MAPOD), as the input for the analysis is based on models, in this case numerical models.

Cracks in the PWAS can be caused by different reasons, like impacts or excessive bending of the structure. They are focused in this section. As already depicted in fig. 4.3, minor cracks do not necessarily penetrate the whole transducer, but start at one side. In these numerical simulations several cracks of different length are simulated.

The generated wave field is evaluated with several SHM methods for structural damage detection. The calculated susceptance spectrum is evaluated with the correlation coefficient based method for PWAS inspection.

A PWAS of *PIC151* material, appendix A.3, with a thickness of $h_{pwas} = 0.2$ mm and a radius of $r_{pwas} = 3$ mm is bonded on a quadratic sample with a thickness of $h_{str} = 1.3$ mm and an edge length of 200 mm with an adhesive layer of $h_{adh} = 0.12$ mm. The crack of the PWAS is modeled as a thin gap with a width of $0.04\,r_{pwas}$, starting from the radius of the PWAS in positive y direction. The crack length is varied in five equidistant intervals from $0.5\,r_{pwas}$ up to $1.5\,r_{pwas}$. Moreover as baseline the undamaged case has been modeled. For a crack length of r_{pwas} the geometrical setup of the PWAS with the crack and the adhesive layer is shown in fig. 5.1.

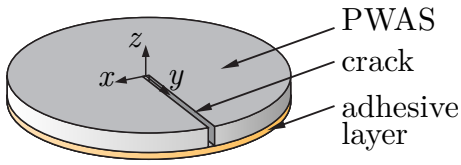

Figure 5.1: Geometrical setup of the bonded transducer and the introduced crack in relation to the global coordinate system

To introduce variability, the thickness and the diameter of the PWAS are varied with ±1% of the original value. In a full factor analysis, this leads to 54 different setups. Each setup is evaluated in the time and frequency domain to analyze the influence of a PWAS defect on the structural damage indicator SDI and the result of the PWAS inspection using the susceptance spectrum represented by DI_{CC}.

The susceptance spectrum is calculated in the frequency domain for 61 frequencies equally distributed between 200 kHz and 800 kHz. The procedure to evaluate the susceptance has already been described in section 4.4.

The changes of the generated wave field are evaluated in the time domain. Instead of modeling a second transducer and its response, the generated wave field is evaluated using the displacement in z-direction at a specified point. Four different points have been evaluated in the numerical model, located in positive and negative x- and y-direction with a distance to the PWAS center of 50 mm. A pre-study has shown that the largest differences in the displacement can be found in positive x-direction. The displacement at this evaluation point is therefore used to build the structural damage indicator. Its location, relative to the PWAS is shown in fig. 5.2. This procedure leads to a worst case evaluation of the POD curve. The displacement is evaluated for time

steps between 0 ms and 0.07 ms. As input signal a five cycle cosine tone burst with a central frequency of 130 kHz is chosen. For applications, this frequency is defined by the SHM system. This combination of evaluated time interval, structural dimensions, and central frequency leads to a displacement signal at the evaluation point, which includes the direct signal, but does not include any reflections from the edges.

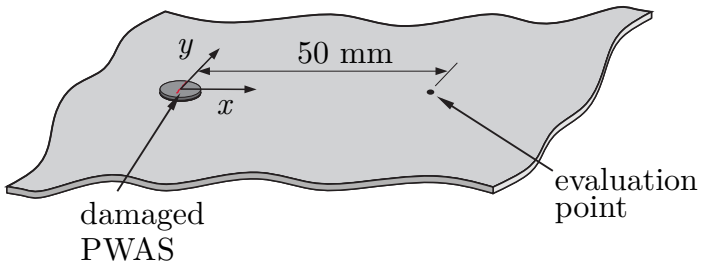

Figure 5.2: Visualization of the evaluation point for the displacement used to calculate the structural damage indicator relative to the defect PWAS

Exemplary outputs in the frequency and time domain are given in fig. 5.3. In the time domain the crack leads to a small decrease of the displacement at the evaluation point. For this exemplary defect no phase shift is visible. In the frequency domain the susceptance spectrum is changed mainly in the resonance interval. As the influence of the resonance phenomenon on the susceptance is decreasing, the susceptance slope is smaller in the second interval with constant slope. No change of the slope in the first interval is visible.

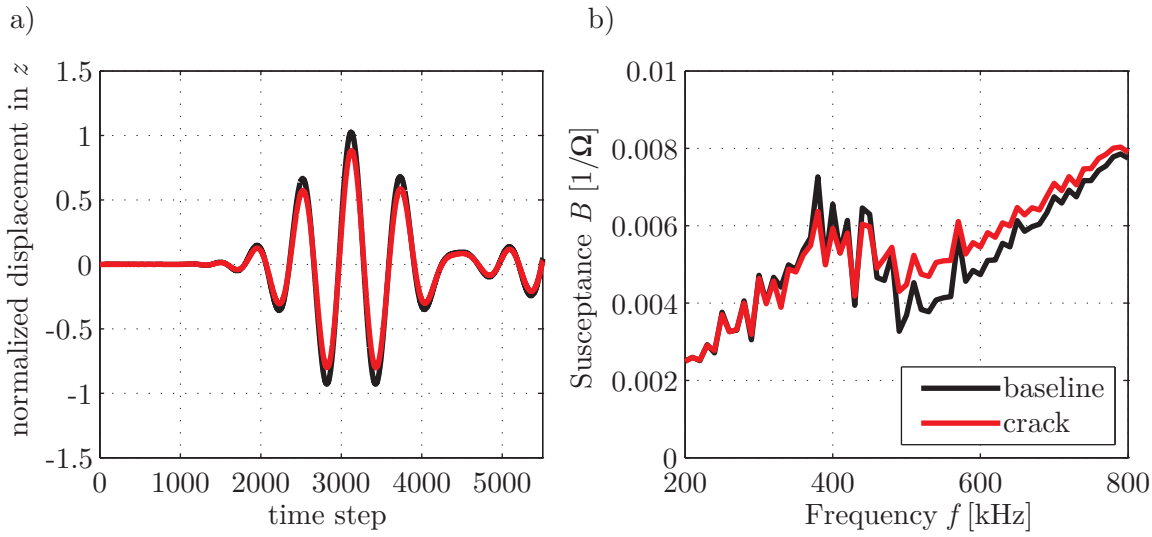

Figure 5.3: Exemplary results for the baseline and the cracked case a) of the normalized displacement in z-direction, evaluated in the time domain, b) of the susceptance spectrum, evaluated in the frequency domain.

As mentioned in section 5.1, for the evaluation of the POD it is necessary to have the threshold DI_{thr} for the PWAS inspection. For this numerical model it is not possible to model noise caused by temperature variations, humidity variations etc. in detail. Therefore, in this numerical example an alternative way to calculate DI_{thr} was used. As described above, the PWAS radius and thickness have been varied with $\pm 1\%$. This is also the case for the undamaged transducer. These nine measurements of the undamaged state have been used to calculate DI_{thr}. The susceptance spectrum of the calculation with nominal parameters is compared to the spectra of the other eight calculations with varied thickness and radius of the transducer. This results in eight values of the damage index for PWAS inspection. From these indices mean and variance are calculated assuming normal distribution. Using a false call rate of 5% this leads to a threshold of $DI_{CC,thr}$ of 0.058. The later calculations of DI_{CC} for the damaged transducers always use the baseline, which is calculated with the same PWAS diameter and thickness.

For the performance evaluation it is also necessary to know the threshold for structural damage detection SDI_{thr} and the influence of a structural damage on the damage indicator from PWAS inspection. For this reason, an exemplary structural damage of small size was modeled. Of course this damage will differ from application to application and in real applications SDI_{thr} is already given by the SHM system. To show the general procedure for this numerical example, an exemplary structural damage is used. This damage is introduced at half distance between the PWAS center and the evaluation point, see fig. 5.4. Its effects on SDI and DI_{CC} are evaluated by numerical modeling and evaluation of displacement and susceptance spectrum in time and frequency domain. The effect on SDI is interpreted as SDI_{thr}.

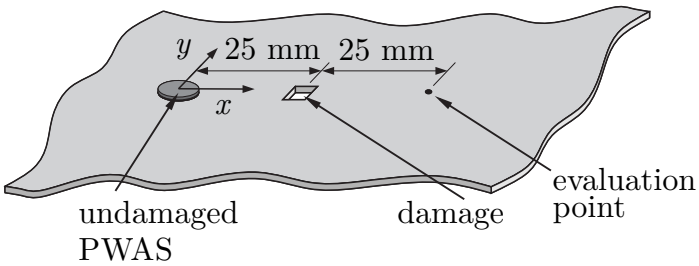

Figure 5.4: Geometrical setup of the exemplary small structural damage in the FE model

The calculated DI_{CC} and SDI are shown in fig. 5.5. All damage indices, which are based on calculations with a cracked transducer, are plotted as stars. They are assigned to their normalized crack size, which is the length of the crack divided by the PWAS

radius. The results for the calculations with a modeled structural damage cannot be assigned to a normalized crack size, as no PWAS crack is present. They are depicted as green lines over the whole range of normalized PWAS crack sizes. Moreover the calculated threshold $DI_{CC,thr}$ is also based on calculations of undamaged transducers. It is therefore also depicted as constant red line over all crack sizes in fig. 5.5a). The green line indicates the influence of structural damage on the damage indicator DI_{CC} in fig. 5.5a). It is located below the threshold $DI_{CC,thr}$. This shows that the modeled structural damage has a negligible influence on the damage indicator from PWAS inspection. Two different structural damage indicators SDI have been evaluated. The structural damage indicator, based on RMS exhibits a green line in the range of the black stars, see fig. 5.5b). This shows that the structural damage has a similar effect on SDI_{RMS} as the defects of the transducer. A different situation is shown for the second structural damage indicator SDI_{CCh}. The effect of a transducer crack on SDI_{CCh} is much smaller than the effect of the structural damage. Using fig. 5.5c) it can be assumed that the PWAS inspection method will be able to detect the crack of the transducer before it leads to an increased false call rate due to increased SDI_{CCh}. For the structural damage indicator SDI_{RMS} this conclusion cannot be drawn as structural damage and PWAS defect have a similar effect on SDI_{RMS}. Therefore, the structural damage indicator SDI_{RMS}, as the more difficult case, is analyzed in the following performance assessment procedure.

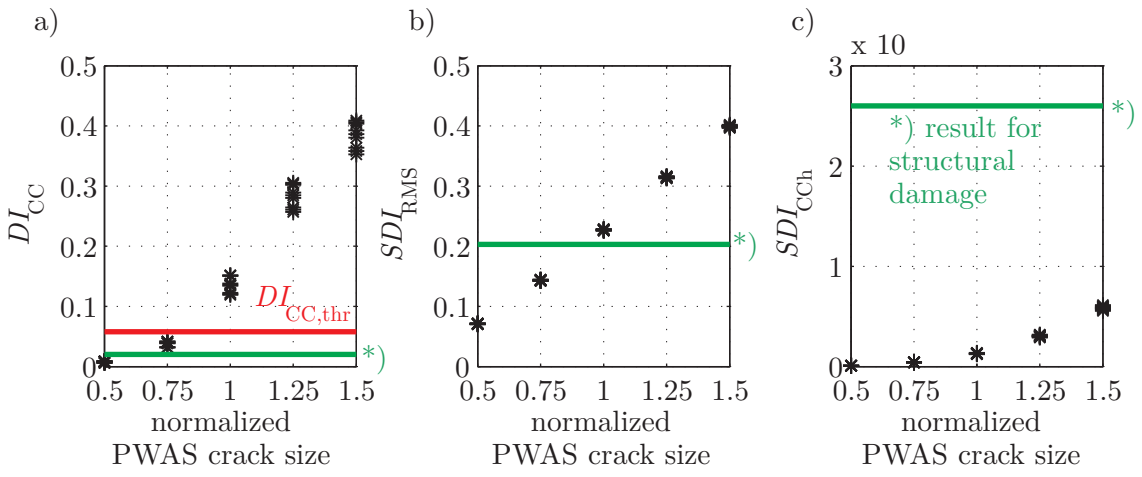

Figure 5.5: Calculated a) DI_{CC} and b) SDI_{RMS} and c) SDI_{CCh} for all FE calculations. All results for a defect transducer are plotted as stars, all results for a modeled structural damage are depicted as green lines, as they cannot be assigned to a specific PWAS crack size. The calculated threshold $DI_{CC,thr}$ is depicted as red line in a).

Using the calculated results for DI_{CC} and SDI_{RMS}, a linear relation between functions of these quantities needs to be found to be able to use the statistical procedure explained in sections 2.2 and 5.1. Fig. 5.6 shows four different possibilities for this linear relation. The linearity is represented best in fig. 5.6 d) with logarithmic scale on both axes, also exhibiting similar scattering of the data in the whole range of data. Therefore, the double logarithmic values are used for the further steps of performance assessment with MAPOD.

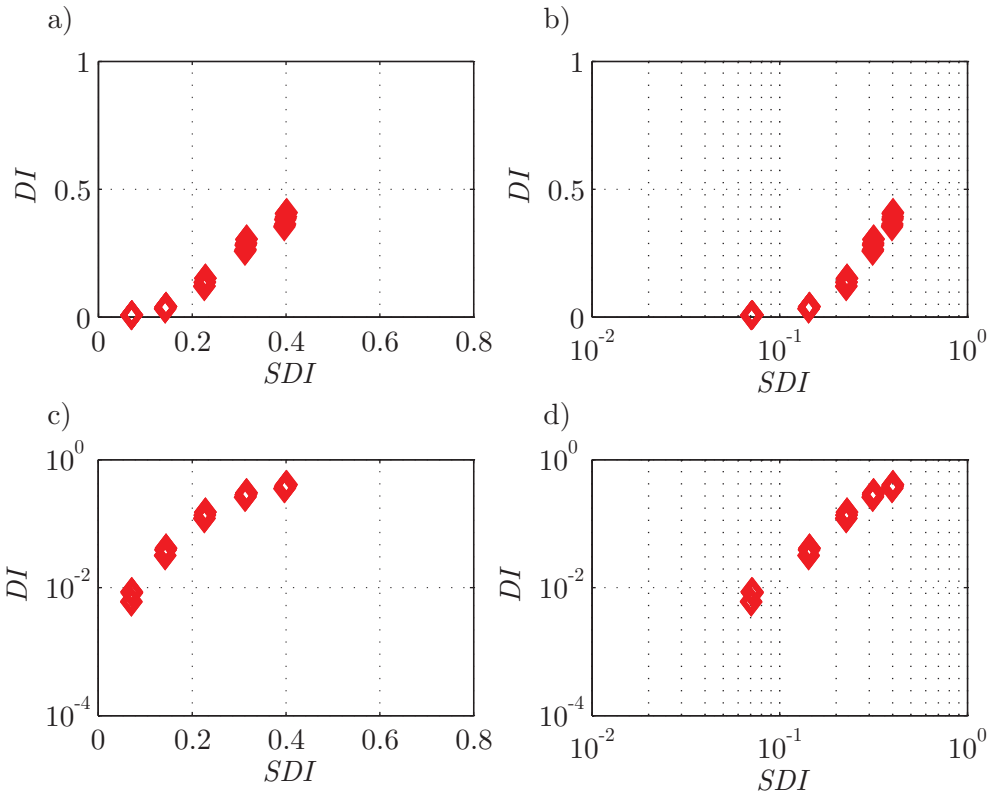

Figure 5.6: DI_{CC} vs. SDI_{RMS} on different scales, a) linear axes, b) logarithmic axis for SDI, linear axis for DI, c) linear axis for SDI, logarithmic axis for DI, d) logarithmic axes

The linear regression, the scattering around the regression line and the crossing of the regression line as well as the threshold of DI are shown in fig. 5.7. The scattering is large and cannot be neglected. For the intersection of the regression line and the threshold line, 50% of the data is above the threshold, and therefore leads to the detection of a defect transducer in the process of PWAS inspection. Additionally, in fig. 5.7 the indices for the representative small structural damage are displayed. From this plot it cannot be analyzed, if for a structural damage indicator with equivalent size, more than 90% of the data exhibits a DI_{CC} above the threshold with a confidence of 95%. For this, the calculation of the POD curve and its confidence bounds is necessary. It

shows the probability of detection, which describes, in the first place, the percentage with which a transducer is identified as faulty, when a defined level of change of the structural damage indicator SDI is reached. Figuratively it is the share of the area of the distributions in fig. 5.7, which is located above the threshold.

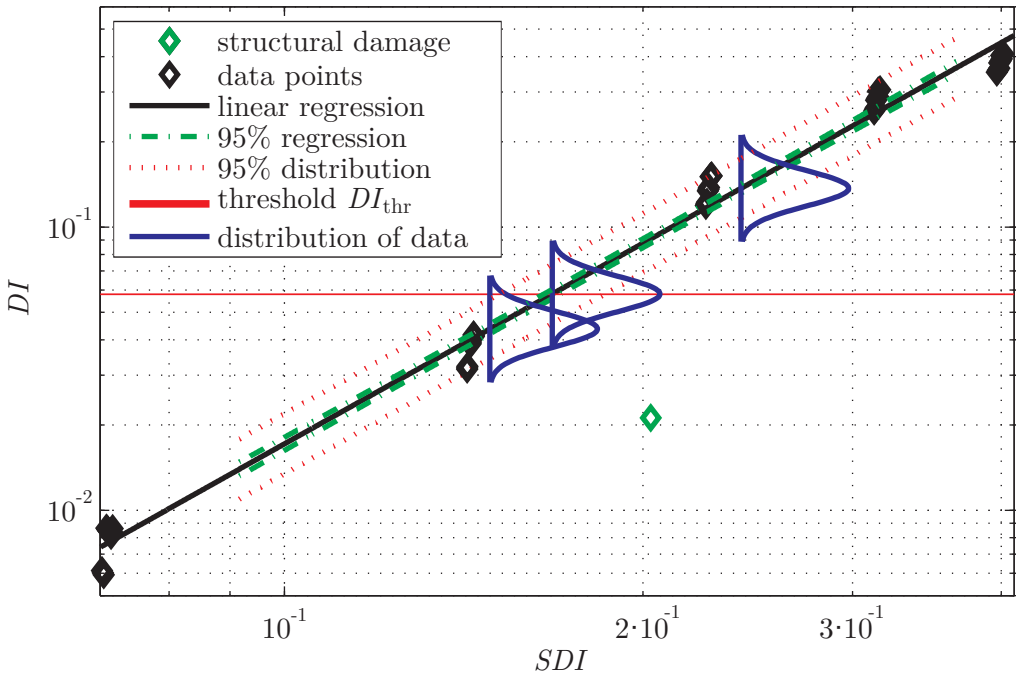

Figure 5.7: Linear regression line for the double logarithmic representation of DI and SDI, including the scattering, the threshold $DI_{CC,thr}$ as well as the calculated point for the representative structural damage

The calculation of the POD leads to a $SDI_{RMS,90|95}$ of 0.19. This value is smaller than 0.2, which is the structural damage indicator for the representative structural damage. The POD curve and the 95% confidence bound as well as the 90|95 confidence bound and the structural damage indicator for the representative structural damage are depicted in fig. 5.8.

It shows that for this combination of SHM system with structural damage indicator SDI_{RMS} and PWAS inspection with DI_{CC}, faulty transducers are detected, before they lead to false alarms due to changes of the wave field which are interpreted by the structural damage indicator as structural damages.

A novel approach to evaluate the merit of PWAS inspection methods is presented. It is based on the idea to combine the output of an inspection method with the effect of a defect on the result of the structural health monitoring system. Statistical methods of POD are used. The applicability is shown, using a numerical model to simulate the EMI spectrum as well as the generated wave field. It presents a MAPOD approach

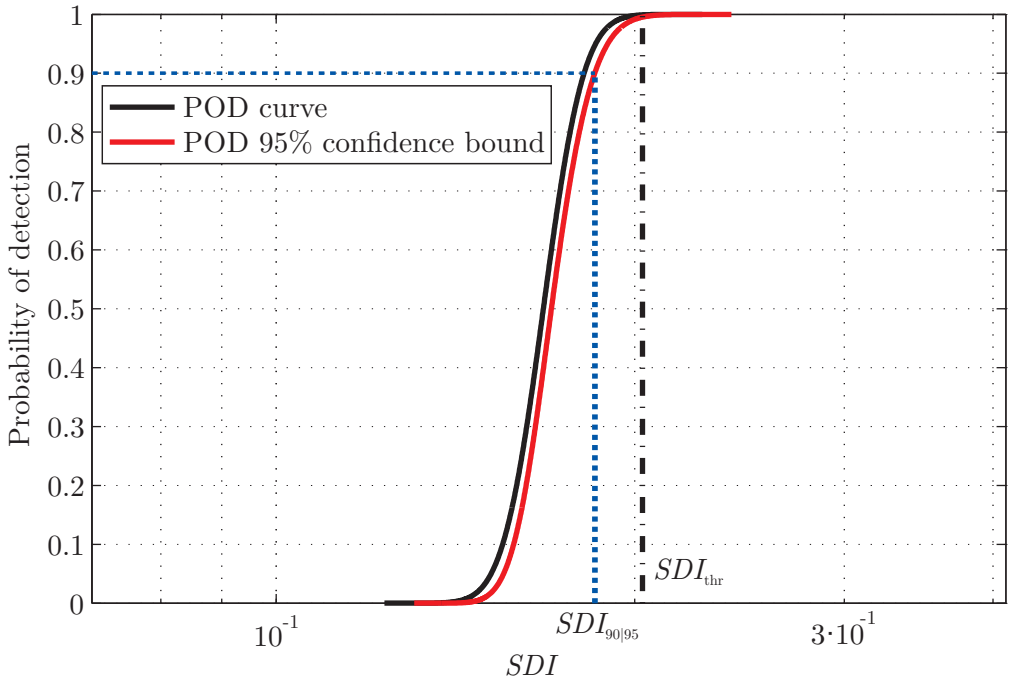

Figure 5.8: POD curve and 95% confidence bound evaluated from the numerically calculated data points.

for PWAS inspection and allows an application-based statement about the inspection method, used for a self-check. The application of this approach to experimental data as well as the application of the PWAS inspection methods, developed in section 4.5 are shown for various experimental setups in the next chapter.

6 Applications

The developed concepts of PWAS inspection and performance evaluation are tested for different defect scenarios on sample and subsystem level. The results are discussed in this chapter in detail, including additional information about the applicability for specified setups. Each section is assigned to an application. In the sections references to the different concepts are specified.

6.1 PWAS inspection under changing temperature

For piezoelectric transducers used in environments with changing temperature, the effect of changing temperature between two measurements on the PWAS inspection performance is of major interest. Two types of defects are included in this application. An embedded transducer of type *Acellent* is exposed to 130 °C for 32 hours, leading to a defect. This scenario is compared to the cut of the transducer with a width of the separated part of 1 mm. This cut is introduced after the heat exposure.

Before damaging the PWAS, 40 baseline measurements of the susceptance spectrum are taken within a temperature range from 20 °C to 85 °C. These baseline measurements are divided into two groups: Training data, consisting of 14 measurements equally distributed over the whole temperature range, and test data with 26 measurements distributed over the whole temperature range. After the heat exposure 42 measurements have been taken, with three measurements at each temperature interval, equally distributed over the temperature range. After the cut of the PWAS, the same amount of measurements at the same temperature intervals has been taken.

Fig. 6.1 shows the measured susceptance spectra for the undamaged case and both types of defects for 20 °C and 80 °C. The difference between the undamaged case and the first defect type is hardly visible. Only when a 1 : 1 direct comparison with data of the same transducer taken at equal temperature conditions is used, they can be

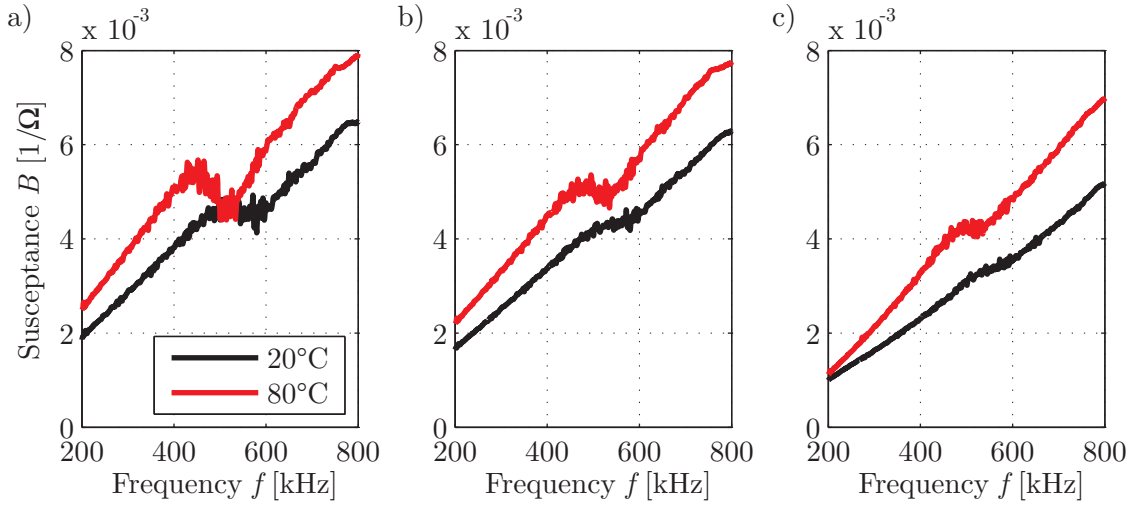

Figure 6.1: Susceptance spectra at 20 °C and 80 °C for a) undamaged case, b) defect type 1: degradation of adhesive and piezoelectric material, c) defect type 2: cut of PWAS

distinguished. Moreover a higher temperature might mask the effect of the second defect type *cut*. The difference between the measurement of the second defect type at 80 °C and the undamaged measurement at about 30 °C would not be visible in the first place. The reduction of the slope caused by the defect and the increase of the slope, caused by the elevated temperature approximately cancel each other. It is therefore necessary to find an automated method, which can distinguish a temperature change from a defect of the PWAS. These data are used to show the applicability of model-based and model-free methods.

6.1.1 Model-based PWAS inspection

First, the data of this experimental setup are evaluated with the help of the two model-based methods, explained in section 4.5.1, one including the temperature information, another one without it.

For both model-based methods it is necessary to define a parameter set p_{insp}. The second defect, introduced in this experiment, will lead to a decrease of the active piezoelectric material volume. The constant $\varphi_a = \frac{\omega}{c} r_{pwas}$ should stay constant, as the defect should not be assumed as axisymmetric. Therefore, in the calculation of the capacitance C a parameter called relative surface $A\%$ is introduced and included in p_{insp} to achieve a parameter with which the surface can be reduced without changing the PWAS radius. The first defect will lead to degradation of the piezoelectric material as well as of the adhesive layer. Therefore, d_{31} and G_{adh} are included in the parameter set p_{insp}, too. For the approach, using the measured temperature information, the

temperature T is not included. For the second approach, which is also applicable if the temperature is unknown, T is included in p_{insp}.

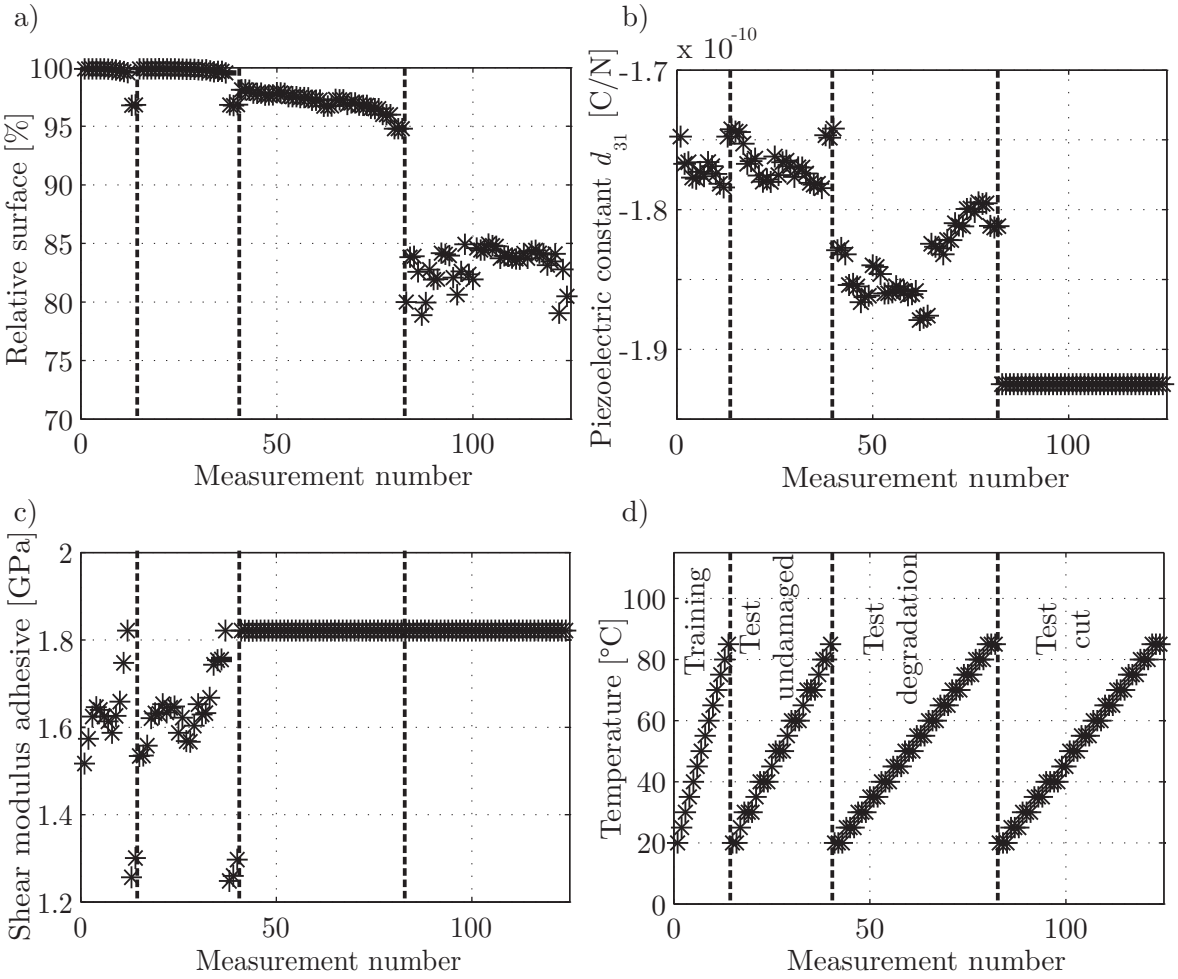

Figure 6.2: Parameters for training data and test data of the undamaged case, defect type 1: degradation of adhesive and piezoelectric material and defect type 2: cut of PWAS. a) estimated area, b) estimated piezoelectric constant d_{31}, c) estimated shear modulus of adhesive, d) measured temperature.

Fig. 6.2 shows the estimated values of the parameters in p_{insp}, as well as the measured temperature for the first approach. Fig. 6.3 shows the estimated values of the parameters in p_{insp} for the second approach, where the temperature is not known. For ease of comparison the measured temperature is included, too.

For the approach with known temperature, the relative surface is estimated almost constant for the undamaged cases, slightly reduced for degradation and reduced by approximately 18% for the cut. The variations of the relative surface over the temperature range are small, which is especially interesting for the second defect type, the cut. For almost the whole temperature range, these findings are also correct for d_{31} and G_{adh}. For measurements at temperatures above 75 °C, the estimated values of

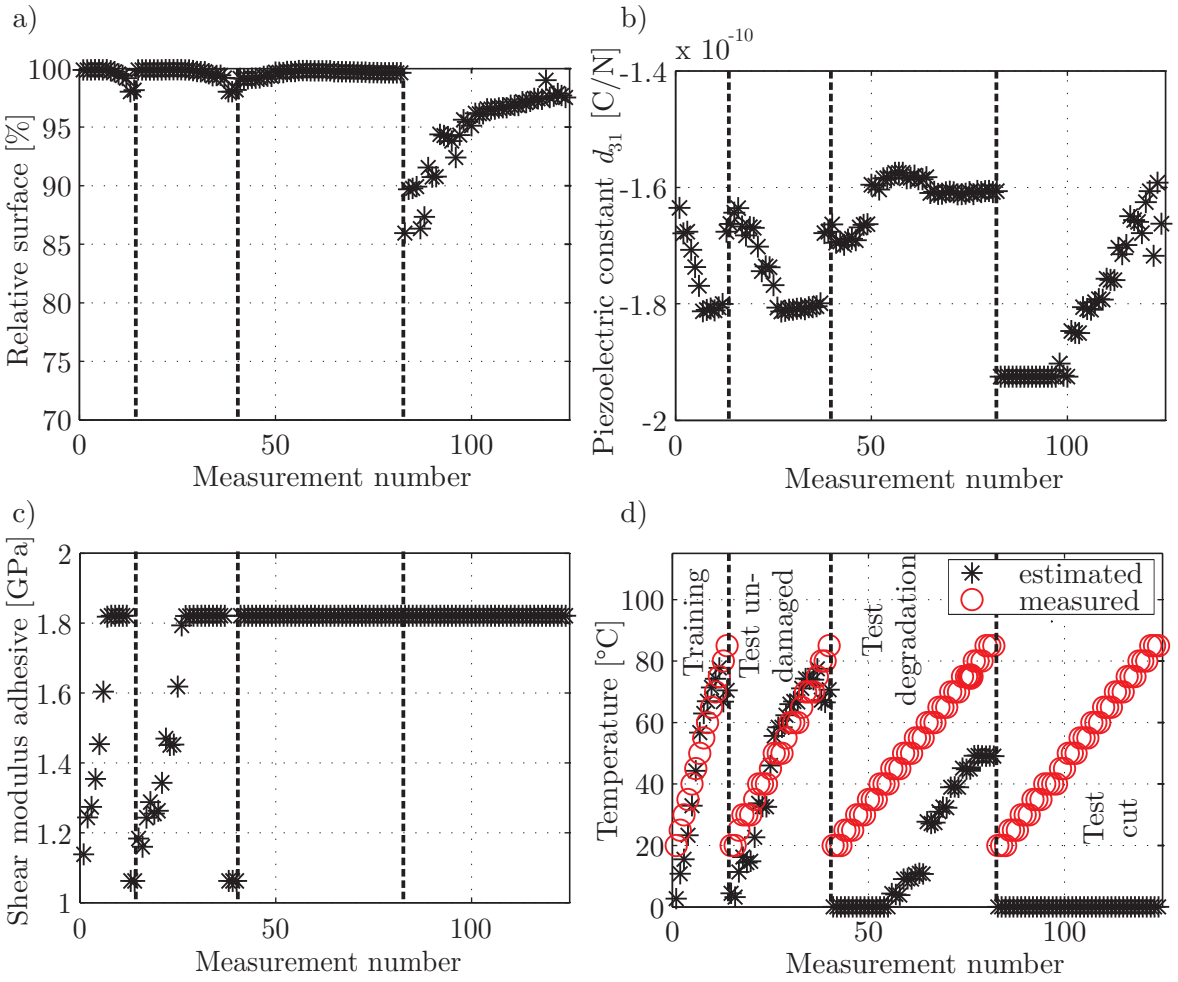

Figure 6.3: Parameters for training data and test data of the undamaged case, defect type 1: degradation of adhesive and piezoelectric material and defect type 2: cut of PWAS. a) estimated area, b) estimated piezoelectric constant d_{31}, c) estimated shear modulus of adhesive, d) measured and estimated temperature.

G_{adh} vary substantially for the undamaged case. For both defects the adhesive shear modulus is estimated to one boundary value of the possible range and therefore the values are constant. For the piezoelectric constant d_{31} only for the second defect type the boundary value is estimated leading to constant estimated values.

As the temperature is not known in the second model-based approach for PWAS inspection, the estimated parameter values show a much higher temperature dependency. This effect is visible best for the estimated values of the second defect type *cut*. The decrease of the susceptance slope leads to an underestimation of the temperature. In fact the temperature is estimated as 0 °C which is the lower boundary of the possible range of temperatures. On the other side, the relative surface is estimated larger than in the first approach, fig. 6.2 a). As both parameters have a similar effect on the susceptance slope, the optimization leads to a parameter set, which differs from

real parameters. Nevertheless, the parameter set for a defect PWAS differs from the pattern, built by parameter sets of the undamaged PWAS. This is shown in fig. 6.4 and fig. 6.5, displaying the results of the model-based PWAS inspection procedures with and without the knowledge about the temperature.

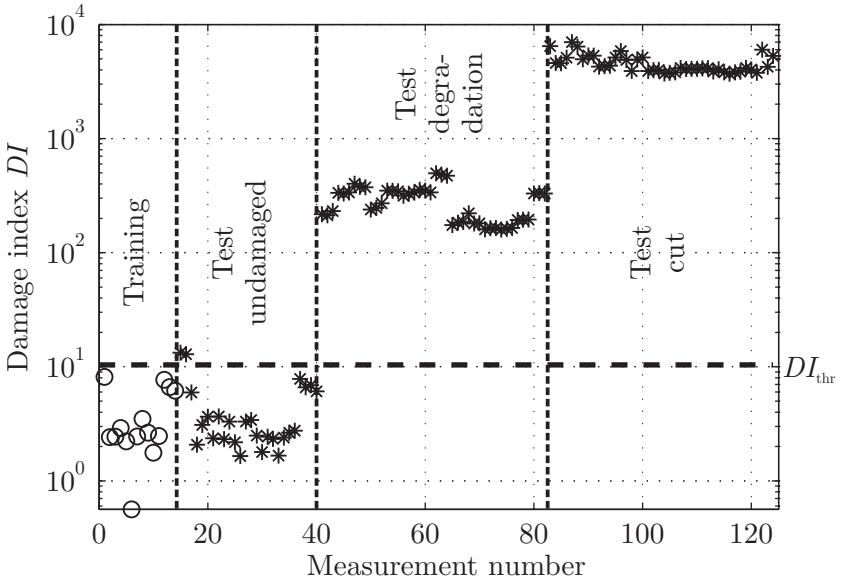

Figure 6.4: Damage indices and threshold calculated for training data and test data of the undamaged case, defect type 1: degradation of adhesive and piezoelectric material and defect type 2: cut of PWAS. The temperature was known as parameter for the estimation of G_{adh}, d_{31} and A.

For the calculation of the damage indices, using the approach with known temperature the *Mahalanobis* squared distance is based on a parameter set, which still includes the temperature although it is not estimated. This is necessary due to the high variability that is introduced into the data by the temperature influence. Both defect types are detected by this approach, see fig. 6.4. The level of the damage indices is nearly constant for both types of defects over the whole temperature range under consideration. No false negatives are present. From the undamaged test data, two damage indices slightly surpass the threshold DI_{thr}, still being much smaller than the smallest damage index of the defect types. Both defects can clearly be detected.

Both types of defects are recognized for the approach, including the estimation of temperature, as well. As shown in fig. 6.5, the damage indices are clearly above the threshold DI_{thr}. The values of the first defect type are smaller than the values of the second defect type, both tested with a constant extent. All undamaged test data result in damage indices below the threshold, marking them as undamaged. The values are smallest for medium temperature while they rise at the boundaries of the considered

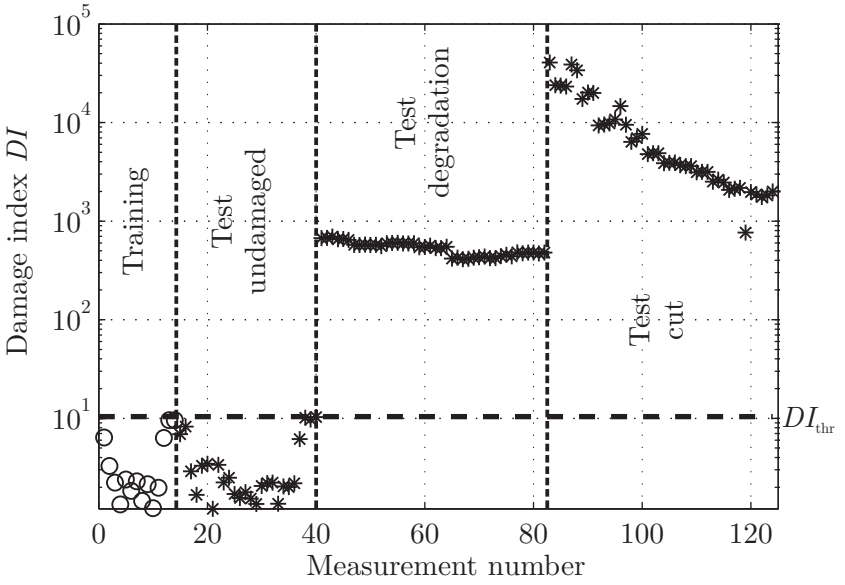

Figure 6.5: Damage indices and threshold calculated for training data and test data of the undamaged case, defect type 1: degradation of adhesive and piezoelectric material and defect type 2: cut of PWAS. The temperature was not known but estimated the same way as G_{adh}, d_{31} and A.

temperature range. Focusing on the defect type cut, a high dependency of the DI from the measurement temperature is visible. With decreasing temperature the damage indices are much higher than for the case of known temperature, for temperatures close to the upper limit of the temperature range, they are a little lower. It is important to note the logarithmic scale on the damage index axis.

Both model-based approaches for PWAS inspection show a good feasibility for the tested data set. Both defects are clearly detected, no false negative cases have been caused. For the approach with known temperature two out of 26 damage indices are slightly above the threshold DI_{thr} but very much below the value of the measurements with defect PWAS. Increasing the number of training data points (here 14) will improve this behavior. No false positives are present for the method with unknown temperature.

The procedure has been evaluated for a second PWAS, which was treated in the same way, leading to similar results, as shown above. The same data was used to show the applicability of similar procedures in (*Buethe* and *Fritzen*, 2013; *Buethe* et al., 2014b).

6.1.2 Model-free PWAS inspection

In a second analysis of the same data, a model-free approach, described in section 4.5.2 is used. From the methods described in that section, the method based on the correlation coefficient is applied, using the damage index DI_{CC}. As the method itself

does not include temperature compensation, the same set of training data, as used before, is established, including the information about the measured temperature. For each measurement from the test data, a matching measurement from the baseline data measured at similar temperature conditions is selected. The correlation coefficient is calculated from these two measurements. The test data remains as it has been defined for the model-based approaches. Fig. 6.6 shows the calculated damage indices DI_{CC} for all test data and the corresponding temperatures.

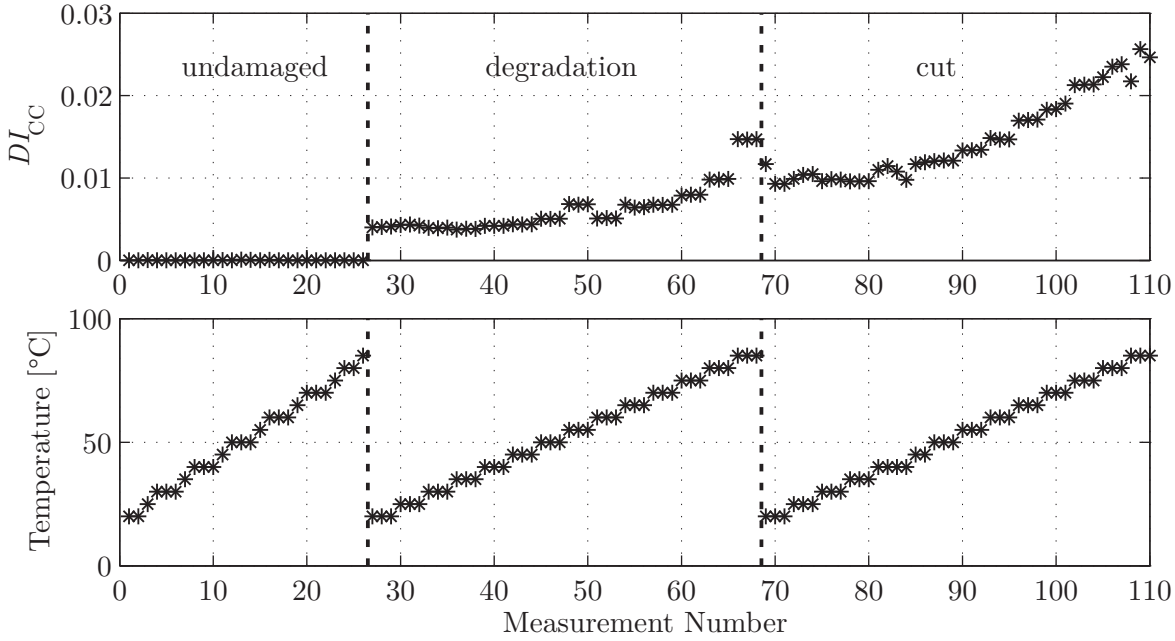

Figure 6.6: Damage indices DI_{CC} and measured temperature evaluated for the test data of the undamaged case, the data of defect type 1: Degradation of adhesive and piezoelectric material and the data of defect type 2: Cut of PWAS.

Using this model-free method, based on the correlation coefficient, all measurements of a defect PWAS result in an increased damage index. They can be clearly separated from the undamaged case for all temperatures. Compared to measurements at the same temperature, the damage indices of the second defect type are larger than the damage indices of the first defect type. For both types a temperature dependency is visible, as the damage indices rise with increasing temperature. The influence of the temperature on DI_{CC} is larger than the differences of DI_{CC} caused by the two different types of defects. The reason for this trend is based on the fact that the correlation coefficient is not sensitive to changes of the susceptance slope. As the large changes shown in fig. 6.1 are dominated by the change of the susceptance slope and these effects are not transferred to DI_{CC}, the differences of the two types of defects are smaller than for the methods shown above. Summarizing, defects are detected for all temperatures

and both types of defects, with the model-free method of PWAS inspection based on the correlation coefficient.

6.2 PWAS inspection after system setup

The use of a baseline-free method for PWAS inspection, as explained in section 4.5.3, is especially important after the setup of the SHM system. At this time hardly any baseline measurement is available. Especially if not all parameters of the bonded transducer are known, model-based methods cannot be used. For these applications, it is necessary to compare the different PWAS within a batch. In section 4.5.3 a baseline-free method, based on the correlation coefficient has been introduced. This method is applied to a data set of 16 transducers, which set up an SHM system on an aluminum structure with constant thickness. The transducers are simple piezoelectric discs with a wrap-around electrode (*PIC255*, $d = 10$ mm, $h = 0.5$ mm). They are bonded with *Z70* adhesive from *HBM*, (*HBM*, 2016). Two of the bonding locations have been slightly contaminated with wax to test if the baseline-free inspection method is able to detect these two defects. The calculated damage indices $DI_{CC,b}$ are shown in fig. 6.7, with PWAS 12 and 16 marked as defect.

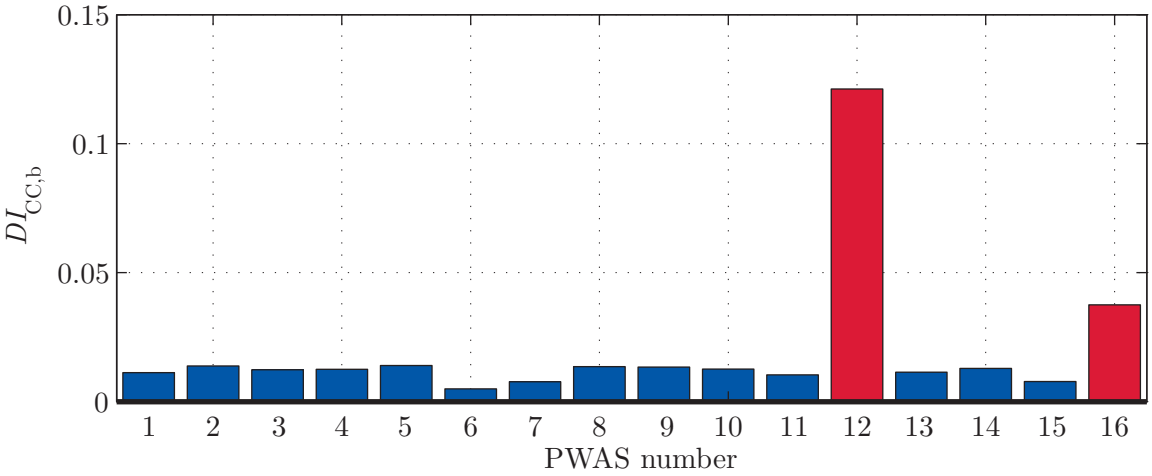

Figure 6.7: Damage indices $DI_{CC,b}$ for all 16 PWAS after SHM system setup. PWAS 12 and 16 are insufficiently bonded due to contamination with wax.

PWAS 12 and 16 exhibit much higher values than all the other transducers, which are perfectly bonded on the structure. It is therefore possible to detect faulty PWAS with this method, even if two transducers are defect. The detection of two faulty PWAS in a batch of 16 transducers is more difficult than the detection of one faulty transducer in

a batch of 8. This can be easily shown by splitting the 16 PWAS into two groups with one defect PWAS each. Compared to the results of fig. 6.7, where there is a factor of 3 between the largest damage index from the undamaged PWAS and $DI_{CC,b}$ from PWAS 16, this factor is 5 for the analysis of PWAS 16 with seven undamaged transducers. The limits of this method can be found when using a reduced set of six undamaged transducers and PWAS 12 and 16. For this set, only PWAS 12 is still detected, while the damage index is not increased for PWAS 16, compared to the damage indices of the other undamaged transducers.

6.3 PWAS breakage caused by bending loads

For applications using piezoelectric transducers on CFRP composite structures, bending loads are a major component in the load collective. As part of EU-project "smart intelligent aircraft structures" (SARISTU), the co-bonding procedure, which has been developed, was tested on sample level. In this section, the applicability of model-free methods to find the critical strain value is tested, using the indicators for model-free PWAS inspection SC, A_R and DI_{CC}, introduced in section 4.5.2. Moreover the methods are tested to see, if their damage indicators are increasing with increasing size of the defect.

As sample, a strip of multilayer CFRP with a co-bonded embedded transducer of type *DuraAct* has been used. The structure has 7 layers with setup [45/0/-45/90/-45/0/45] and is made of M21/T800 prepreg from *Hexcel*. Its dimensions are 165 mm x 20 mm x 1.3 mm. The transducer has a diameter of 6 mm and a thickness of 0.2 mm. The used piezoelectric material is *PIC255*. The samples are manufactured by *Airbus* in Bremen.

The CFRP strip is loaded in a four-point bending test. The load is slowly increased to provide a quasi-static load. The EMI spectrum is measured before the loading and in fixed strain intervals. It is recorded in an unloaded condition. The strain is measured with a strain gauge at the CFRP sample, showing the strain at the bottom of the transducer. The top layer of the transducer exhibits increased values of strain. As the design criteria are referring to the structure, the measurement position on the structure is favorable. An independent information about the PWAS state is achieved by micrographs of the PWAS. Defects like cracks are visible through the embedding *Kapton* layer, as already shown in fig. 4.3. To ensure a good image quality, the surface of the *Kapton* layer is polished before starting with the experiments. Moreover the crack

is audible. The sample is loaded until a strain of 1% is reached. The experimental setup is shown in fig. 6.8. The results for one specimen are shown here. The strain measurements have been evaluated with *Diadem*, the EMI measurements were taken with the *PZTInspector*, see the appendix A.1 and (*Fritzen* et al., 2014).

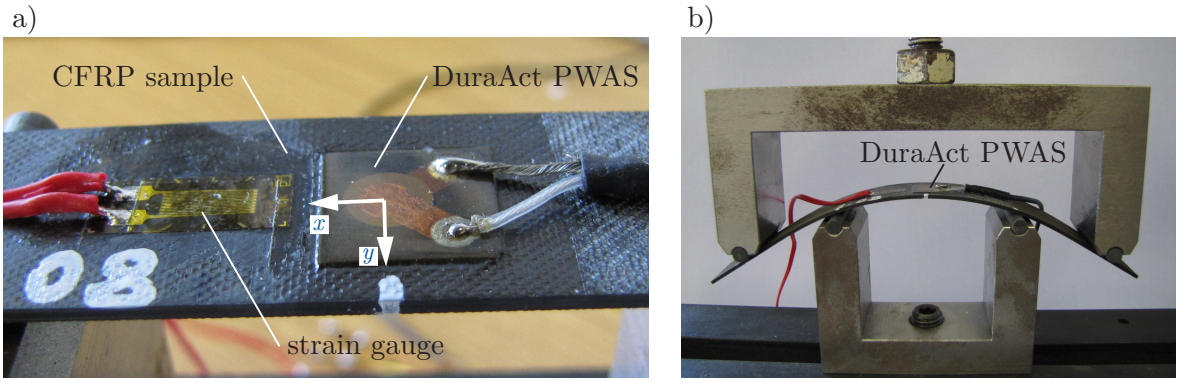

Figure 6.8: a) CFRP sample with co-bonded PWAS of type *DuraAct* and strain gauge. b) Experimental setup of four-point bending test.

For the examined sample, a first short crack is visible at a strain of 0.5%. This value is consistent with results from *Moix-Bonet* et al., see (*Moix-Bonet* et al., 2014). The resistance and the susceptance spectra, measured in unloaded condition, show deviations. With further increased load, the cracks accumulate, deviations in the susceptance and resistance spectrum increase. Fig. 6.9 shows the micrographs for two levels of the defect, fig. 6.10 shows the susceptance and resistance spectra.

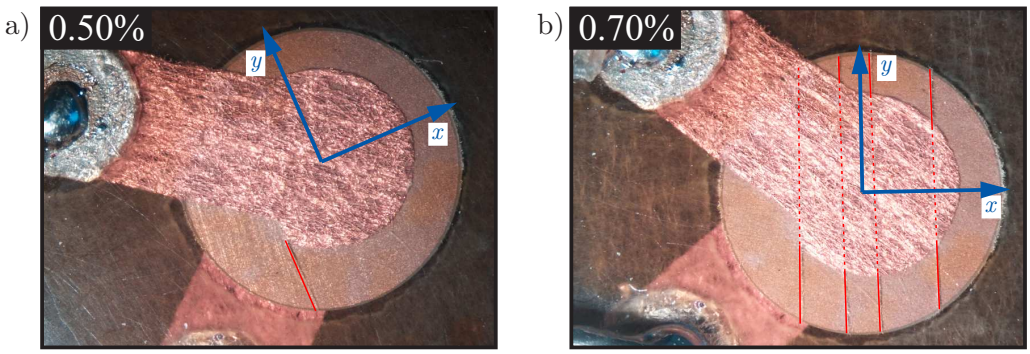

Figure 6.9: Cracks in the *DuraAct* embedded transducer after bending in a four-point bending test with strains of a) 0.5% and b) 0.7%, measured at the surface of the bending sample. The cracks can be seen though the *Kapton* layer. The orientation of the PWAS is given by the coordinate system, which is also given in fig. 6.8.

While the spectra of the defect transducers are equivalent to the spectra of the undamaged case in the lower frequency range up to 300 kHz, the resonance clearly changes. In the resistance spectrum, a shift to lower frequencies as well as a decrease in amplitude is visible. The susceptance spectrum also changes, shifting the resonance to lower

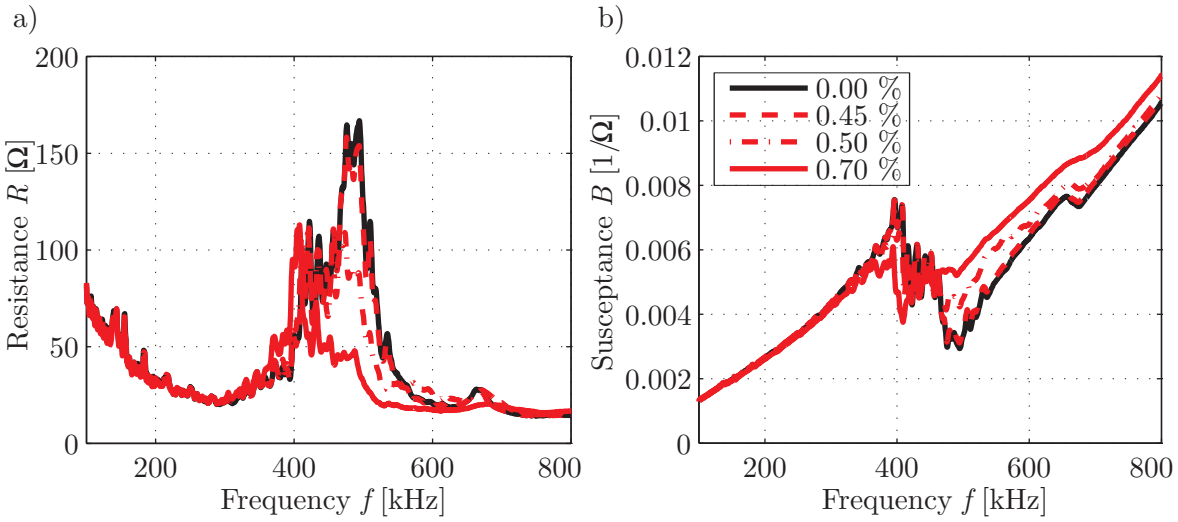

Figure 6.10: a) Resistance spectrum b) susceptance spectrum of the *DuraAct* transducer after exposure to different levels of strain. While for 0.45% no cracks have been present, first cracks occurred at a strain level of 0.5%. At 0.7% multiple cracks have been present.

frequencies and decreasing the effect of the resonance, which also leads to a change of the susceptance slope in the frequency range after the resonance.

Using this data, the model-free methods based on the slope coefficient SC, the area under the resistance spectrum A_R and the correlation coefficient based damage index DI_{CC} are evaluated, see fig. 6.11. The slope coefficient is evaluated for frequencies lower than 250 kHz, the other two methods are evaluated in a frequency range between 250 and 640 kHz. While the slope coefficient is not useful at all for this type of defect, A_R and DI_{CC} show good results. The defect state separates from the undamaged state. Additionally, a clear trend of the calculated value with an increased size of the defect is visible for A_R and DI_{CC}.

The use of DI_{CC} and A_R are therefore favorable for the PWAS inspection, especially if cracks are anticipated as possible failure mode for co-bonded embedded PWAS.

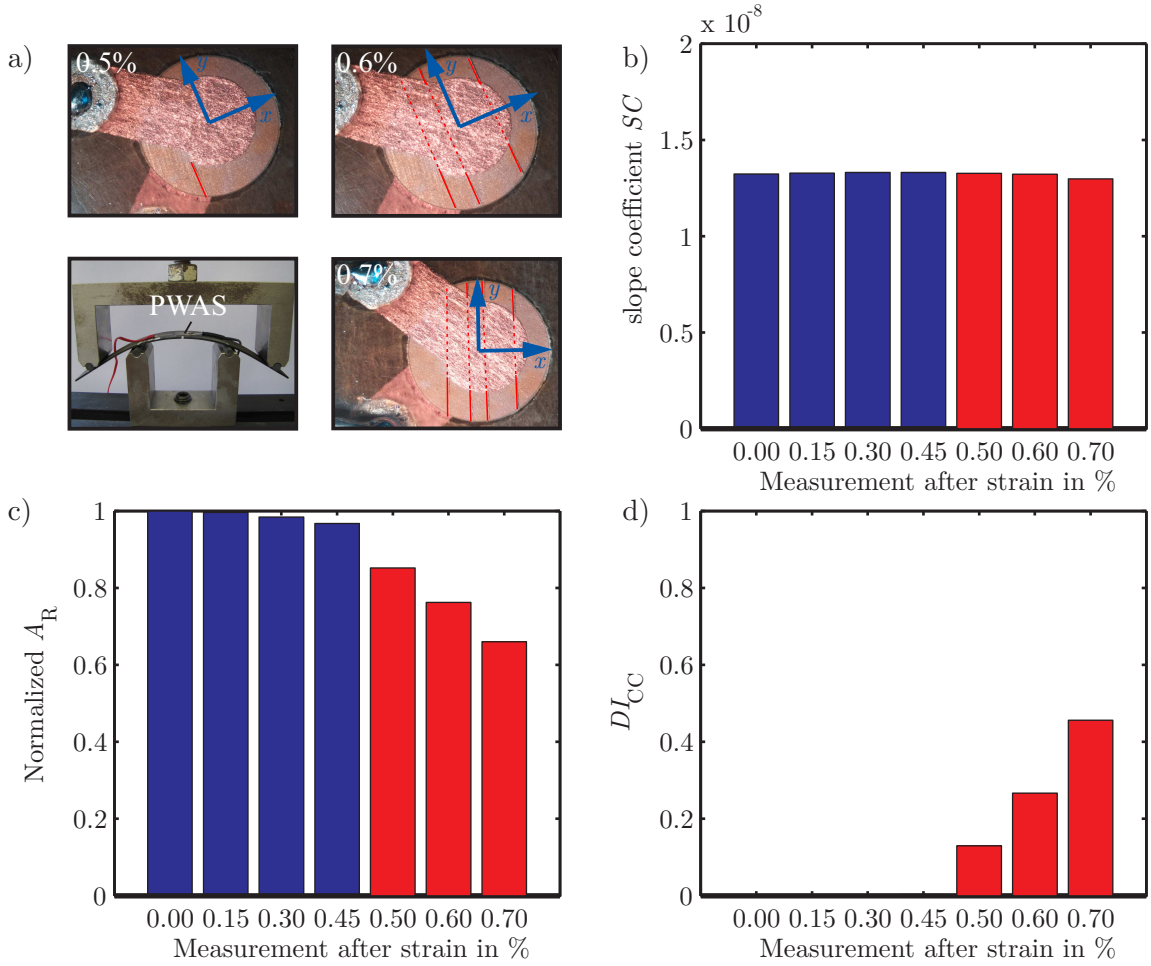

Figure 6.11: a) Visualization of the defects, caused by strain levels of 0.5%, 0.6%, and 0.7%. b) Slope coefficent SC, c) Area under the resistance spectrum A_R, d) DI_{CC}, each evaluated for measurements of four undamaged and three defect states of a co-bonded transducer on a CFRP sample.

6.4 PWAS breakage under cyclic loading

Based on quasi static experiments, similar to the experiment detailed in section 6.3, fatigue tests were conducted, using the same kind of samples, consisting of co-bonded embedded transducers on CFRP strips. The experiments have been conducted by *Airbus* in Bremen. For the fatigue tests, four groups with six samples each are build. The different groups are assigned to four strain levels, which are given in percentage of the maximum bearable strain, 35%, 47%, 58% and 70%. Here a maximum bearable strain of 0.58% = 5800 μm/m has been determined. During the tests, for every loading/unloading cycle the electrical signal was measured and plotted over the strain at the strain gauge. A shift of the electrical signal at constant strain implies a crack. This procedure has been suggested in (*Gall*, 2012), details for these measurements are given in (*Moix-Bonet* et al., 2014). It can be used perfectly for laboratory experiments, e.g.

with the aim of evaluating a $S-N$ curve from *Wöhler* fatigue tests. As constantly running measurements are necessary for this procedure, it is inappropriate for the PWAS inspection of SHM systems. For this reason the EMI spectra are recorded. The resistance and susceptance spectrum for an exemplary transducer at a strain level of 70% is shown in fig. 6.12.

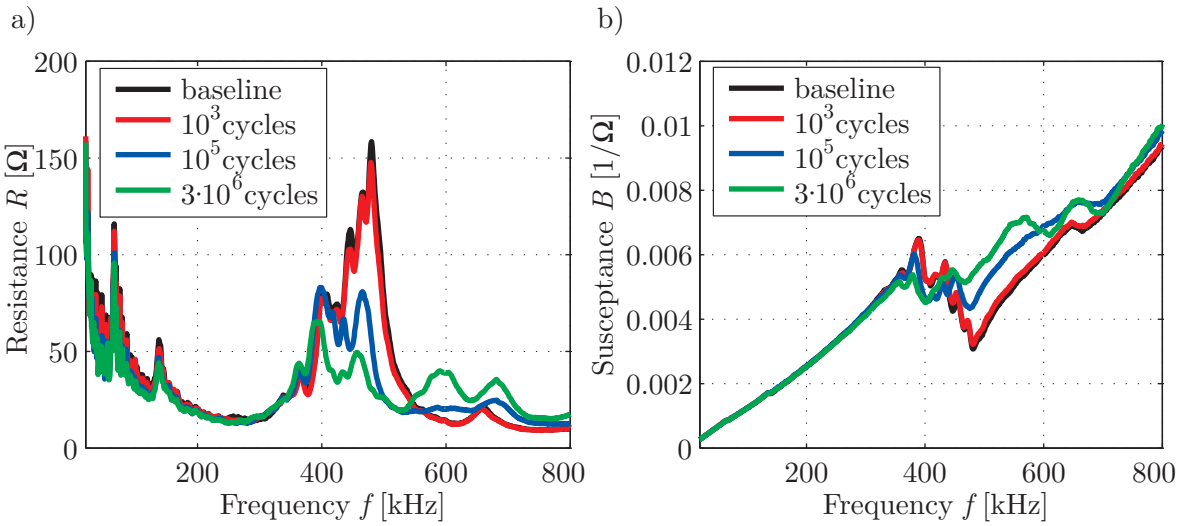

Figure 6.12: a) Resistance spectrum, b) Susceptance spectrum for an exemplary transducer under cyclic bending load.

In the resistance spectrum, a decrease of the peak is clearly visible with increasing number of load cycles. In the susceptance spectrum the resonance slightly shifts to lower frequencies and its effect on the susceptance spectrum is less pronounced. Additional resonances are visible at approximately 600 kHz. These results coincide with the results from the static loading, confirming that the same kind of defect can be assumed. The severity of the defect, here number and length of cracks, is increasing with increasing number of cycles.

In this application the changes of the EMI, expressed with A_R and DI_{CC} are focused to show that the defect caused by fatigue is detected by these model-free PWAS inspection methods. Again the frequency range from 250 to 640 kHz was evaluated. The results are shown in figs. 6.13 and 6.14.

The trend of both methods A_R and DI_{CC} is the same. While for the lowest strain level no fatigue defect is visible, two samples at the 47% level are defect. For the 58% level four PWAS are clearly defect, one sample shows minor deviations. All six samples at 70% level are clearly defect. With increasing number of load cycles, DI_{CC} is increasing, see fig. 6.13. For a very high number of cycles the damage indices reach a limit for

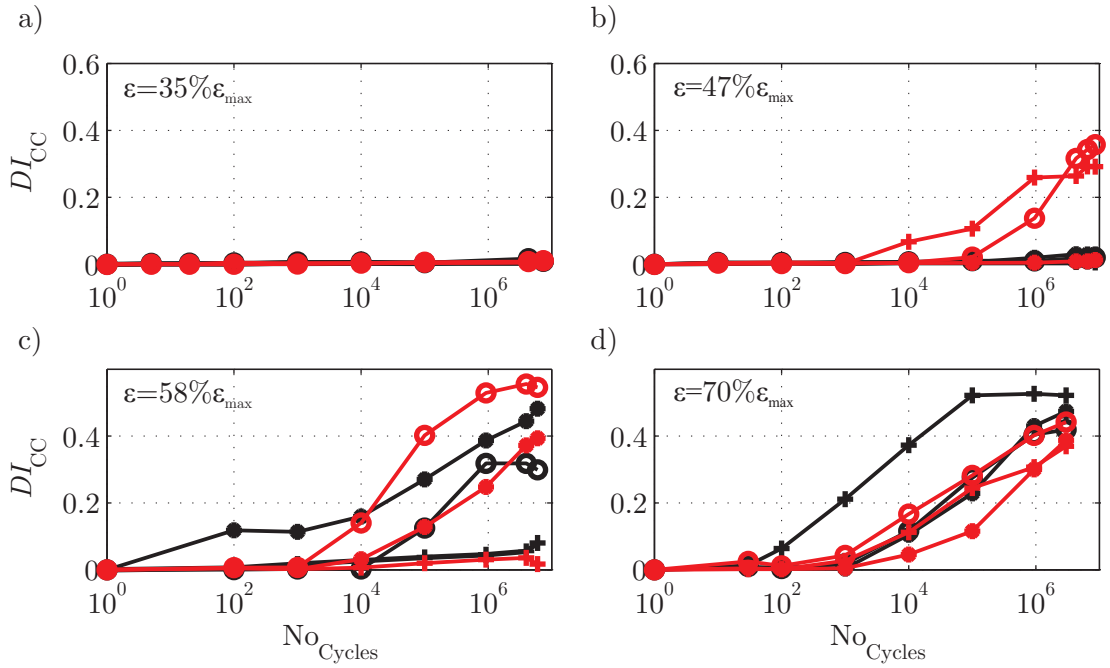

Figure 6.13: Correlation coefficient based damage indicator DI_{CC} for six samples at each of the four strain levels, which are given in percentage of the maximum bearable strain, a) 35%, b) 47%, c) 58% and d) 70%. The values are given for different numbers of load cycles until a maximum of approx. 8.5 million cycles.

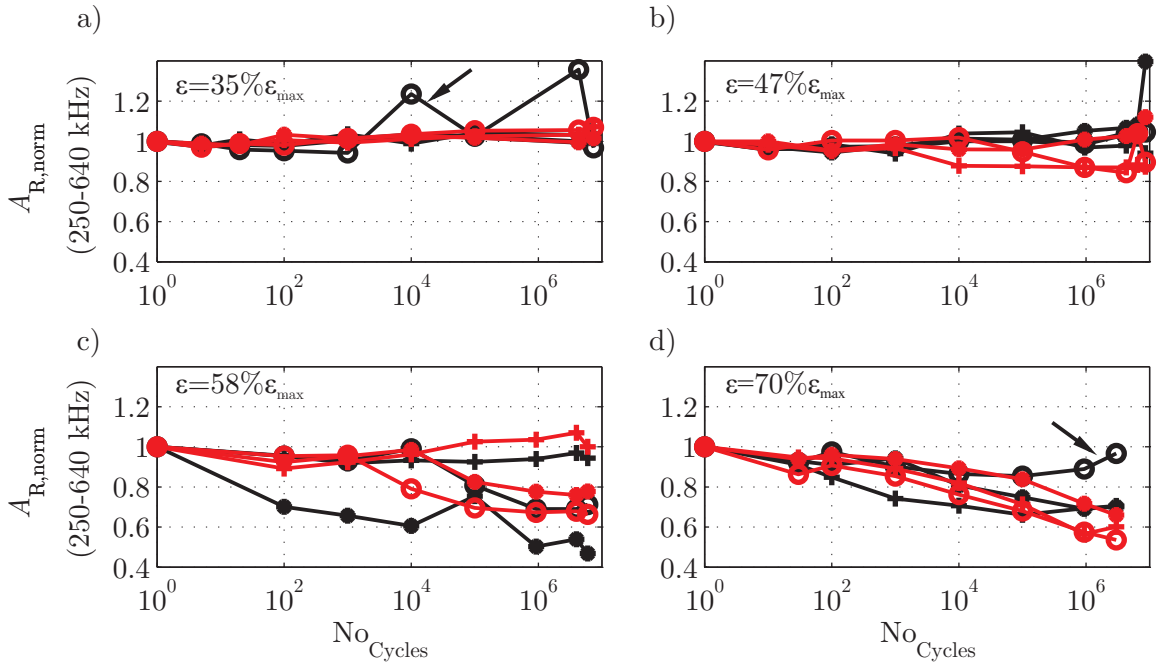

Figure 6.14: Normalized area under the resistance curve A_R for six samples at each of the four strain levels, which are given in percentage of the maximum bearable strain, a) 35%, b) 47%, c) 58% and d) 70%. The values are given for different numbers of load cycles until a maximum of approx. 8.5 mio. cycles. The resistance spectra of the two curves, marked in a) and d) are discussed in detail.

the two higher load levels, possibly due to constant size of defects. For three defect samples a small decrease of the damage indices can be found, which is much smaller

than the difference to the baseline. Compared to the results of DI_{CC}, the results from the normalized area under the susceptance spectrum A_R are slightly more obscure, see fig. 6.14. Some samples show an increased area in one measurement but return to their baseline value in a subsequent measurement. These variations can be bigger than the influence of PWAS defect. This is especially the case for one transducer at the lowest strain level, which exhibits two peaks, and one transducer at the highest strain level. Its normalized area decreased to 80% before the values begin to rise again and almost reach 1. The curves of both transducers are marked in fig. 6.14. These effects have different reasons and shall be explained, showing the resistance and susceptance spectra, see figs. 6.15 and 6.16.

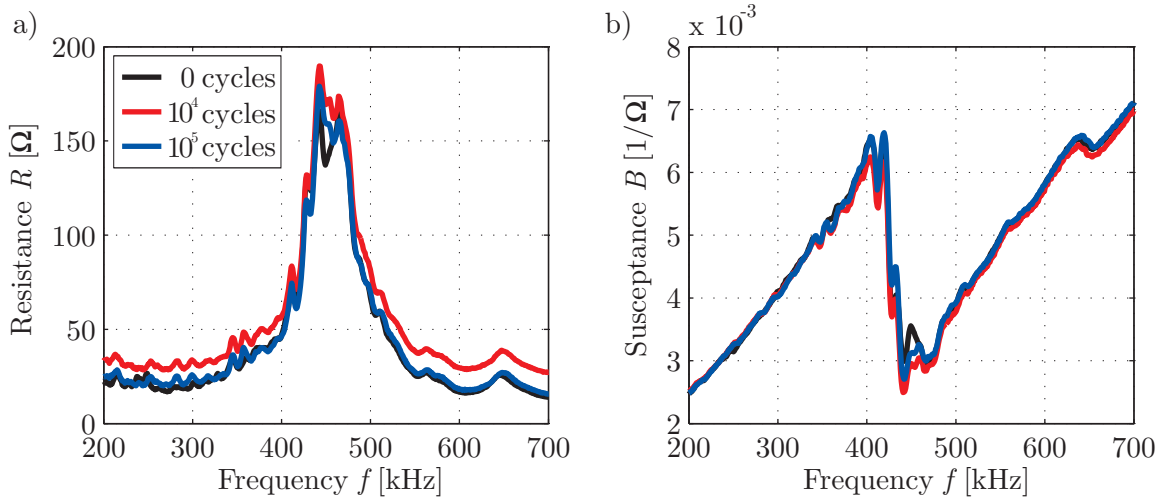

Figure 6.15: a) Resistance spectrum, b) Susceptance spectrum for the marked PWAS at 35% strain level in fig. 6.14 at specified number of cycles.

In fig. 6.15 the susceptance and resistance spectra of the baseline and measured after 10^5 cycles are very similar. This is also the case after 10^4 cycles for the susceptance, but the amplitude of the resistance spectrum is increased. It seems like in this measurement an additional *Ohm*ic resistance is added to the measurement. Although this also has a small decreasing effect on the susceptance spectrum, DI_{CC} is less influenced than A_R. The susceptance spectrum is therefore independent of the number of cycles while being sensitive to defects of the PWAS.

In fig. 6.16 another effect is shown. The further increase of the defect size leads to a shift of the resonance. This effect has been observed in other experiments if e.g. for spalling. Calculating the area under the resistance curve now leads to a larger value due to a new resonance in the used frequency spectrum. It might be assumed that due to the fatigue loading, first a crack developed and afterwards two or more parts

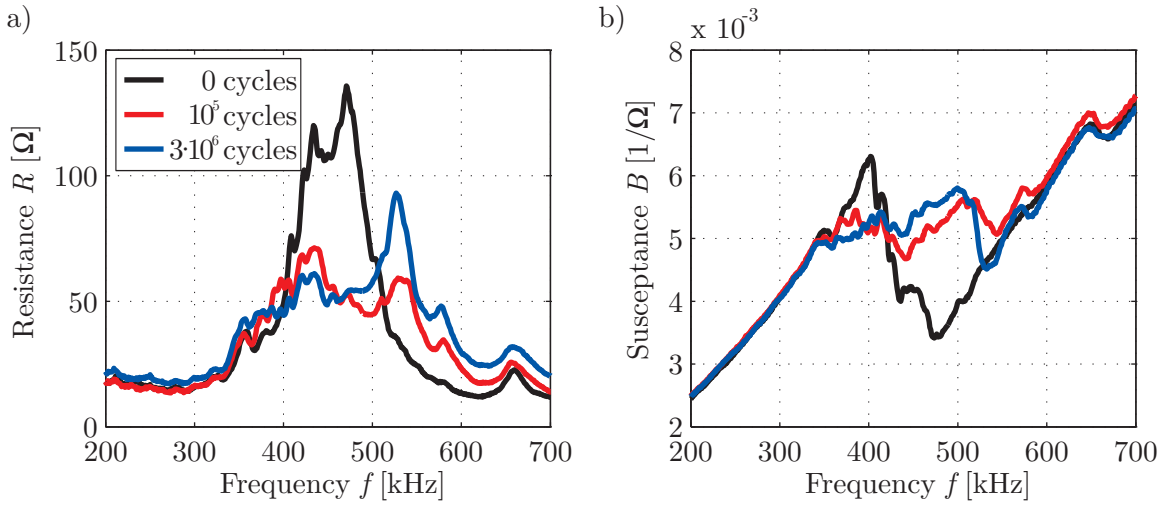

Figure 6.16: a) Resistance spectrum, b) Susceptance spectrum for the marked PWAS at 70% strain level in fig. 6.14 at the specified number of cycles.

of the PWAS slightly changed their location, leading to this effect. This is a further development of the defect size which is misinterpreted by using A_R. Nevertheless, the PWAS would have been labeled as defect many cycles ago. Manual evaluation of the resistance spectrum leads to the same conclusions as the automated evaluation of DI_{CC}. Alternative ways of using the resistance spectrum automatically as well as additional steps of data filtering might improve the results of A_R.

The results of DI_{CC} are consistent with final checks via micrographs of all samples, which have been made at *Airbus* by *M. Moix-Bonet*. The single transducer at 58% level, which only showed minor deviations with DI_{CC} exhibits a single non-central crack, which is shorter, compared to the central cracks of all other transducers, clearly separated as defect. It is assumed that this transducer can still be used for SHM. For the sake of completeness also the slope coefficient SC has been analyzed for this data. Only one transducer from the group with 70% of the maximum bearable strain can be clearly separated and identified as defect. The results are not shown in detail here, see (*Buethe* et al., 2014a). This type of transducer defect cannot be recognized with the help of the slope coefficient. Nevertheless, SC is sensitive for many other types of defects, especially if spalling is detached from the PWAS.

6.5 Detection of debonding

The inspection of debonded transducers is especially interesting for those applications, which combine a very hard transducer with a comparably flexible structure. For com-

binations like these, the bonding layer might fail and debond the PWAS from the structure. Parts of the transducer are not connected to the structure anymore and energy transfer in both directions is limited to the remaining bonded area. The general effects of debonding on the generated wave field have already been discussed in section 3.3, a glimpse on the effects on the susceptance spectrum is given in section 4.1. This application gives a detailed insight of the effects of debonding on the susceptance and compares two possible methods of PWAS inspection. In particular the slope coefficient SC and the correlation coefficient-based damage index DI_{CC} are compared. Afterwards the performance of DI_{CC} is evaluated in detail using the method, established in chapter 5.

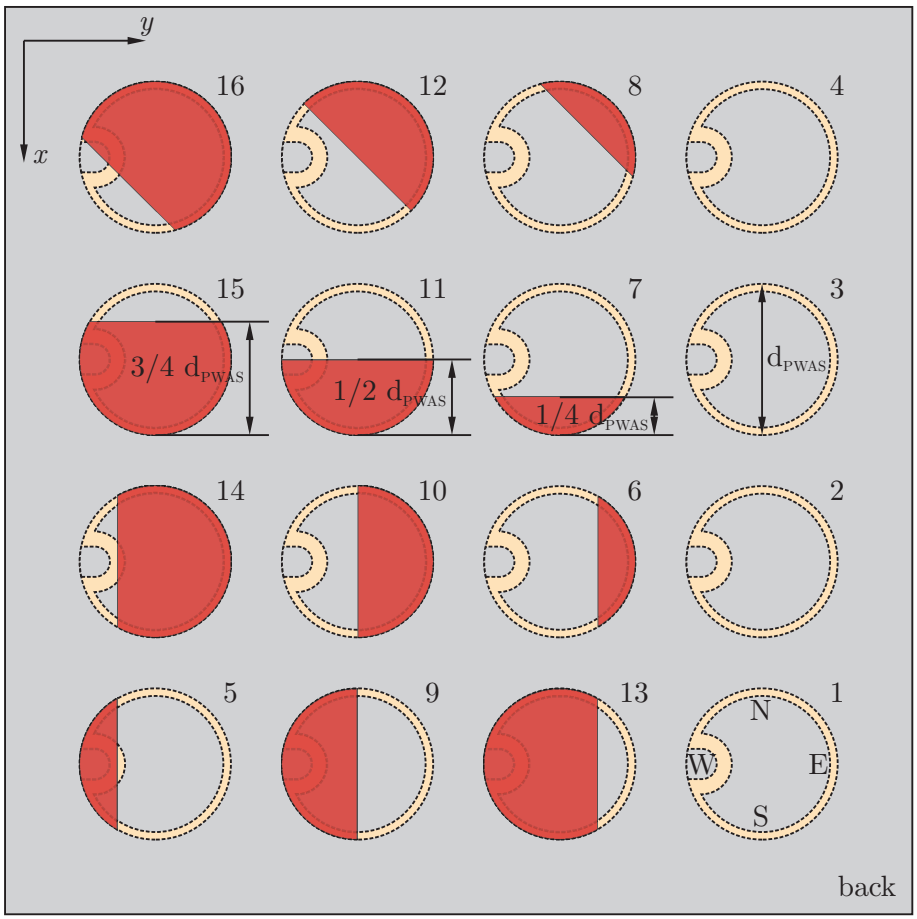

Figure 6.17: Sketch of the experimental setup, focusing the orientation of the wrap-around electrode and the debonded area, marked in red, of 16 PWAS, not proportional.

The experimental setup is shown in fig. 6.17 and is detailed in (*Golub* et al., 2014).

16 simple disc-shaped transducers of type *PIC151* are bonded on an aluminum plate with size 500 mm × 550 mm and thickness 2 mm. The transducers have a thickness of 0.25 mm and a diameter of 10 mm. Four transducers are fully bonded (PWAS 1-4), all other transducers show partial debonding. The debonding is caused by the

use of teflon foil, which prevents the adhesive layer to fully cover the PWAS-structure interface. The foil is removed after the bonding process is finished. Four partially debonded PWAS exhibit a debonded area of approx. 20%, which is consistent with a width of the debonded area of 1/4 of the diameter (PWAS 5-8). Four transducers are 50% debonded (PWAS 9-12) and four transducers are 80% debonded (PWAS 13-16). The orientation of the debonded area in relation to the location of the wrap-around electrode has been changed. The location of the wrap-around electrode is in the west W, also the other orientations are given with cardinal points, see PWAS 1 in fig. 6.17.

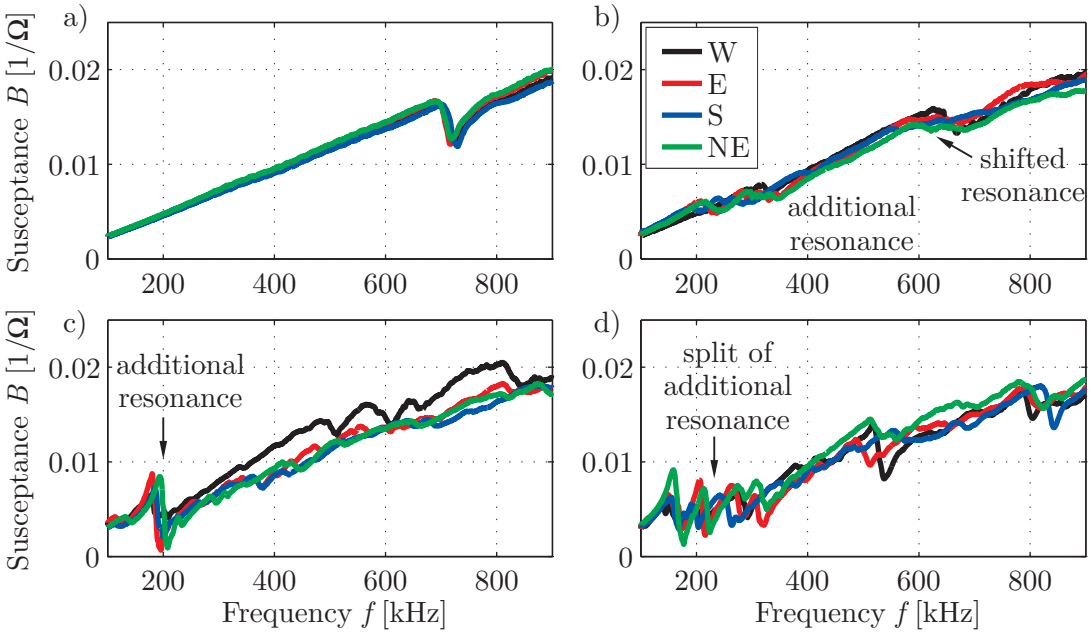

Figure 6.18: Susceptance spectra of all PWAS of the experimental setup, shown in fig. 6.17. The orientation of the debonding is given with cardinal points, as indicated on PWAS 1 in fig. 6.17. a) Spectra of the undamaged PWAS 1-4, b) 25% of diameter debonded, c) 50% of diameter debonded, d) 75% of diameter debonded.

The measured susceptance spectra for the four different stages, undamaged, 20%, 50%, and 80% debonded area are depicted in fig. 6.18. The measurements are recorded at ambient temperature. For the debonded PWAS, an additional resonance can be found between 200 kHz and 350 kHz. Its characteristics are more pronounced with increasing debonding. A shift of the original resonance towards lower frequencies is visible and its features are less pronounced. For the highest debonding rate the new resonance is split into several similar frequencies. With increasing debonding size the trend of a higher slope in the low frequency range up to 150 kHz can be recognized, although a regression line over the whole frequency range from 100 kHz to 900 kHz will lead to similar results for the debonded and undamaged case.

In fig. 6.19 and fig. 6.20 the evaluation of the slope coefficient SC and the correlation coefficient-based damage index DI_{CC} are shown for five measurements of each transducer. All measurements are taken at ambient temperature.

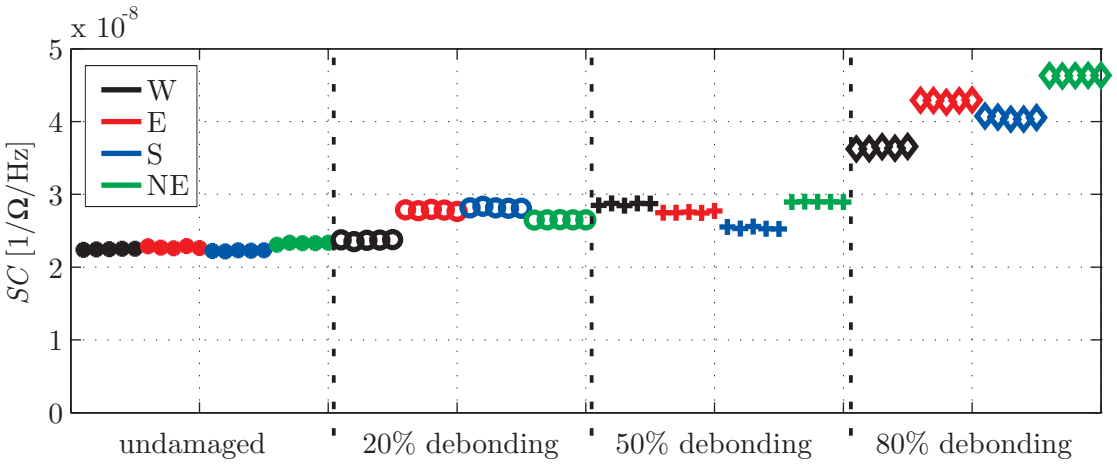

Figure 6.19: Evaluation of the susceptance slope for all transducers with five measurements at each transducer. The different stages of the debonding are marked on the x-axis, the color coding marks the different orientation of the debonded area in relation to the wrap-around electrode.

As the debonding is introduced during the bonding process, no baseline measurement from exactly the same transducer is available. It is therefore necessary to use the baseline from another transducer. For the calculated susceptance slope coefficient SC, given in fig. 6.19, no normalization is used. The slope coefficient is evaluated in a frequency range from 40 kHz to 150 kHz. The values can be compared to the first values from the fully bonded transducers. All debonded transducers show an increase of the susceptance slope. Depending on the orientation of the debonded area the differences to the undamaged state are quite small - factor 1.06 for the smallest value of a defect transducer. The highest debonding rate can be clearly separated from the undamaged state, exhibiting a significantly increased slope coefficient.

Contrary to the evaluation of the susceptance slope coefficient SC, DI_{CC} cannot be calculated without a baseline measurement. As no baseline measurement from exactly the same transducer is possible, PWAS 1 was used as baseline for all transducers. This is possible, as all transducers ought to be the same and are bonded to the same continuous structure at comparable places using the same procedure. Nevertheless, this introduces some error and reduces the sensitivity of this method. The value of the damage index DI_{CC} for the other undamaged transducers gives an estimate of the error that is introduced to the calculation of DI_{CC} by this use of a baseline from another

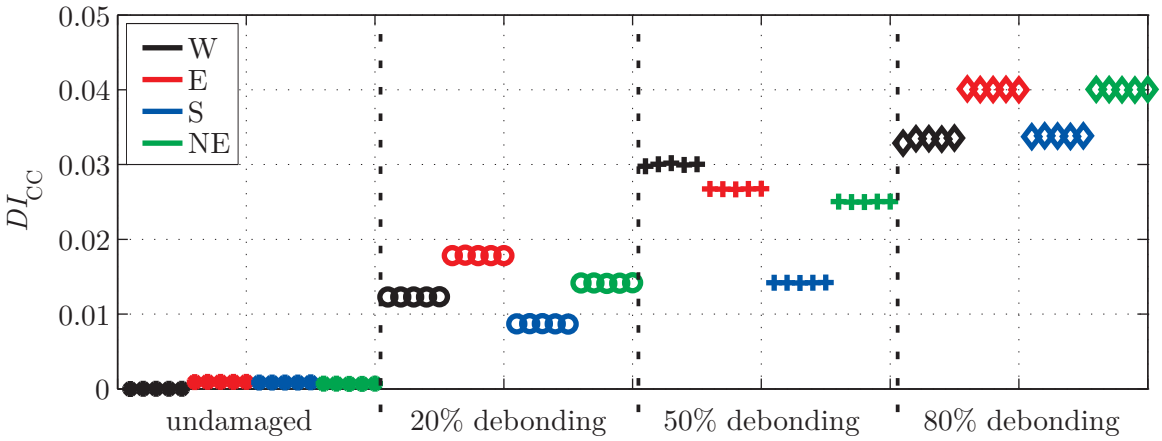

Figure 6.20: Evaluation of DI_{CC} for all transducers with five measurements at each transducer. The different stages of debonding are marked on the x-axis, the color coding marks the different orientation of the debonded area in relation to the wrap-around electrode.

transducer. These differences are caused by minor changes of material and geometric parameters of the bonded transducers.

All debonded transducers show an increased damage index DI_{CC}, which can be clearly separated from the undamaged state, see fig. 6.20. The calculated damage indices for the fully bonded transducers are much smaller than the smallest damage index of a bonded transducer, approx. by factor 10. The different orientations of the debonding lead to different levels of the damage index. NE and E are not located very close to the wrap-around electrode. Both show similar results and their damage indices are higher than those of W and S. An exception is the 50% debonding west, which shows higher damage indices than the other three locations for this state.

For the inspection of PWAS to find debonded transducers, DI_{CC} has proven to be feasible. Its performance and possible conditions for an SHM system for structural damage detection shall be evaluated, using the procedure described in chapter 5.

As damage indicator for PWAS inspection DI_{CC} is chosen, as structural damage indicator SDI, the deviation of baseline and new measurement evaluated with RMS has been chosen. An actuation frequency of 60 kHz is assumed. Contrary to the introduced procedure to calculate DI_{CC} and SDI_{RMS}, as discussed previously, for this application no baseline measurements from the same transducer are available. Therefore, all measurements are compared to PWAS 1, which is an undamaged transducer, fully bonded to the structure. This adaptation of the procedures introduces additional scattering and noise in the data, which has to be taken into account in the evaluation.

For the calculation of SDI_{RMS}, no sensor data of neighboring, fully bonded transducers is available in this experimental setup. Similar to the procedure used in section 5.2, the generated wave field itself is used. At a distance of 20 mm to the center of the PWAS, the velocity perpendicular to the surface of the structure is measured at 18 points at the circumference with a LDV. The measured velocity is used to calculate SDI_{RMS}. Only the first wave package is used, which does not include any reflections from boundaries. This reduction of signal length is necessary as in this experimental setup, the transducers have different distances to the edges of the plate and therefore exhibit different patterns of reflection. The first wave package signal is compared at every point at the circumference to the signal of the equivalent point from PWAS 1. From this comparison SDI_{RMS} is calculated. Following this procedure, 18 different values of SDI_{RMS} are generated for each transducer.

The values are depicted in polar plots for all debonded transducers in fig. 6.21. The values of SDI_{RMS} show a high angular depencency. The pattern consists of two main lobes resulting in a peanut-like shape. This pattern is oriented according to the location of the debonding. All transducers with a debonding rate of 20% are depicted with a maximum structural damage index of 0.5, 50% with a maximum of 2 and 80% debonding with a maximum of 5, to show the similar pattern for all defect sizes. Compared to the other cases with 20% debonding, SDI_{RMS} is very small for the case of debonding directly under the wrap-around electrode. The pattern of SDI_{RMS} is oriented with its main axis from north to south $N - S$, if the debonding is located in the south. This statement can be adopted accordingly for all other debonding orientations.

The calculation of DI_{CC} for the inspection of PWAS is transferred from the calculations above, see fig. 6.20 using only one measurement for each transducer. This results in one value of DI_{CC} for each transducer. PWAS 1 is again used as reference.

In the first step of the procedure to evaluate the performance, described in section 5.1, a linear relationship of DI and SDI is realized. As shown in figs. 6.21 and 6.22, the variation of SDI_{RMS} is comparably large at the circumference of a transducer. For each transducer the median value of SDI_{RMS} is marked to show the trend of increasing DI_{CC} with increasing SDI_{RMS}. A linear trend can be approximated with logarithmic scale on SDI_{RMS}.

The resulting linear regression is shown in fig. 6.23. It is based on all data points. An alternative solution is the use of median values or maximum values for each transducer.

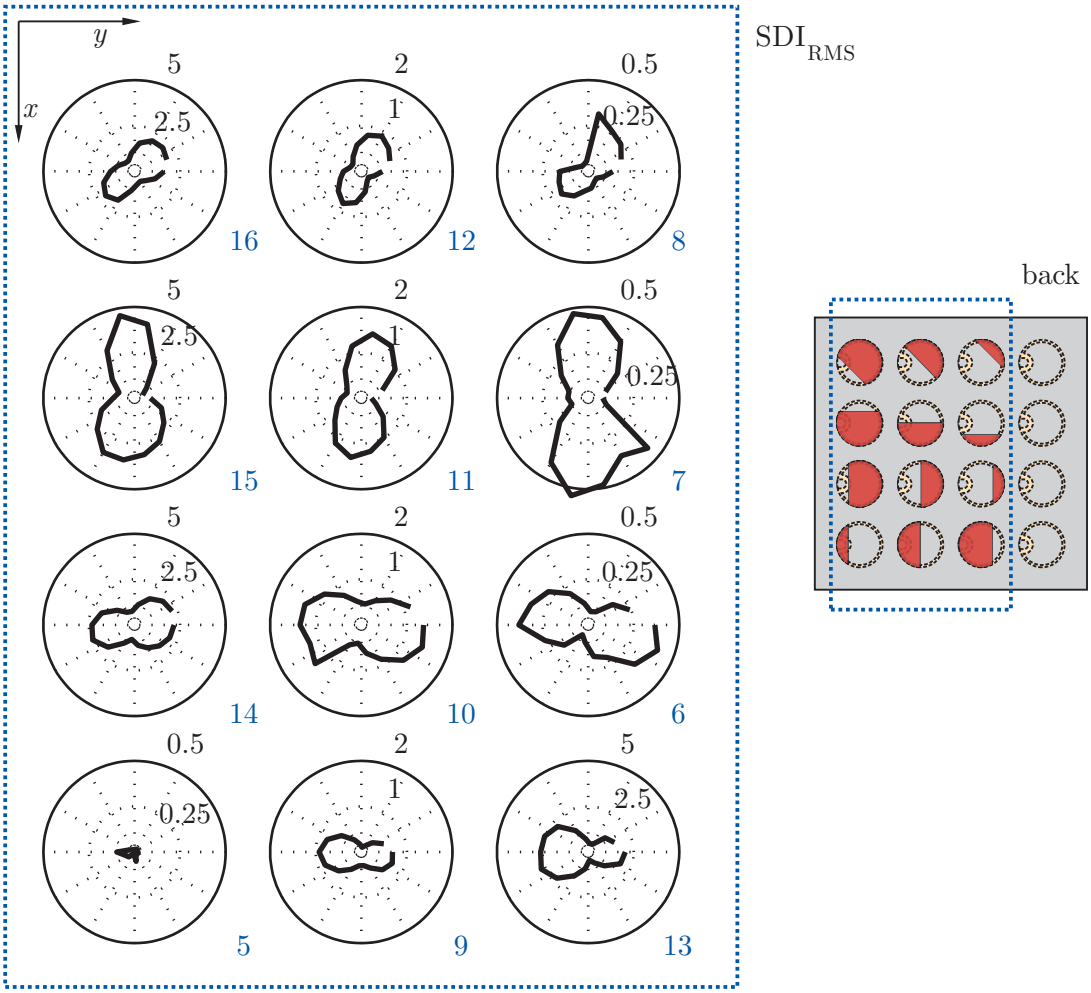

Figure 6.21: Structural damage indices SDI_{RMS} for all debonded transducers given in polar plots. For each PWAS 18 values of SDI_{RMS} are given at the circumference. Its values are highly angular dependent, caused by the direction of the debonding and the location of the wrap-around electrode. The direction of debonding and the location of the wrap-around electrode are depicted in the small sketch on the right. For the different levels of debonding, three different maximum values are defined for the polar plots.

This leads to more conservative results, which are based on a smaller amount of data, as only 12 instead of 216 points are used to build the regression. In any way the variance of the data around the regression line is very high, which is visualized by the blue *Gauss*ian distributions.

From the linear regression the POD for defects, which have a certain effect on the structural damage detection SDI, can be calculated. For this the threshold DI_{CC} has to be defined. In this application example, the DI_{CC} of PWAS 2-4 have also been calculated and used as an indicator for the value of the threshold. The POD curve and its 95% confidence interval are given in fig. 6.24. A POD of 90% with a confidence of 95% is reached at an SDI of approximately $SDI_{90|95} = 0.1$. For an SHM

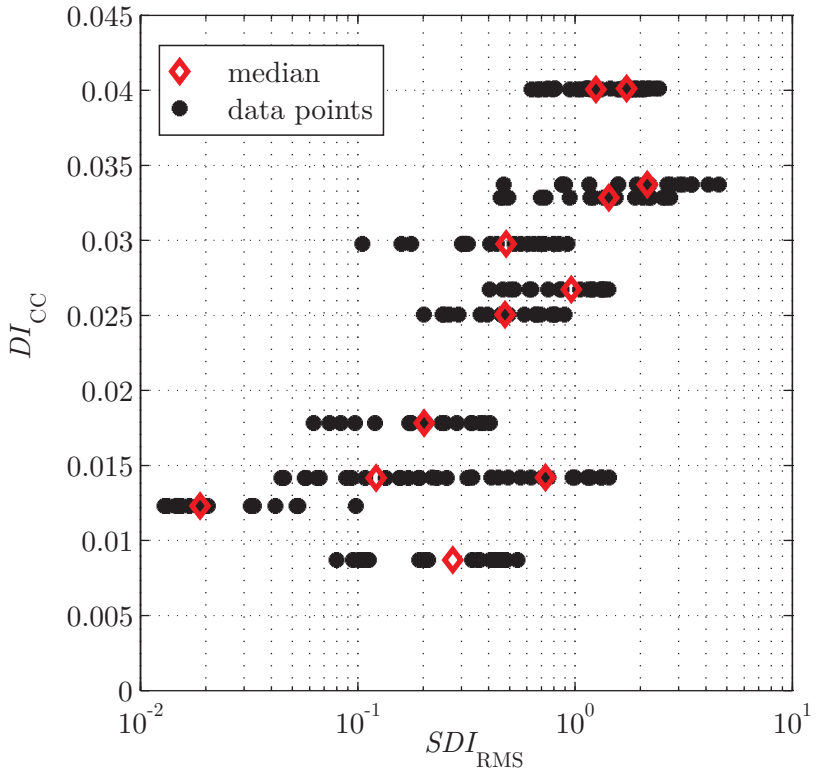

Figure 6.22: Damage index DI_{CC} from PWAS inspection plotted vs. the structural damage index SDI_{RMS}. For SDI_{RMS} logarithmic scale is used.

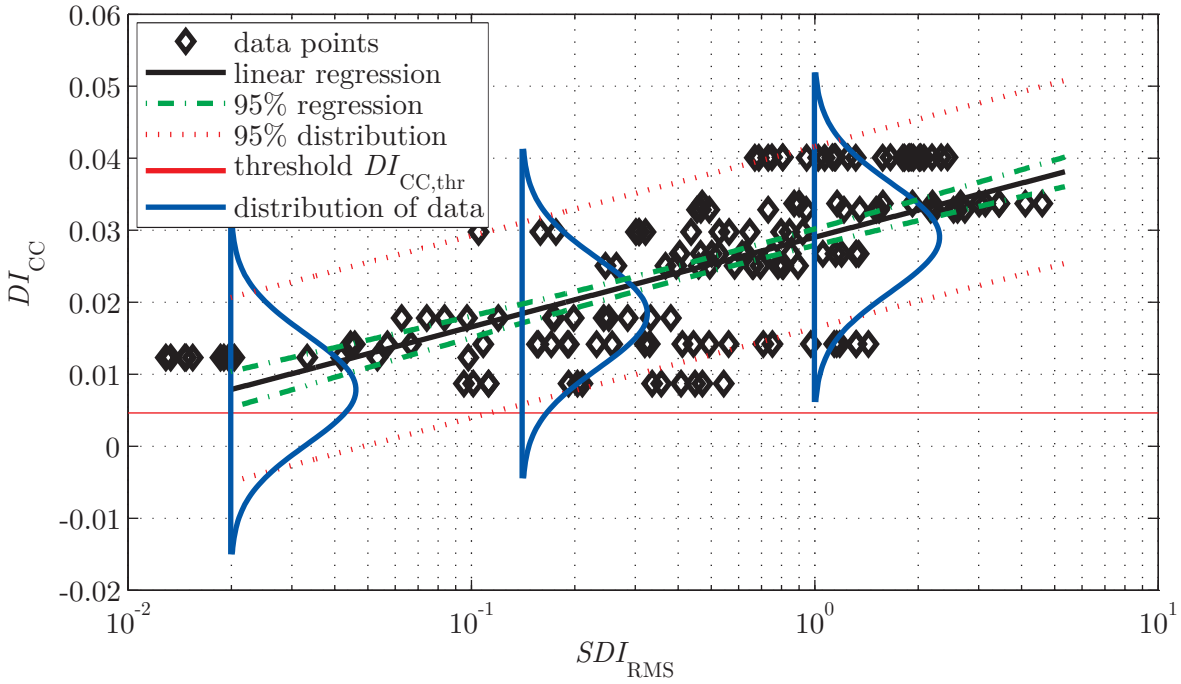

Figure 6.23: Linear regression line for all SDI_{RMS} - DI_{CC} data, threshold for DI_{CC} and statistical boundaries. These quantities build the basis for the calculation of the POD-curve.

system mounted on this structure using this type of transducer, the threshold SDI_{RMS} therefore should be larger than 0.1 to guarantee a satisfying low level of false calls due

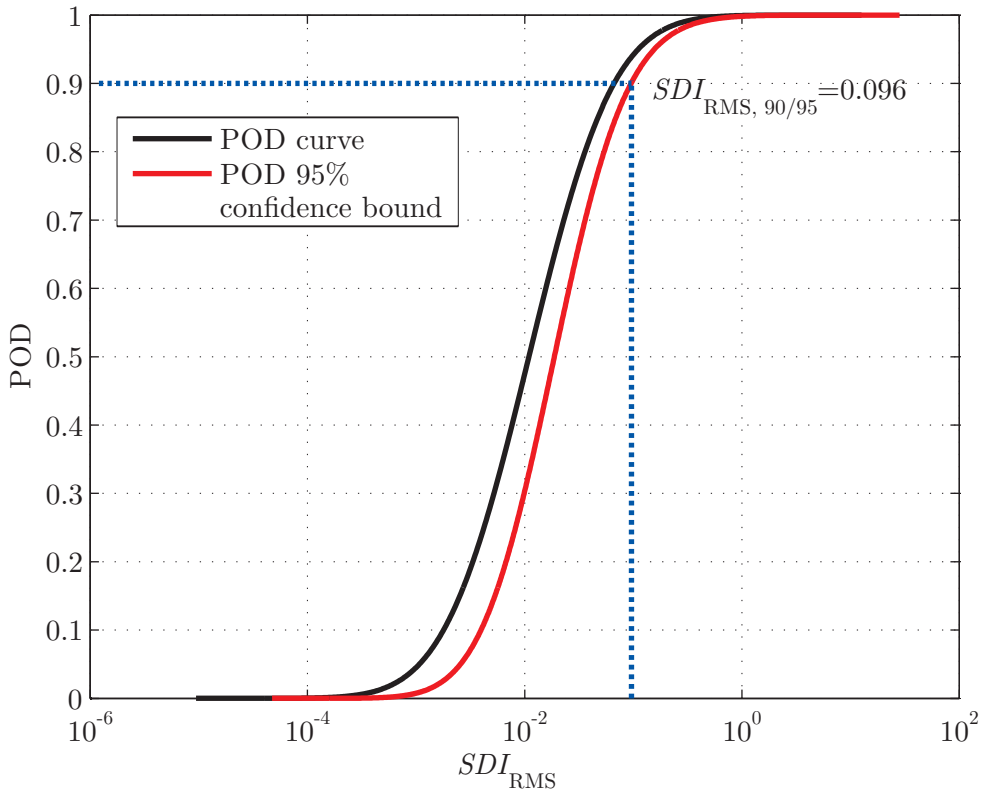

Figure 6.24: POD curve and its 95% confidence interval for the data depicted in fig. 6.23.

to sensor breakage, using DI_{CC} for the inspection of PWAS. The same calculations have been repeated with the use of PWAS4 instead of PWAS 1 as baseline, leading to the same level of $SDI_{90|95}$.

For this application example, several adaptations and restrictions are present, which have to be kept in mind when evaluating the results. Instead of using a baseline of the transducer itself, a baseline from another transducer was used, as the defect has already been introduced in the bonding process during manufacturing. The effect of this adaptation possibly has a different effect on SDI and DI. The same effect has an influence on the calculation of the threshold $DI_{CC,thr}$. From a statistical point of view, it is not correct to take all 216 data points as independent, as only 12 physical realizations exist. The chosen procedure leads to results, that are slightly too low due to a confidence level, which is artificially improved by the multiple use of one physical realization. The introduced defect sizes are quite large. Therefore, no data are available, which show a defect transducer, whose DI is still near or below DI_{thr}. For more than half of the POD curve the regression line is not based on interpolation but on extrapolation. As the variance of the data is already very big, this leads to additional uncertainty.

Nevertheless, the analysis of this application data with the performance assessment method described in section 5.1 gives an estimation about the applicability with a given SHM system and algorithm. It shows a possible procedure, which can be adopted for other applications with other combinations of methods for PWAS inspection with DI and structural damage detection with SDI. Qualification and certification activities for SHM systems will claim a self-check of the SHM system. This novel performance assessment method allows to verify, whether the method of PWAS inspection fits to the SHM system with its requirements.

6.6 Door surround structure

The door surround structure (DSS) is a complex structure, which was developed in SARISTU as part of the integration scenario called "Fuselage assembly integration and testing". The integration scenario includes four large structures. They include all hardware-based testing for the fuselage, developed in SARISTU, and enable integration and verification processes, (*SARISTU Proposal - Large scale Integrated Project*). Major test campaigns have been executed in this integration scenario. The DSS, depicted in fig. 6.25, is a full scale composite fuselage panel, which is equipped with an integrated SHM system, and includes a door cutout and stiffeners. The structure has not been designed for a specific loading but has a representative design with skin, stiffening omega-shaped stringers, normal frames and two ladder structures. The DSS is designed in a double symmetric way. The SHM system consists of 584 piezoelectric transducers, which are embedded in 126 layers. Two different kinds of layers have been installed. One type is the *SMART Layer* from *Acellent*, the other type includes the *DuraAct* transducers from *Invent*. The combination of all layers builds a large SHM sensor network, which can be used for acousto-ultrasonics. A detailed description of the DSS, its development and manufacturing is given in (*Schmidt* et al., 2016).

The DSS is used in SARISTU in order to show that the embedding of the transducers with a co-bonding process works. It is also used to verify the acousto-ultrasonics approach established in one of the application scenarios of SARISTU. Details about these topics can be found in (*Bach* et al., 2016). For the validation of the acousto-ultrasonics approach to find damages in the structure, more than 100 impacts have been applied to the structure. The impact positions are depicted in fig. 6.26.

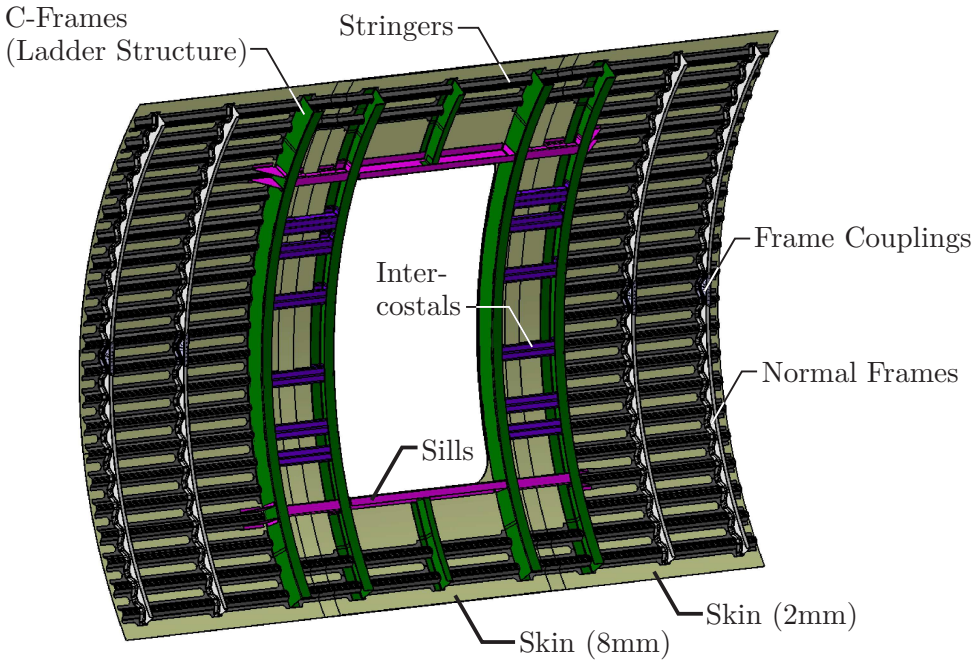

Figure 6.25: DSS with representative design, including omega-stringers, ladder structure and different thicknesses of the skin, depicted without SHM network, (*Schmidt* et al., 2016).

In this work, a detailed analysis of the integrated transducers after manufacturing and after impacting of the structure is presented. For this analysis several facts are important and will be discussed here briefly.

Firstly, each of the 126 layers in the transducer network includes up to five PWAS. The cabling for each layer is done manually. The connection cables of several layers are grouped in sub-D connectors for the connection to an SHM data acquisition system, called *Scan Genie* from *Acellent*. It is a hardware component with supportive software. Each of the 20 sub-D connectors contains the cables of up to 5 layers. The data acquisition system limits the number or transducers, which can be used in parallel. The testing of the structure is therefore split into two parts, the upper and the lower part of the DSS. To be able to test the whole structure, some layers, which are located at the edge of the two parts, are connected twice, so they belong to the upper and the lower part. The procedure enables the monitoring of the whole structure without blind spots. The different cable lengths and the connectors have an influence on the measured susceptance spectrum.

Secondly, all layers are co-bonded on the skin of the DSS. This skin has three different thickness zones. Most of the structure has a thickness of 2 mm. These areas are not in the vicinity of the door cutout. Next to the door cutout the skin exhibits a thickness of 8 mm. Between these two thickness zones, the transition zone has a thickness with

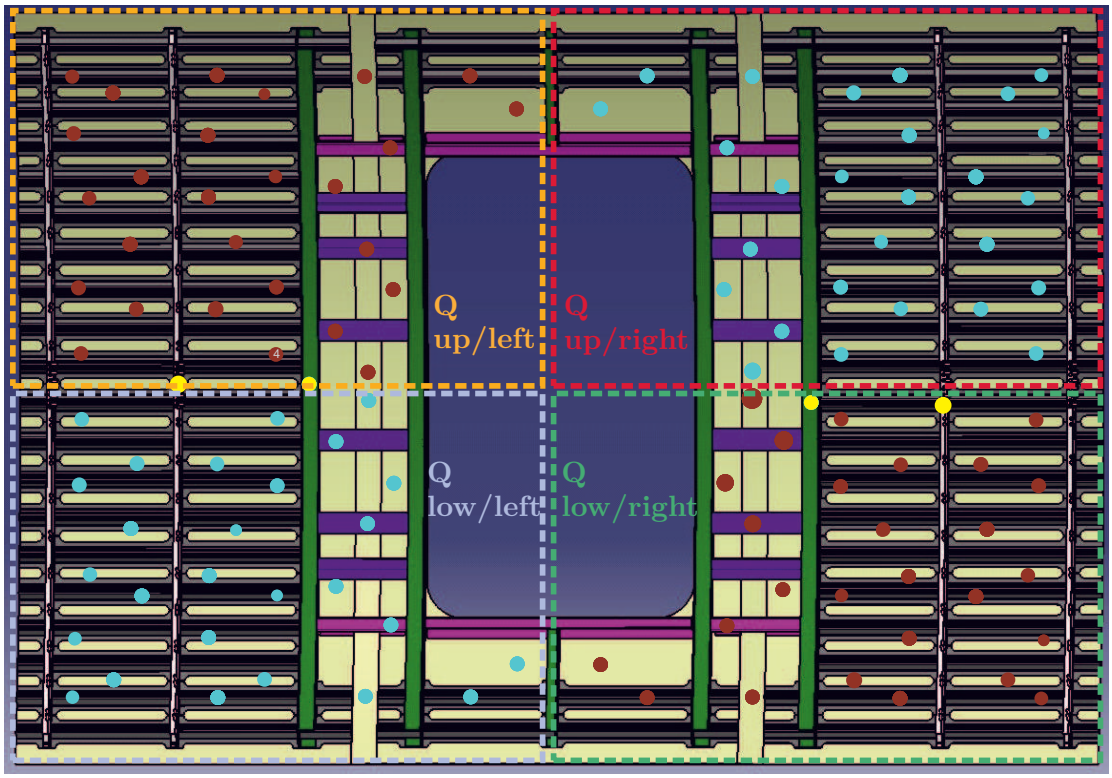

Figure 6.26: Impact positions on the DSS and marked quadrants, adapted from (*Bach* et al., 2016).

an approximately constant thickness gradient. The steps in the thickness have a height of the thickness of one layer of the composite material, used to manufacture the DSS. The transducers are placed in all three thickness zones. The thickness of the structure has an influence on the susceptance spectrum.

Thirdly, the geometrical and material parameters of the two different types of transducers, integrated in the structure, are similar but not equivalent. Their cabling within the layer is different. While the *Acellent* circuits are printed, the *DuraAct* circuits include small cables, which are embedded in ethylene propylene diene monomer (EPDM), which is a ductile polymer. The *DuraAct* transducers are embedded with an embedding layer at both sides of the PWAS. The *SMART Layer* from *Acellent* have no embedding layer below the PWAS. This influences the susceptance spectrum.

The DSS has been manufactured at the *DLR* in Stade. The skin lay-up has been done by an automated fiber placement robot, all 126 layers have been placed by hand with the help of a laser positioning system. This manual placement is time-intensive and needs to be automated for mass production. The skin with the sensor network is placed in an autoclave for curing of the skin and co-bonding of the transducers. All other parts, shown in fig. 6.25 have been manufactured separately and bonded or assembled

after the autoclave process. The cabling of the network is done manually after the assembly has been finished. During the manufacturing the transducers are checked by measuring the capacitance. As described in section 2.6, to check if any major PWAS defect occurred, the measurement of the capacitance is a very simple method. Also a breakage of the cabling can be detected by controlling the capacitance. It is a very rudimentary check, but, it is very fast and a useful method for preliminary checks. It has been shown, that all 584 transducers survived the manufacturing process.

For the detailed analysis of the integrated transducers after manufacturing as well as after impacting of the structure, the susceptance spectra of all transducers are measured. These measurements have been conducted with the *PZT Inspector*, which is described in detail in appendix A.1. With this equipment the 20 sub-D connectors can be used and data of all transducers, connected to one sub-D connector can be measured in one measurement cycle. One measurement of a sub-D connector takes about 35 s. The experimental setup with the *PZT Inspector*, the notebook with the measurement software, and the DSS in the background are shown in fig. 6.27.

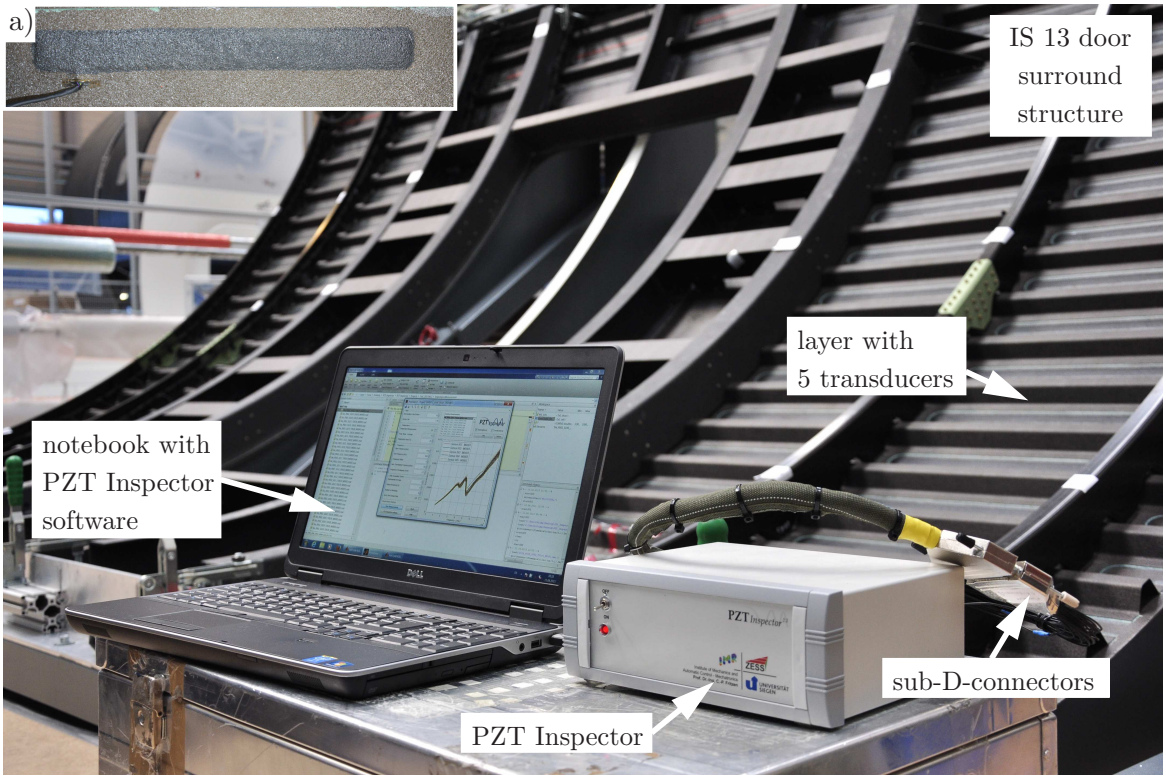

Figure 6.27: Experimental setup, showing the DSS, the *PZT Inspector* with measurement notebook, and the connection to the SHM network, a) shows a detail on a layer of type *DuraAct*.

For each transducer repetitive measurements have been taken. This analysis focuses the frequency range from 200 kHz up to 800 kHz, which includes the resonance of the transducer. The susceptance spectrum has been measured from all transducers. Some measurements have been conducted while the data acquisition system of the AU-based SHM system was connected to the other half of the transducers, some have been measured without any other devices connected to the transducer network. The structure has been grounded at all times.

The susceptance spectra of the complete sensor network have been measured at the beginning of the impact campaign and at the end of the impact campaign. This enables the analysis of the transducers after manufacturing and after being used for damage detection in the test campaign. The measurements have been conducted at the *DLR* in Stade in an air-conditioned production hall. This makes it possible to execute all measurements at an almost constant temperature and humidity. Environmental changes do not have to be taken into account for the analysis of the data.

For the analysis of selected transducers, data from the *Scan Genie* from *Acellent* are used. Connector boxes link the sub-D connectors with the data acquisition system. Using one transducer as actuator, the surrounding transducers are used as sensors and their signal is recorded. The signal of the direct neighboring transducers is not recorded to reduce the size of the recorded data. For further details see (*Bach* et al., 2016).

The whole analysis of all 584 transducers is documented in (*Buethe*, 2015) in detail. Here exemplary data and its analysis is shown to highlight major effects and issues.

Pre-test analysis

All transducers exhibit an appropriate susceptance spectrum. Most of the variance of the data can be explained by one of the facts listed above, like length of the cable, type of transducer and thickness of the structure. The thickness of the structure has some effect on the susceptance resonance behavior, while the general slope is approximately constant. The cables have an influence on the slope, as shown in section 4.2 and fig. 4.13. The spectra of the two lower quadrants for all transducers placed on the 2 mm skin are depicted in fig. 6.28. The deviation of the spectra regarding the slope is comparatively large. It is approximately the same for both quadrants.

The spectra of some sub-D connectors show a frequency dependent damping of the susceptance spectrum. As this effect depends on the sub-D connector and is constant for all transducers linked to one connector, this seems to result from the connection and

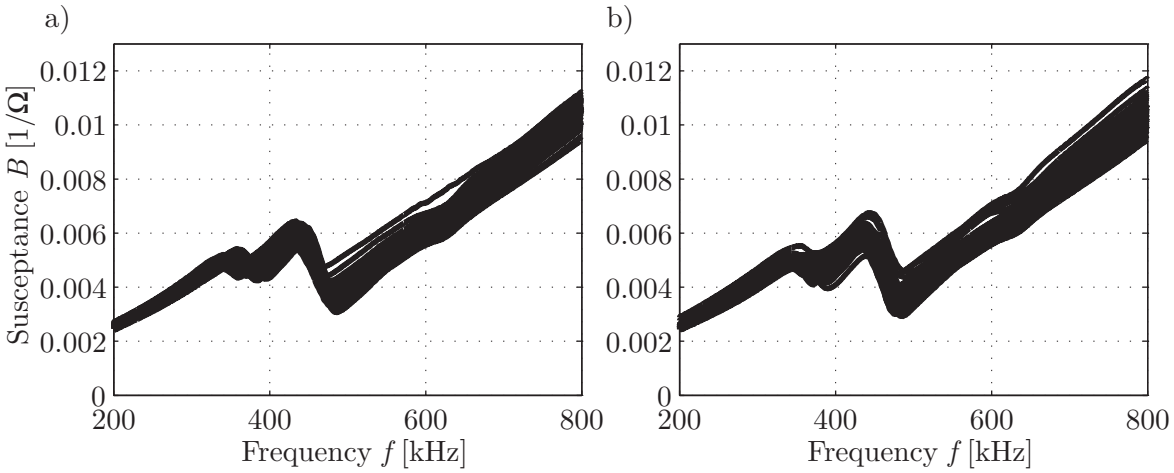

Figure 6.28: Susceptance spectra of the two lower quadrants, selecting all transducers, which are placed on the thin skin, a) left, b) right quadrant.

has to be corrected before analyzing the data. For this correction a *MATLAB*-based program has been developed and tested. For future measurements, this effect, possibly caused by the interference of the two data acquisition systems, connected to the SHM system, or insufficient grounding of the measurement device, should be prevented.

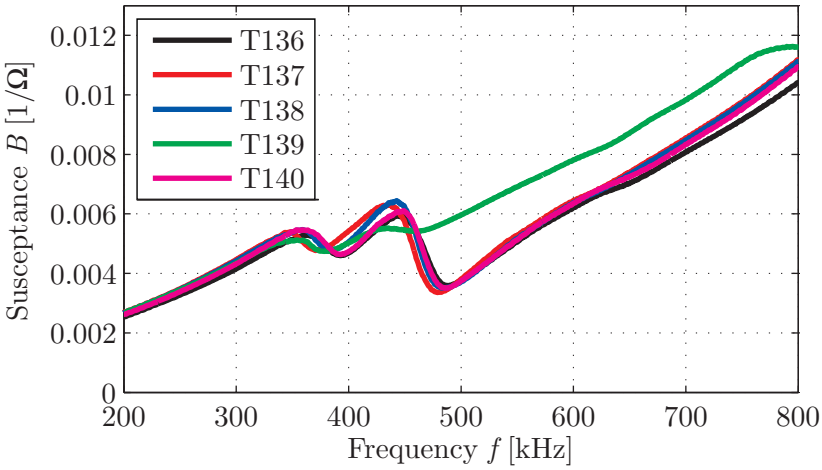

Figure 6.29: Susceptance spectra of all transducers of one layer. PWAS T139 differs from the others.

Fig. 6.29 shows the susceptance spectra of five transducers, which are part of the same layer and therefore connected to the same sub-D connector with almost the same cable length. While four transducers have a very similar spectrum, transducer T139 differs from the others. The general appearance is similar with linear slope, resonance interval and second linear slope. The differences are possibly caused by variations in the bonding quality. Due to the manual application of the transducers, differences in the placement of the single transducers of one layer can be induced. This

difference in the bonding quality will possibly also have an effect on the quality of the energy transfer from transducer to structure. During the setup of the AU-based data acquisition system, it has been revealed that different transducer paths have a much lower signal than other paths with similar length and location. This observation supports the assumed reason for the differences in the susceptance spectrum.

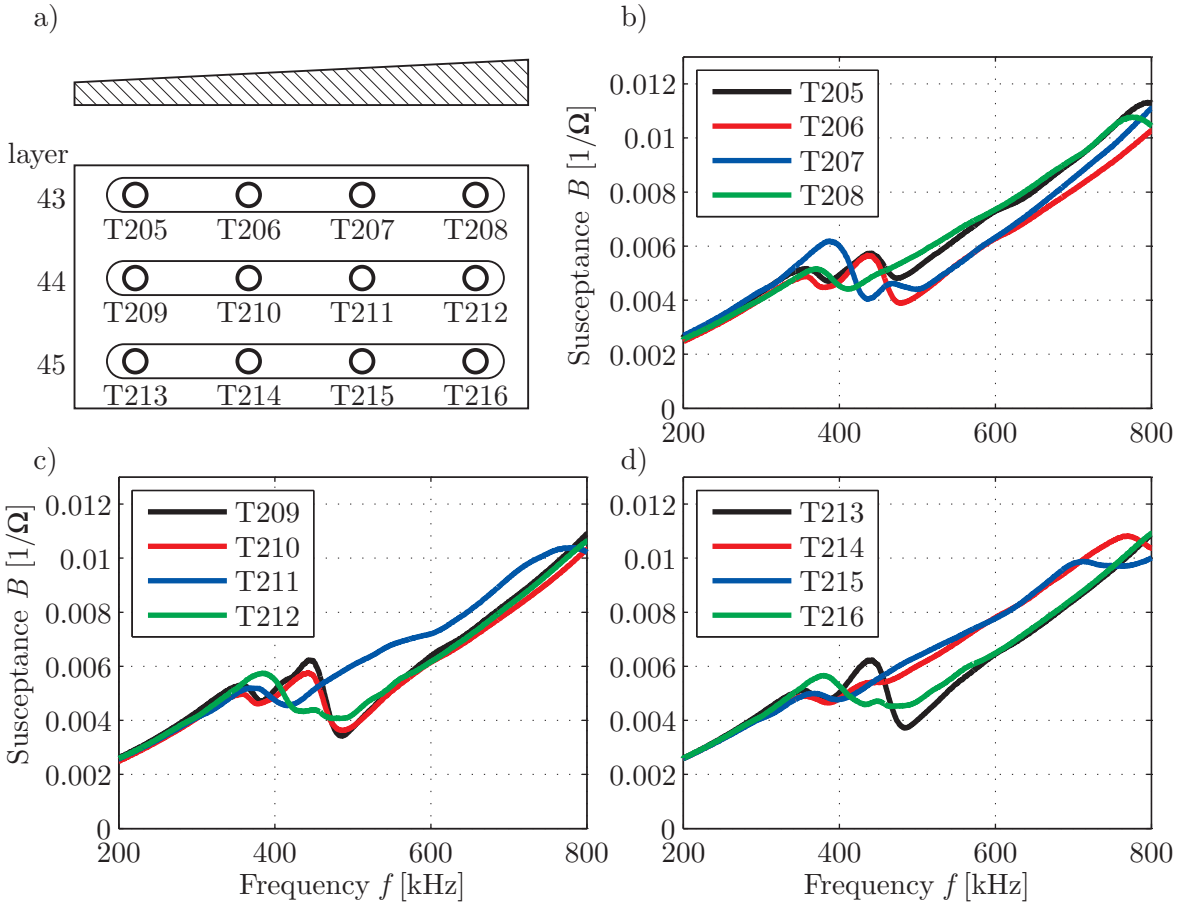

Figure 6.30: Susceptance spectra of 12 transducers from three layers b) 43, c) 44, d) 45, positioned on the thickness transition zone. a) shows the location of the transducers on the DSS.

The spectra of transducers, placed on the thickness transition zone show higher variation, see fig. 6.30. On the one hand these variations are caused by the changing thickness of the structure beneath the PWAS. On the other hand, other factors have an influence, which can be seen in the comparison of three layers, all placed at the same thickness ramp of the structure. The layers are arranged in a way that the transducers T205, T209 and T213 should be placed at the same thickness. Nevertheless, the spectra do not coincide. The same is true for other groups like T206, T210 and T214, etc. It can be assumed that the placement of the transducers on the thickness

transition zone is more difficult due to the ending layers of the CFRP. This leads to higher variations in the bonding quality.

Another factor, which might cause variations in the spectra is the curing of the material of the structure. The manual placement of the layers took some time so not all layers are placed on the uncured material at the same time. Although the skin was cured on time, these time differences might result in different bonding conditions for the transducers of different layers.

Post-test analysis

The comparison of the susceptance spectra of the pre- and the post-test measurements is done visually and with the help of the correlation coefficient-based method for PWAS inspection, introduced in section 4.5.2. Here the data of two exemplary layers, layer 2 and layer 80 with 5 respectively 4 transducers are analyzed. Starting with layer 2, the susceptance spectra in fig. 6.31 a) show that the baseline data is corrupted with an additional frequency dependent damping. It is possibly caused by a bad grounding or the interference of the two measurement systems. For the use of the model-free PWAS inspection method, the baseline data is cleaned. The resulting spectra are shown in fig. 6.31 b). In this spectra it is visible, that two PWAS, T8 and T9, differ from their baseline after the impact campaign. The differences are comparably small, the slope of the spectra is very similar.

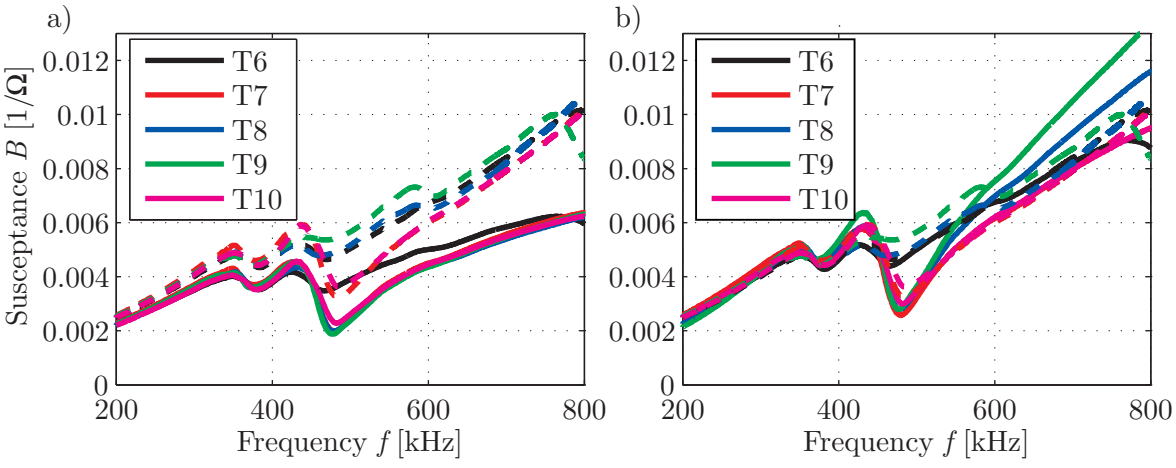

Figure 6.31: Susceptance spectra of the pre (solid lines) and post (dashed lines) impact measurements for all transducers of layer 2, a) original measurements, b) cleaned baseline measurements.

The results of the model-free PWAS inspection method for layer 2 is depicted in fig. 6.32. The calculated damage indices lead to the assumption that T8 and T9 are defect, as their values for DI_{CC} are much larger than the values of the other three

transducers. The calculation is based in the cleaned susceptance spectra from fig. 6.31 b).

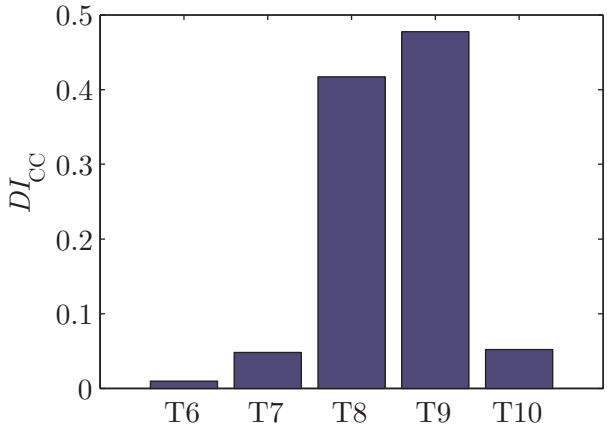

Figure 6.32: Calculated damage indices of all transducers in layer for the correlation coefficient based PWAS inspection, using the corrected susceptance spectra.

The results show, that T8 and T9 exhibit some degradation, which can be caused by small cracks of the PWAS. However, they can possibly still be used for SHM, but might cause small variations, which induce additional noise and might either cause false calls or increase the minimum visible structural damage size.

The susceptance spectra of layer 80 are depicted in fig. 6.33 a). T362 shows minor deviations from the baseline after the impact campaign. Major changes of the susceptance spectrum can be seen for T364. The susceptance slope has decreased significantly, which leads to the assumption of total failure of the transducer.

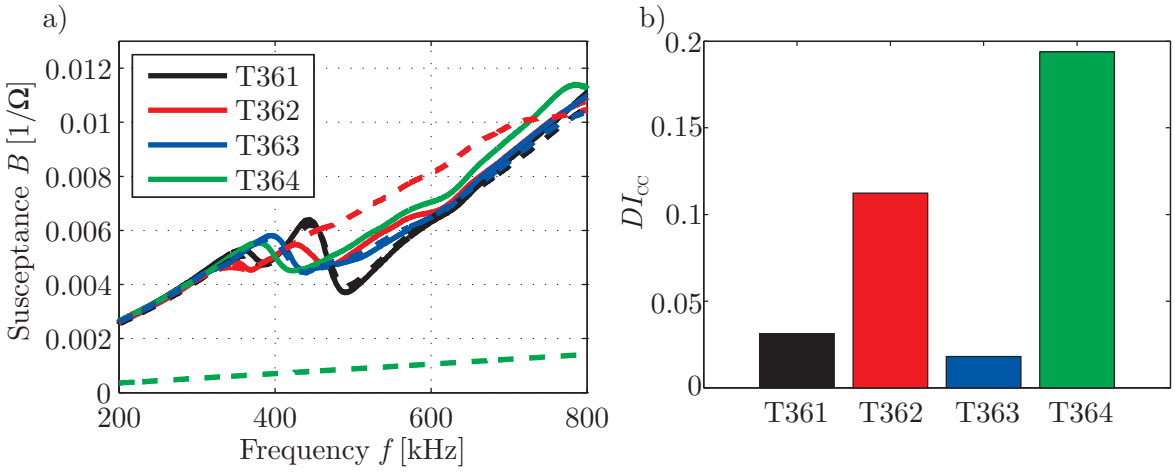

Figure 6.33: Data analysis for all transducers of layer 80, a) shows the susceptance spectra of the pre and post impact measurements, b) shows the calculated damage indices for the correlation coefficient based PWAS inspection.

The calculated damage indices DI_{CC} in fig. 6.33 b) show increased values for T362 and T364, with T364 exhibiting the larger values, although DI_{CC} does not focus on the change of the slope. The results show, that T364 has a substantial defect and cannot be used for SHM any more, hence should be excluded from the data analysis.

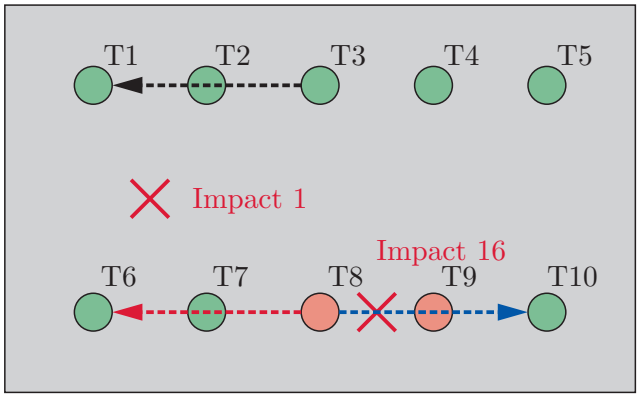

Figure 6.34: Location of transducers, paths and impacts for the wave propagation analysis of T8.

For two inspected transducers, T8 and T364, also the wave propagation shall be analyzed. The analysis is difficult as the wave propagation is also changed by impacts. It is limited to the first wave package to only include the direct path between actuator and sensor. Only those frequencies are chosen, where the S_0 mode is dominant and the S_0 mode is used for the analysis, which is less sensitive to the introduced structural damages. The measurement device from *Acellent* also exhibits a lot of crosstalk, which has to be eliminated before the data can be used for analysis. Only those frequencies have been chosen for which the elimination can be done by deleting the time interval that includes the crosstalk, to prevent other effects. For more advanced methods of dealing with the crosstalk see (*Loendersloot* et al., 2015). The analysis of the wave propagation by comparing different similar paths can be seen as a simple visual interpretation of the use of mutual information, (*Kraemer* and *Fritzen*, 2007). The visual analysis of the wave propagation signals is complemented by an additional basic analysis with three structural damage indicators evaluated for the first wave package.

For the analysis of transducer 8, the paths 1-3 and 6-8 are used. They have a similar distance to the introduced impact 1. The observed section of the DSS is shown in fig. 6.34.

The recorded signals for path T1-T3 are shown in fig. 6.35 for three frequencies, 150 kHz, 170 kHz, and 190 kHz. Baseline and the signals, recorded after the impact campaign are quite similar, which leads to the visual hiding of the baseline. However,

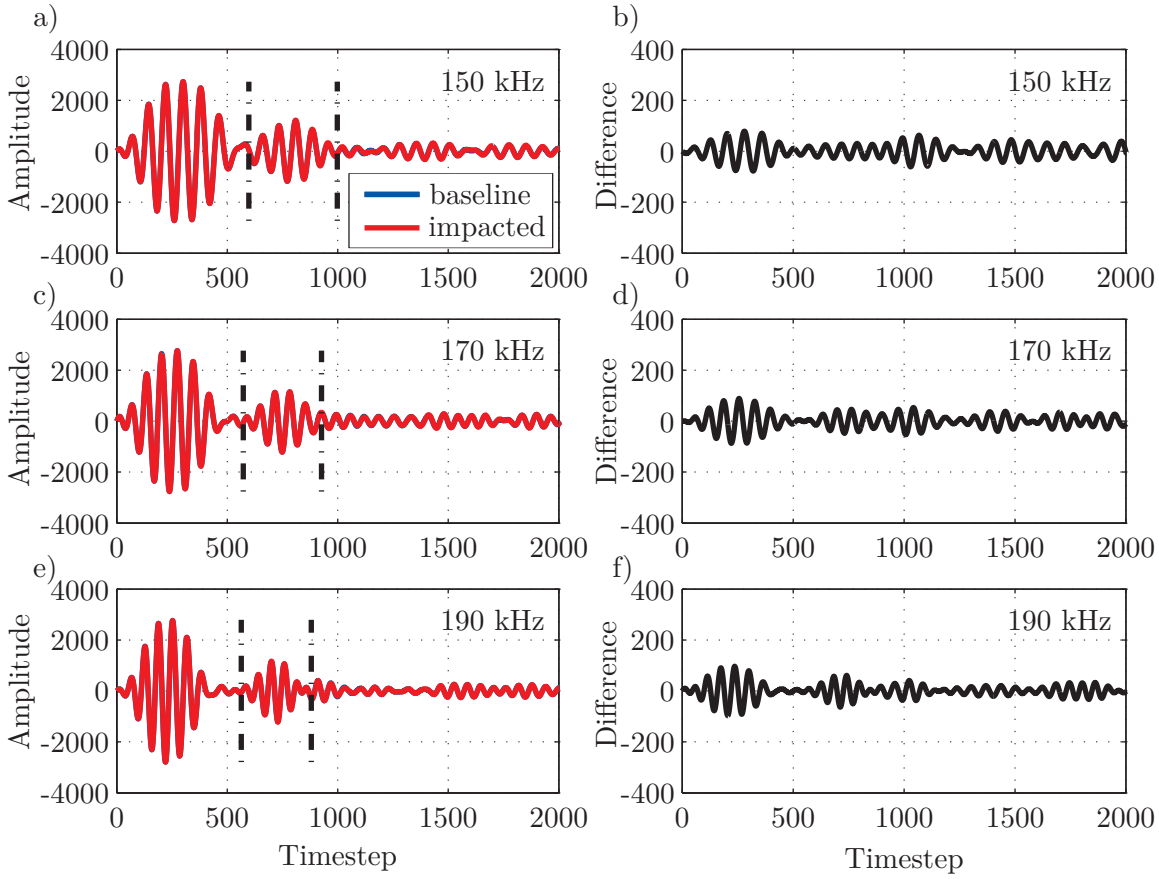

Figure 6.35: Signals of the baseline state and after the impact campaign for path T1-T3 on the left and difference of the two signals on the right for three different frequencies, 150 kHz, 170 kHz, and 190 kHz. As the original signals are very similar, only the data set of the impact campaign is visible. It hides the baseline state. The S_0 package is marked with dash-dotted lines.

the differences on the right give an impression on variations between the two signals. Focusing the direct signal, the S_0 package is marked in the time lines. The difference signals are small in the marked interval.

The recorded signals for path T6-T8 are shown in fig. 6.36 in the same manner as in fig. 6.35. The difference signals are larger than for path T1-T3 in the marked interval and in the following time interval, which includes the effects caused by the damage between T8 and T9.

To show that the effect of a structural defect, caused by impact 16, is larger than the effect of the changes of T8, the recorded signals and difference signals for path T8 to T10 are also shown in fig. 6.37. The difference signals are larger in the marked interval and in the proceeding time intervals.

The impact of the degradation of T8 for an SHM system can also be shown by evaluating the changes of structural damage indices. Three structural damage indices SDI_{CC},

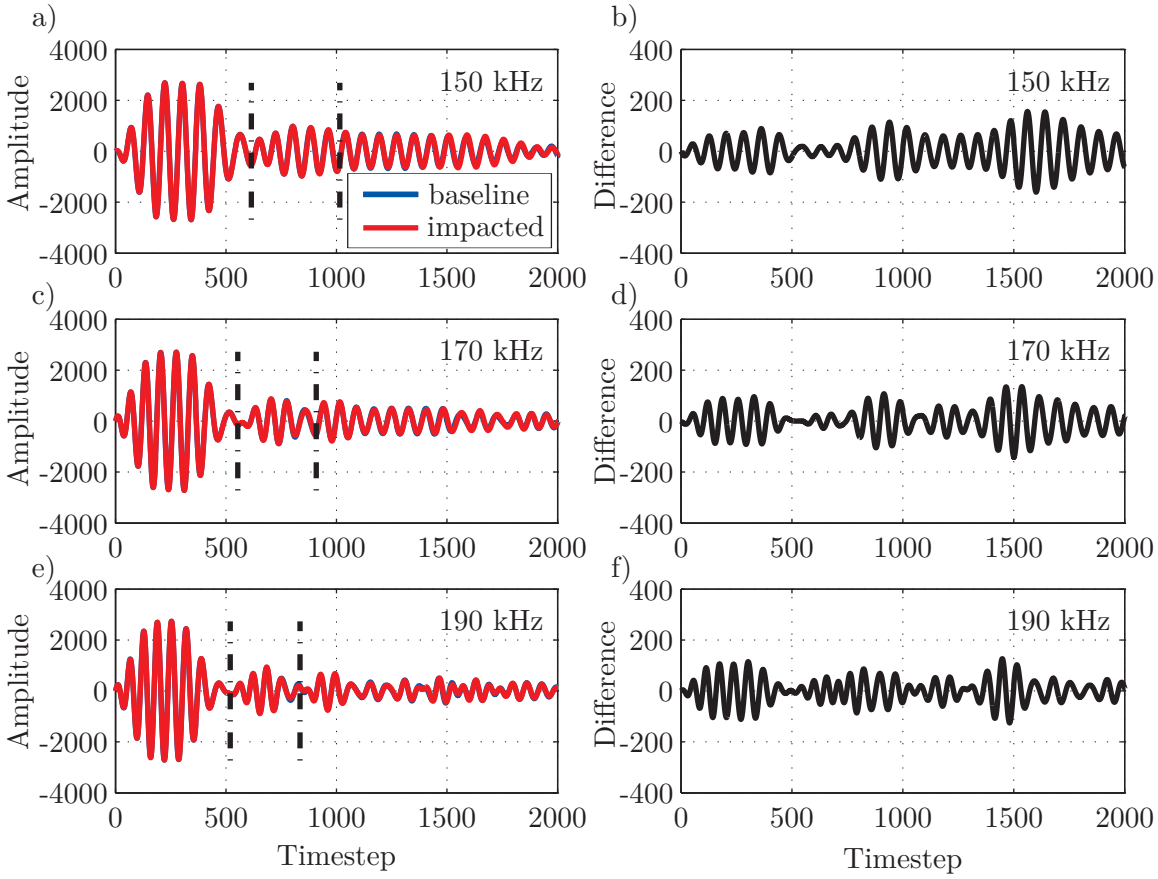

Figure 6.36: Signals of the baseline state and after the impact campaign for path T6-T8 on the left and difference of the two signals on the right for three different frequencies, 150 kHz, 170 kHz, and 190 kHz. As the original signals are very similar, only the data set of the impact campaign is visible. It hides the baseline state. The S_0 package is marked with dash-dotted lines. The difference signal is larger than for the path T1-T3.

SDI_{CCh} and SDI_{RMS} have been introduced in section 2.1.4 and are used here to show the impact on the SHM system. The results are depicted in fig. 6.38 for SDI_{CCh} and SDI_{RMS} and in fig. 6.39 for SDI_{CC}. For the calculation of the structural damage indices only the marked time interval including the first arrival of the S_0 mode is used. The structural damage indices are evaluated for frequencies between 150 kHz and 200 kHz. It is expected to have the highest values for T8-T10, slightly lower values for T6-T8 and the smallest values for T1-T3.

SDI_{RMS} shows increased values for T8-T10, which includes a structural damage on the direct path between the two transducers. The other two paths approximately have the same level. The impact of degradation of T8 on SDI_{RMS} is small. This is different for SDI_{CCh}. Here for frequencies from 160 kHz to 180 kHz the values for path T6-T8 are even larger than the values for path T8-T10. The degradation of T8 has significant influence on the structural damage indicator. The expected behavior is visible for

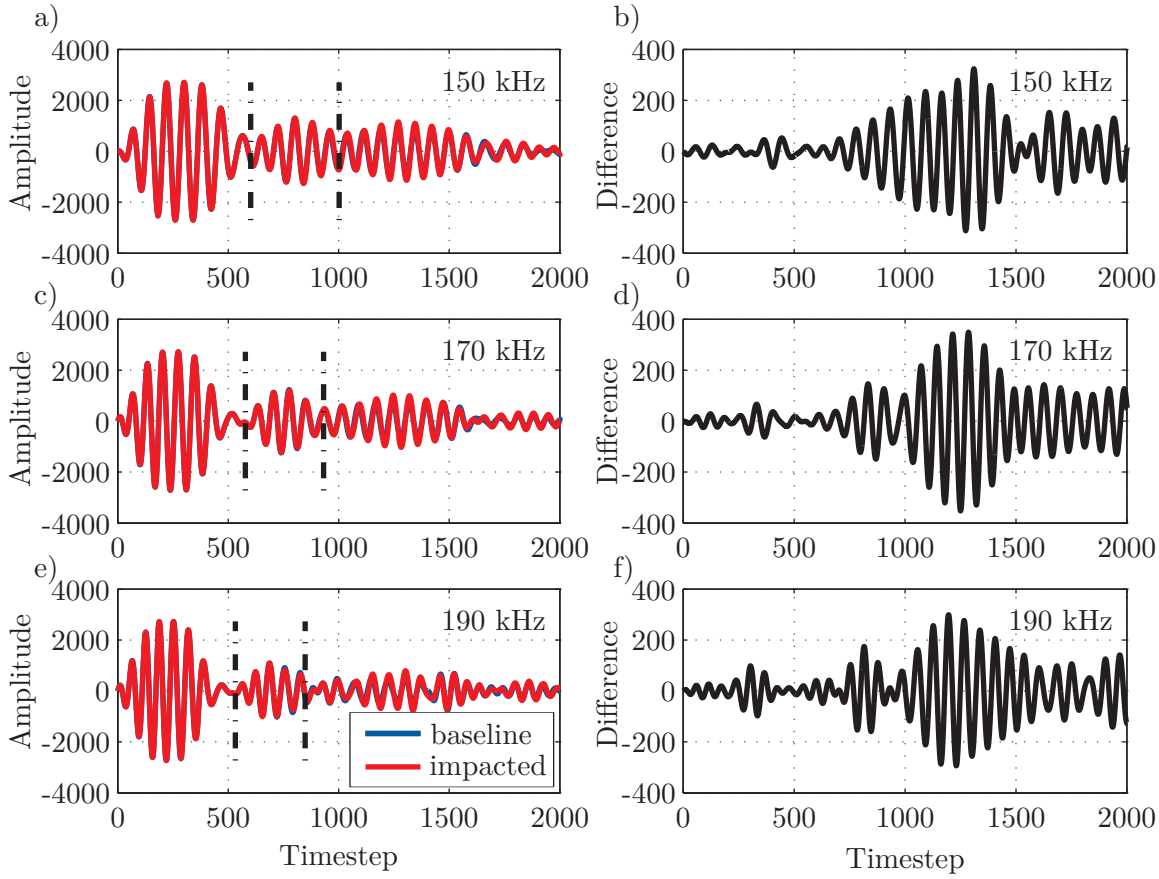

Figure 6.37: Signals of the baseline state and after the impact campaign for path T8-T10 on the left and difference of the two signals on the right for three different frequencies, 150 kHz, 170 kHz, and 190 kHz. As the original signals are very similar, only the data set of the impact campaign is visible. It hides the baseline state. The S_0 package is marked with dash-dotted lines. The difference signal is increased compared to the other two paths T1-T3 and T6-T8.

SDI_{CC} over the whole frequency range under consideration. The degradation of T8 has an effect, nevertheless, the effect of the introduced structural damage is larger than the effect of the degradation.

For the analysis of transducer 364, the paths 359-364 and 360-363 are used. They have a similar distance to the introduced impact 104, as it is visible in fig. 6.40 showing the observed section of the DSS.

As already anticipated from changes of the susceptance spectrum, T364 shows a severe defect. No difference is build, but the signals themselves are shown for T360-T363 and T359-T364, fig. 6.41. The signals clearly show a change, caused by the defect of T364. Only minor signals are visible after the decay of the crosstalk at the beginning of the time line.

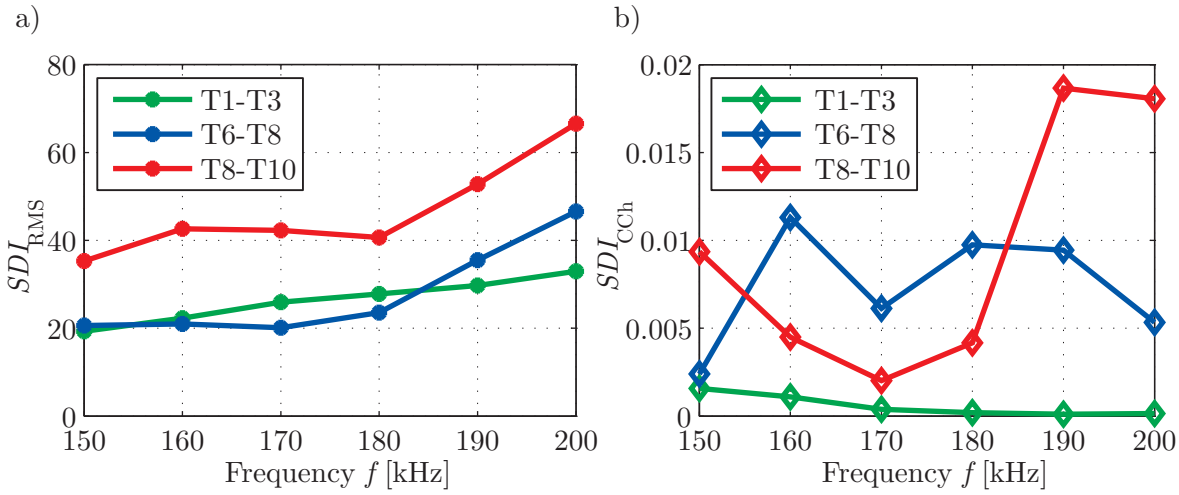

Figure 6.38: Structural damage indices a)DI_{RMS} and b) DI_{CCh}, evaluated for three paths. T1, T3 and T6 as well as T10 are undamaged, T8 gives indications of degradation, a structural damage was introduced between T8 and T10.

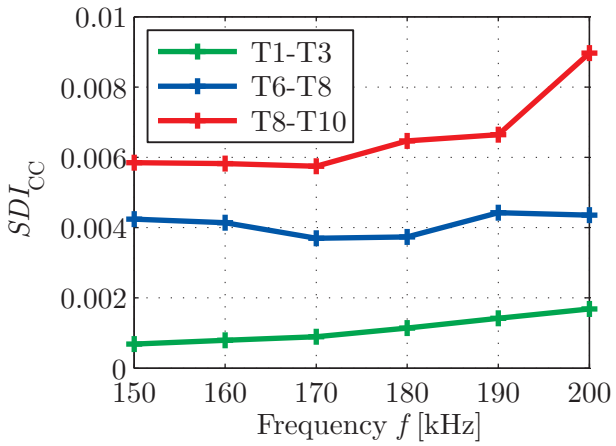

Figure 6.39: Structural damage indices DI_{CC}, evaluated for three paths. T1, T3 and T6 as well as T10 are undamaged, T8 gives indications of degradation, a structural damage was introduced between T8 and T10.

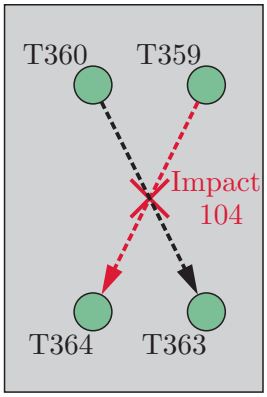

Figure 6.40: Location of transducers, paths and impact for the wave propagation analysis of T364.

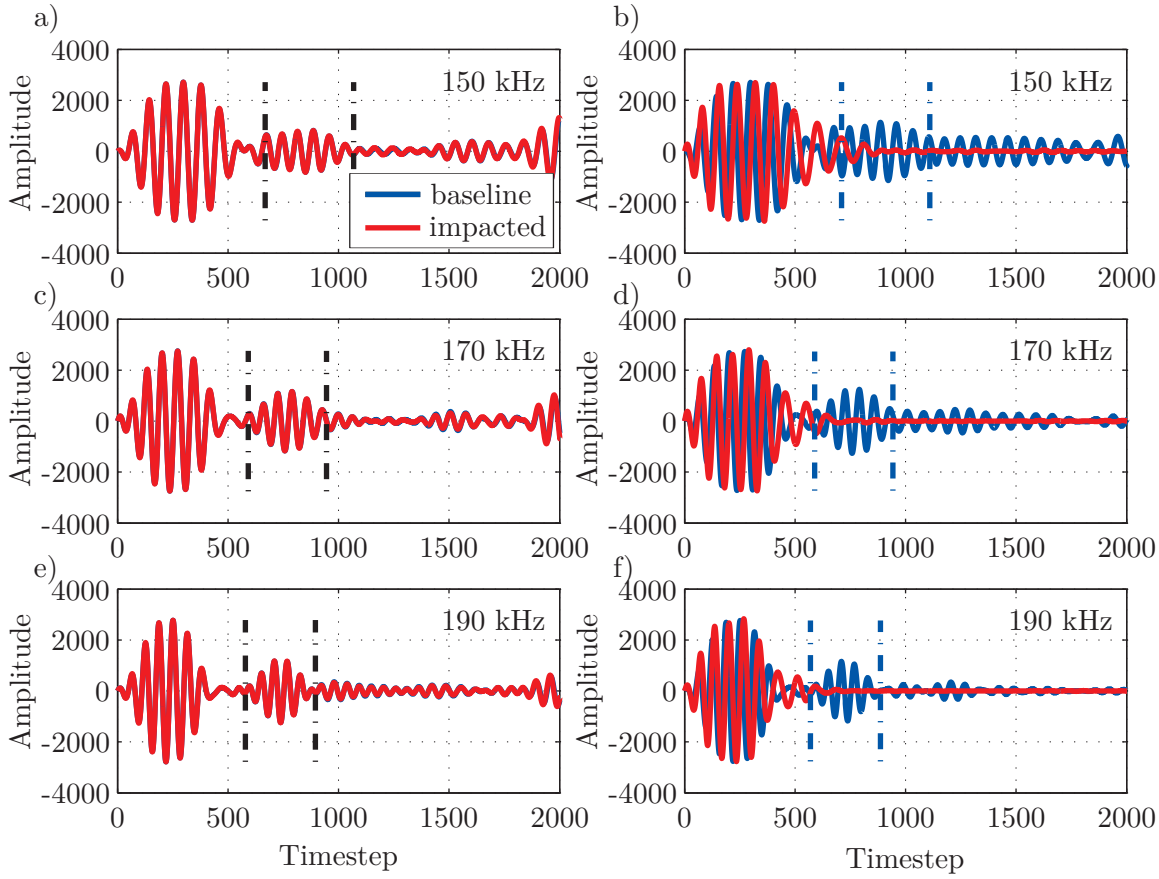

Figure 6.41: Signals of the baseline state and after the impact campaign for path T360-T363 on the left and of path T359-T364 on the right for three different frequencies, 150 kHz, 170 kHz, and 190 kHz. The S_0 package is marked with dash-dotted lines. The influence of the defect of T364 is clearly visible for all selected frequencies.

Either this transducer 364 is not connected any more or it exhibits a very heavy defect and should be replaced and not taken into account for any damage detection with the SHM system.

For the DSS application, it can be summarized that the use of the PWAS inspection methods developed in this work is possible. Additional effort is necessary to study the statistical parameters of the susceptance spectra for large structures and manual placement of sensors on large structures.

7 Conclusion

In this work it has been shown that the inspection of piezoelectric wafer active sensor (PWAS) is of major importance. Methods for the inspection have been developed and successfully proven to be applicable for structural health monitoring (SHM) systems. Throughout the whole work supportive application examples, based on experimental and numerical investigations, are provided. In this way it contributes to the transfer of SHM into industrial applications, enabling a self-check of piezoelectric transducers.

The necessary basics are elaborated at the beginning. Fundamental theories used in the work are explained, for further information a manifold of references are available. These basics include information about acousto-ultrasonics and acousto-ultrasonics (AU)-based SHM as well as details about the physics of PWAS and derivations about the electro-mechanical impedance (EMI) of PWAS. Before presenting an overview about the state of the art for PWAS inspection, the concept of probability of detection (POD) has been explained. The overview includes methods of testing sensors in general and focuses on the analysis of PWAS and EMI-based examinations with PWAS in the context of SHM.

A detailed analysis of the different defects of piezoelectric transducers and their effects on the propagating wave field used for SHM is demonstrated. To develop methods for PWAS inspection, the evaluation of the operational conditions and possible failure modes of the transducers is of major importance. As main failure types breakage of the transducer, degradation of the transducer and the bonding layer, debonding of the transducer from the structure and contamination of the bonding surfaces have been identified. The use of measurements taken with a laser *Doppler* vibrometer (LDV) enables the insight into the vibrations of the transducer itself and makes it possible to visualize the generated wave field with high resolution. It has been shown that for different types of transducers similar defects lead to different consequences for the generated wave field. Embedded and simple transducers show significantly different changes in the generated wave field in case of breakage. This leads to the statement

that it is necessary to take into account the effects of PWAS defects on the generated wave field to evaluate the defect.

A method to introduce precise defects and test varying parameters is the numerical simulation of the experimental setup and the generated wave field. The simulation is used to analyze the effects in detail. It has been shown with two examples that it is possible to model different types of defects and simulate the propagating wave field with the finite element method (FEM). For the representation of the piezoelectric effect a commercial multiphysics finite element (FE) program was chosen and tested.

With the EMI a physical quantity is put into focus, which has proven to be sensitive to defects of PWAS. The detailed analysis of this physical quantity is necessary to be able to see the interconnections of application parameters and the susceptance spectrum. Examples for these parameters are not only physical dimensions as well as material constants but also possible defects. In this work existing models of the EMI spectrum have been used, adapted and extended to focus on those factors in the EMI spectrum that are affected by the transducer itself and its bonding conditions. The bonding layer has been modeled including its frequency dependency, which is especially important for comparably thick adhesive layers, i.e. up to tenth of mm. A frequency spectrum that includes the resonances of the transducer is necessary to be able to use the EMI spectrum for the inspection of PWAS. The effects of environmental and operational conditions (EOC) on the EMI are included in the model for the parameter “temperature” by adding a temperature dependency of the most significant parameters of the established model. The model has been validated with experimental data of different transducers. Its use makes it possible to understand the nature of the EMI spectrum and predict changes of the spectrum caused by modifications of the application parameters.

Moreover, a method of model-based PWAS inspection has been introduced, which uses the developed model as part of the baseline, to which new spectra are compared. For this method complete knowledge about the transducer and its application conditions is necessary, as many parameters are needed to use the model. Alternative methods for PWAS inspection, based on recorded EMI spectra are presented in this work, enabling an inspection even if no complete parameter set is available. A method based on the recorded EMI spectra of a batch of transducers is developed, which allows a system check after installation during commissioning of the SHM system. For these methods well established procedures for the comparison of data have been selected

and applied for PWAS inspection procedures. The analysis of the EMI spectrum is completed by the numerical modeling and simulation of this quantity. Using a commercial multiphysics FE program the spectrum is evaluated in the frequency domain. The numerical simulation is validated with experimental data. The modeling makes it possible to use the same model for the analysis of the generated wave field and the resulting EMI spectrum.

A novel procedure to evaluate the performance of PWAS inspection methods has been introduced in this work. It is based on the assumption that the quality of a PWAS inspection method can only be evaluated by taking into account the effects of PWAS defects on the generated wave field. The defect of a PWAS influences the SHM system reliability. The size of the defect of the PWAS is of minor relevance, of highest importance are the effects of the defect on the PWAS inspection method and the SHM system output for structural damage detection. Adapting the concept of POD, which is state of the art for performance assessment of non-destructive testing (NDT) methods, a procedure is developed, which combines the output of the PWAS inspection method under consideration with a quantity describing the effects of a defect PWAS on the output of the SHM system for structural damage detection. The result of this procedure makes it possible to specify, whether the PWAS inspection method under consideration can be used in combination with the structural damage detection method of the SHM system in the specified way, without an increase of the false call rate. Moreover, possibilities for adaptations of thresholds within the two methods are determined.

The use of numerical methods for the detailed analysis of the performance of a PWAS inspection method with the novel procedure, developed in this work, enables the evaluation on a model-based foundation. This procedure is called model-assisted probability of detection (MAPOD). The procedure is detailed in this work for the specified defect of transducer breakage for a simple piezoelectric transducer. It shows the applicability of the procedure with numerical methods.

Various applications are shown using the methods developed in this work. Taking into account the effects of EOC, the inspection of PWAS under changing temperature conditions is demonstrated. Model-based as well as model-free methods are applied to the same data set to show advantages and disadvantages of the methods.

The method for system check after installation during commissioning of the SHM system is tested for a batch of 16 transducers, including two transducers with a defect

bonding layer. This type of defect is of major importance for secondary bonded transducers.

The defect “breakage” is momentous for embedded transducers, which can be co-bonded to carbon fiber reinforced plastic (CFRP) structures. Bending loads on the structure can cause transducer breakage as the transducer is made of brittle ceramic material. For this application the newly developed methods for model-free PWAS inspection are compared to established procedures also based on the EMI. It is shown that this defect is only detectable with the newly introduced methods. The procedure is adapted to applications with defect of PWAS under cyclic loading. The recording of data over an extended time interval raises additional phenomena like the change of EOC. Their influences on the results for PWAS inspection are discussed in detail.

Model-free PWAS inspection methods are used to detect the defect “debonding”. For this defect it is shown with the help of an experimental setup, that large debondings are detected with the existing method for PWAS inspection. The introduced new methods reliably detect the debonding also for small debonded areas. The performance of the PWAS inspection method using DI_{CC} is evaluated for this defect using the novel procedure to evaluate the performance of PWAS inspection methods developed in this work. For this purpose also the generated wave field and the effects of PWAS defects on the output of the structural damage detection method are analyzed. Using DI_{CC}, false calls for the SHM system caused by debonded transducers can be eliminated.

A large scale application is presented in form of the application scenario door surround structure (DSS). The DSS is a full scale composite aircraft fuselage panel, including a door cutout, which is equipped with an integrated SHM system, containing 584 embedded transducers. The investigations at the DSS, which have been performed in the EU-project “smart intelligent aircraft structures” (SARISTU), have shown that the susceptance is suitable to be used for PWAS inspection. The challenges of increased sample size and complexity are emphasized and recommendations for the adaptation of the methods developed in this work for complex structural parts are given. The procedure of PWAS inspection is shown for exemplary transducers with two different defect levels. It is complemented by the analysis of the changes in the generated wave field.

In this work it has been demonstrated that PWAS inspection works and is suitable for the application in SHM systems. It includes the detailed analysis of the generated

wave field and the resulting EMI spectrum to enable in-depth understanding of the effects of PWAS defects.

Further Steps

Depending on the SHM system and its EOC, it is still necessary to include the effect of temperature in the MAPOD-based performance evaluation. Moreover, different types of transducer defects, conceivable for one application, need to be compared to identify the most severe defect for the SHM system under operation. Difficulties of the MAPOD approach can be found in the determination of thresholds for the PWAS inspection method, as for thresholds noise caused by changes of the EOC, and variability in the production and application of transducers are of major importance. The procedure also has to prove for the application with more advanced methods for structural damage detection, as in this work only basic approaches for structural damage detection have been used to show the proof of concept.

References

Acellent technologies, Inc. (2005). *SMART Layer (single side shielding) - Engineering Data Sheet*.

Aldrin, *J.C.*, *E.A. Medina*, *E.A. Lindgren*, *C.F. Buynak*, and *J.S. Knopp* (2011). "Protocol for Reliability Assessment of Structural Health Monitoring Systems Incorporating Model-assisted Probability of Detection (MAPOD) Approach". In: *8th International Workshop on Structural Health Monitoring*. Stanford, USA.

Bach, *M.* (2012). "Damage Detection Assessment by means of Acousto Ultrasonics". In: *Wissenschaftstag 2012 - DLR Braunschweig*.

Bach, *M.*, *C.-P. Fritzen*, *B. Eckstein*, and *H. Speckmann* (2007). "Self-Diagnostic Capabilities of Piezoelectric Transducers Using the Electromechanical Impedance". In: *6th International Workshop of Structural Health Monitoring*. Stanford, USA.

Bach, *M.*, *N. Dobmann*, *B. Eckstein*, *M. Moix-Bonet*, and *C. Stolz* (2013). "Reliability of Co-Bonded Piezoelectric Sensors on CFRP Structures". In: *9th International Workshop on Structural Health Monitoring*. Stanford, USA, pp. 536–543.

Bach, *M.*, *N. Dobmann*, and *M. Moix-Bonet* (2016). "Damage introduction, detection and assessment at CFRP door surrounding panel". In: *Smart Intelligent Aircraft Structures (SARISTU) - Proceedings of the Final Project Conference*. Springer.

Baljak, *V.*, *K. Tei*, and *S. Honiden* (2012). "Classification of Faults in Sensor Readings with Statistical Pattern Recognition". In: *Sensorcomm 2012: 6th International Conference on Sensor Technologies and Applications*. Rome, Italy.

Benaicha, *A.*, *M. Guerfel*, *N. Bouguila*, and *K. Benothman* (2010). "New PCA-based Methodology for Sensor Fault Detection and Localization". In: *8th International Conference of Modeling and Simulation*. Hammamet, Tunisia.

Berens, *A. P.* (1988). "NDE Reliability Data Analysis". In: *ASM Metals Handbook*. 9: Nondestructive Evaluation and Quality Control. Vol. 17. ASM International, Materials Park, pp. 689–701.

Berlincourt, *D.* and *H. H. A. Krueger* (2000). *Properties of piezoelectricity - Technical Publication TP-226*. Tech. rep. Morgan Electro Ceramics.

Bhalla, *S.* and *C. K. Soh* (2004). "Electromechanical impedance modeling for adhesively bonded piezo-transducers". In: *Journal of Intelligent Material Systems and Structures* 15.12, pp. 955–972.

Blackshire, *J. L.*, *V. Giurgiutiu*, *A. Cooney*, and *J. Doane* (2005). *Characterization of Sensor Performance and Durability for Structural Health Monitoring Systems*. Tech. rep. Air Force Research Lab.

Blackshire, *J. L.*, *S. Martin*, and *A. Cooney* (2006). *Characterization and Modeling of Bonded Piezoelectric Sensor Performance and Durability in Simulated Aircraft Environments*. Tech. rep. AFRL-ML-WP-TP-2006-427. Air Force Research Lab.

Bochuang Ceramic, Inc. (2008). *Piezoelectric Ceramic Materials Data Sheet*. last acess 2016/10/15. URL: `http://www.boceramic.com/products.asp?id=179`.

Boege, *W.* and *W. Plaßmann* (2007). "Handbuch Elektrotechnik". In: Vieweg. Chap. Leitungen, pp. 950 –977.

Boehme, *B.*, *M. Roellig*, and *K. Wolter* (2010). "Measurement of viscoelastic material properties of adhesives for SHM sensors under harsh environmental conditions". In: *11th International Conference on Thermal, Mechanical Multi-Physics Simulation, and Experiments in Microelectronics and Microsystems (EuroSimE)*. Bordeaux, France.

Boller, *C.* (2000). "Next generation structural health monitoring and its integration into aircraft design". In: *International Journal of Systems Science* 31.11, pp. 1333–1349.

Buethe, *I.* (2011). "Modellgestützte Fehlererkennung an piezoelektrischen Sensoren - Validierung mit Hilfe von experimentellen Untersuchungen und FE-Berechnungen". MA thesis. Universität Siegen.

Buethe, *I.* (2015). *SARISTU - IS 13 Door Surrounding Structure - Transducer Inspection with the Electro-Mechanical Impedance (EMI)*. Tech. rep. Universität Siegen.

Buethe, *I.* and *C.-P. Fritzen* (2013). "Investigation on Sensor Fault Effects of Piezoelectric Transducers on Wave Propagation and Impedance Measurements". In: *Comsol Conference*. Rotterdam, Netherlands.

Buethe, *I.*, *M. Moix-Bonet*, *P. Wierach*, and *C.-P. Fritzen* (2014a). "Check of Piezoelectric Transducers Using the Electro-Mechanical Impedance". In: *7th European Workshop on Structural Health Monitoring*. Nantes, France.

Buethe, *I.*, *B. Eckstein*, and *C.-P. Fritzen* (2014b). "Model-based detection of sensor faults under changing temperature conditions". In: *Structural Health Monitoring* 13.2, pp. 109–119.

COMSOL (2013). *COMSOL 4.4 Reference Manual*.

Chang, *F.K.* (2014). "The need of SHM Quantification for Implementation, Keynote speach". In: *7th European Workshop of Structural Health Monitoring*. Nantes, France.

Cheng, *R. C. H.* and *T. C. Iles* (1988). "One-Sided Confidence Bands for Cumulative Distribution Functions". In: *Technometrics* 30.2, pp. 155–159.

Corporation, *Henkel* (2002). *Hysol EA 9394 - Epoxy Paste Adhesive*. Tech. rep. Henkel Cooperation.

Department of Defense (2009). *Department of Defense Handbook, Nondestructive Evaluation System Reliability Assessment, MIL-HDBK-1823*. Department of Defense.

Dobmann, *N.*, *M. Bach*, and *B. Eckstein* (2014). "Challenges of an Industrialized Acousto-Ultrasonic Sensor System Installation on Primary Aircraft Structure". In: *7th European Workshop on Structural Health Monitoring*. Nantes, France.

Dugnani, *R.* (2009). "Dynamic Behavior of Structure-mounted Disk-shape Piezoelectric Sensors Including the Adhesive Layer". In: *Journal of Intelligent Material Systems and Structures* 20.13, pp. 1553–1564.

Dunia, *R.*, *S. J. Qin*, *T. F. Edgar*, and *T. J. McAvoy* (1996). "Identification of faulty sensors using principal component analysis". In: *AiChE Journal* 42.10, pp. 2797–2812.

Eckstein, *B.* (2007). "Applikation und Funktionstest von piezoelektrischen Sensoren für zustandsüberwachende Systeme mittels Lambwellen in der Luftfahrt". Diplomarbeit. Universität Siegen.

FA SHM, *Fachausschuss Zustandsüberwachung* (2014a). "15. Sitzung des Fachausschusses Zustandsüberwachung". In: *ZfP Zeitung* 139. Ed. by *Deutsche Gesellschaft für zerstörungsfreie Werkstoffprüfung (DGZfP)*, p. 4.

FA SHM, *Fachausschuss Zustandsüberwachung* (2014b). *SHM 01 - Strukturprüfung mit geführten Wellen als Sonderform des Ultraschalls*.

Faria, *A. R.* de (2003). "The impact of finite-stiffness bonding on the sensing effectiveness of piezoelectric patches". In: *Smart Materials & Structures* 12.4, N5–N8.

Farrar, *C. R.*, *G. Park*, and *M. Todd* (2010). *Structural Health Monitoring Using Statistical Pattern Recognition - A 2 Day Short Course*. printed. Training material, Tokyo.

Farrar, *C.R.* and *K. Worden* (2012). *Structural Health Monitoring: A Machine Learning Perspective*. Wiley.

Figueiredo, *E.*, *G. Park*, *C. R. Farrar*, and *K. Worden* (2009). *Structural Health Monitoring Algorithm Comparisons Using Standard Data Sets*. Tech. rep. Los Alamos National Laboratory.

Friswell, *M. I.* and *D. J. Inman* (1999). "Sensor validation for smart structures". In: *Journal of Intelligent Material Systems and Structures* 10.12, pp. 973–982.

Fritzen, *C.-P.* (2012). *Structural Health Monitoring - Grundkonzepte, neuere Entwicklung und Anwendungsmöglichkeiten*. Vortrag im DGZfP Arbeitskreis Dresden.

Fritzen, *C.-P.*, *J. Moll*, *R. Chaaban*, *B. Eckstein*, *P. Kraemer*, *M. Klinkov*, *G. Dietrich*, *C. Yang*, *Ke. J. Xing*, and *I. Buethe* (2014). "A Multifunctional Device for Multichannel EMI and Guided Wave Propagation Measurements with PWAS". In: *7th European Workshop on Structural Health Monitoring*. Nantes, France.

Gall, *M.* (2012). "Experimentelle und numerische Untersuchungen zur Lebensdauer von flächigen piezokeramischen Sensor- / Aktor-Modulen". Dr.-Ing. dissertation. Karlsruher Institut für Technologie.

Gall, *M.*, *B. Thielicke*, and *I. Schmidt* (2009). "Integrity of piezoceramic patch transducers under cyclic loading at different temperatures". In: *Smart Materials & Structures* 18.10, p. 104009.

Gandossi, *L.* and *C. Annis* (2010). *ENIQ report No 41: Probability of Detection Curves: Statistical Best-Practices*. ENIQ TGR TECHNICAL DOCUMENT 41 - EUR24429 EN. ENIQ - European Network for Inspection and Qualification.

Gautschi, *G.* (2002). *Piezoelectric Sensorics*. Springer.

Giurgiutiu, *V.* (2007). *Structural Health Monitoring: with Piezoelectric Wafer Active Sensors*. Structures and Fracture ebook Collection Series. Elsevier Science.

Giurgiutiu, *V.* (2014). *Structural Health Monitoring: with Piezoelectric Wafer Active Sensors*. 2nd ed. Structures and Fracture ebook Collection Series. Elsevier Science.

Giurgiutiu, *V.* and *A. Zagrai* (2002). "Embedded Self-Sensing Piezoelectric Active Sensors for On-Line Structural Identification". In: *Transactions of the ASME*.

Golub, *M. V.*, *I. Buethe*, *A. N. Shpak*, *C.-P. Fritzen*, *H. Jung*, and *J. Moll* (2014). "Analysis of Lamb Wave Excitation by the Partly Debonded Circular Piezoelectric Wafer Active Sensors". In: *11th European Conference on Non-Destructive Testing (ECNDT 2014)*. Prague, Czech Republic.

Graff, *K.F.* (1975). *Wave Motion in Elastic Solids*. Dover Books on Engineering Series. Dover Publications.

HBM (2016). *Z70 Schnellklebstoff Gebrauchsanweisung*. Tech. rep. HBM.

Ha, *S.* and *F. K. Chang* (2010). "Adhesive interface layer effects in PZT-induced Lamb wave propagation". In: *Smart Materials & Structures* 19.2, p. 025006.

Heinzel, *G.*, *A. Rüdiger*, and *R. Schilling* (2002). *Spectrum and spectral density estimation by the Discrete Fourier transform (DFT), including a comprehensive list of window functions and some new flat-top windows*. Tech. rep. Hannover: Albert-Einstein-Institut.

Hooker, *M. W.* (1998). *Properties of PZT-Based Piezoelectric Ceramics Between -150 and 250°C*. Tech. rep. CR-1998-208708. NASA.

Huesch, *D.* (2015). "Erstellen eines Auswertealgorithmus zur Validierung von Schadensindikatoren piezoelektrischer Wandler für verschiedene Schadensarten". Bachelorarbeit. Universität Siegen.

IRE (1961). "IRE Standards on Piezoelectric Crystals: Measurements of Piezoelectric Ceramics". In: *Proceedings of the IRE* 49.7, pp. 1161–1169.

Ikeda, *T.* (1996). *Fundamentals of Piezoelectricity*. Oxford science publications. Oxford University Press.

Jaffe, *B.*, *W.R. Cook*, and *H.L.C. Jaffe* (1971). *Piezoelectric Ceramics*. Non-metallic solids. Academic Press Inc. Ltd.

Jones, *M.K.* and *D.L. Parker* (2011). "Detecting the Debonding of Adhesively Mounted Sensors in an Optimally Designed Structural Health Monitoring System". In: *8th International Workshop on Structural Heath Monitoring*. Ed. by *F.-K. Chang*. Stanford, USA.

Kamas, *T.*, *V. Giurgiutiu*, and *B. Lin* (2015). "E/M impedance modeling and experimentation for the piezoelectric wafer active sensor". In: *Smart Materials & Structures* 24.11, p. 115040.

Kohonen, *Teuvo* (2001). *Self-Organizing Maps*. English. Vol. 30. Springer Series in Information Sciences. Springer.

Kolerus, *J.* (2008). *Zustandsüberwachung von Maschinen - Das Lehr- und Arbeitsbuch für den Praktiker*. Vol. 4. Expert-Verlag.

Kraemer, *P.* and *C.-P. Fritzen* (2007). "Sensor fault identification using autoregressive models and the mutual information concept". In: *Damage Assessment of Structures VII* 347, pp. 387–392.

Kullaa, *J.* (2010). "Detection, identification and quantification of sensor fault". In: *Proceedings of ISMA 2010 including USD2010*. Leuven, Belgium, pp. 893–907.

Kullaa, *J.* (2011). "Distinguishing between sensor fault, structural damage, and environmental or operational effects in structural health monitoring". In: *Mechanical Systems and Signal Processing* 25.8, pp. 2976–2989.

Lamb, *H.* (1917). "On Waves in an Elastic Plate". In: *Proceedings of the Royal Society of London A: Mathematical, Physical and Engineering Sciences* 93.648, pp. 114–128.

Lanzara, *G.*, *Y. Yoon*, *Y. Kim*, and *F. K. Chang* (2009). "Influence of Interface Degradation on the Performance of Piezoelectric Actuators". In: *Journal of Intelligent Material Systems and Structures* 20.14, pp. 1699–1710.

Lee, *S.J.* (2009). "Development of Smart Piezoelectric Transducer Self-sensing, Self-diagnosis and Tuning Schemes for Structural Health Monitoring Applications". PhD thesis. Carnegie Mellon University.

Lee, *S.J.* and *H. Sohn* (2006). "Active self-sensing scheme development for structural health monitoring". In: *Smart Materials & Structures* 15.6, p. 1734.

Lee, *S.J.* and *H. Sohn* (2010). "Piezoelectric transducer self-diagnosis under changing environmental and structural conditions". In: *Ultrasonics, Ferroelectrics, and Frequency Control, IEEE Transactions on* 57.9, pp. 2017–2027.

Lee, *S.J.*, *H. Sohn*, and *J.W. Hong* (2010). "Time Reversal Based Piezoelectric Transducer Self-diagnosis Under Varying Temperature". In: *Journal of Nondestructive Evaluation* 29.2, pp. 75–91.

Li, *F.*, *Z. Xu*, *X.Y. Wei*, and *X. Yao* (2009). "Determination of temperature dependence of piezoelectric coefficients matrix of lead zirconate titanate ceramics by quasi-static and resonance method". In: *Journal of Physics D-applied Physics* 42.9, p. 095417.

Liang, *C.*, *F.P. Sun*, and *C.A. Rogers* (1994). "Coupled Electromechanical Analysis of Adaptive Material Systems - Determination of the Actuator Power-consumption and System Energy-transfer". In: *Journal of Intelligent Material Systems and Structures* 5.1, pp. 12–20.

Loendersloot, *R.*, *I. Buethe*, *P. Michaelidos*, *M. Moix-Bonet*, and *G. Lampeas* (2015). "Damage Identification in Composite Panels - Methodologies and Visualisation". In: *Smart Intelligent Aircraft Structures (SARISTU) - Proceedings of the Final Project Conference*. Springer, pp. 579–604.

Maplesoft TM (2016). *Maple online presentation*. last acess 2016/10/30. URL: `www.maplesoft.com/products/Maple/`.

Masson, *P.*, *N. Quaegebeur*, *K. Mulligan*, *P.-C. Ostiguy*, and *A. Le Duff* (2013). "Increasing the robustness in damage imaging for SHM". In: *International Symposium on SHM and NDT*. Lyon, France.

Mengelkamp, *G.* (2006). "Entwicklung einer Intelligenten Struktur - Eine Kombination globaler und lokaler Verfahren zur Schadensdiagnose". Dr.-Ing. dissertation. Universität Siegen.

Moharana, *S.* and *S. Bhalla* (2014). "Influence of adhesive bond layer on power and energy transduction efficiency of piezo-impedance transducer". In: *Journal of Intelligent Material Systems and Structures*.

Moix-Bonet, *M.*, *I. Buethe*, *M. Bach*, *C.-P. Fritzen*, and *P. Wierach* (2014). "Durability of Co-bonded Piezoelectric Transducers". In: *2nd International Conference on System-Integrated Intelligence: Challenges for Product and Production Engineering*. Bremen, Germany.

Moll, *J.* (2011). "Strukturdiagnose mit Ultraschallwellen durch Verwendung von piezoelektrischen Sensoren und Aktoren". Dr.-Ing. dissertation. Universität Siegen.

Moll, *J.*, *M. V. Golub*, *E. Glushkov*, *N. Glushkova*, and *C.-P. Fritzen* (2012). "Non-axisymmetric Lamb wave excitation by piezoelectric wafer active sensors". In: *Sensors and Actuators A-physical* 174, pp. 173–180.

Möser, *M.* (2012). *Technische Akustik*. 9th ed. Springer Vieweg, p. 537.

Möser, *M.* and *W. Kropp* (2010). *Körperschall*. 3rd ed. Springer.

Mujica, *L.E.*, *J. Rodellar*, *A. Fernandez*, and *A. Guemes* (2011). "Q-statistic and T-2-statistic PCA-based measures for damage assessment in structures". In: *Structural Health Monitoring - an International Journal* 10.5, pp. 539–553.

Mulligan, *K.*, *P. Masson*, *S. Létourneau*, and *N. Quaegebeur* (2011). "An Approach to compensate for the degradation of the monitoring system in damage detection". In: *Smart Materials, Structures and NDT in Aerospace Conference*. Montreal, Canada.

Mulligan, *K.R.*, *N. Quaegebeur*, *P. Masson*, *L.-P. Brault*, and *C. Yang* (2014). "Compensation of piezoceramic bonding layer degradation for structural health monitoring". In: *Structural Health Monitoring* 13.1, pp. 68–81.

Ostachowicz, *W.*, *P. Kudela*, *M. Krawczuk*, and *A. Zak* (2012). *Guided Waves in Structures for SHM - The Time-Domain Spectral Element Method*. Wiley.

Overly, *T. G. S.* (2007). "Development and Integration of Hardware and Software for Active-sensors in Structural Health Monitoring". MA thesis. University of Cincinnati.

Overly, *T.G.*, *G. Park*, *K.M. Farinholt*, and *C.R. Farrar* (2009). "Piezoelectric Active-Sensor Diagnostics and Validation Using Instantaneous Baseline Data". In: *IEEE Sensors Journal* 9.11, pp. 1414–1421.

PICeramic (2004). *Piezokeramische Materialien und Bauelemente*. Data Sheet. PICeramic.

PICeramic (2005). *Piezoceramic Materials - Fundamentals, Characteristics and Applications*. Data Sheet. PICeramic.

PICeramic (2007). *DuraAct - Piezoelectrische Flächenwandler für Industrie und Forschung*. Data Sheet. last access 2016/10/15. PICeramic.

Pacou, *D.*, *M. Pernice*, *M. Dupont*, and *D. Osmont* (2002). "Study of the interaction between bonded piezo-electric devices and plates". In: *1st European Workshop on Structural Health Monitoring*. Paris, France.

Park, *G.*, *C.R. Farrar*, *F.L.* di *Scalea*, and *S. Coccia* (2006a). "Performance assessment and validation of piezoelectric active-sensors in structural health monitoring". In: *Smart Materials & Structures* 15.6, pp. 1673–1683.

Park, *G.*, *C.R. Farrar*, *A.C. Rutherford*, and *A.N. Robertson* (2006b). "Piezoelectric Active Sensor Self-Diagnostics Using Electrical Admittance Measurements". In: *Journal of Vibration and Acoustics* 128.4, pp. 469–476.

Park, *G.*, *T.G.S. Overly*, and *C.R. Farrar* (2007). "Piezoelectric Active-Sensor Diagnostic and Validation Process for SHM Applications". In: *6th International Workshop on Structural Health Monitoring*. Dresden, Germany.

Park, *S.*, *C.-B. Yun*, and *D. J. Inman* (2008). "Structural health monitoring using electro-mechanical impedance sensors". In: *Fatigue & Fracture of Engineering Materials & Structures* 31.8, pp. 714–724.

Pawar, *D.N.* (2014). "Investigation on Sensor Faults based on Impedance and Acousto-Ultrasonic Measurements: Experimental Comparison of different Approaches". Studienarbeit. Universität Siegen.

PiezoSystems, *Inc.* (2011). *Introduction to Piezo Transducers*. last access 2016/10/15. URL: `http://www.piezo.com/catalog8.pdf%20files/Cat8.22,23,24,25,62,63&64.pdf`.

Pranatyasto, *T.N.* and *S.J. Qin* (2001). "Sensor validation and process fault diagnosis for FCC units under MPC feedback". In: *Control Engineering Practice* 9.8, pp. 877–888.

Ray, *A.* and *R. Luck* (1991). "An introduction to sensor signal validation in redundant measurement systems". In: *IEEE Control Systems Magazine* 11.2, pp. 44–49.

Rayleigh, *L.* (1885). "On Waves Propagated along the Plane Surface of an Elastic Solid". In: *Proceedings of the London Mathematical Society* 1, pp. 4–11.

Rencher, *A.C.* (2002). *Methods of Multivariate Analysis*. John Wiley & Sons.

Rose, *J.L.* (2004). *Ultrasonic Waves in Solid Media*. Cambridge University Press.

Rugina, *C.*, *D. Enciu*, and *M. Tudose* (2015). "Numerical and experimental study of circular disc electromechanical impedance spectroscopy signature changes due to structural damage and sensor degradation". In: *Structural Health Monitoring* 14.6, pp. 663–681.

Rytter, *A.* (1993). "Vibrational based inspection of civil engineering structures". PhD thesis. Department of Building Technology and Structural Engineering, Aalborg University.

Schmidt, *D.*, *A. Kolbe*, *R. Kaps*, *P. Wierach*, *S. Linke*, *S. Steeger*, *F.v. Dungern*, *J. Tauchner*, *C. Breu*, and *J. Newman* (2016). "Development of a Door Surround Struc-

ture with Integrated Structural Health Monitoring". In: *Smart Intelligent Aircraft Structures (SARISTU) - Proceedings of the Final Project Conference*. Springer.

Schubert, L. (2012). "Zustandsüberwachung an Faserverbundwerkstoffen mit geführten Wellen". Dr.-Ing. dissertation. Technische Universität Dresden.

Schulte, R.T. (2010). "Modellierung und Simulation von wellenbasierten Structural Health Monitoring - Systemen mit der Spektral-Elemente Methode". Dr.-Ing. dissertation. Universität Siegen.

Sirohi, J. and *I. Chopra* (2000). "Fundamental Understanding of Piezoelectric Strain Sensors". In: *Journal of Intelligent Material Systems and Structures* 11, pp. 246–257.

Sohn, H. (2009). *Piezoelectric Sensor and its Applications, Asian Pacific Summer School*. Korea Advanced Institute of Science and Technology.

Sohn, H., C.R. Farrar, F.M. Hemez, D.D. Shunk, D.W. Stinemates, B.R. Nadler, and *J.J. Czarnecki* (2004). *A Review of Structural Health Monitoring Literature: 1996-2001*. Tech. rep. Los Alamos National Laboratories.

Su, Z. and *L. Ye* (2009). *Identification of Damage Using Lamb Waves : From Fundamentals to Applications*. Springer.

Sun, T.L. and *S.N. Atluri* (2001). "Effects of piezoelectric sensor/actuator debonding on vibration control of smart beams". In: *International Journal of Solids and Structures* 38, pp. 9033–9051.

Taylor, S.G., G. Park, K.M. Farinholt, and *M.D. Todd* (2013). "Diagnostics for piezoelectric transducers under cyclic loads deployed for structural health monitoring applications". In: *Smart Materials & Structures* 22.2, p. 025024.

TiePie. Programmer's Manual - TiePie DLLs. TiePie engineering.

TiePie (2002). *HANDYSCOPE HS3 instrument description*. TiePie engineering.

TiePie (2012). *Handyscope HS3 Instrument manual*. Data Sheet.

Tinoco, H.A., A.L. Serpa, and *A.M. Ramos* (2010). "Numerical Study of the Effects of Bonding Layer Properties on Electrical Signatures of Piezoelectric Sensors". In: *Mecanica Computational* XXIX, pp. 8391–8409.

Torres-Arredondo, M.A. (2013). "Acoustic Emission Testing and Acousto-Ultrasonics for Structural Health Monitoring". Dr.-Ing. dissertation. Siegen: Universität Siegen.

Vary, A. (1988). "The Acousto-Ultrasonic Approach". English. In: *Acousto-Ultrasonics - Theory and Application*. Ed. by *Jr. Duke* J.C. Plenum Publishing, pp. 1–21.

Woelcken, P. SARISTU Proposal - Large scale Integrated Project.

Wolf, R.A. and *S. Trolier-McKinstry* (2004). "Temperature dependence of the piezoelectric response in lead zirconate titanate films". In: *Journal of Applied Physics* 95.3, pp. 1397–1406.

Worden, K. (2003). "Sensor Validation and Correction using Auto-Associative Neural Networks and Principal Component Analysis". In: *IMAC-XXI: Conference & Exposition on Structural Dynamics*. Orlando, USA.

Worden, K. and *J.M. Dulieu-Barton* (2004). "An Overview of Intelligent Fault Detection in Systems and Structures". In: *Structural Health Monitoring* 3.1, pp. 85–98.

Worden, K., W.J. Staszewski, and *J.J. Hensman* (2011). "Natural computing for mechanical systems research: A tutorial overview". In: *Mechanical Systems and Signal Processing* 25.1, pp. 4–111.

Xing, K.J. (2016). "Experiments an Simulation in Structural Health Monitoring Systems Using the E/M Impedance and Cross Transfer Function Methods". Dr.-Ing. dissertation. Universität Siegen.

Xing, *K.J.* and *C.-P. Fritzen* (2007). "Monitoring of Growing Fatigue Damage Using the E/M Impedance Method". In: *Key Engineering Materials* 347, pp. 153–158.

Xu, *Y.G.* and *G.R. Liu* (2002). "A modified electro-mechanical impedance model of piezoelectric actuator-sensors for debonding detection of composite patches". In: *Journal of Intelligent Material Systems and Structures* 13.6, pp. 389–396.

Yee, *B.G.W.*, *F.H. Chang*, *J.C. Couchman*, *G.H. Lemon*, and *P.F. Packmann* (1976). *Assessment of NDE reliability data*. Tech. rep. NASA.

Yelve, *N.P.*, *M. Mitra*, and *P.M. Mujumdar* (2014). "Higher harmonics induced in lamb wave due to partial debonding of piezoelectric wafer transducers". In: *NDT & E International* 63.0, pp. 21–27.

Zhou, *D.*, *J.K. Kim*, *D.S. Ha*, *J.D. Quesenberry*, and *D.J. Inman* (2009). "A System Approach for Temperature Dependency of Impedance- Based Structural Health Monitoring". In: *SPIE Vol. 7293*. San Diego, USA.

Appendix

A.1 Experimental and numerical setups

A.1.1 1D-LDV mounted on an x-y-table

The 1D helium-neon laser *Doppler* vibrometer (LDV) used in this work is a measurement device from *Polytec* from 1998. The device is composed of a *CLV 700* measurement head with a *CLV 800* laser unit, connected to a vibrometer controller *CLV 1000*. This controller is equipped with an output module *CLV M002*, a decoder module *CLV M030* and an input module *CLV M200*. The equipment is based on analog technique and gives an output of $\pm 10V$ proportional to the measured velocity in direction of the laser beam.

The 1D LDV is mounted on a x-y-table with a separate controller, controlling the stepping motors of the two axes (stepping motor controller *C116-4* from *isel*). It is controlled via a serial connection using *MATLAB*. The x-y-table includes a vertical clamping of the measurement samples at the top of the measurement range, which enables a clamping at one edge of the sample, e.g. a plate.

The data acquisition is also controlled with *MATLAB*. A portable two channel measurement device with arbitrary waveform generator, called *Handyscope HS3* builds the connection between vibrometer controller and computer with *MATLAB*. Moreover it is used to actuate the PWAS, which generates the wave and its velocity field. This way also the triggering is controlled. The experimental setup is displayed in fig. A.1.

The used programs to operate the experimental setup are based on previous work of *Florian Schulz* and *Dr. Jochen Moll*.

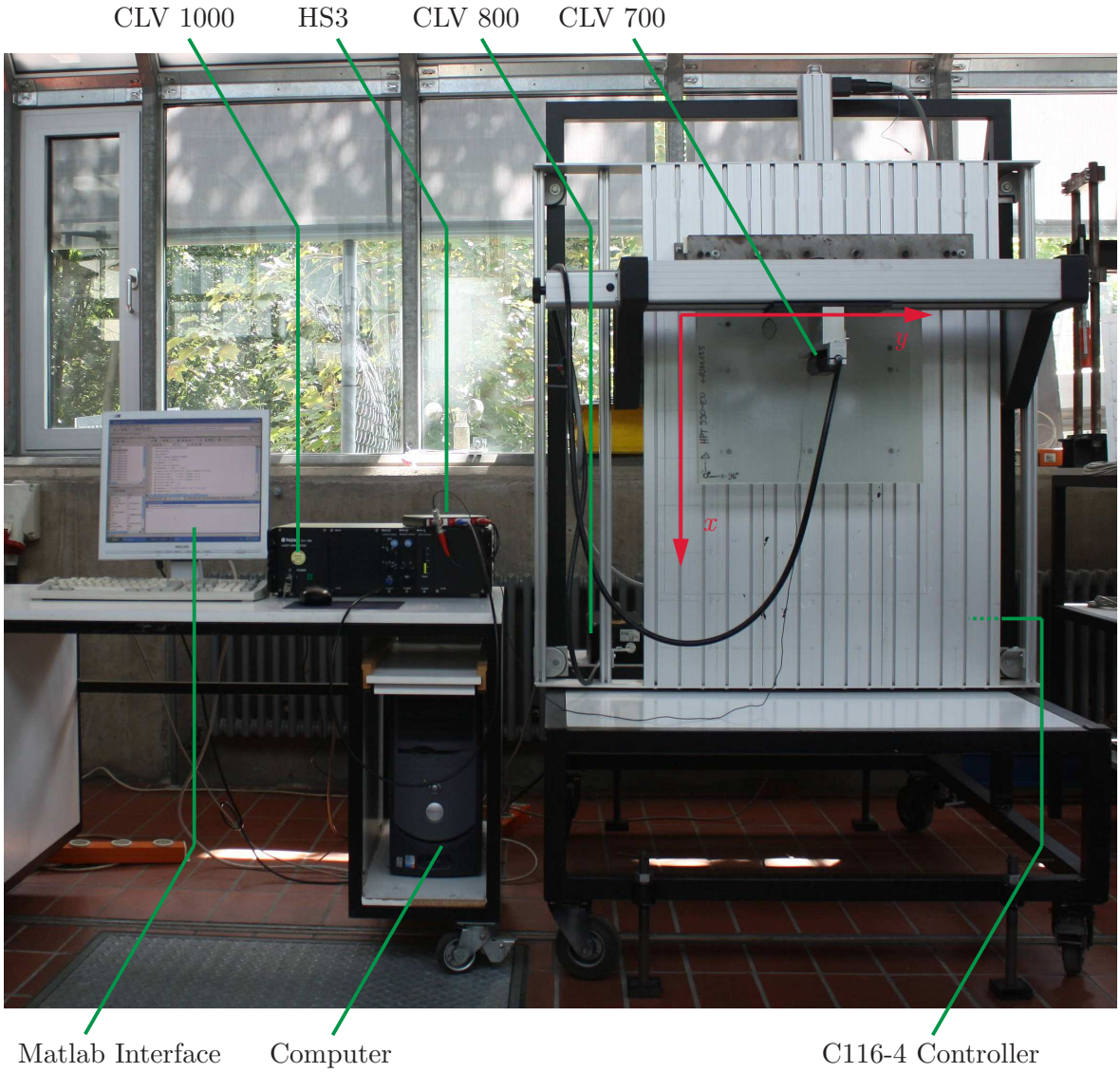

Figure A.1: Experimental setup of the 1D LDV mounted on an x-y-table

A.1.2 3D scanning LDV

The 3D scanning helium-neon LDV used in this work is a measurement device from *Polytec* called *PSV-500-3D Scanning Vibrometer*. The system includes data acquisition devices and enables to measure the velocity of an object in all three directions. With the scanning feature the device performs an automatic scan of a given surface area. The scanning heads are mounted on a test rig, developed in a student team project at the *University of Siegen*. The actuating signal is generated by an external signal generator, *Agilent Waveform Generator*. If necessary a wideband power amplifier from *krohn-hite cooperation* is included. The generated signal is also recorded from the measurement device in the *PSV-500-3D*. All recorded signals can be saved as universal file format and transferred to *MATLAB*. The experimental setup is shown in fig. A.2.

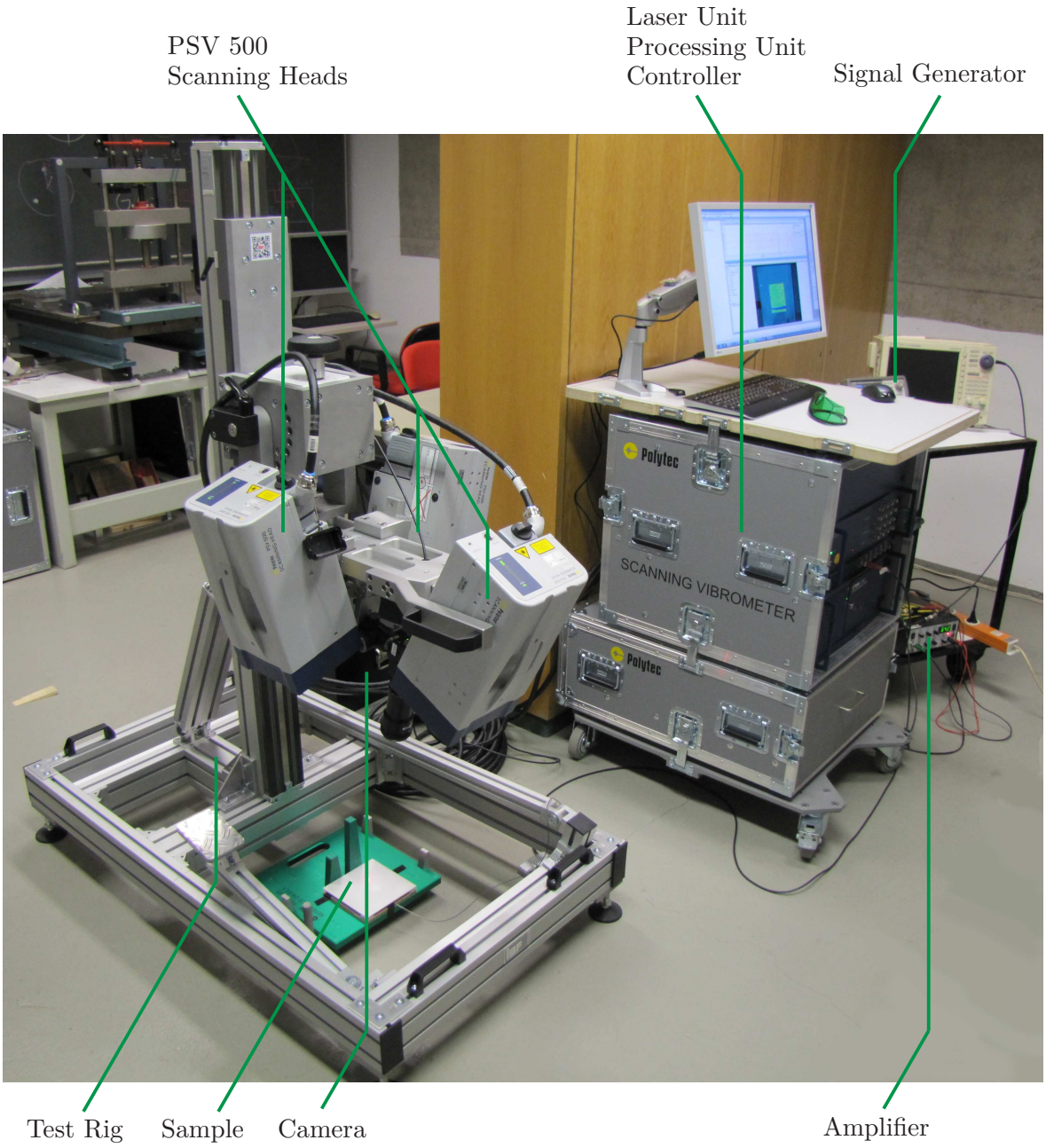

Figure A.2: Experimental setup of the 3D scanning LDV

A.1.3 TiePie Handyscope HS3

The *Handyscope HS3* is a portable two channel measurement device with an arbitrary waveform generator included. It can be used with its own software or controlled via *MATLAB* with specific libraries and dll's. A detailed documentation is given in *Programmer's Manual - TiePie DLLs*; *TiePie*, 2002; *TiePie*, 2012. The *HS3* is powered via USB connection. The output range of the waveform generator is ±12 V, with a 14 bit resolution at 50 MS/s. The data acquisition system has a scalable sensitivity in 9 steps between ±200 mV and ±80 V and a resolution of 12 bit at a sampling fre-

quency of 50 MS/s. The device has a limited memory of 128 Kbyte. In this work the device was controlled by *MATLAB*. The used codes are very much based on work of *Dr. Jochen Moll* and *Dr. Miguel Torres-Arredondo*.

A.1.4 PZT Inspector

The *PZT Inspector* is a measurement device, for the wave propagation and EMI analysis with PWAS-based SHM systems. Up to 32 channels can be measured subsequently at the same time. The device was developed in the working group of *Prof. Dr.-Ing. Claus-Peter Fritzen* to enable a low-cost automatic measurement of multiple channels. This is realized via switching of the channels within the device and the use of only two channels for data acquisition and one waveform generator. A detailed description of the device is given in (*Fritzen* et al., 2014).

To analyze the structure using guided waves, several commonly used signals can be used as actuation signal. The combinations of transducers, building the network of the SHM system, are to be defined. Compared to the usage of a single *Handyscope HS3* due to the compact design of the *PZT Inspector*, increased crosstalk is present. If crosstalk is present, the input signal can also be seen in all receiving signals. The phenomenon is common for multichannel devices, e.g., the *ScanGenie* from *Acellent*. Especially if the transducers are not located directly next to each other, this phenomenon can coped with by not taking into account the time interval at the beginning of the time series, which includes only the cross talk. If two transducers are located closely, this leads to an overlapping of the crosstalk and the sensed signal from the propagating wave. For these cases, data cleansing is necessary.

For the measurement of the EMI the electrical measurement circuit, which is presented in (*Overly*, 2007) is applied. A frequency sweep is used as input signal the measured output is proportional to the current of the PWAS. As the device is connected to the PWAS via cabling, the measured EMI spectrum includes the influences of the connecting cables.

A.1.5 Tool drop setup

To simulate tool drop, a small drop tower has been used. Either one mass of 26.2 g or one mass with an additional mass of 27.3 g can be dropped on the sample from a

specific height. 5 different heights are prepared. This way the kinetic energy can be varied between 40 mJ and 290 mJ.

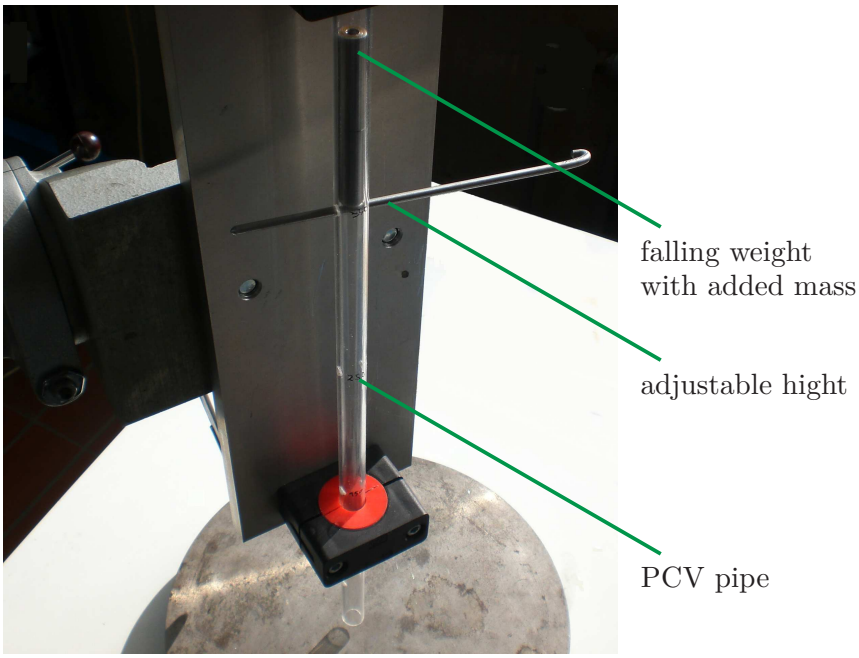

Figure A.3: Tool drop setup

The experimental setup has been part of a Bachelor thesis by *Dennis Hüsch* (*Huesch*, 2015).

A.1.6 Numerical setup - COMSOL

In this work *COMSOL multiphysics* has been used for all FE calculations. Version 4.4.0.15 is used and the standard software is extended with the structural mechanics module and the *LiveLink* for *MATLAB*. A big advantage of the FE software *COMSOL* is the implementation of multiphysics phenomena. The piezoelectric effect is already implemented in the software and an easy-to-use graphical user interface simplifies the implementation for the problem to be solved. Especially for parameter analysis the use of the interface between *MATLAB* and the *COMSOL* server, called *LiveLink* is of great use. Problems can be programmed in *MATLAB* and solved with the *COMSOL* server. Likewise problems, already built up with *COMSOL* can be exported as source code to *MATLAB*. For a parameter analysis the change of a few or a single parameter of the model in the programming can be easily realized with *MATLAB*. The entire calculation is done by the *COMSOL* server after initialization from *MATLAB*. Afterwards, the necessary output parameters can be retrieved from the *COMSOL* server via

the automated interface and reused for data analysis in *MATLAB*. This simplifies the evaluation of parameter analysis.

Meshing For the modeling of the PWAS in 3D, the PWAS itself is modeled with triangles, which are swept over the thickness of the PWAS. The same mesh is continued over the thickness of the adhesive layer. The PWAS as well as the adhesive layer is modeled with two elements over the thickness for the case described in chapter 3 and chapter 4. The mesh is continued over the thickness of the structure as well with two elements over the thickness. In the vicinity of the PWAS the structure is meshed with triangles, for the rest of the structure, quads are used. The transition from circular PWAS to rectangular structure is realized by using a so called O-grid. Fig. A.4 shows an exemplary meshing as it is realized for all numerical calculations with *COMSOL*.

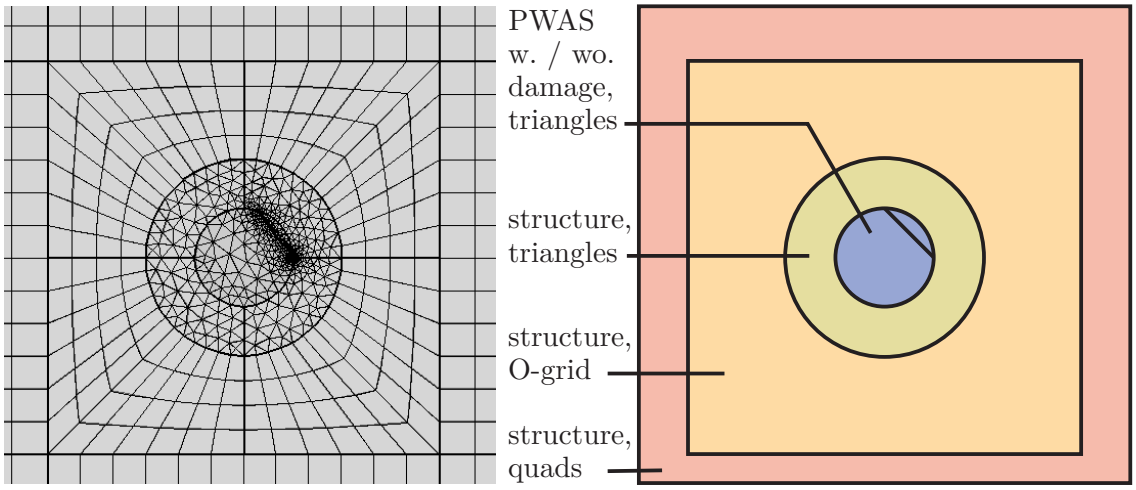

Figure A.4: Meshing of the PWAS and the structure. The third dimension is realized by sweeping the mash over the thickness.

For the 2D model of the PWAS rectangular elements are used.

Time domain For the solving of the problem in time domain an input signal has to be given to *COMSOL*. It is possible to include a *MATLAB*-based function and use the interface of *COMSOL* and *MATLAB* for this. Tests have shown, that this method is very time consuming due to the repetitive information exchange of the two software systems. Another method is the input of an interpolation list directly to *COMSOL*. It can be imported as txt-file with two columns, one being the time and the second one the parameter value. For the use of the table an interpolation of the parameters, for data points between the given data points, is given. This method is much faster and therefore used in this work. A disadvantage is the necessity of separate txt-files for different frequencies or number of cycles within the windowed cosine train.

In the time domain several solver configurations are implemented in *COMSOL*. A series of tests regarding the stability of the calculations lead to this configuration: For the method, used for time stepping, the *generalized alpha* method was used. The steps are given manually by a fixed time step and the amplification factor for higher frequencies was chosen to be 0.75. For other configurations the problem easily gets numerical unstable leading to troubles in the parameter analysis and no or completely incorrect results.

For some cases the size of the plate can be modeled smaller than the size of the original structure. To minimize the effects on the result a parameter study has to be made to find a sample size at which the first wave package and the reflections at edges do not overlap and a change of size has negligible effect on the stiffness of the structure, as it is seen by the PWAS.

Frequency domain In the frequency domain frequency spectra of parameters can be calculated. To calculate the admittance spectrum the implementation of damping for electrical and mechanical parameters is of major importance. For the models used in this work, loss factors for specified parameters are defined. Other possibilities include *Rayleigh* damping and isotropic loss factor for mechanical parameters. In the frequency domain the standard solver and its configurations have been chosen, which is the *PARADISO* solver. These configurations have proven to be numerically stable. Dependent variables are the displacement vector for all nodes and additionally the voltage for all nodes belonging to a piezoelectric material.

A.2 Derivations

A.2.1 Wave speeds for different types of waves

- axial bar, non-dispersive

$$c = \sqrt{\frac{E}{\rho}} \tag{A.1}$$

- flexural waves in beams, dispersive

$$c_{ph} = \left(\frac{EI}{m'}\right)^{\frac{1}{4}} \sqrt{\omega} \tag{A.2}$$

$$I = \frac{h^3 b}{12} \tag{A.3}$$

$$m' = bh\rho \tag{A.4}$$

$$c_g = 2c_{ph}\left(\omega\right) \tag{A.5}$$

- straight crested axial plate wave, non-dispersive

$$c_L = \sqrt{\frac{1}{1-\nu^2}\frac{E}{\rho}} \tag{A.6}$$

- straight crested shear plate waves, non-dispersive

$$c_s = \sqrt{\frac{G}{\rho}} \tag{A.7}$$

- straight crested flexural plate waves, dispersive

$$c_f = \left(\frac{Eh^2}{12\rho\left(1-\nu^2\right)}\right)^{\frac{1}{4}} \sqrt{\omega} \tag{A.8}$$

- pressure wave in unbounded elastic body, non-dispersive

$$c_L = c_p = \sqrt{\frac{1-\nu}{\left(1+\nu\right)\left(1-2\nu\right)}\frac{E}{\rho}} \tag{A.9}$$

- shear wave in unbounded elastic body, non-dispersive

$$c_t = c_s = \sqrt{\frac{1}{2\left(1+\nu\right)}\frac{E}{\rho}} = \sqrt{\frac{G}{\rho}} \tag{A.10}$$

A.2.2 Derivation of the admittance Y_p for a rectangular PWAS

To get to the following equation, several steps are necessary, see (*Ikeda*, 1996; *Giurgiutiu*, 2014).

$$Y_p(\omega) = i\omega C_0 \left(1 - k_{31}^2 \left(1 - \frac{\tan(k\frac{l}{2})}{k\frac{l}{2}}\right)\right) \tag{A.11}$$

Starting from the piezoelectric equations in *Cartesian* coordinates:

$$S_1 = s_{11}^E T_1 + d_{31} E_3 \tag{A.12}$$

$$D_3 = \varepsilon_{33}^T E_3 + d_{31} T_1. \tag{A.13}$$

Using the equation of motion for longitudinal vibration in x-direction:

$$\rho \frac{\partial^2 u_1}{\partial t^2} = \frac{1}{s_{11}^E} \frac{\partial^2 u_1}{\partial x_1^2} \tag{A.14}$$

$$\frac{1}{c^2} \frac{\partial^2 u_1}{\partial t^2} = \frac{\partial^2 u_1}{\partial x_1^2}, \tag{A.15}$$

$c = \sqrt{\frac{1}{\rho s_{11}^E}}$ being the wave speed of the 1D axial wave in a bar. The equation of motion can be solved with separation of variables.

$$\begin{aligned} u_1 &= X_{u1}(x_1) T_{u1}(t) \\ &= \left[A \sin(k x_1) - B \cos(k x_1)\right] T_{u1}(t) \end{aligned} \tag{A.16}$$

with the wave number $k = \frac{\omega}{c}$. To solve this equation boundary conditions have to be used. The stress is zero at the edges of the transducer, $x_1 = \pm l/2$. The displacement is zero for $x_1 = 0$ for symmetry reasons. Moreover the time dependent part is neglected in the first place. Equation (A.12) is used

$$T_1 = \frac{S_1}{s_{11}^E} - \frac{d_{31}}{s_{11}^E} E_3 \tag{A.17}$$

$$0 = \frac{S_1|_{l/2}}{s_{11}^E} - \frac{d_{31}}{s_{11}^E} E_3 \tag{A.18}$$

$$S_1|_{l/2} = d_{31} E_3 = d_{31} \frac{V}{h} \tag{A.19}$$

using u_1:

$$u_1 = A\sin(kx_1) \tag{A.20}$$

$$S_1 = \frac{\partial u_1}{\partial x_1} = kA\cos(kx_1) \tag{A.21}$$

$$S_1|_{l/2} = kA\cos(k\frac{l}{2}) = d_{31}\frac{V}{h} \tag{A.22}$$

This leads to

$$A = d_{31}\frac{V}{h}\frac{1}{k\cos(k\frac{l}{2})} \tag{A.23}$$

$$u_1 = d_{31}\frac{V}{h}\frac{\sin(kx_1)}{k\cos(k\frac{l}{2})}. \tag{A.24}$$

Equation (A.13) now can be used to calculate the current I.

$$I = \dot{Q} \tag{A.25}$$

$$Q = \int_A D_3 \mathrm{d}A \tag{A.26}$$

$$D_3 = \varepsilon_{33}^T E_3 + d_{31}\left(\frac{S_1}{s_{11}^E} - \frac{d_{31}}{s_{11}^E}E_3\right) \tag{A.27}$$

$$= \varepsilon_{33}^T E_3\left(1 - k_{31}^2\right) + \frac{d_{31}}{s_{11}^E}S_1 \tag{A.28}$$

$$k_{31} = \frac{d_{31}^2}{s_{11}^E \varepsilon_{33}^T} \tag{A.29}$$

with k_{31} being the electromechanical coupling coefficient.

$$I = i\omega\int_A D_3 \mathrm{d}A \tag{A.30}$$

$$= i\omega\int_l\int_w \varepsilon_{33}^T E_3\left(1 - k_{31}^2\right)\mathrm{d}x_2\mathrm{d}x_3 + i\omega\int_l\int_w \frac{d_{31}^2 V}{s_{11}^E h}\frac{\cos(kx_1)}{k\cos(k\frac{l}{2})}\mathrm{d}x_2\mathrm{d}x_3 \tag{A.31}$$

$$= i\omega\varepsilon_{33}^T\frac{V\,w\,l}{h}\left(1 - k_{31}^2\right) + i\omega\frac{d_{31}^2 V\,w}{s_{11}^E h}\frac{2\sin(k\frac{l}{2})}{k\cos(k\frac{l}{2})} \tag{A.32}$$

Using the capacitance $C_0 = \varepsilon_{33}\frac{wl}{h}$ simplifies to

$$I = i\omega V C_0\left(1 - k_{31}^2\right) + i\omega V\frac{C_0}{l}k_{31}^2\frac{2}{k}\tan(k\frac{l}{2}). \tag{A.33}$$

This leads to an admittance of

$$Y_p(\omega) = i\omega C_0 \left(1 - k_{31}^2 \left(1 - \frac{\tan(k\frac{l}{2})}{k\frac{l}{2}}\right)\right) \tag{A.34}$$

for the rectangular PWAS showing longitudinal vibration.

A.2.3 Derivation of the capacitance and the inductance to model the EMI spectrum with a simple electric circuit

To obtain the known formula for Y_p the following definitions for C_0, C_1 and L_1 are necessary to model according to fig. 2.17 without *Ohm*ic resistance, see (*Ikeda*, 1996).

$$Y_p(\omega) = i\omega C_0 \left(1 - k_{31}^2 \left(1 - \frac{\tan(k\frac{l}{2})}{k\frac{l}{2}}\right)\right) \tag{A.35}$$

$$C_0 = \frac{\varepsilon_3 3^T}{t}(1 - k_{31}^2) \tag{A.36}$$

$$C_1 = \frac{8}{\pi^2}\frac{k_{31}^2}{1 - k_{31}^2}C_0 \tag{A.37}$$

$$L_1 = \frac{1}{\omega^2 C_1} \tag{A.38}$$

$$Y_p(\omega) = i\omega C_0 + \frac{1}{i\left(\omega L_1 - \frac{1}{\omega}C_1\right)} \tag{A.39}$$

A.2.4 Derivation of the equation of motion for a disk-shaped transducer

Based on fig. 4.9 here the derivation of eq. (4.14) is given. All derivatives of θ have already been erased.

$$\mathrm{d}m\ddot{u}_r = \sum \mathrm{d}F_r \tag{A.40}$$

$$\mathrm{d}m = \mathrm{d}V\rho = \mathrm{d}r\, r\mathrm{d}\theta\mathrm{d}z\rho \tag{A.41}$$

$$\ddot{u}_r = -\omega^2 u_r \tag{A.42}$$

$$-\rho\mathrm{d}r\, r\mathrm{d}\theta\mathrm{d}z\, \omega^2 u_r = -T_{rr} r\mathrm{d}\theta\mathrm{d}z + \left(T_{rr} + \frac{\partial T_{rr}}{\partial r}\mathrm{d}r\right)(r + \mathrm{d}r)\,\mathrm{d}\theta\mathrm{d}z \tag{A.43}$$

$$+ (-T_{\theta r} + T_{\theta r})\cos\left(\frac{\mathrm{d}\theta}{2}\right)\mathrm{d}r\mathrm{d}z \tag{A.44}$$

$$- T_{\theta\theta}\sin\left(\frac{\mathrm{d}\theta}{2}\right)\mathrm{d}r\mathrm{d}z - T_{\theta\theta}\sin\left(\frac{\mathrm{d}\theta}{2}\right)\mathrm{d}r\mathrm{d}z \tag{A.45}$$

with $\sin\left(\frac{\mathrm{d}\theta}{2}\right) = \frac{\mathrm{d}\theta}{2}$ for small angles:

$$-\rho \mathrm{d}r\, r\mathrm{d}\theta \mathrm{d}z\, \omega^2 u_r = T_{rr}\mathrm{d}r\mathrm{d}\theta\mathrm{d}z + \frac{\partial T_{rr}}{\partial r}\mathrm{d}r\,(r+\mathrm{d}r)\,\mathrm{d}\theta\mathrm{d}z - 2T_{\theta\theta}\frac{\mathrm{d}\theta}{2}\mathrm{d}r\mathrm{d}z \tag{A.46}$$

$$-\rho r\omega^2 u_r = T_{rr} + \frac{\partial T_{rr}}{\partial r}r + \frac{\partial T_{rr}}{\partial r}\mathrm{d}r - T_{\theta\theta} \tag{A.47}$$

$$-\rho\omega^2 u_r = \frac{\partial T_{rr}}{\partial r} + \frac{T_{rr} - T_{\theta\theta}}{r}, \tag{A.48}$$

neglecting $\frac{\partial T_{rr}}{\partial r}\mathrm{d}r$ which is small in the second order. For the next step eqs. (4.11) and (4.12) are used. The derivative of eq. (4.11) leads to

$$\frac{\partial T_{rr}}{\partial r} = \frac{1}{s_{11}^E\,(1-\nu^2)}\left(\frac{\partial^2 u_r}{\partial r^2} + \nu\frac{\partial u_r}{\partial r}\,\frac{1}{r} - u_r\frac{1}{r^2}\nu\right) \tag{A.49}$$

Placed into eq. (A.48):

$$\begin{aligned}-\rho\omega^2 u_r =& \frac{1}{s_{11}^E\,(1-\nu^2)}\left[\frac{\partial^2 u_r}{\partial r^2} + \nu\frac{\partial u_r}{\partial r}\,\frac{1}{r} - u_r\frac{1}{r^2}\nu\right.\\ &\left. + \frac{1}{r}\left(\frac{\partial u_r}{\partial r} + \nu\frac{u_r}{r} - d_{31}E_z\,(\nu+1) - \nu\frac{\partial u_r}{\partial r} - \frac{u_r}{r} + d_{31}E_z\,(\nu+1)\right)\right]\end{aligned} \tag{A.50}$$

$$\begin{aligned}-\rho\omega^2 u_r =& \frac{1}{s_{11}^E\,(1-\nu^2)}\left[\frac{\partial^2 u_r}{\partial r^2} + \nu\frac{1}{r}\,\frac{\partial u_r}{\partial r} - \nu\frac{u_r}{r^2} + \frac{1}{r}\left(\frac{\partial u_r}{\partial r}\,(1-\nu) + \frac{u_r}{r}\,(\nu-1)\right)\right]\\ =& \frac{1}{s_{11}^E\,(1-\nu^2)}\left[\frac{\partial^2 u_r}{\partial r^2} + \frac{1}{r}\,\frac{\partial u_r}{\partial r} - \frac{u_r}{r^2}\right]\end{aligned} \tag{A.51}$$

Using the velocity of the 2D straight crested axial plate wave $c_L{=}c = \sqrt{\frac{1}{(1-\nu^2)s_{11}^E\rho}}$:

$$-\frac{\omega^2}{c^2}u_r = \frac{\partial^2 u_r}{\partial r^2} + \frac{1}{r}\,\frac{\partial u_r}{\partial r} - \frac{u_r}{r^2} \tag{A.52}$$

A.3 Material parameters

A.3.1 Piezoelectric materials

Material type		PIC 151	PIC 155	PIC 255
piezoelectric constants ($10^{-12}\ \frac{\mathrm{C}}{\mathrm{N}}$)	d_{31}	-210	-165	-180
	d_{33}	-500	360	400
	d_{15}	–	–	550
compliance ($10^{-12}\ \frac{\mathrm{m}^2}{\mathrm{N}}$)	s_{11}^E	15.0	15.6	16.1
	s_{33}^E	19.0	19.7	20.7
mechanical quality factor	Q_m	100	80	80
relative permittivity	$\varepsilon_{11}^T/\varepsilon_0$	1980	1400	1650
	$\varepsilon_{33}^T/\varepsilon_0$	2400	1450	1750
dielectric loss factor (10^{-3})	$\tan\delta$	20	20	20
Poisson's ratio	ν	0.34	0.34	0.34
density	$\rho(\ \frac{\mathrm{kg}}{\mathrm{m}^3})$	7800	7800	7800

Table A.1: Material parameters for PIC 151, PIC 155 and PIC 255 according to *PICeramic*, 2005

$\varepsilon_0 = 8.85\ 10^{-12}\ \frac{\mathrm{F}}{\mathrm{m}}$

A.3.2 Material parameters of a cable

For the modeling of the cabling, the following values represent a typical cable, used in this work.

characteristic impedance	Z_{char}	Ω	50
capacitance per m of cable	C_c	$\frac{\mathrm{F}}{\mathrm{m}}$	$95 \cdot 10^{-12}$
resistance per m of cable	R_c	$\frac{\Omega}{\mathrm{m}}$	$310 \cdot 10^{-3}$
conductivity of the isolation per m of cable	G_c	$\frac{1}{\Omega\mathrm{m}}$	$2 \cdot 10^{-12}$

Table A.2: Material parameters for a cable